

# Computational Description of Chemical Bond Formation Using Neural-Network Potentials: H-Atom Scattering from Graphene

Dissertation

for the award of the degree

“Doctor rerum naturalium”

of the Georg-August-Universität Göttingen

within the doctoral program Chemistry

of the Georg-August University School of Science (GAUSS)

submitted by

**Sebastian Wille**

from **Rinteln, Deutschland**

Göttingen, May, 2022

## **Thesis Committee**

### **Supervisor:**

Prof. Dr. Alec M. Wodtke  
Physikalische Chemie I  
Institut für Physikalische Chemie

### **Second Supervisor:**

Prof. Dr. Jörg Behler  
Theoretische Chemie  
Institut für Physikalische Chemie

### **Third Supervisor:**

Dr. Oliver Bünermann  
Physikalische Chemie I  
Institut für Physikalische Chemie

## **Examination Board**

### **Reviewer:**

Prof. Dr. Alec M. Wodtke  
Physikalische Chemie I  
Institut für Physikalische Chemie

### **Second Reviewer:**

Prof. Dr. Jörg Behler  
Theoretische Chemie  
Institut für Physikalische Chemie

### **Further Members of the Examination Board**

Prof. Dr. Burkhard Geil  
Biophysikalische Chemie  
Institut für Physikalische Chemie

Prof. Dr. Ricardo A. Mata  
Computerchemie und Biochemie  
Institut für Physikalische Chemie

Prof. Dr. Claus Ropers  
Festkörper und Nanostrukturen  
IV. Physikalisches Institut

Prof. Dr. Martin Suhm  
Physikalische Chemie II  
Institut für Physikalische Chemie

**Date of the oral examination: 29.06.2022**



---

---

# Quotes

I had to visit Nepal to realize that staircases are not for me.

*(Nathan Daelman)*

In the end, everything will converge

*(Jan Weinreich)*

Also 1 kilo flops, pathetic...

*(Martin L. Paleico)*

unleash your potential

*(Author unknown)*

Don't talk about it, just fit it

*(Author unknown)*

The way to get started is to quit talking and begin doing

*(Walt Disney)*

Success is not final, failure is not fatal: it is the courage to continue that counts.

*(Winston S. Churchill)*

The greatest glory in living lies not in never falling, but in rising every time we fall

*(Nelson Mandela)*

If you are going through hell, keep going.

*(Winston S. Churchill)*

To improve is to change; to be perfect is to change often.

*(Winston S. Churchill)*

Now this is not the end. It is not even the beginning of the end. But it is, perhaps, the end of the beginning.

*(Winston S. Churchill)*

I am like a tank - slowly but surely

*(Dima)*

The most beautiful things about human beings is that they give meaning to everything they do and that is around them. We give meaning to life itself. We are nothing more than numerous cells and chemical reactions strung together by biology and yet we spend our lives creating art dedicated to and searching the world (and ourselves) with the goal of uncovering the meaning for the lives that we are living. While pessimistic, the above quote is true. Nothing inherently has meaning, but the meaning that we give it makes it wonderful and worth having.

*(Bioshock Infinite)*

Your aim must be to take All-under-Heaven ('Tianxia') intact. Thus your troops are not worn out and your gains will be complete. This is the art of offensive strategy.

---

*(Sun Tzu, The Art of War, Chapter III, Line 11)*

I may not have gone where I intended to go, but I think I have ended up where I needed to be.

---

*(Douglas Adams, The Long Dark Tea-Time of the Soul)*

I love deadlines. I love the whooshing noise they make as they go by.

---

*(Douglas Adams, The Salmon of Doubt)*

There is a theory which states that if ever anyone discovers exactly what the Universe is for and why it is here, it will instantly disappear and be replaced by something even more bizarre and inexplicable. There is another theory which states that this has already happened.

---

*(Douglas Adams, The Restaurant at the End of the Universe)*

Space is big. You just won't believe how vastly, hugely, mind-bogglingly big it is. I mean, you may think it's a long way down the road to the chemist's, but that's just peanuts to space.

---

*(Douglas Adams, The Hitchhiker's Guide to the Galaxy)*

Kōdai-in, formerly known as **Nene** (this is the origin of the name of the subroutine inside the MDT2 framework) was an aristocrat and Buddhist nun, founder of the temple Kōdai-ji in Kyoto, Japan. She was formerly the principal samurai wife of Toyotomi Hideyoshi, a man who would later become one of the three great unifiers of Japan. As the matriarch figure of the Toyotomi clan, she led all diplomatic affairs that had to do with the imperial court, and monitored the daimyos' families who were being held hostage at Osaka Castle. As the wife of Hideyoshi, Nene is most famous for being one of his closest aides and confidantes. The daughter of a samurai, she had many familial connections that netted Hideyoshi several retainers. Nene was known to have been an intelligent woman who, at times, advised Hideyoshi on matters of governance by sending him letters. When Hideyoshi unified Japan, Nene often went with him to attend parties. She was courteous and respectful to her guests on every occasion. After her death in 1624 and burial within the temple compound, she was posthumously given the name of Hikari no Tenshi or "Angel of Light".

---

*(taken from: <https://en.wikipedia.org/wiki/Kōdai-in> on September 29th 2021)*

Strive for Excellence

---

*(Tsz Wai Ko (Kenko))*

Die Kunst des Verhandelns ist es, seinen Gegenüber so schnell über den Tisch zu ziehen, dass er die dabei entstehende Reibungshitze als Nestwärme empfindet.

---

*(Nils Hertl)*

I'm living the healthy lifestyle

---

*(Nils Hertl)*

Keep fighting

---

*(Tsz Wai Ko (Kenko))*

it's all wrong, it's all a lie...

---

*(Martin L. Paleico)*

---

nihil verum est, omnia licet – nothing is true, everything is allowed

---

*(Friedrich Nietzsche, Thus spake Zarathustra)*

Omnia rerum principia parva sunt – The beginnings of all things are small

---

*(Marcus Tullius Cicero (106-43))*

a minore ad maius – from smaller to bigger

---

*(famous Latin phrase)*

You don't drive mother nature, you ride it

---

*(Theofanis Kitsopoulos)*

When you can measure what you are speaking about, and express it in numbers, you know something about it

---

*(William Thomson, 1st Baron Kelvin (Lord Kelvin))*

Scientists should always state the opinions upon which their facts are based

---

*(Author unknown)*

The only way to survive a mad world is to embrace the madness

---

*(Victor Strand)*

You're only given a little spark of madness, you mustn't lose it

---

*(Robin Williams)*

There is still a lot to learn and there is always great stuff out there, even mistakes can be wonderful

---

*(Robin Williams)*

Never give up – never surrender.

---

*(Mathasar, 'Galaxy Quest')*



---

---

# Acknowledgments

First of all, I would like to thank my supervisor Prof. Alec Wodtke. Not only for the opportunity to spend many exciting years on a very interesting and beneficial project, but also in a very heart-warming and delightful group which manages albeit their sheer size to deeply welcome everybody. From the very first day on, you have seen something in me, which even I was never aware of. Although it was a very hard task, but your burning passion was able to help me overcoming any obstacles and the fire was also spreading on me. I didn't found just work, but a passion. Without that I might not be able to make it till the very end.

Many thanks goes to Sascha, who guided me during the whole time of my PhD. I learned so many work and non-work related things from you and would like to once more thank you very much that I could always talk to you and you never stopped pushing me back in the right direction. Whenever I needed you the most, you were there and helped me out. Greetings to your wife.

Although I am not officially part of the Behler group, over the years at some point I felt as a member of the group. Many thanks to Jörg and his group who helped me to never feel like a guest, but part of the group. Like Sascha, you also never stopped helping me, guiding me and you were also there whenever I needed to talk. Keep on the welcoming atmosphere you created, it was a pleasure to work with you. And also thanks a lot for the non-work related talks and meetings, this really helped to not feel alone and overcome all obstacles.

I would like to thank Prof. Dr. Claus Ropers, Prof. Dr. Martin Suhm, Prof. Dr. Burkhard Geil and Prof. Dr. Ricardo Mata to be part of my examination board and for your survey.

Best regards to my office co-workers and friends Martin, Kenko, Jan, Nathan, Marco, Jascha, Sven and Nils.

In the future, I will miss the routine soccer plays, the weekly happy hour parties, the out-of-work activities and furthermore the atmosphere of

I have met so many amazing people in not only one but three work groups. My special thanks are for the whole Wodtke, the whole Behler and the whole Mata group. I will miss our get-togethers after work, the board game evenings and the off-work meetings with so many amazing people. I did not only found collaborators, workmates but especially best friends for life.

Once more, I would like to thank my proofreaders Dr. Martin Paleico, Dr. Nils Hertl and Dr. Tsz Wai Ko for your time, comments and suggestions on the way to the finish.

Mostly forgotten, but a very honest thank you very much to all the Secretaries I had the privilege to meet during my years. They were doing much more than just their job, I always felt their passion and deep care for the group. i) Wodtke group: From the MPI office I greatly thank Inge for becoming a friend I love to share my thoughts with, Aria for giving her best to follow big foot steps. In the University office I thank Kerstin for her ever welcoming atmosphere she created. Greetings to your daughter! I furthermore thank Ilke for her life-affirming way that also touches me. Greetings to your son! ii) Behler group: I thank Iris for also doing her best to fit big foot steps. Your friendly way is heart-warming. iii) Mata group: Last but

definitely not least I very much thank Karin for her mother-like guidance. I deeply appreciate all the countless things you did for me. Although we are not related, but it always felt like there is a much deeper bond. I will miss your own way and all the people I met because of you. I wish you a wonderful life and enjoy your retirement, you deserve it!

I would like to honorable mention Ricardo Mata. During my Bachelor and Master thesis he guided me and stopped my struggling to quit my studies. Without the amazing topic and time I spend in your group I wouldn't be here. Although I didn't stayed with you for my PhD, your spirit guided me through even harder times. Without your recommendation, I might not be part of the Wodtke group. Without explicitly said, I dedicate my thesis not entirely but to a great part to you and once more thank you very much from the bottom of my heart. This also counts for the amazing people I had the honour to meet during my stays in your group. At this point I would like to also and once more thank my former supervisors Johannes M. Dieterich (Bachelor) and Mirko Paulikat (Master).

I would also say many thanks to Rainer. Over the years, I honestly enjoyed our discussions, grumbling about politics and anything else. I learned so many work and non-work related things, which I will carry my whole life in deep respect and appreciation of your work. Like the secretaries, you do so much more than just your job, keep on!

And I thank all of you for not just doing your job, you do so much more for all of us. With you all, we are getting a family.

Last but definitely not least I would like to thank my whole family who never grew tired in supporting me. Especially a very warm and grateful thank you for everything to my parents for their seemingly infinite morally and mentally support over all the years during my studies to the very end. Thank you for giving me a safe haven during the pandemic.

---

---

# Abstract

When a hydrogen or a deuterium atom is interacting with a graphene surface during scattering events, its energy loss determines if the projectile will be adsorbed or scattered. The energy loss highly depends on the initial conditions of the projectile and the surface. Unlike for metal and insulator surfaces, a barrier to C–H bond formation is involved, which is the movement of a single carbon atom out of the surface plane (puckering) and by that rehybridization of the C-atom from  $sp^2$  to  $sp^3$ . In the experiments, a bimodal branching of the translational energy and scattering angle distribution is observed. One signal corresponds to a quasi-elastic channel, where the impinging atom loses only a minor fraction of its initial kinetic energy. The location of this channels' maximum intensity can be reasonably well estimated with a simple binary collision model. The second signal corresponds to inelastic scattering events, where the projectile loses a large fraction of its initial kinetic energy. Previous studies using a reactive empirical bond order potential are in good agreement with incidence kinetic energies of  $\approx 1$  eV, but could not reproduce the distribution of scattering with  $\approx 2$  eV incidence kinetic energy at given incidence conditions.

Machine learning potentials are best known to bridge the gap between accuracy and performance. To study the bond formation of H- and D-atoms with graphene with high dimensional neural network potentials, I implemented the existing description of neural network potentials in our developed molecular dynamics program and generated a high-dimensional neural network for H-atoms at a free-standing graphene surface. The performance of this new potential to accurately describe the experiment is much better than the previously reported reactive bond order potential. The neural network potential is able to capture the correct branching of the two channels observed in the experiment and can even reproduce subtle differences seen in energy loss distributions for different hydrogen isotopes. But still, systematic differences can be seen, especially for small incidence polar angles, where out-of-plane scattering is more likely.

New experiments for a H-atom scattering along the surface normal indicate that nuclear quantum effects might play a more important role in the scattering dynamics than previously anticipated. Therefore, classical and path-integral based simulations are compared to full-quantum mechanical simulations based on wave-package propagation. Classical simulations are incapable to predict the correct energy loss and scattering distributions from experiment for higher incidence kinetic energies of the projectile. Path-integral based simulations improve the description, but only taking all quantum effects into account offers the best description of H-atom scattering from graphene with normal incidence direction.





---

---

# Table of Contents

<b>List of Abbreviations</b>	<b>xiii</b>
<b>1 Introduction</b>	<b>1</b>
<b>2 Theory</b>	<b>5</b>
2.1 Born Oppenheimer Approximation . . . . .	5
2.2 Density Functional Theory . . . . .	7
2.2.1 Dispersion Correction . . . . .	9
2.3 Neural Network Potentials . . . . .	10
2.3.1 Overview . . . . .	10
2.3.2 Supervised Learning . . . . .	10
2.3.3 Feed-Forward Neural Networks . . . . .	11
2.3.4 High-Dimensional Neural Network Potentials . . . . .	14
2.4 Molecular Dynamics . . . . .	19
2.4.1 Classical Dynamics . . . . .	19
2.4.2 Velocity-Verlet integration scheme . . . . .	20
2.4.3 Thermostats . . . . .	21
2.4.4 Ring Polymer Molecular Dynamics . . . . .	21
2.4.5 Path Integral Langevin Equation . . . . .	24
<b>3 Computational Details</b>	<b>27</b>
3.1 VASP . . . . .	27
3.1.1 INCAR . . . . .	27
3.1.2 KPOINTS . . . . .	28
3.1.3 POSCAR . . . . .	28
3.1.4 POTCAR . . . . .	28
3.2 FHI-aims . . . . .	28
3.2.1 control.in . . . . .	29
3.2.2 geometry.in . . . . .	29
3.3 RuNNer . . . . .	29
3.3.1 input.nn . . . . .	29
3.3.2 input.data . . . . .	30
3.4 md_tian_xia . . . . .	31
3.5 md_tian_xia_2 . . . . .	31
3.5.1 md_tian.inp . . . . .	33
3.5.2 nene.pes . . . . .	34
3.6 Implementation of NN into MDT2 . . . . .	35
3.7 Improvements of MDT2 . . . . .	37
3.8 Reference Data Set . . . . .	39

3.9	Molecular Dynamics Simulations . . . . .	41
3.10	Ring Polymer Molecular Dynamics Simulations . . . . .	41
<b>4</b>	<b>Studying the C–H bond formation by analyzing scattering experiments</b>	<b>45</b>
4.1	Previous Studies . . . . .	46
4.1.1	Graphene . . . . .	46
4.1.2	Atom Scattering Experiments . . . . .	48
4.2	HDNN-PES . . . . .	53
4.2.1	Evaluation of the quality of the PES . . . . .	53
4.2.2	Discussion of the underlying DFT data . . . . .	62
4.3	Classical MD Simulations . . . . .	68
4.3.1	Comparison to RAT Experiment . . . . .	72
4.3.2	Comparison to HBEAM Experiment . . . . .	137
4.4	Quantum Simulations . . . . .	142
4.4.1	Comparison to RAT Experiment . . . . .	142
4.4.2	Comparison to HBEAM Experiment . . . . .	145
<b>5</b>	<b>Conclusions and Outlook</b>	<b>153</b>
<b>A</b>	<b>Appendix</b>	<b>155</b>
A.1	High-dimensional neural network potential energy surface . . . . .	155
A.1.1	Symmetry Functions for the H on Graphene System . . . . .	155
A.1.2	Architecture . . . . .	156
A.1.3	Dispersion plots . . . . .	157
A.2	Input files . . . . .	159
A.3	Random number generators . . . . .	169
A.4	DFT data . . . . .	170
A.5	Determining the timestep in molecular dynamics simulations . . . . .	175
A.6	Energy loss pathways example trajectories . . . . .	176
A.7	Scattering trajectories . . . . .	180
	<b>Bibliography</b>	<b>186</b>

---

---

# List of Abbreviations

2G-HDNNP	second generation (High-Dimensional) Neural Network Potential
3G-HDNNP	third generation of High-Dimensional Neural Network Potential
4G-HDNNP	fourth generation of High-Dimensional Neural Network Potential
ACSF	Atom-Centered Symmetry Function
AF	Activation Function
ASE	Atomic Simulation Environment (Python library)
BO	Born Oppenheimer
BOA	Born Oppenheimer Approximation
BOMD	Born-Oppenheimer Molecular Dynamics
CMD	Centroid Molecular Dynamics
CVD	Chemical Vapor Dissociation
D2	Grimme van-der-Waals correction on the D2 level
D3	Grimme van-der-Waals correction on the D3 level
DFT	Density Functional Theory
DOF	Degree of Freedom
EMFT	Embedded Mean Field Theory
EMT	Effective Medium Theory
FFNN	Feed-Forward Neural Network
FFT	Fast Fourier Transformation
FHI-aims	Fritz Haber Institute ab initio molecular simulations
FIRE	Fast Inertial Relaxation Engine
GA	Genetic Algorithm
GAP	Gaussian Approximation Potentials
GEKF	Global Extended Kalman Filter
GGA	Generalized Gradient Approximation
HDNNP	High-Dimensional Neural Network Potential

ID	Identification
KF	Kalman Filter
KRR	Kernel Ridge Regression
KS	Kohn Sham
LAMMPS	Large-scale Atomic/Molecular Massively Parallel Simulator
LDA	Local Density Approximation
LQE	linear quadratic estimation
MB	Maxwell Boltzmann
MCTDH	Multi-Configuration Time-dependent Hartree
MD	Molecular Dynamics
md_tian	Molecular Dynamics Tian Xia
MDT2	Molecular Dynamics Tian Xia 2
MEP	Minimum Energy Path
ML	Machine Learning
MLP	Machine Learning Potential
NAO	numeric-atom centered orbital
NI	Non-Interacting
NN	Neural Network
NNP	Neural Network Potential
NVE	microcanonical ensemble with fixed particles (N), Volume (V) and energy (E)
NVT	canonical ensemble with fixed particles (N), Volume (V) and temperature (T)
PAW	projector-augmented wave
PES	Potential Energy Surface
PI	Path Integral
PILE	Path Integral Langevin Equation
PIMD	Path Integral Molecular Dynamics
PIP	Permutation Invariant Polynomials
QM	Quantum Mechanics
RAT	Rydberg Atom Tagging
REBO	Reactive Empirical Bond Order
RMSE	Root-Mean Square Error
RNG	Random Number Generator
RPMD	Ring Polymer Molecular Dynamics
RuNNer	RuNNer Neural Network Energy Representation
SE	Schrödinger Equation
SF	Symmetry Function
SNAP	Spectral Neighbor Analysis Potentials
SOAP	Smooth Overlap of Atomic Positions
SVM	Support Vector Machines

---

tanh	Hyperbolic Tangent Function
TDSE	Time Dependent Schrödinger Equation
TISE	Time Independent Schrödinger Equation
TS	The Tkatchenko–Scheffler van-der-Waals-TS method
USPP	ultrasoft-pseudopotentials
VASP	Vienna Ab-initio Simulation Package
vdW	van der Waals
VMI	Velocity Map Imaging
VP	Variational Principle
ZORA	relativistic scaled zeroth order regular approximation
ZPE	Zero Point Energy



---

---

# Introduction

Nothing is more important than heterogeneous catalysis [1, 2] in our modern society to gain access to pharmaceuticals, fertilizer, drugs and many more chemicals [3]. Most heterogeneous catalysts are solids, interacting with substrates in the liquid or gaseous reaction mixture. To increase the performance of catalysts and to develop new materials, a fundamental understanding of the mechanisms, elementary steps and processes occurring in these reactions is needed.

In gas-surface interactions it is essential to characterize the energy dissipation of molecules to the surface and vice versa. Atom and molecular beam scattering experiments have become a very important tool to elicit the dynamics of gas-surface interactions, when combined with quantum state resolved laser analysis. By analyzing the scattering of atoms and molecules from surfaces, one can get insights into energy exchange processes. These processes influence adsorption, desorption, diffusion, and reaction dynamics. All these elementary processes provide valuable insights to the catalytic active material which in turn might be used for optimization of the catalytic process or development of superior catalytic materials.

Prominent examples for surface catalyzed reactions are the hydrogenation of olefines using Raney-Nickel [4], ammonia production via the Haber-Bosch process with the help of an iron-based surface [5, 6] as well as the conversion of chemisorbed carbon monoxide and water to saturated hydrocarbons in the presence of metal catalysts, which is known as Fischer-Tropsch synthesis [7].

When atoms or molecules approach surfaces in a molecular beam experiment, they can either stick or scatter. Several scattering mechanisms have been established in the past. One mechanism is referred to as trapping desorption [8]. In this mechanism, molecules transfer a sufficient amount of the initial translational energy to the surface and the molecule adsorbs, and remains at the surface for a long time until it thermally desorbs again. In some cases, the interaction time is too short to equilibrate the molecule and it scatters directly. Here, the final distributions of the projectile degrees of freedom (DOFs) depend on incidence parameters of the scattering. This is often referred to as a memory effect. Signatures of this effect are narrow angular distributions close to the specular angle. Also final translational and rotational energies scale with the incidence energy. This has been reported for NO scattering from a Ag(111) surface [9].

The first elementary step in heterogeneous catalysis is adsorption of atoms and molecules from the gas-phase to the surface. Here, two different kinds of adsorption states exist —

physisorption and chemisorption. In the former case, the adsorbant is bound in a well that is caused by dispersion interactions whereas the formation of chemical bonds takes place in the latter case. Several mechanisms for reactions on surfaces are already known and characterized. The most prominent examples are Langmuir-Hinshelwood [10], Eley-Rideal and Mars-van Krevelen reaction mechanisms [11], depending on how the initial adsorption takes place.

In direct scattering processes, inelastic scattering occurs. Applying the concepts of classical collisions — and e.g. phonons are internal DOFs — the scattering process intrinsically is inelastic and there is an energy transfer observable. Energy from the impinging molecule can excite surface DOFs and vice versa. Despite the details of energy transfer, if a particle collides with a surface only once, it still contains information of the incidence conditions. However, long interaction times, i.e. many collisions lead to equilibration of the impinging projectile and no conclusion of the incidence conditions can be drawn anymore. If these equilibrated projectiles eventually desorb, their velocity distribution can be described with a Maxwell-Boltzmann distribution (MB).

To simulate the scattering dynamics of atoms or molecules with surfaces, both electronic and phonon reservoir and rearrangements have to be accounted for in full-dimensions (internal DOF). If due to the interaction electronic excitations occur, we have to employ simulation tools which go beyond the commonly applied Born-Oppenheimer approximation (BOA) [12, 13].

There has been an increased development both on experimental and theoretical tools, but still modeling gas-surface interactions under industrial conditions, i.e. undefined surfaces at high pressures, remains challenging to this day. Thus we are engaged to reduce the complexity and establish benchmark systems. The purpose behind this approach is to identify individual elementary steps in the dynamics between adsorbates and surface which can be later applied for studying catalytic processes under industrial conditions.

Using atoms as projectiles reduces the projectile's degrees of freedom to the translational ones. Scattering from single crystal surfaces with well-defined crystallographic orientations under ultra-high vacuum conditions decrease the complexity even further. As mentioned above, an established tool are atomic and molecular beam experiments. Combined with laser state resolved studies, they can help to unravel the underlying dynamics. Investigating the energy transfer mechanisms between atoms and surfaces is a key step for adsorption—the first elementary step for chemical conversions taking place on surfaces.

The simplest projectile possible is a hydrogen atom due to its low mass and simple electronic structure. The results from a scattering experiment, where an H-atom scatters from a Xe(111) surface [14], could be reproduced using an electronically adiabatic picture for the energy loss of the projectile. In this mechanism, the translational energy of the projectile is distributed to the surface, exciting phononic surface states. The resulting energy losses are very small, because of the inefficient energy transfer from the projectile to the substrate's lattice, which can be rationalized with the large mass mismatch between H and Xe. When an Au(111) single crystal is used as substrate instead, the recorded energy losses are much larger—ranging from small energy gains to relative energy losses larger than 95% with respect to the incidence kinetic energy. It could be shown that the dominant energy transfer channel is the creation of electron-hole pairs, which gives rise to high sticking probabilities [15]. Here, the commonly applied Born-Oppenheimer approximation fails and only molecular dynamics with electronic friction simulations were capable to reproduce the experiments [15–18]. Recently, it could be shown that this process is not restricted to fcc, but can be applied to bcc metal surfaces, too [19].

Besides metals, another material class, which have zero-band gaps, are semimetals; the probably best-known example for this class is graphene [20]. Its peculiar electronic structure, i.e. no band-gap and no density of states at the Fermi level, makes graphene an excellent benchmark system to study the role of the electronic structure on the very effective non-adiabatic



energy transfer channel found for H-atom scattering from metal surfaces.

It has been demonstrated that epitaxial graphene on metal substrates like Pt and Ir can be considered as quasi free-standing graphene, because there are only small interactions due to weak dispersion forces [21–23]. Experiments on H-atom scattering from graphene were performed using the Rydberg atom tagging (RAT) machine [24]. With this it is possible to create an H-atom beam with a very narrow energy distribution. The energy is tunable and scattering angle resolved time-of-flight distributions can be measured in high resolution.

Previous to this thesis, an empirical reactive bond order (REBO) potential was developed by fitting it to embedded mean field theory (EMFT) data in order to study the dynamics of H atom scattering from graphene with MD simulations [25]. From this investigation, it could be shown that the scattering can be described in an electronically adiabatic picture using a single PES. This is supported by the small density of states at the Fermi level, making electron hole pair excitations negligible small on the energy range of the experiment and investigated here.

In comparison to metals and insulators, the scattering of H-atoms from graphene was found to be unique, because a barrier is involved in the scattering process. The barrier is the movement of a single carbon surface atom out of the flat and highly-symmetrical surface plane. During the movement – referred to as puckering – the carbon atom changes from a  $sp^2$  to a  $sp^3$  configuration. Structurally, this can be described by changing the trigonal planar to a tetrahedral geometry. By this, a diamond like structure is locally formed.

H-atom scattering from graphene can follow two different pathways, which we will henceforth call channels. In one case the impinging atom comes from the gas phase, scatters before crossing the barrier, and re-emerges into the gas phase. This event can be regarded as quasi-elastic scattering and occurs close to the middle of a six-membered carbon ring. The incoming particle loses only a small fraction of its initial kinetic energy. This pathway is therefore referred to as the fast channel. It is even possible that the projectile can gain kinetic energy due to transfer from the surface to the projectile, but this depends highly on the initial conditions.

In the second channel, depending on the incidence conditions, the atom crosses the barrier and forms a transient C–H bond. If the projectile manages to distribute its initial kinetic energy to the surface, it will be adsorbed. If the energy transfer is not rapid enough, the projectile can surpass the barrier again and subsequently enters the gas phase with a significant translational energy loss. Because of the high energy loss, this pathway will be called the slow channel. The barrier and its involvement in the scattering explains the unexpected high sticking probability of H-atoms. It was also reported, that once a covalent bond is formed, there is a high diffusion barrier of about 1 eV [26, 27], independent if in-plane or out-plane diffusion and recombination with other adsorbed H-atoms is considered.

Despite the qualitative agreements between the REBO-PES based MD simulations with the experiment, quantitative differences can be seen. Although these simulations can distinguish between the slow and fast channel, they fail to reproduce the branching of the two scattering channels (ratio of signals) for a given experimental condition. This short-coming can be attributed to the high RMSE of 175 meV ( $\approx 7$  meV per atom) of the REBO-PES. The aim of this thesis is to provide a better PES to improve the description of the H-atom scattering dynamics from graphene. The method of choice are full dimensional neural network potentials as these potential energy functions are highly flexible because they are not based on a physical model, and thus can be fitted to input data with a high accuracy.

With the RAT machine [24] one can also conduct D-atom scattering experiments. However, the isotope effect on the scattering dynamics from graphene has not been theoretically studied for incidence kinetic energies larger than 1 eV. Another purpose of this thesis is to fill this blank spot by comparing new simulations to their experimental counterparts.

Furthermore, it could be shown that taking nuclear quantum effects into account when performing ring-polymer molecular dynamics simulations, the nuclear-quantum effect seems

to be small [28] when comparing to RAT experiment. However, new results from HBEAM experiment using velocity map imaging (VMI) technique [29] indicate that quantum effects could play a larger role in the H-atom scattering dynamics along the surface normal from graphene than previously anticipated. Those experimental findings were the driving force to compare classical molecular dynamics simulations and path-integral based simulations with full-quantum mechanical simulations based on wave-package propagation. All of those calculations are based on the Neural-Network potential developed during my PhD research. This thesis is organized in the following way: In Chp. 2, an overview of the concepts and methods used in this thesis can be found. Additionally, the important properties of graphene, H-atom scattering and especially H-atom scattering from graphene is given in more detail. This is followed by a list of used programs in Chp. 3, whereas Chp. 4 contains a detailed analysis of H- and D-atom scattering from a free-standing graphene sheet. The scattering done in MD simulations using a high-dimensional neural network potential energy surface (HDNN-PES), which involved the extension of our surface scattering program to make simulations on Neural-Network potentials possible. The dependence on the incident polar angle and incident kinetic energy of the projectile is analyzed. The section is followed by the influence of the surface temperature on the scattering processes. This chapter also discusses the quality of the HDNN-PES by comparing the results of the MD simulations to the corresponding experiments performed on the RAT machine [24]. In addition, calculations to experiments conducted on a recently constructed apparatus have been performed. In those experiments, ultra-short H-atom pulses impinge the graphene along the surface normal and the velocity map imaging (VMI) based detection scheme allows for a much broader angle resolution. These calculations are complemented with MCTDH-based simulations, which have been conducted in the course of a collaboration between the working group of Fabien Gatti and us, to give a broader picture of the entangled nature of H-atom scattering from graphene [30].

The results are summarized in the last chapter and possible improvements of the current PES are given as well. The appendix provides technical details and offers supporting material for the main part. Additionally, the trajectories used and characteristics for H- and D-atoms at different conditions is given to improve the readability of Chp. 4.

---



---

# Theory

In this chapter, a brief overview of the required physical concepts will be given that form the basics of this work. First, the Born-Oppenheimer approximation is explained in detail. Density functional theory is the method of choice to calculate electronic structure data which are in turn used to fit a machine learning potential. The potential is used in molecular dynamics simulations. A section is dedicated to the description of propagation algorithms, which describe the dynamics with and without quantum effects. Finally, the multi-configuration time-dependent Hartree method will be explained since it accounts for quantum effects in a more fundamental way.

## 2.1 Born Oppenheimer Approximation

In quantum mechanics (QM), the wave function  $\Psi$  contains all information of the system and thus allows access to all of its properties. The wavefunction represents a valid solution to the Schrödinger equation (SE), a linear partial differential equation. In the non-relativistic form, the time-dependent Schrödinger equation (TDSE) [31]

$$\hat{H}\Psi(x, R, t) = i\hbar \frac{\partial}{\partial t} \Psi(x, R, t) \quad (2.1)$$

describes the dynamics of a system of particles. Here,  $\hat{H}$  is the many-particle Hamiltonian operator,  $x = (\sigma, r)$  is a shorthand notation for the spin and spatial coordinate of an electron, respectively. With  $R$  describing the position of the nuclei,  $i$  as the imaginary unit, the fundamental constant  $\hbar = \frac{h}{2\pi}$  with  $h$  as Planck's constant and  $t$  is the variable of time.

The Hamiltonian ( $\hat{H}$ ) consists of terms for the kinetic ( $\hat{T}$ ) and the potential ( $\hat{V}$ ) energy of particles in a system

$$\hat{H} = \hat{T} + \hat{V}. \quad (2.2)$$

The operator for the kinetic energy is

$$\hat{T} = -\frac{\hbar^2}{2m} \nabla^2, \quad (2.3)$$

whereas the operator for the electrostatic or Coulomb potential energy reads

$$\hat{V} = \frac{q_1 q_2}{4\pi\epsilon_0 |r|}. \quad (2.4)$$

In a system with  $n$  electrons and  $N$  nuclei, the Hamiltonian

$$\begin{aligned} \hat{H} = & \underbrace{\sum_{i=1}^n -\frac{\hbar^2}{2m_e} \nabla_i^2}_{\hat{T}_e} + \underbrace{\sum_{j=1}^N -\frac{\hbar^2}{2M_j} \nabla_j^2}_{\hat{T}_n} \\ & + \underbrace{\frac{1}{2} \sum_{i \neq k}^n \frac{e^2}{4\pi\epsilon_0 |r_i - r_k|}}_{\hat{V}_{ee}} + \underbrace{\frac{1}{2} \sum_{j \neq l}^N \frac{Z_j Z_l e^2}{4\pi\epsilon_0 |R_j - R_l|}}_{\hat{V}_{nn}} - \underbrace{\sum_{i=1}^n \sum_{j=1}^N \frac{Z_j e^2}{4\pi\epsilon_0 |r_i - R_j|}}_{\hat{V}_{en}} \end{aligned} \quad (2.5)$$

is composed of several terms,  $\hat{T}_e$  is the kinetic energy of the electrons and  $\hat{T}_n$  describes the kinetic energy of the nuclei, respectively. The electrostatic repulsion of electrons is expressed in  $\hat{V}_{ee}$ , whereas the repulsion of the nuclei is denoted by  $\hat{V}_{nn}$  and the electrostatic attraction is given as  $\hat{V}_{en}$ . Here,  $\nabla$  is the nabla operator and  $\nabla^2$  is also known as the Laplacian operator. The charges for the nuclei are expressed as  $q_n = Ze$ , with  $Z$  being the atomic number and  $M$  is their mass. For the electrons the charge for the electrons is  $q_e = -e$  and  $m_e$  is their mass.

A Hamiltonian that only considers the electronic part can be defined by splitting the Hamiltonian from Eq. (2.5) into

$$\hat{H}^{\text{BO}}(\mathbf{R}) = \hat{H} - \hat{T}_n, \quad (2.6)$$

which will be referred to as the Born-Oppenheimer (BO) Hamiltonian [32] and will not include the momenta of nuclei anymore. Thus, the corresponding Hamiltonian depends only parametrically on the positions of the nuclei. The general Hamiltonian can be split and in the time-independent Schrödinger Equation (TISE), just the Hamiltonian respecting only the electronic contributions is used [31, 33], which provides eigenfunctions and -values for a fixed set of nuclear configurations

$$\hat{H}^{\text{BO}}(R) \Psi(x, R) = E^{\text{BO}}(R) \Psi(x, R) \quad (2.7)$$

A single eigenvalue is a single potential energy surface (PES). For each atomic configuration, the eigenfunctions are chosen to be orthonormal and the eigenvectors form a complete basis set.

The many-body wavefunction  $\Psi$  can be expressed as a linear combination of BO wavefunctions

$$\Phi(x, R, t) = \sum_i \phi_i(R, t) \Psi_i^{\text{BO}}(x, R), \quad (2.8)$$

with  $\phi_i$  as nuclear wavefunction chosen to obey the normalization condition in the *Born-Huang ansatz* [34]. Still, no approximations are introduced. Assuming adiabatic behavior, the nuclear motion is decoupled from electronic dynamics, which is supported by the difference of the masses of electrons with respect to nuclei. The resulting cross-terms tend to be small and therefore they normally are neglected. This assumption is called the Born-Oppenheimer Approximation (BOA) [12, 13]. The dynamics of the nuclei are now describable with a single BO surface. All in all, this leads to a Hamiltonian that only accounts for the electronic contributions [35] of the total energy

$$\hat{H}^{\text{el}} = \hat{T}_e + \hat{V}_{ee} + \hat{V}_{nn} + \hat{V}_{en}. \quad (2.9)$$

Molecular dynamic simulations applying the BOA are referred to as Born-Oppenheimer molec-

ular dynamics (BOMD) [36]. Nevertheless, if the energetic difference of individual BO states becomes very small, the BOA will fail and theories going beyond have to be considered [37].

However, graphene has a very small density of states (DOS) at the Fermi level, which means that there is only a small number of occupied as well as unoccupied states. This explains, why non-adiabatic dynamics do not play any role at least on the energy range of scattered particles used in experiment. In short, to describe the H-atom scattering from graphene, a single PES is sufficient to use in MD simulations, which are based on the BOA.

## 2.2 Density Functional Theory

As mentioned before, in the dynamics of H-atom scattering from graphene, no excited electronic states are analyzed. In this work, density functional theory (DFT) is chosen to generate the electronic structure data containing energies and forces.

The common procedure to develop a PES is to fit a model potential to accurate electronic structure data based on solving the TISE (Eq. (2.7)). However, considering many-body systems with a lot of degrees of freedom (DOF), solving the TISE soon becomes cumbersome for bigger systems (100 DOF and upwards). In contrast, DFT reduces the dimensionality by making use of the electronic density which solely depends on three spatial coordinates. Applying the BOA, the nuclei of the treated molecules are seen as fixed, which generates a static external potential, in which the electrons are moving in.

Two theorems by Hohenberg and Kohn form the basis of DFT [38]. The first theorem states that there is a one-to-one relation between the electronic ground-state density  $\rho_0(r)$  and the external potential  $v(r)$ . Consequently, the external potential is a unique functional of the electronic ground-state density. This means that the electronic wavefunction and the energy can be expressed based on the electronic ground-state density. The second theorem states that the energy of a system for a given external potential  $v_0$  is minimized according to the variational principle (VP)

$$E_{v_0}[\rho] > E_0 \quad \text{for} \quad \rho(r) \neq \rho_0(r), \quad (2.10)$$

$$E_{v_0}[\rho] = E_0 \quad \text{for} \quad \rho(r) = \rho_0(r). \quad (2.11)$$

Without solving the Schrödinger equation and by instead using the VP in order to solve the variational equation, the ground-state density is accessible. By using functionals, the properties of a many-electron system can be determined. These functionals are spatially dependent on the electron density.

In principle the functionals are universal, but the exact form is unknown and approximations are needed. However, direct approximations are not good enough. The kinetic energy is calculated from a single Slater determinant, but is just an approximation, because non-interacting electrons are considered. To resolve this problem, the Kohn-Sham (KS) formalism defines introduces orbitals again and a (fictitious) system of non-interacting (NI) particles, reproducing the exact electronic ground-state density [39].

Since the exact ground-state density is not known, a set of auxiliary one-electron functions  $\phi$  (single-particle orbitals) are used to approximate the density

$$\rho_{\text{approx}} = \sum_{i=1}^{N_{\text{elec}}} |\phi_i|^2, \quad (2.12)$$

which will yield the number of electrons  $N_{\text{elec}}$  of the system by integrating over the volume. Using single-particle orbitals, a single Slater Determinant [40] can be used to represent the

total energy functional as

$$E^{\text{KS}}[\rho] = T_e[\rho] + V_{v_0}[\rho] + V_{ee}[\rho] \quad (2.13)$$

$$= T_{e(\text{NI})}[\rho] + V_{v_0}[\rho] + V_C[\rho] + E_{\text{xc}}. \quad (2.14)$$

Here,  $V_C$  is the classical Coulomb energy and the exchange-correlation functional can be written as

$$E_{\text{xc}}[\rho] = T_e[\rho] - T_{e(\text{NI})}[\rho] + V_{ee}[\rho] - V_C[\rho]. \quad (2.15)$$

Additionally, the functional includes the difference between the real and the non-interacting system with respect to its kinetic energy.

The exchange-correlation functional is not analytically known, therefore approximations have to be introduced. Analog to the Fock operator in the Hartree-Fock method, here the KS operator is applied. In the Thomas-Fermi-Dirac model, the first formulations for kinetic and exchange energy were derived for the uniform electron gas [41, 42].

Considering a uniform electron gas (which is equivalent assuming the density to be a slowly varying function), the local density can be estimated for each point on a grid (local density approximation, LDA) [43–45]. The energy is then accessible via integration. For a spin-unpolarized system the LDA approximation is

$$E_{\text{xc}}^{\text{LDA}}[\rho] = \int \rho[\mathbf{r}] \varepsilon_{\text{xc}}^{\text{LDA}}(\rho[\mathbf{r}]) d\mathbf{r}, \quad (2.16)$$

with  $\varepsilon$  being the energy density. The exchange and correlation terms have a linear decomposition

$$E_{\text{xc}}[\rho] = E_{\text{x}}[\rho] + E_{\text{c}}[\rho]. \quad (2.17)$$

In spin-polarized systems, where the densities for different spins are not equal, LDA has to be extended to account for individual spin densities. This method is called local spin density approximation (LSDA) [46, 47]. The exchange and correlation energy  $E_{\text{xc}}$  of the system is then

$$E_{\text{xc}}^{\text{LSDA}}[\rho_{\alpha}, \rho_{\beta},] = \int d\mathbf{r} \rho(\mathbf{r}) \varepsilon_{\text{xc}}^{\text{LDA}}(\rho_{\alpha}, \rho_{\beta},), \quad (2.18)$$

with  $\alpha$  and  $\beta$  representing different spin densities. When investigating closed shell systems, LSDA is equal to LDA.

To improve on LDA, the electron gas can be assumed to be non-uniform. In the generalized gradient approximation (GGA) [48–50] approach, not only the density, but also its derivative is considered. This can be seen as a Taylor series with LDA being the starting point to fulfill a more exact description of the electrons. In GGA, the functional only depends on densities and their derivatives at a given point, not on a space volume

$$E_{\text{xc}}^{\text{GGA}}[\rho] = \int \rho(\mathbf{r}) \varepsilon_{\text{xc}}^{\text{GGA}}[\rho(\mathbf{r}), \nabla \rho(\mathbf{r})] d\mathbf{r}. \quad (2.19)$$

In GGA one distinguishes between two types of functionals, first with parameters fitted to experimental data and second parameter-free forms. A very prominent and of the latter type is the Perdew-Burke-Ernzerhof (PBE) functional [51]. Known for its general application and rather accurate results, it is used for a wide range of systems. It was therefore the functional of choice in this work.

To further increase the accuracy of the xc functional, higher order gradient or meta-GGA methods using higher-order derivatives of the electronic density [52–54] are available as logical extensions of GGA.

Different models using exact exchange are often denoted hyper-GGA or hybrid methods [55].

In the following, the B3LYP (Becke, 3-parameter, Lee–Yang–Parr) functional [47, 48, 56, 57] as an example of the hybrid methods will be presented since it was used to benchmark the system of interest and might become important in future analysis. Hybrid functionals split the exchange energy into two parts. First, a fraction of the exact exchange from HF [58–62] is used  $E_x^{\text{HF}}$  whereas the rest is derived from LDA and GGA. The form of B3LYP is

$$E_{\text{xc}}^{\text{B3LYP}} = (1 - a) E_x^{\text{LSDA}} + a E_x^{\text{HF}} + b \Delta E_x^{\text{B88}} + (1 - c) E_c^{\text{LSDA}} + c E_c^{\text{LYP}}, \quad (2.20)$$

with a part of the exchange energy taken from the B88-GGA (Becke 1988 enhancement factor) functional [63, 64] and parts for the correlation energy are taken from the LYP-GGA (Lee–Yang–Parr) functional [48]. The parameters  $a$ ,  $b$  and  $c$  are obtained by fitting to experimental data.

In principle, only two variables have to be set in DFT, the basis set as well as the xc functional. The basis set is needed, because DFT also uses orbitals, which have to be represented by basis functions.

### 2.2.1 Dispersion Correction

Despite the successes of DFT, weak interactions due to dispersion forces (part of van der Waals type interactions) arising from correlation are not described [65, 66]. Commonly, correction terms are applied to account for non-local dependence. An example for correction is given by Grimme on the D2 level [67] and can be expressed like

$$E_{\text{disp}} = -\frac{1}{2} \sum_{i=1}^N \sum_{j=1}^N \sum_{\mathbf{L}}' \frac{C_{6ij}}{r_{ij,L}^6} \cdot f(r_{ij,L}). \quad (2.21)$$

Summations are over all atoms  $N$  and prime indicates  $i \neq j$  when  $L = 0$ .  $C$  is the dispersion coefficient for atom pair  $ij$ , the distance between atom  $i$  in the reference cell  $L = 0$  and atom  $j$  in cell  $L$  is given by  $r_{ij,L}$ , whereas the definition of the Fermi type damping function is

$$f(r_{ij,L}) = s_6 \cdot \left( 1 + \exp \left( -d \left( \frac{r_{ij}}{s_R R_{0ij}} - 1 \right) \right) \right)^{-1}, \quad (2.22)$$

whose role is to determine the short-range behavior of the dispersion correction. It is also needed to avoid double-counting effects of electron correlation at intermediate distances. Also, near-singularities for small distances should be avoided [68].

To derive the parameters of the correction term, one uses the combination rules

$$C_{6ij} = \sqrt{C_{6ii} C_{6jj}} \quad (2.23)$$

and

$$R_{0ij} = R_{0i} + R_{0j}, \quad (2.24)$$

to obtain parameters for interactions across different elements. Here,  $R_0$  is the element specific reference atomic van der Waals (vdW) radius.

In this work, also analytic Grimme dispersion corrections on the D3 level [69] are used for benchmark as well as the numeric correction introduced by Tkatchenko and Scheffler (TS) [70]. TS is similar to D2, but dispersion coefficients and damping function are charge-density dependent. D3 in contrast to D2 use geometry-dependent dispersion coefficients, they are adjusted based on the local geometry.

## 2.3 Neural Network Potentials

In this section an introduction to machine learning potentials (MLPs) is given and specifically neural network potentials (NNPs) are described. Here, the method of neural networks (NNs) is explained in detail and how it is used to develop a full-dimensional potential energy surface (PES).

### 2.3.1 Overview

Machine Learning (ML) is part of artificial intelligence and is not explicitly programmed to make predictions or decisions [71]. With the help of computer algorithms, they can improve automatically based on the data and by experience. A model is developed based on the sample data and applied in many fields for pattern recognition and data mining [72]. They become important when the development of conventional algorithms is difficult or unfeasible.

Traditionally, the vast field of ML is divided into three broad classes. Depending on the specific input and available feedback to the learning system, this leads to the classes of [73]

1. Reinforcement learning,
2. Unsupervised learning,
3. Supervised learning (Regression, Classification).

The first class is used to train an artificial intelligence to learn how to play even complex games (for example Go [74]), the second class is used to discover representation of input data and group it by its properties and the third class is subdivided into Regression and Classification type. Both are designed to predict an output from a given input. Classification means to predict a single output from several possible outputs whereas regression means to best describe a single property depending on several parameters. The first is used for recognition of voices, faces and many more, while the latter type can be applied to estimate properties of a given geometry.

### 2.3.2 Supervised Learning

Despite recent development of high-performing algorithms used in several fields and rapid increase of computational power, application of first principles methods is still limited to rather small systems due to their tremendous demands. To gain insights into complex systems, MLPs have been successfully introduced to combine acceleration of computer simulations (on the level of force field potentials) but keeping quantum mechanical accuracy. They offer a PES fitted to accurate electronic structure data. The energy of a system can be given as a parametric function of nuclear coordinates, offering a relation between the geometry (e.g. atomic positions in Cartesian space) and properties (energies, forces, etc.) related to this specific geometry. It is fundamental that there is a very rigorous connection between input and output, otherwise any ML based algorithm will fail.

There are many different machine learning methods in the field of supervised learning to construct a PES, such as NNs, kernel ridge regression (KRR) [75, 76], Support Vector Machines (SVMs; but rarely used to construct a PES) [77] and Spectral Neighbor Analysis Potentials (SNAPs; linear version of GAPs) [78]. Gaussian Approximation Potentials (GAPs) as a prominent example are part of kernel-based MLPs [79].

Here, artificial neural networks [80] as part of the regression type of the supervised learning class will be presented, which are in principle able to represent unknown (and even complex) real-valued functions of any dimensionality to high accuracy [81, 82]. To generate a PES, NNs



will be fitted to accurate electronic structure data from DFT calculations offering energies and forces. Although DFT is the most common used data to fit NNs, in principle any accessible electronic structure data can be used. It is not like that the NN is restricted to DFT, but the system under investigation must be able to be described. So far, larger systems can only be efficiently treated by DFT.

The different steps needed to develop a machine learning potential are given in Fig. 2.1 and will be explained in detail in the following.

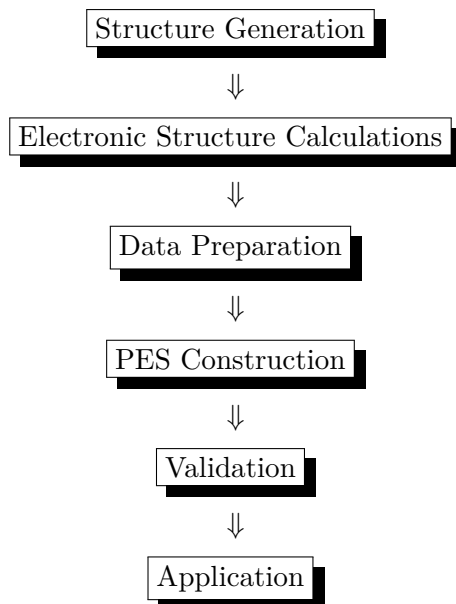


Figure 2.1: Workflow to construct a MLP. Reference energies and forces of given geometries are calculated using electronic structure methods. These data points are used to fit the PES and increase the data set in an iterative way for searching missing configurations. After validation, the PES can be used for example in MD simulations.

In ML based potentials, the available descriptors can be arbitrarily combined with the method. Currently, there are a few prominent combinations of those. This is not about compatibility reasons, but the personal preferences of the developers [83]. What makes NNPs interesting for us is their long history and the largest diversity in terms of methods and concepts [84] and also the fact that the framework containing the description of the neural networks was also programmed in Fortran, which was highly beneficial for us from a technical point of view.

### 2.3.3 Feed-Forward Neural Networks

Inspired by biology, neural networks are adapted from the connection in the brain built by neurons. NNs can be categorized into (deep) feed-forward, convolutional and recurrent types and many more [86]. Feed-forward NN (FFNN) are also known as artificial NN. They have been well known for a long time [87–89] and are used in this work. A scheme of different types of NN and how they are categorized can be seen in Fig. 2.2 to just give an overview of the field.

In the feed forward network, all nodes are fully connected and information flows from the input layer to the output layer without back loops. There can be several layers between the input and the output, which are called hidden layers. An example of a simple feed-forward neural network is shown in Fig. 2.3. The coordinates of the system under investigation enter the network in the input layer. Every node in all layers is a simple mathematical function and create an output that is passed to all nodes in the next layer. Each node in the next layer

receives an input from all nodes of the previous layer. All input is passed to internal functions that combine the given input with weights and biases, which are the fitting parameters of the NN. If NNs have the same architecture – the same number of layers and nodes per layer – they have equal number of weights and biases, but their values differ due to different data sets and fitting procedures (training of NNs). Weights are between all nodes and depend on the fitting. They act on the input functions and on the activation functions (AF) [90, 91], which are acting on each node. Weights are multiplicative and scale the flow of information. Biases depend on the data set and act only on activation functions of the hidden layers and the output layer. Unlike the weights, biases are additive and shift the AF. Both weights and biases moderate the communication inside the whole network. It is therefore possible, that there are zero-responses between nodes meaning weights can be positive, negative and also zero.

In the hidden layers, an activation function is acting on all nodes (artificial neurons). AFs have several purposes but they also have to fulfill some requirements. They have to be continuous non-linear functions substituting the early used step functions. The purpose is to mimic the activation threshold in biological neurons. These functions have the property of converging to constant numbers for very negative and very positive arguments. In between they have a non-linear region, enabling the NN to represent any shape of functions. The only exception is the output node, where always a linear form is used to avoid any restrictions. AFs introduce

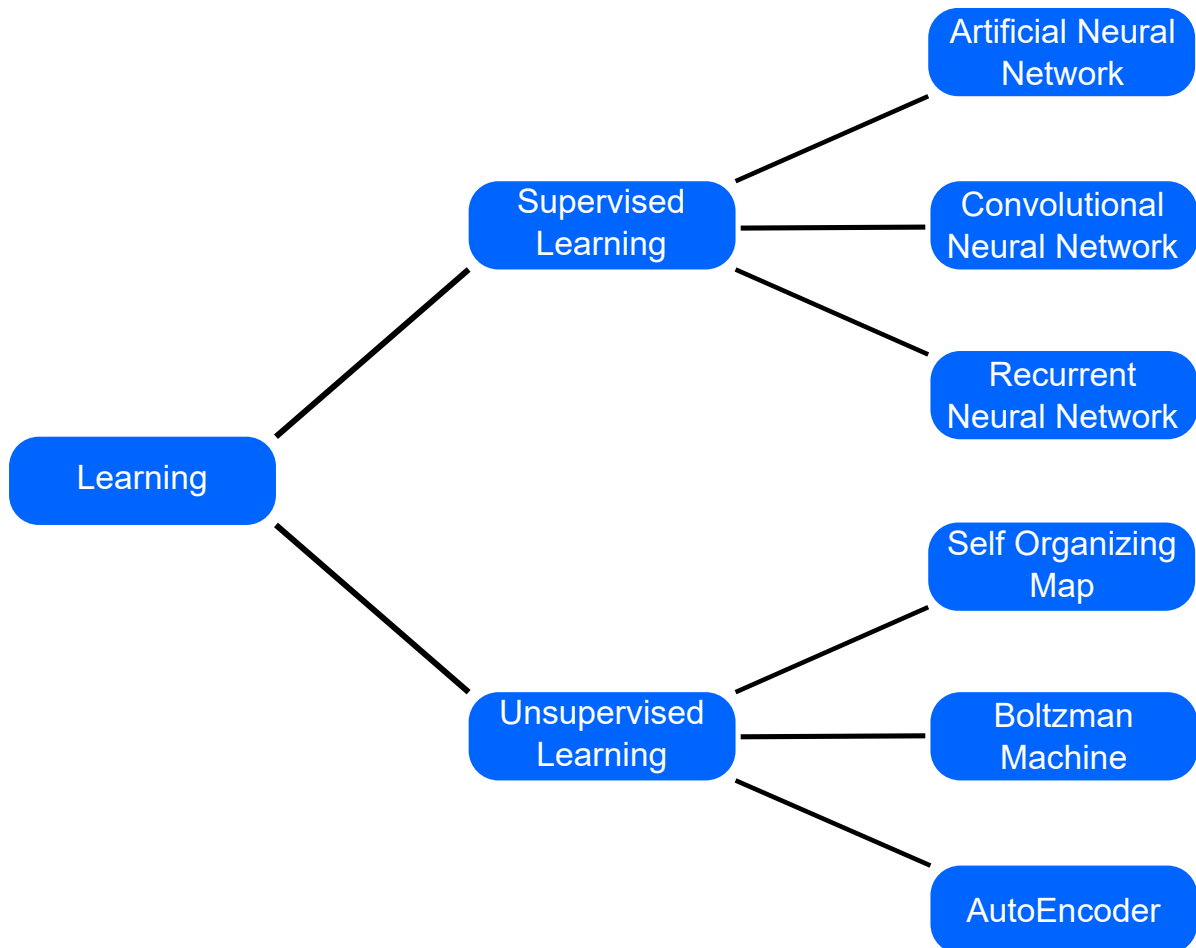


Figure 2.2: Architecture of the classification for different learning types of machine learning or deep learning field. In this work, artificial (feed-forward) NN as part of supervised learning have been utilized [85].

non-linearity and they make NNs universal function approximators [81, 82]. It is an ongoing task searching for different and better suited activation functions [90].

Many of different AFs can be used: Cosine, exponential, Gaussian, harmonic, softplus, sigmoid (comparing to biological neurons they have a similar form) and hyperbolic tangent (tanh) functions [92]. In this work, the tanh is the function of choice and is shown in Fig. 2.4. Since as simple mathematical functions with well known derivatives (analytically accessible, higher-order derivatives) are used as activation functions, the prediction of properties like forces (1st derivative) and Hessians (2nd derivatives) are easy and quickly accessible. Forces are used to propagate the system in classical molecular dynamics (MD) simulations. The Hessians can be used for normal mode analysis (calculation of molecular frequencies, phonon analysis etc.).

With the above mentioned functions, the NN can be expressed as an analytical function of the form given in Eq. (2.31) in Sec. 2.3.4. These first generation NNs [93] are able to reproduce a target PES, because their form is analytic. Backpropagation [94] is used to fit the parameters of the NN to represent the structural properties offered in the input data set. This method has some limitations, though. Invariant input means that the energy expression is the same for structures that are rotated or translated or have a permutation of elements. The first generation of NNPs could only describe low dimensional molecular systems of fixed system size.

## Atomic NN

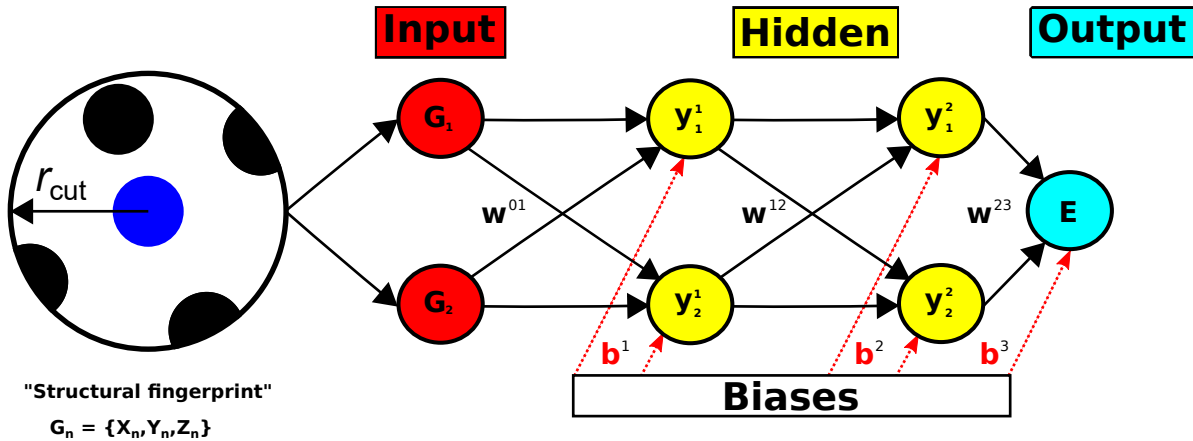


Figure 2.3: Diagram of a feed-forward atomic neural network (NN). For every atom in the system all interactions are considered inside a given cutoff radius. The input has to be given to account for invariance in form of symmetry functions (SF). Beforehand, the Cartesian coordinates have to be converted to SF (denoted as  $G$ ), which depend on the atomic environment inside a given cutoff radius ( $r_{\text{cut}}$ ). The network consists of 2 input nodes (2 SF), 2 nodes for the first as well as the second hidden layer and a single node for the output layer (energies  $E$ ). Because simple mathematical functions with well known derivatives are used, not only the energies, but also their derivatives with respect to positions (forces, hessian) can be predicted. Here, weights  $w$  and biases  $b$  are the parameters of the NN. Weights are between all nodes (black arrows) and depend on the fitting. They act on symmetry functions as well as activation functions, whereas the biases act on the activation functions of every node inside the hidden and output layer and they depend on the data set. Weights are multiplicative and biases additive.

### 2.3.4 High-Dimensional Neural Network Potentials

Solving the limitations of the first generation methods [93] led to the introduction of second generation high-dimensional neural network potentials (2G-HDNNP) by Behler and Parrinello [95–98] as shown in Fig. 2.5. Two modifications were added, first the total energy of the system is split into individual partitioned, fictitious atomic energies, where the contribution is determined by individual atomic neural network potentials (NNPs). The NNPs account for each atom of the same element, meaning for each element the set of weights and biases is the same. In other words, the element-specific atomic NNs share weights and biases. Second, symmetry functions (SFs) are used for the input layer.

Like before, the Cartesian coordinates have to be converted to an invariant input (internal coordinates). This means that translated or rotated structures will result in the same energy and also permutation of the underlying atoms of each element have to be considered to result in the exact same energy.

Many descriptors are fulfilling those needs, whereas the most popular and widely used are atom centered symmetry functions (ACSFs) [99], smooth overlap of atomic positions (SOAP) [100], Gaussian Processes to build a bispectrum matrix of spherical harmonics [101–103] and permutation invariant polynomials (PIP) [104], where the latter can only treat small systems and are of minor importance.

ACSFs offer a way to describe high-dimensional systems with a large number of atoms and they depend on positions of all neighbor atoms. In this work, many-body ACSFs are used,

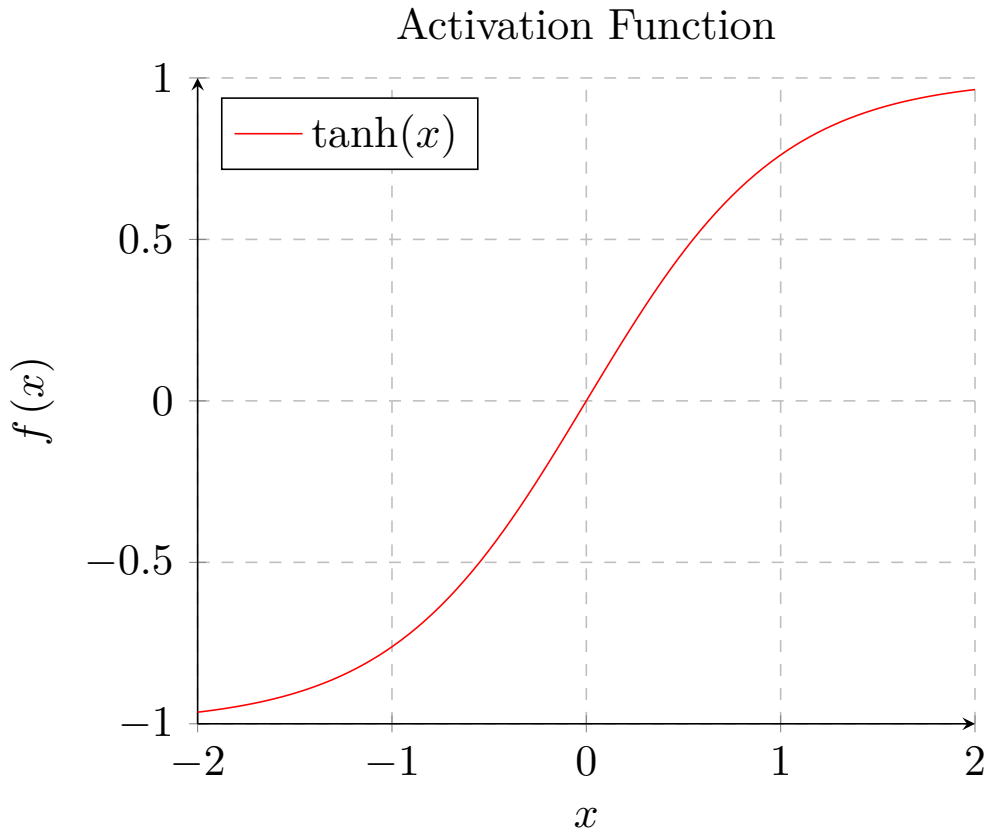


Figure 2.4: Graphical representation of the hyperbolic tangent function ( $\tanh$ ) as used as activation function with a linear behavior close to 0, converging to constant numbers (-1 and 1) for very large or small input values and a non-linear behavior in between.

which are indicated by  $G$ . For a single atom they describe its environment up to a given cutoff radius and offer a structural fingerprint of the environment. The cutoff function is a central part of the used symmetry function (SF), because otherwise it would not be extendable to larger systems. SFs help to fulfill this behavior, because they got to zero beyond the cutoff. A suitable function to fulfill those requirements has to be continuous and differentiable.

A variety of cutoff functions exist and a common example utilizes a cosine function

$$f_c(R_{ij}) = \begin{cases} 1 & R_{ij} \leq R_{\text{inner},c} \\ \frac{1}{2} [\cos(\pi X) + 1] & R_{\text{inner},c} \leq R_{ij} \leq R_c \\ 0 & R_{ij} > R_c, \end{cases} \quad (2.25)$$

where  $X$  is defined as

$$X = \frac{R_{ij} - R_{\text{inner},c}}{R_c - R_{\text{inner},c}}. \quad (2.26)$$

Usually, the inner cutoff  $R_{\text{inner},c}$  is set to zero, which simplifies Eq. 2.25 and 2.26.

By construction, SFs are many-body functions and the actual input of the NN. The SFs can be categorized into radial and angular type. Radial SFs describe the distribution of neighboring atoms and can be interpreted as continuous coordination numbers of the considered atom

## HDNNP

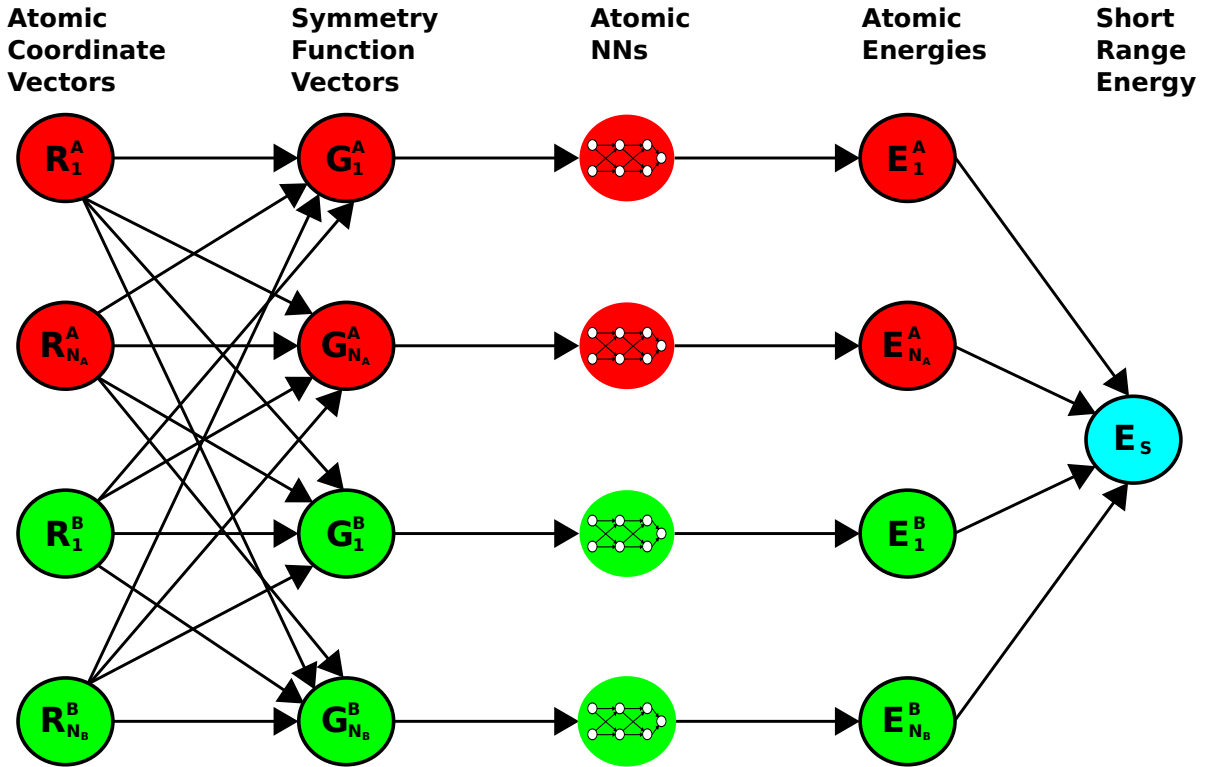


Figure 2.5: Example scheme of a high dimensional neural network potential (HDNNP) for a system with two elements. The schemes for Atomic NNs are shown in Fig. 2.3. As can be seen in the diagram, to get a description of the total system, the energies from single atoms using atomic NNs are summed up. For each element, the values for the weights and biases are shared. This means, that in principle for each element there can be different architectures and also symmetry functions to describe the interactions.

whereas angular SF are constructed by summing up all values of angles considering all triplets of atoms around the central atom.

A variety of functional forms can be utilized for both types of SFs [99, 105, 106]. Different mathematical shapes of functions can serve for specific problems. The form depends on the purpose, which system will be investigated.

The functional form for the radial SF used in this work is [105]

$$G_i^{\text{radial}} = \sum_j \exp[-\eta(R_{ij} - R_s)]^2 \cdot f_c(R_{ij}). \quad (2.27)$$

Considering the environment of atom  $i$ , the indices of all atoms inside the cutoff are denoted as  $j$  and  $R_{ij}$  is the distance between the central atom  $i$  and atom  $j$ . The radius of the shell around the considered atom is determined by the shift  $R_s$  and  $\eta$  is the width of the Gaussian.

For the used angular SF the functional form is

$$G_i^{\text{angular}} = 2^{1-\zeta} \sum_{j,k} (1 + \lambda \cos(\Theta_{ijk}))^\zeta \cdot \exp\left[-\eta(R_{ij}^2 + R_{jk}^2 + R_{ik}^2)\right]^2 \cdot f_c(R_{ij}) \cdot f_c(R_{jk}) \cdot f_c(R_{ik}). \quad (2.28)$$

Again, the environment of central atom  $i$  is considered.  $\Theta_{ijk}$  is the angle centered around atom  $i$  with the neighbors  $j, k$  being inside the cutoff. A set of angular functions resulting in a fingerprint for the chemical environment can be generated by using different exponents  $\zeta$  and the positions of the extrema can be adjusted using  $\lambda \pm 1$ .

Although there are some tools available to construct a set of suitable SF based on the minimum distance in the structures of the underlying data set, it also needs some effort to adjust the parameters for the fitting procedure. Together with the number of nodes and hidden layer(s) they describe the architecture of the used NN and have to be set before the fitting.

Although explicitly shown here, NNPs are not restricted to energies. Atomic (partial) charges can be fitted as well. Furthermore, it could be shown that NNPs can also predict the spin of a given structure [107]. This can be any property of interest, the only restriction is, that the property of interest must have a dependence on the structure. For example, different electronic states that of the same structure are not distinguishable by a single NNP. In this case, different NNPs with one for each electronic state have to be used.

The third generation of HDNNPs (3G-HDNNP) is capable to predict local charges, accounting for long-range electrostatic interactions. Finally, the fourth generation of HDNNPs (4G-HDNNP) make use of non-local information to account for electrostatic interactions [108, 109]. In all cases similar schemes of atomic NNs are used, but instead of energies, atomic (partial) charges can be trained. As mentioned before, in principle, if there is any property related to a specific structure, a NN can be used to fit to these data.

In the most general picture according to 4G-HDNNP (and 3G-HDNNP), the total energy of a system has a short range and an electrostatic contribution. The short range contribution is a many-body interaction of atoms inside a cutoff radius whereas the electrostatic part describes Coulombic interactions of charges centered around atoms.

$$E_{\text{tot}} = E_{\text{short}} + E_{\text{elec}}. \quad (2.29)$$

In this work the electrostatic contribution was not included. This term corrects for local changes in the electronic structures induced by long range charge transfer. There are no charges in the graphene system investigated in this thesis. Additionally, including charges would make developing and application more demanding, which is crucial when simulating millions of trajectories. Consequently and as mentioned, the total energy is just the short range energy according to the picture of 2G-HDNNP. The short range energy is derived by summing up all

element specific atomic energies predicted in using atomic NNs as presented before.

$$E_{\text{tot}} = E_{\text{short}} = \sum_{\nu=1}^{N_{\text{elem}}} \sum_{\mu=1}^{N_{\text{atoms},\nu}} E_{\mu}^{\nu}. \quad (2.30)$$

For each atom in the system the environment-dependent energetic contribution to the short range energy can be analytically obtained. Here,  $\nu$  runs over all elements present in the total system and  $\mu$  over all atoms of this element. The atomic energy is estimated by an element specific atomic neural network

$$E_{\mu}^{\nu} = f_1^3 \left( b_l^3 + \sum_{k=1}^{N_{\text{hid},2}} w_{kl}^{23} \cdot f_k^2 \left( b_k^2 + \sum_{j=1}^{N_{\text{hid},1}} w_{jk}^{12} \cdot f_j^1 \left( b_j^1 + \sum_{i=1}^{N_G} w_{ij}^{01} \cdot G_{i,\mu\nu} \right) \right) \right). \quad (2.31)$$

with  $G$  being the symmetry functions,  $f$  denote the activation functions,  $b$  describes the biases whereas  $w$  are the weights. The superscript of the weights and biases indicate which inter-layer connection is described. 0 indicate the input, 1 and 2 the hidden and 3 the output layer.  $N_{\text{hid},1}$  is the number of nodes in the first and  $N_{\text{hid},2}$  the number of nodes in the second hidden layer, respectively. Weights and biases are the parameters of the NN, where weights have a multiplicative and biases have an additive effect on the activation functions, as mentioned in Sec. 2.3.3.

For a HDNNP, forces are obtainable as a derivative of the predicted atomic energies with respect to the positions. When in Cartesian space, three sets of forces are obtained per atom in the system, one for each direction. For an atom  $k$ , the force acting on component  $\tau = x, y, z$  can be expressed as

$$F_{k,\tau} = - \frac{\partial E_{\text{tot}}}{\partial R_{k,\tau}} = - \sum_{i=1}^{N_{\text{atoms}}} \frac{\partial E_i}{\partial R_{k,\tau}}, \quad (2.32)$$

with  $\tau$  representing Cartesian coordinates. Here,  $E_{\text{tot}}$  is the total energy output for the whole system, whereas  $E_i$  is the atomic energy. Since only interactions inside the cutoff are considered, the forces also have to respect this aspect. The sum will be constrained and the chain rule can be applied to separate the derivatives containing SF terms. Unlike the energies, the forces effectively depend on twice the cutoff radius around the central atom  $k$  under consideration, which leads to

$$F_{k,\tau} = - \sum_{i=1}^{N_{R_c}} \frac{\partial E_i}{\partial R_{k,\tau}} = - \sum_{i=1}^{N_{R_c}} \sum_{j=1}^{M_i} \frac{\partial E_i}{\partial G_{i,j}} \frac{\partial G_{i,j}}{\partial R_{k,\tau}}. \quad (2.33)$$

with  $i$  as neighbor of  $k$ ,  $N_{R_c}$  giving the number of all neighbors with respect to  $k$ . Again,  $R_c$  is the cutoff radius,  $M_i$  gives the number of SF of atom  $i$  and  $G_{i,j}$  stands for the symmetry function number  $j$  of atom  $i$ . This condition is essential to achieve consistent energies and forces, needed in molecular dynamics simulations to conserve energies.

Some comments the fitting procedure for a HDNNP: The main part and in analogy to further schemes on fitting procedures in the field of ML, a loss function [110–112] is used to have an expression for the accuracy of the fit and a way for optimization. Here, an error function is introduced in the same manner. In the case of the energies predicted by the NN, the error function can be expressed as

$$\Gamma(E) = \frac{1}{N_{\text{data}}} \sum_i^{N_{\text{data}}} \left( E_i^{\text{NNP}} - E_i^{\text{REF}} \right)^2. \quad (2.34)$$

For the forces it is similar, but it will be for all directions in Cartesian space.

The number of structures that form the data set used for the fitting is denoted as  $N_{\text{data}}$ . There are two different energy expressions.  $E^{\text{REF}}$  is the reference target energy from electronic structure calculations and  $E^{\text{NNP}}$  indicates the energy predicted by the NN for this structure, respectively. Optimization in this case means, that the quantity  $\frac{\partial \Gamma}{\partial a}$  is minimized. The weights and biases of the NN are expressed in  $a$ . Weights and biases are initialized in a random fashion, but the interval and the way can be chosen, according to the needs for the investigated system; this procedure is called rescaling. The update of weights and biases is done employing the adaptive global extended Kalman filter (GEKF) [113]. The Kalman filter (KF) procedure [114] is also known as linear quadratic estimation (LQE) and is sometimes also termed Stratonovich–Kalman–Bucy filter because of its inventors [115–119]. Known to increase the signal-to-noise ratio in measurements, the KF is applied in time series analysis. The KF produces estimates of unknown variables and a joint probability distribution over the variables. Furthermore, the KF is commonly used for topics such as signal processing and econometrics. However, the extended KF [120] is the non-linear version of the Kalman filter and was designed for non-linear state estimation, autonomous or assisted navigation and GPS [121].

Training of the network is done iteratively [122], where the steps are called epochs. In each epoch, forces and energies are taken from structures, where the predicted properties have the largest deviation with respect to the data set. To measure the quality of the fit in each epoch, the root mean square error (RMSE) is calculated for the energies as well as the forces [106] according to

$$\begin{aligned} \Gamma_{\text{short}} = & \frac{1}{N_{\text{energies}}} \sum_{i=1}^{N_{\text{energies}}} \left( \frac{E_i^{\text{REF}} - E_i^{\text{NNP}}}{N_{\text{atoms}}} \right)^2 \\ & + \gamma \frac{1}{N_{\text{forces}}} \sum_{j=1}^{N_{\text{forces}}} \left( F_j^{\text{REF}} - F_j^{\text{NNP}} \right)^2, \end{aligned} \quad (2.35)$$

where  $N_{\text{energies}}$  data set of the energies and  $N_{\text{forces}}$  the data set of the forces, respectively. Here,  $F_i^{\text{NNP}}$  is the predicted and  $F_i^{\text{REF}}$  the reference force component. The scaling factor, which adjusts the relative importance of the force accuracy in the training of the ANN is given as  $\gamma$ . The weights of the ANN are optimized in order to decrease the error of the loss function [108]. For the energies and forces this quantity is expressed as the square root of the error function

$$\text{RMSE}(E, F) = \sqrt{\Gamma(E, F)}. \quad (2.36)$$

In principle, the epochs could be infinitely extended to further increase the accuracy of the fit. But since the interpolation capacity of the fit is of utmost interest, the question is less about the best way to just reproduce the structures in the training set but also to predict structures from the validation set with high accuracy. To create these sets, the data set is split into a subset, that is used to actually fit the potential (training set) whereas the remaining structures form a validation (test) set and the RMSE is calculated as well. If the RMSE of both sets are diverging, there is a indication for overfitting and that the configuration space of the reference data set is not well sampled. The best fit is achieved when the error for the training set is lowest and there is only a minor divergence between the two different sets. The standard approach is to target an error of 1 meV per atom for the energies and 100 meV Å<sup>-1</sup> for the forces [97].

To aim for the best possible fit, the underlying architecture of the NN is one of the most important factors. Too few nodes and layers may result in a function that is too unflexible to accurately reproduce the data, whereas too many nodes and layers will lead to a highly flexible function, where overfitting is more likely. Also, there have to be enough DOFs represented by the SF, but too many DOF will lead to overfitting, resulting in a fit with less accuracy.



HDNNPs are able to learn PESs for a wide variety of chemical systems, with high transferability and they can be easily expanded to larger systems. Thus, NNPs don't have a size limitation. Though, they have other limitations: Their functional form has no underlying physical expression and they have a poor extrapolation capability outside the configuration space of the underlying data. It is crucial to carefully check for poorly sampled regions in the PES before application. This means several stages of validation have to be passed through. For structures outside the configuration space, extrapolation warnings will help, whereas for the check for holes inside the PES different architectures of HDNNPs have to be applied to cross check each other [122].

## 2.4 Molecular Dynamics

In molecular dynamics (MD) the classical equations of motions are solved on an potential energy surface to obtain the time evolution of a system. When applied to many-particle systems, a general analytic solution is not accessible. Thus, only numerical methods can be used. This means that we can only integrate the equations of motions using finite differences for the time (time-steps). Furthermore, one needs symplectic integrators, which are designed for the numerical solution of Hamilton's equations. These integrators preserves the canonical character of the equations of motion, they conserve the phase space (symplectic) [123–127].

### 2.4.1 Classical Dynamics

The dynamics of a Hamiltonian system of particles can be described using the Lagrangian equation of motion [128, 129]

$$\frac{d}{dt} \left( \frac{\partial L}{\partial \dot{q}_i} \right) - \frac{\partial L}{\partial q_i} = 0, \quad (2.37)$$

where the generalized coordinates and their derivatives with respect to time (velocities) are expressed as  $q_i$  and  $\dot{q}_i$ , respectively.  $p$  and  $q$  are so called canonical coordinates. The two terms of the Lagrange function

$$L = T - V \quad (2.38)$$

are the kinetic energy  $T$  and the potential  $V$ . Here, the usual expression for the kinetic energy is

$$T = \frac{1}{2} \sum_i m_i \dot{\mathbf{r}}_i^2 \quad (2.39)$$

and the forces  $\mathbf{F}_i$  can be estimated using Newton's second equation in differential form

$$\mathbf{F}_i = -\frac{\partial V}{\partial \mathbf{r}_i} = m \frac{\partial^2 \mathbf{r}_i}{\partial t^2} = \frac{\partial L}{\partial \mathbf{r}_i}, \quad (2.40)$$

when using cartesian coordinates  $\mathbf{r}_i$ . Newton's equation of motion can be derived using Euler–Lagrange Eq. (2.37) [36]

$$m\ddot{\mathbf{r}}_i - \mathbf{F}_i = 0. \quad (2.41)$$

When introducing generalized momenta  $p_i$  that are conjugate to the coordinates

$$p_i = \frac{\partial L}{\partial \dot{q}_i} \quad (2.42)$$

the Hamiltonian for the system can be defined like

$$H = \sum_i \dot{q}_i p_i - L. \quad (2.43)$$

The Hamiltonian resembles the energy assuming the potential does not depend on the time  $t$  and the velocities  $\dot{q}_i$ . Then, the Hamiltonian equation of motion can be written as

$$\dot{q}_i = \frac{\partial H}{\partial p_i}, \quad (2.44)$$

$$\dot{p}_i = -\frac{\partial H}{\partial q_i}. \quad (2.45)$$

In a system using Cartesian coordinates one gets

$$\dot{\mathbf{r}}_i = \frac{\mathbf{p}_i}{m_i}, \quad (2.46)$$

$$\dot{\mathbf{p}}_i = \mathbf{F}_i. \quad (2.47)$$

Note in Eq. (2.41) a system of  $3N$  second-order differential equations is used while Eq. (2.47) contains a system of  $6N$  first-order differential equations. Although equivalent, both systems lead to different discrete algorithms used to solve the corresponding equations.

### Taylor expansion

The simplest way to discretize the equations of motion is to expand them in a Taylor series. The change of the positions and velocities from one time step to the other can be derived using

$$\mathbf{r}_i(t + \Delta t) = \mathbf{r}_i(t) + \Delta t \mathbf{v}_i(t) + \frac{\Delta t^2}{2m_i} \mathbf{F}_i(t) + \frac{\Delta t^3}{3!} \ddot{\mathbf{r}}_i(t) + \mathcal{O}(\Delta t^4), \quad (2.48)$$

$$\mathbf{v}_i(t + \Delta t) = \mathbf{v}_i(t) + \frac{\Delta t}{m_i} \mathbf{F}_i(t) + \frac{\Delta t^2}{2} \dot{\mathbf{v}}_i(t) + \frac{\Delta t^3}{3!} \ddot{\mathbf{v}}_i(t) + \mathcal{O}(\Delta t^4). \quad (2.49)$$

Where  $r$  is the position,  $v = \dot{r}$  the velocity,  $a = \frac{\mathbf{F}}{m} = \ddot{r}$  the acceleration and  $b = \ddot{v}$  the hyperaccelerations [62] (also known as jerk [130]). A multitude of propagators have been proposed, for example  $n$ -order integration schemes like Runge-Kutta [131–133], Beeman [134–136] and others [133, 136]. Here, the focus will be on Verlet-like algorithms.

### 2.4.2 Velocity-Verlet integration scheme

In the Verlet algorithm the velocities can only be obtained from a time step further in time. Moreover, updating the positions gives rise to numerical imprecision [137, 138]. To obtain both positions and velocities in the current time step, the leap-frog algorithm [137, 139–142] can be applied. Here, numerical imprecisions are minimized, but still velocities are not accessible in an ad-hoc manner. To derive positions, velocities and forces at the same time, we use the Velocity-Verlet algorithm [139, 143]. The update of the positions and velocities is estimated according to

$$\mathbf{r}_i(t + \Delta t) = \mathbf{r}_i(t) + \Delta t \mathbf{v}_i(t) + \frac{\Delta t^2}{m_i} \mathbf{F}_i(t) + \mathcal{O}(\Delta t^3), \quad (2.50)$$

$$\mathbf{v}_i(t + \Delta t) = \mathbf{v}_i(t) + \frac{\Delta t}{m_i} (\mathbf{F}_i(t) + \mathbf{F}_i(t + \Delta t)) + \mathcal{O}(\Delta t^3). \quad (2.51)$$

Algebraically, the Velocity-Verlet algorithm is equivalent to the original Verlet scheme. Although rather simple, the Velocity-Verlet scheme is very stable and is a symplectic integrator. This explains why it is widely used in MD simulations.

### 2.4.3 Thermostats

The canonical (NVT) [144–149] ensemble, the number of atoms  $N$ , the volume  $V$  as well as the temperature  $T$  are preserved. This is therefore often referred to as the *NVT* ensemble. In this ensemble, the energy of processes is constantly exchanged with a thermostat. A variety of thermostat algorithms are available to realistically introduce a mechanism, which can exchange energy from the boundaries of a MD simulation. Therefore, the canonical ensemble is approximated via rescaling the velocities. The Nosé-Hoover-Thermostat [150], Nosé-Hoover chains, the Berendsen thermostat, Langevin dynamics and the Andersen thermostat are popular methods. In this work, the *Andersen Thermostat* was used [144, 151].

As a way to simulate such system, we rely on stochastic forces acting on the atoms in order to change their kinetic energy, which is similar to Brownian motion. The result will be that the average of any property in a trajectory is equal to the canonical ensemble. The equations of motion of a  $N$  particle system in Volume  $V$  are the hamiltonian equations, Eq. (2.44) and (2.45). In the latter equation a stochastic collision term is added. The momentum of each particle is affected by the stochastic collisions in an instantaneous event. The collisions that occur are Poisson processes and statistically uncorrelated. Evolution of the state between collisions are according to Eq. (2.44) and (2.45). Initially, the desired temperature  $T$  of the (artificial) bath the system stays in contact with and the rate of the collision  $\nu$  has to be set. The heat bath has a Maxwell Boltzmann (MB) velocity distribution with energy distributed randomly among all particles of the bath. The probability of a collision in a time interval is then  $\nu \Delta t$ . In the beginning of a simulation the particular times of a collision are set by using random numbers and the time intervals are distributed according to

$$P(t) = \nu \exp(-\nu t), \quad (2.52)$$

with  $P(t) \Delta t$  being the probability that an interval takes place between  $t$  and  $\Delta t$ . (Alternatively, random numbers can be used to choose which atom will collide.) The system is given enough time after each collision to equilibrate to the desired temperature. The canonical ensemble is used to equilibrate a surface structure to the desired surface temperature, but we are basically interested in the microcanonical ensemble (NVE) [152, 153] to analyze energy dissipation pathways. We use the *Andersen Thermostat* purely for heating up our systems of interest because of its simplicity and ease of utilization.

### 2.4.4 Ring Polymer Molecular Dynamics

Quantum effects cannot be treated directly in classical MD simulations. Because hydrogen atoms are very light and fast traveling particles, neglecting quantum effects might lead to changes in the scattering behavior and thus changes the distribution of energy loss spectra. This is especially of importance, because in the scattering a barrier is involved, which is due to a rehybridization of a surface carbon atom. Depending on the system, effects like tunneling and zero point energy (ZPE) might lead to drastical changes when evaluating rate constants for proton transfer reactions [154].

Introduced in 2004, Ring Polymer Molecular Dynamics (RPMD) [155, 156] offer a way to account for quantum effects in MD simulations. Keeping the methodology from classical MD simulations, the imaginary-time path integral (PI) formalism is adopted to exploit the exact equilibrium mapping between a quantum mechanical particle and a classical ring polymer [155, 157]. With this method, tunneling and zero point energies can be approximated. A classical ring polymer is isomorphic to a quantum particle in the limit of assigning an infinite number of beads. Real-time quantum coherence (wave-like behavior) is neglected, which results in less demanding trajectories compared to the full quantum treatment. Assuming the coherence

vanishes quickly due to thermal averaging or strong intermode coupling, RPMD can provide insights to influence of quantum effects. Atoms are no longer treated as points but exist in an extended space in analogy to a necklace, fully characterized by their number of beads  $P$  and connected via harmonic springs. The difference of the classical picture, where  $P = 1$  and an example of the extended space with 4 beads ( $P = 4$ ) can be seen in Fig. 2.6.

In summary, RPMD make use of PI and is classical MD in the extended ring polymer phase space. RPMD as well as centroid MD (CMD) are two distinct extensions to Path Integral MD (PIMD) [158], with the latter not being of interest here, because this will go beyond the scope of this thesis.

Although the atoms exist in an extended phase space, a single PES is sufficient. The inter-bead interaction is handled by the propagator of the MD, whereas for a single bead the same PES describing the total system is used to derive its specific properties (energies, forces). In the short-time and high-energy limit, the quantum mechanical results are correct. In principle, an exact treatment of the quantum Boltzmann operator with an approximate treatment of the real-time evolution based on classical mechanics is realized [159–163].

In the following, a brief overview of the main aspects and derivations is given. Furthermore, common literature will be offered for RPMD and path integrals, where appropriate.

RPMD is an algorithm developed for time evolution of ring polymers. Therefore, the Hamiltonian is split into a sum of a free ring polymer part and a potential energy part. The two parts can be combined in a symplectic integration scheme, where the phase space density evolves under the influence of the propagator. A convenient way for integration is the constant

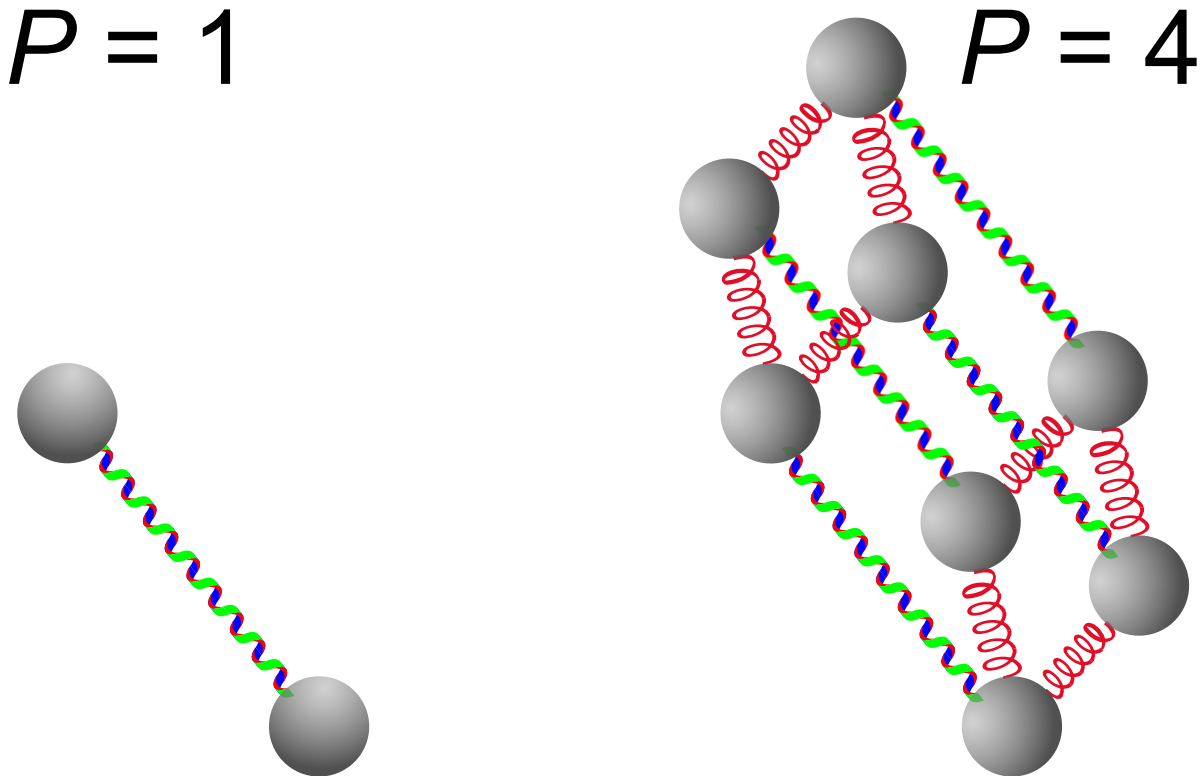


Figure 2.6: Scheme for the carbon-carbon interaction of atom  $i$  and  $j$  in the classical limit (Trotter number  $P = 1$ ). Example of atoms having 4 beads ( $P = 4$ ), forming what can be thought of as a "ring polymer molecule". The harmonic springs between beads are in red, and red/green/blue curly bonds represent the classical intermolecular pair potential.

transformation between bead and normal mode representation, because the use of FFT is efficient. In the following the main steps of the algorithm are given.

1. exact evolution of the ring polymer momenta through time interval  $\frac{\Delta t}{2}$  (under influence of the Hamiltonian)
2. transform bead to normal mode representation
3. exact evolution of the ring polymer coordinates and momenta through time interval  $\Delta t$  (under the influence of the free ring polymer Hamiltonian)
4. transform normal mode representation back to bead representation
5. further exact evolution of ring polymer momenta through time interval  $\frac{\Delta t}{2}$  (under influence of the Hamiltonian)

In RPMD,  $H_n(\mathbf{p}, \mathbf{q})$  is the classical Hamiltonian of a fictitious ring polymer consisting of  $n$  copies of the system, connected by harmonic springs. In the full form the Hamiltonian can be written as

$$H_n(\mathbf{p}, \mathbf{q}) = \sum_{s=1}^P \left\{ V(\mathbf{q}_i^{(s)}, \dots, \mathbf{q}_N^{(s)}) + \sum_{i=1}^N \left[ \frac{(\mathbf{p}_i^{(s)})^2}{2m_i} + \frac{m_i}{2} \left( \frac{P}{\beta \hbar} \right)^2 (\mathbf{q}_i^{(s)} - \mathbf{q}_i^{(s-1)})^2 \right] \right\}, \quad (2.53)$$

where the classical potential function is denoted as  $V$ , the common definition  $\beta = (k_B T)^{-1}$  is used and  $P$  is called the Trotter number and give the number of beads with bead index  $s$ . Here, the term for the kinetic energy is extended by formula that is analog to a spring potential of the form

$$V_{\text{spring}}(x) = \frac{1}{2} k (x - x_0)^2. \quad (2.54)$$

In the high-temperature limit, the radius of the ring polymer shrinks to zero, because the force constant become very large. Here,  $\beta \hbar \omega_{\text{max}} \ll 1$ , with  $\omega$  being the highest vibrational frequency in the physical problem. In the large atomic mass limit, the term for the spring constant is large as well, which correspond to the classic case. Secondary, in the limit  $t \rightarrow 0$ , classical MD is recovered, because the ring polymer is reduced to a single point. This behavior can be seen from the definition of the radius of gyration

$$r_G(\text{free}) = \sqrt{\frac{\beta \hbar^2}{4m} \left( 1 - \frac{1}{P^2} \right)}, \quad (2.55)$$

which describes a free ring polymer [164].

In analogy to the Hamiltonian equations of motion as shown in Eq. (2.44) and (2.45), for PIMD the equations of motion can be formulated. For the velocities this looks like

$$\frac{d\mathbf{q}_i^{(s)}}{dt} = \frac{\partial \hat{H}}{\partial \mathbf{p}_i^{(s)}} = \frac{\mathbf{p}_i^{(s)}}{m_i} \quad (2.56)$$

whereas for the momenta one can write

$$\frac{d\mathbf{p}_i^{(s)}}{dt} = \frac{\partial \hat{H}}{\partial \mathbf{q}_i^{(s)}} = -m_i \left( \frac{P}{\beta \hbar} \right)^2 (2\mathbf{q}_i^{(s)} - \mathbf{q}_i^{(s-1)} - \mathbf{q}_i^{(s+1)}) - \frac{\partial V(\mathbf{q}_i^{(s)}, \dots, \mathbf{q}_N^{(s)})}{\partial \mathbf{x}_i^{(s)}} \quad (2.57)$$

The extension with respect to classical MD can be seen best in the term for the kinetic energy,

where the "virial" energy estimator [165] is

$$E_{\text{kin}} = \frac{3}{2\beta} + \frac{1}{2NP} \sum_{i=1}^N \sum_{s=1}^n \left( \mathbf{q}_i^{(s)} - \bar{\mathbf{q}}_i \right) \frac{\partial V(\mathbf{q}_1^{(s)}, \dots, \mathbf{q}_N^{(s)})}{\partial \mathbf{q}_i^{(s)}} \quad (2.58)$$

with the centroid  $\bar{\mathbf{q}}_i$  being derived by averaging over all beads of the  $i^{\text{th}}$  ring polymer necklace

$$\bar{\mathbf{q}}_i = \frac{1}{n} \sum_{s=1}^P \mathbf{q}_i^{(s)} \quad (2.59)$$

In Eq. (2.58), the first term is estimated by considering  $\frac{1}{2} k_B T$  for each translational degree of freedom (DOF) in the classical picture. The contribution from quantum fluctuations is expressed in the second term. Without an external field, the term will cancel out. The term becomes noticeable when simulating condensed matter systems at low temperatures, due to the Heisenberg uncertainty principle. The kinetic energy of the beads is higher the more the bead is contracted under the influence of external forces. The more the beads are localized, the higher the fluctuations of the momenta. Using RPMD in scattering simulations was justified elsewhere [158]. In short, although the interaction between an impinging particle with a surface is far from equilibrium conditions, there is no indications preventing the use of this approach in non-equilibrium systems. Furthermore, the quality of the insights gained from RPMD simulations will be cross-checked with the more accurate MCTDH method to account for all nuclear quantum effects [166].

## 2.4.5 Path Integral Langevin Equation

To heat up a system that exists in an extended phase space i.e. using ring polymers, the Path Integral Langevin Equation (PILE) [167, 168] is used. Bussi and Parrinello have shown how a Langevin thermostat can be combined with the velocity verlet algorithm [169]. In classical statistical mechanics, it provides an efficient sampling of the canonical distribution. In the classical MD picture, when there is only a single bead, this equation is reduced to the Langevin equations of motion [164]. The momentum update is done in a three-step manner:

1. use an orthogonal transformation matrix  $\underline{\underline{C}}_{jk}$  to convert Cartesian coordinates  $j$  to normal modes  $k$  (Eq. 2.60)
2. each normal mode of the ring polymer experiences a random force and friction as shown in Eq. (2.61)
3. transfer normal modes back into Cartesian coordinates, according to Eq. (2.62)

with  $\gamma^{(k)}$  as friction coefficient for normal mode  $k$ ,  $\boldsymbol{\xi}^{(k)}$  represents the vector of independent Gaussian numbers. The transformation between the Cartesian coordinates and normal modes to represent the system is done by using fast fourier transformations (FFT), well known for their performance and efficiency.

$$\tilde{\mathbf{p}}^{(k)} \leftarrow \sum_{j=1}^n \mathbf{p}^{(j)} \underline{\underline{C}}_{jk} \quad (2.60)$$

$$\tilde{\mathbf{p}}^{(k)} \leftarrow \exp\left(-\frac{\Delta t}{2} \gamma^{(k)}\right) \tilde{\mathbf{p}}^{(k)} + \sqrt{\frac{m_i}{P k_B T} (1 - \exp(-\Delta t \gamma^{(k)}))} \boldsymbol{\xi}^{(k)} \quad (2.61)$$

$$\tilde{\mathbf{p}}^{(j)} \leftarrow \sum_{k=0}^{n-1} \underline{\underline{C}}_{jk} \tilde{\mathbf{p}}^{(k)} \quad (2.62)$$

The only required initial input parameter is the friction coefficient  $\gamma$  of the centroid mode. This mode describes the movement of a full ring polymer. Whereas the friction coefficients for the normal modes can be estimated analytically by minimizing the autocorrelation time for the Hamiltonian of the harmonic oscillator [167]. This is in analogy to the *Andersen thermostat*, where the interaction time of the particles in the system with the heat bath has to be set.

The algorithm consists of a sequence of exact evolutions, which are performed using approximate Hamiltonians. Because it is symplectic, the ring polymer phase space volume is preserved, if the timestep is chosen to be sufficiently small.





---

# Computational Details

In this chapter, an overview of all used programs and tools will be provided. Starting with the used electronic structure codes VASP and FHI-AIMS, the stand-alone Fortran program RuNNer used to construct high-dimensional neural network potentials is described. The molecular dynamics code `md_tian` is described, which was developed in our group and used to simulate the scattering of atoms and molecules from surfaces. Furthermore, its successor MDT2 is described. In this program the RuNNer subroutines implementing the HDNN-PES providing the energies and forces were integrated, which can be seen as RuNNer-MDT2 interface.

The MCTDH package used for quantum molecular dynamics has been used by our collaborators [30] and the details will not be mentioned here, because this will be beyond the scope of my work.

This chapter is meant to be the foundation of a full manual for the MDT2 code along with a guideline of how to conduct proper DFT calculations serving as input data for PES fitting procedures. This is why I also explain the structure of the input files which are used in the standard electron structure codes VASP and FHI-aims. The small manual given here will be extended and offered as well on the GitHub webpage [170].

## 3.1 VASP

The method of choice in this work to generate electronic structure data is the Vienna Ab-initio Simulation Package (VASP) in the version 5.3.5 [171–174]. This code uses a plane-wave basis set and requires several input files to initialize a calculation, which will be explained in the following.

### 3.1.1 INCAR

The main keywords and settings are provided in the INCAR file. An example file is given in Lst. A.1 in the appendix. This counts for all following given example files. DFT at the GGA level of theory using PBE functional with a planewave basis is used in combination with Grimme D2 dispersion correction. The kinetic energy cutoff has been set to 400 eV. Spin polarization in the electronic structure calculations are included. The tetrahedron method with Blöchl corrections [175, 176] using the default value of 0.2 eV as the smearing parameter is applied to

treat partial occupations. When relaxing the electronic degrees of freedom, the threshold for the change in energy between iteration steps is set to  $10^{-5}$  eV. A normal precision of calculations is used in combination with a very fast diagonalization algorithm in the self-consistent steps. The minimum number of SCF steps is 4 and it cannot exceed 300 steps.

### 3.1.2 KPOINTS

The number of k-points sampling the irreducible Brillouin zone is set in the KPOINTS file. An example how the KPOINTS file looks like is given in Lst. A.2. The Monkhorst-Pack scheme [177] with a  $8 \times 8 \times 1$   $\Gamma$ -centered  $k$ -point mesh is used to sample the surface Brillouin zone for a single hydrogen atom on a 24 carbon atom graphene surface.

### 3.1.3 POSCAR

In the POSCAR file, not only the positions of each atom but also information concerning the simulation cell, number and symbol of elements is given. An example structure file is offered in Lst. A.3. With two atoms per unit cell the  $3 \times 4$  surface cell consists of 24 carbon atoms in total and is  $8.55 \text{ \AA} \times 7.40 \text{ \AA}$  in size. 3D periodic boundary conditions have been applied with  $13 \text{ \AA}$  vacuum perpendicular to the graphene sheet to ensure that the periodic images of the surfaces are non-interacting and that hydrogen atoms can be included at a maximum separation of  $6 \text{ \AA}$  from the surface. The cell must contain enough lateral space to ensure that the H-atom does not see its periodic image. There have to be enough C-atoms to enable the impinging particle to distribute the energy to surface phonons.

### 3.1.4 POTCAR

The POTCAR file has to be manually put together in a modular way. If more than one species (element) is present in the system (in the POSCAR file), the different files have to be merged. Note, the order has to be the same as given in the POSCAR file. In principle, one can decide between ultrasoft pseudopotentials (USPP) and projector-augmented wave (PAW) potentials [174, 175]. The latter are used in this work, although both types of pseudopotentials can be transformed into each other. The motivation of using pseudopotentials is to reduce the basis set size and number of electrons as well as inclusion of relativistic and other effects. Core electrons with a highly oscillating wavefunction near the nucleus are described in an effective (pseudo-) potential, replacing the Coulomb potential of the Hamiltonian. Reducing the complexity makes a plane-wave basis set practical to use. Normally, the PAW method is used for the pseudopotentials because of performance reasons.

In this work, to model the core and valence electron interactions, the PAW approach was used. For H-atoms PAW potentials are used in the version "PAW\_PBE H 15Jun2001" and for the C-atoms the version "PAW\_PBE C 08Apr2002" was used, respectively.

## 3.2 FHI-aims

The Fritz Haber Institute ab initio molecular simulations (FHI-aims) code was used as additional electronic structure code [178–183]. FHI-aims uses numeric-atom centered orbitals (NAO) as basis set. In contrast to VASP, there is only a single input file named control.in aside the structure file called geometry.in.

This electronic structure was used to cross check for the data generated by VASP and helped to identify problems in the underlying DFT data. Therefore, I will only give a brief overview according to the Manual [184]. In the following, the two input files are inspected in detail.

### 3.2.1 control.in

The main input file contains all required settings for the calculations and an example file is given in Lst. A.4. The B3LYP functional was utilized and vdW corrections are added using the Tkatchenko-Scheffler (TS) scheme [70]. Spin polarized calculations are carried out explicitly setting the spin in the geometry file as shown next. Relativistic effects are included by using the scaled zeroth order regular approximation (ZORA) [185, 186]. 3D periodic boundary conditions have been included by defining a  $k$ -point density approximately equivalent to a  $6 \times 6 \times 1$  mesh. Again, the threshold for the change in energy between iteration steps is set to  $10^{-5}$  eV. There are different levels of basis sets available for each atomic species: light, tight and very-tight. Additionally, the really tight basis set is available but should only be used for specific testing scenarios, not in a production run, since it is computationally very expensive. To calculate Energies at least a light ("tier 1") basis set for the H-atom and all C-atoms is needed, respectively. This basis set is pre-constructed and includes all occupied orbital functions. A small set of unoccupied orbital functions is included as well. Higher basis sets are in ascending order tight ("tier 2") or very tight ("tier 3"). Even higher "tier" levels are accessible, depending on the element. In case of the C-atoms, even a "tier 4" basis set can be assigned.

### 3.2.2 geometry.in

In analogy to the POSCAR file in VASP, the structure is given in the geometry.in file. Here, the lattice vectors had to be set explicitly starting with the keyword `lattice_vector`. Cartesian coordinates have to be given for each atom starting with the keyword `atom` and the element symbol is given last. Unlike in VASP, here the spin has to be given in the structure file below the specific atom having a spin starting with the keyword `initial_moment`. This can be seen in Lst. A.5.

## 3.3 RuNNer

To construct high-dimensional neural network potentials, the RuNNer Neural Network Energy Representation (RuNNer) code was used [187]. Following the last given reference, it will direct the user to the online manual.

RuNNer needs two input files, first the main input file `input.nn` and the structure file `input.data` containing the information of all structures with corresponding energies and forces (and charges, if available) from electronic structure calculations. The program uses a bottom-up approach to finally offer a PES. It is operated in constructive modes. In mode 1, the values for the symmetry functions are calculated and the data set is split into the training and a validation (test) set in a random fashion. In mode 2, the PES is fitted whereas in mode 3 the obtained weights and biases are used to predict properties (e.g. energies and forces) of a given structure.

### 3.3.1 input.nn

In the `input.nn` file, the different types of NNs are defined. For the H on graphene system, only the short range NN is required. The exact same file can be used in all different modes. The first mode is used to calculate the values for the symmetry functions in the data set, in mode 2 the PES is fitted and mode 3 is used to predict the properties (energies and forces if requested) of a given structure using the PES.

There exist two types of short NN, Behler-Parrinello atomic or pair. Here, the Behler-Parrinello atomic NN is used. In the system, there are two elements, H-atom and C-atoms,

their element symbol has to be given and the seed for the random number generator (RNG) is set as well as which type of RNG should be used. If the total energy of a structure is higher than the threshold (Ha atom<sup>-1</sup>), the structure is not used for the fitting. Beforehand, structures are chosen to fulfill certain criteria (energy, bond length), so all structures in the data set can be used for the fitting. Although structures with a too small bond length have been removed from the data set, the threshold is set that structure with a bond length below 0.1 Å are ignored. This also helps to avoid problems arising when calculating symmetry function values. The architecture has been set to two hidden layers with 15 nodes for each layer. The hyperbolic tangent activation function is used for all hidden layers and the output layer uses a linear activation function. 10% of the structures from the reference data set are arbitrarily chosen for validation (test set), most structures are used for the fitting (training set). The test set is completely independent of the training set and is used to validate the fit and also to account for overfitting. Type two of radial symmetry function is used, which is equivalent to  $G_i^2$ . For the angular symmetry functions type 3 is used, which is equivalent to  $G_i^4$ . Both types of SF are described in Ch. 2. A complete list with used SF can be seen in Tab. A.1 and A.2. The values of the symmetry functions are rescaled to have a range from 0 to 1. The values of the weight parameters have been initialized with random numbers in the interval from -1 to 1. Additionally, a preconditioning scheme was applied to reduce the initial root-mean-square error (RMSE). To reduce the probability of being trapped in local minima, the training data was presented in a random order in each of the 200 iterations (epochs). To further reduce the RMSE, after 100 iterations, the program was stopped and restarted from that epoch to re-initialize the parameters of the fitting algorithm. After each epoch, the current weights are written to disk. From the available information of forces, only 1% is used to further increase the fit of the energies. The common protocol is to use most or all energies and only a small fraction of forces to increase the overall RMSE of the fit. To reduce the demanding RAM in the fitting, the number of structures being present at one time was set to 2000, whereas in prediction mode the number is automatically set to the number of atoms in the structure, but for simplicity it was manually set to avoid a warning message. Forces have to be explicitly requested, because otherwise only energies are predicted. It is also possible to check, if the sum of all forces is zero. Especially when using NNPs in MD simulations, it is also possible to reduce the output. This is done by including `md_mode`. At least for H-atom scattering on graphene it turned out that using symmetry function groups slightly increases the performance, which is the reason why it is used here.

An example file containing all the above mentioned settings can be seen in Lst. A.6.

### 3.3.2 input.data

In the `input.data` file all structures to fit the NNP are offered. All information for a single structure is given between the `begin` and `end` keywords. Starting with the `comment` keyword, comments can be included (for example settings from electronic structure calculations, system specific information etc.). The lattice vectors are given starting with the `lattice` keyword. All information for a single atom is given after the `atom` keyword. First, the Cartesian coordinates in  $x$ ,  $y$  and  $z$  are given followed by the element symbol, the atomic charge and the atomic energy. Finally, forces in  $x$ ,  $y$  and  $z$  direction are given. In case, the investigated system is charged, the total charge is given after the `charge` keyword. The total energy of the structure is given after the `energy` keyword. Note, the unit for distances is Bohr, the energies are given in Hartree (Ha), the charge is given in  $e$  whereas the forces are expressed in Ha Bohr<sup>-1</sup>. A single structure how the `input.data` file has to look like is shown in Lst. A.7.

### 3.4 md\_tian\_xia

The self-written Molecular Dynamics Tian Xia (md\_tian) code was developed in the Wodtke group by Svenja M. Janke, Sascha Kandratsenka and Daniel J. Auerbach [188]. The code implements Newtonian and Langevin dynamics for the simulation of an H-atom interacting with *fcc* and *bcc* metal surfaces [15, 19] using a full dimensional effective medium theory (EMT) PES [189, 190] and the programming language is Fortran. With the Levenberg-Marquardt approach it is possible to fit the PES to electronic structure data. Furthermore, a genetic algorithm (GA) has been made available as a wrapper script to improve the fitting procedure in terms of accuracy as well as performance. A more detailed overview is given in Refs. [188, 191, 192].

### 3.5 md\_tian\_xia\_2

The Molecular Dynamics Tian Xia 2 (MDT2) code [170] is the successor of the md\_tian code with new organization, general applicability and a modular based structure. Again, the programming language is Fortran. Marvin Kammler improved and extended the program. With this improvement, H-atom scattering on all *fcc* and *bcc* metals is possible [19]. So far also ring polymer molecular dynamics can be performed, allowing to account for tunneling and zero point energy (ZPE) effects in the simulations. Additional potentials can be included as well as propagation methods, independent from each other. The reactive empirical bond order (REBO) potential has been added to the available potentials. In principle, different potentials can be used to describe specific interactions only. The flowchart of the MDT2 program is shown in Fig. 3.1.

The equilibrium geometry of the system of interest is used to initialize simulations in the *NVT* ensemble. To heat up the system, there are two thermostats available: The *Andersen* and *Path Integral Langevin Equation* (PILE). The system is heated up to the desired temperature and after equilibration, the positions as well as velocities are saved as a snapshot. This snapshot is then used to initialize simulations in the *NVE* ensemble. From a long trajectory, snapshots after a given timestep are used to generate configurations that can be chosen when simulating scattering trajectories. Normally, this is done using the mxt (binary) format.

In MDT2, there are several input files on different levels. The main input file is normally named md\_tian.inp, but can be arbitrarily named. In the main input file, for each used potential a potential-depending file and its path has to be given, containing the potential specific parameters. Normally, the naming follows the rule by first giving the name or acronym of the potential and they end on .pes, but again this is up to the user.

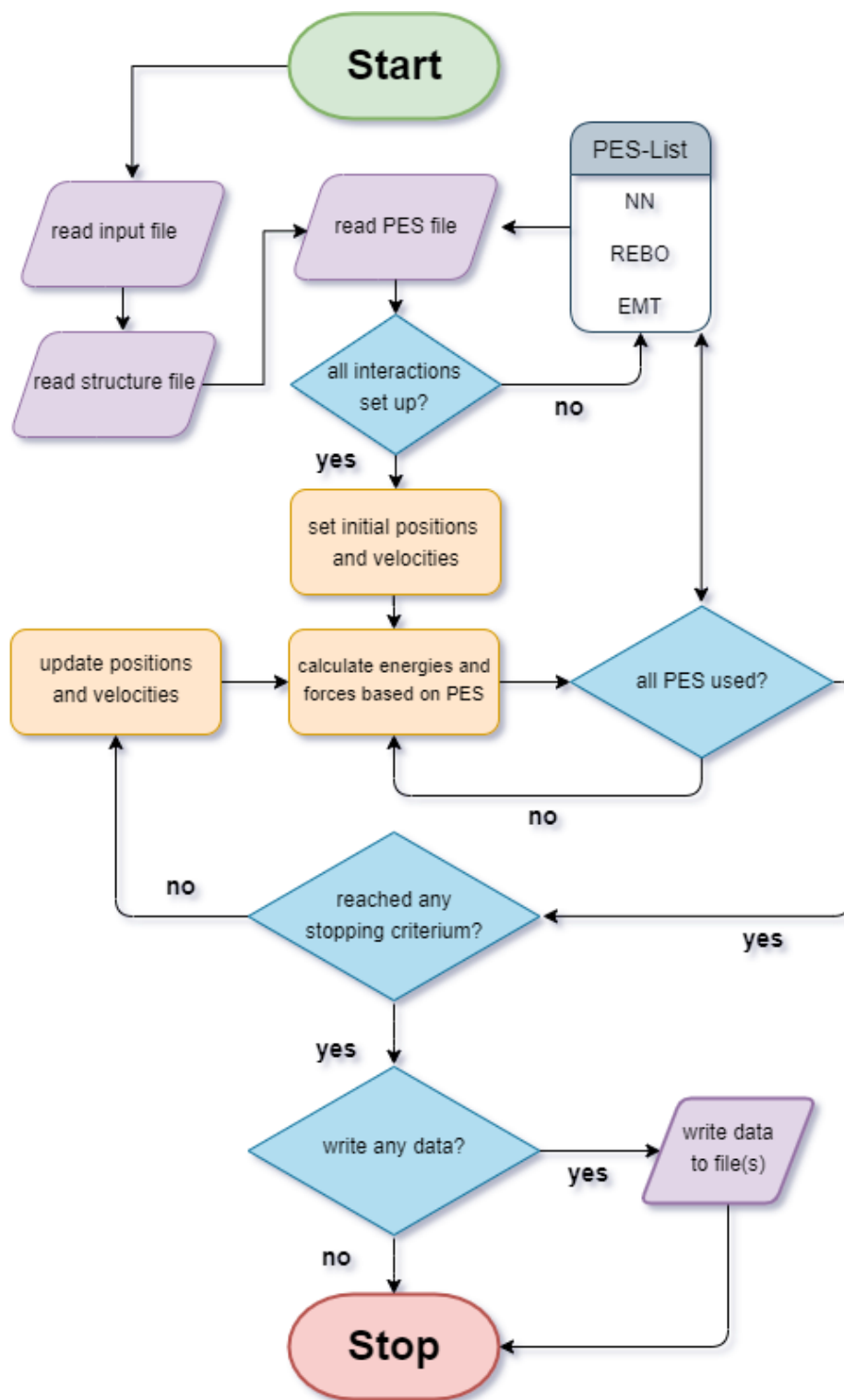


Figure 3.1: Flowchart of the program MDT2 [170]. After initialization, the interaction matrix is build up according to the PES(s) used. The main loop of the program is to calculate energies and forces for all used PESs, to decide if positions and velocities are updated or if any stopping criterion is reached (list in text). This flowchart was generated using [193].

### 3.5.1 md\_tian.inp

```

run md
rng_seed traj_id
start 1
ntrajs 10000
nsteps 2000
step 0.1
projectile 1 H 1.0 ver
lattice 1 C 12.0 ver
Einc 1.92
polar 50
azimuth 0
pip r r 6.0
pul 6.1
Tsurf 300
Tproj 300
conf merge 'conf/proj/' 1 'conf/latt/' 1000
pes 'pes/nene.pes'
output scatter 1

```

Listing 3.1: Example MDT2 md\_tian.inp file

An example of a typical input file as used in MD simulations to perform scattering trajectories is given in Lst. 3.1.

In MDT2, there exist three different run modes. Minimization of a given structure using the (FIRE) algorithm is requested by using the *min* keyword, fitting REBO parameters can be done by using *min* keyword and performing MD simulations with the *run* keyword. Depending on the run mode, structure files and their path have to be given in the main input file. So far, the POSCAR and mxt (binary) format can be read in. Normally, the system is split up into the projectile and the surface. Beforehand, from a single long trajectory (ps to ns) in the *NVT* ensemble screenshots are extracted in the mxt format to account for different surface configurations created from thermal movement. This is crucial, because the scattering trajectories take place on a rather short timescale compared to the preparation. With this procedure it should be guaranteed that the surface is sampled enough to not be trapped in local minima and to bias the simulations. The same procedure is applied in the case of the projectile. For a single atom, just a single structure is used, but for molecular projectiles, internal vibrational as well as rotational DOFs have to be considered and will be sampled again using the procedure of taking screenshots from a *NVT* trajectory beforehand. When performing RPMD simulations, the same counts for atoms when using more than a single bead, because they affect both the projectile as well as the surface.

After the start keyword, the number of the trajectory can be set. This has several advantages. This number is used to seed the RNG and will therefore lead to different initial conditions. With this attempt, it is also possible to meaningful split the simulations to many cores, leading to an elegant parallelization scheme. For example, if we double the number of cores used for calculations, we also double the number of trajectories run at the same time. Furthermore, it is also possible to re-calculate a single trajectory out of a series of many trajectories for further analysis. The **ntrajs** keyword is used to set the number of trajectories to be calculated and **nsteps** sets the maximum allowed number of time steps. With this, we have a stopping criterion to not calculate infinitely long trajectories, if the projectile is adsorbed and is not released. The step keyword sets the time interval for integration and is given in femtoseconds

(fs). As already mentioned, the system of interest is split into the projectile and the surface. The properties for the projectile are given after the projectile keyword. The first number denotes the number of projectiles followed by a sequence of the element symbol, the mass of the element and the abbreviation of the propagator used to upgrade forces and positions of the particles in the simulations. This is repeated until all elements have been defined. The same procedure is applied in the case of the surface, if it is an alloy, for example. The only difference is, that all information is given after the lattice keyword. If using the *NVT* ensemble, the Andersen (**and**) method can be used or PILE (**pil**) in case of performing RPMD simulations. If only a single bead is set, PILE can be used to heat up a classic system as well. For both algorithms, a time constant has to be set.

For simulations in the *NVE* ensemble, the initial conditions of the projectile have to be set. The initial kinetic energy is given in eV after the **Einc** keyword, whereas its initial polar as well as azimuth angle in  $^{\circ}$ . The polar angle is with respect to the  $z$ -axis and the azimuth angle is with respect to the  $x$ -axis. The initial position of the projectile can be either set explicitly giving the  $x$ ,  $y$  and  $z$  coordinates or  $r$  can be used to do this in a random fashion. With the projectile upper limit (**pul**) a stopping criterion can be set. If the  $z$ -coordinate of the projectile exceeds this limit after a time step, the trajectory is stopped and the final conditions are saved. The temperature in Kelvin (K) of the projectile as well as the surface have to be explicitly given after the **Tsurf** and **Tproj** keyword. The starting structure is given after the **conf** keyword. Normally, **merge** is used and the system is split beforehand into the projectile (**proj**) and surface (**latt**) part. Here, the path to the screenshots from previous simulations has to be given as well as the number of possible structures that can be picked. Which structure should be used is decided randomly. Additionally, the path to the potential file containing the potential specific parameters has to be given here. Furthermore, it can be decided, which scheme of RNG should be used. Because of performance reasons, using **traj\_id** turned out to be very efficient and offers a very well sampled uniform distribution. In this case, the number of the current trajectory is used to seed the RNG. After the output keyword, several output formats can be given. When calculating a large number of trajectories, normally only the keyword **scatter** is present. It checks for all mentioned stopping criteria and collects all information in the beginning and at the end of a simulation. Further output formats and information can be found in [170].

When using MDT2 to perform MD simulations, a detailed input file is given in Lst. A.8.

### 3.5.2 nene.pes

In principle, the potential files can be arbitrarily named like the input file, but it is common practice to use the potential name, abbreviation or acronym as first part and the file ends on .pes, which has to also be given in the main input file, as mentioned before.

In the potential file, all permutations of projectile and surface elements has to be defined, enabling to describe all interactions even by more than one potential. First, after the **pes** keyword the abbreviation of the potential that should be used to describe the following interaction is given. With giving the element symbols and after that the definition if the element is part of the projectile or lattice, the matrix has to be set. This can be seen in the file giving below in this subsection.

Depending on the requested potential, several parameters have to be given in the potential file. When using HDNNP, the potential file is named **nene.pes**, with **nene** being a short notation for neural networks. Furthermore, the naming is based on the real person Nene, the wife of one of the three great unifiers of Japan in the Sengoku period (16th Century). Here, the interested reader might also read the entry in the quotes or [194–196].

For the HDNNP, only two parameters have to be given. First, the folder containing all



needed files for the NNP. In the folder, the following files have to be present

- input.nn
- scaling.data / scalinge.data
- weights.XXX.data / weightse.XXX.data

As mentioned before, the input.nn file is the main input file containing the architecture of the NN and all SF, the scaling.data file contains all biases and there has to be a weight file for each element present in the system. The format of the weight files is weights.XXX.data, with XXX being the atomic charge. In case of H-atom scattering from graphene, there are two weight files, the one for the H-atom is weights.001.data and the one for all C-atoms is weights.006.data, respectively. In case of using 4G-HDNNPs, when including an additional NNP for the electrostatic part, a complete set of biases and weights for this NN has to be given, too. The naming is to add a single e at the end of the prefix. These files are automatically generated by RuNNer during the fitting mode. An example for the files needed for RuNNer or its subroutines implemented in MDT2 is not given here. Check Sec. 3.3.1 for the input.nn file and also consider the RuNNer Manual for further details [197].

Nevertheless, some notes for the input.nn file when used in MDT2: To avoid unnecessary warnings, the points\_in\_memory should be manually set to the number of atoms in the structure and runner\_mode should be 3, although it will be set by default. The keyword calculate\_forces should be given, since in MD forces had to be predicted as well. By default, they are turned on, but explicitly giving the keyword saves a warning message. Most of the output is suppressed by switching on md\_mode and as mentioned before, to sort the SF by groups slightly increases the performance.

Secondly, the optional keyword maxnum\_extrapolation\_warnings can be given to manually set the maximum number of extrapolation warnings allowed before stopping the program. If no keyword is given, there will be effectively no stopping criterion. If the keyword is given, the following number defines the threshold. This is because of performance reasons but also to avoid creating unusable results outside the configuration space of the underlying potential.

An example file is given in Lst. A.9

## 3.6 Implementation of NN into MDT2

This section is constructed to give an overview of the steps performed in order to couple the description of a neural network potential in the RuNNer program written by Jörg Behler with our molecular dynamics program, MDT2, presented in 3.4 and 3.5. Here, the purpose is to collect the offered information from different sources in one place.

To describe the scattering from H-atom from a graphene surface one needs an accurate, full-dimensional PES. And this PES is used to predict energies and forces to update positions and velocities in MD simulations. There are very common used MD programs like LAMMPS, for example. But as far as we know, there is no implementation of the EMT formalism in such programs. Although there is a general realization to couple NNs formulated in RuNNer with an MD program (referred to as RuNNer-LAMMPS), the necessity to use NNP in a surface scattering program is at hand. In RuNNer-LAMMPS the energy and force evaluations are provided by the n2p2 neural network library [198] utilized in MD simulations performed using LAMMPS [199]. To investigate surface scattering using machine-learning based potentials, the treatment of neural-networks as formulated in the RuNNer program is included into our MD simulation program called MDT2. Both programs are mentioned in previous sections.

During the process to finally create a fast hybrid program, there was also a very early attempt, which is referred to as the slow version. In this version, the information is passed from MDT2

to RuNNer as a whole program. With this, soon a working version was established performing simulations to obtain results, which could be compared to scattering experiments. Depending on the hardware, where the program runs on, it could take around a minute up to several minutes on average to calculate a single scattering trajectory. In short, I highly recommend using not only the latest intel compiler but also the *MKL* library for best performance when compiling MDT2.

Since both programs are written in Fortran, no new code or more demanding re-writing of already existing code is needed. Although, a lot of existing code especially when reading in the information from input files had to be re-written. The reason is, that due to the different structure of the two programs the subroutines could not be used directly. At the same time this has the advantage to cross check input offered in MDT2 with that from RuNNer. This detection allows to have sanity checks which helps to reduce not only missing or corrupt files but also user specific errors and is crucial when properly simulating particles. This is especially of importance, since files from the RuNNer framework are used next to files needed in MDT2. Changes in future versions of the RuNNer framework has been accounted for by giving the location in the source code where each part has been taken from RuNNer framework to update existing code. However, the subroutines calculating properties of a given structure (energies, forces etc.) are used as they are in RuNNer. This has the advantage to not destroy or re-write the most crucial parts that are needed for the potential used, it also makes it easier to update those subroutines in the future, when changes occur. And at least so far it seems, there are a lot of changes coming in the future, because many people are constantly updating and improving the RuNNer framework.

A flowchart of the MDT2 program [170] is shown in Fig. 3.1. Necessary input files are first the input file that will initialize the program. The structure file can be read in as it is, but in most cases the system is split up into projectile and surface geometry files. This procedure has the advantage, that several surface geometries can be sampled and the projectile can be initialized anywhere in the simulation cell as determined in the input file. By this, structural bias is negated. This is also of importance, because the scattering process happens on very small time scales, where the surface does not have enough time to fully reach its equilibrated state after collision events.

Next, the PES file containing all interactions and which PES is used to describe them is read in. In MDT2 it is from the technical site possible to combine different PESs for specific interactions. For example and what was already done is that a REBO potential describes the interaction of an H-atom with a graphene surface but the interaction of the graphene surface with a substrate – in this example a Pt(111) metal surface – is described by a LJ potential. Although one can discuss how accurate the description is, this is also possible by using a NNP instead of the REBO/LJ hybrid potential. And at least so far, in the future a single NNP will be used to include substrates in the system. The coupling of PESs was mainly done, because the REBO potential is not extendable to describe metals speaking from the perspective of the graphene and EMT is not able to describe directed electron densities like there are in graphene (C–C bonds). EMT can describe the delocalized bonds occurring in metals but fails to properly describe covalent bonds.

After setting up all interactions and assigning the potentials that should be used as descriptors, final positions and velocities are assigned to each atom if not already read in from structure files. Common procedure is to use positions and velocities from snapshots from previous performed MD simulations using *NVT*-ensemble. Otherwise, velocities are assigned according to a MB distribution using an Andersen or PILE thermostat.

In the main part, for each step energies and forces are calculated for all utilized PESs to update positions and velocities if no stopping criterion appeared. Stopping criteria can be:

**steps** maximum number of allowed steps per trajectory reached

**projectile upper limit** projectile exceeded set  $z$ -coordinate above surface

**trajectory** after the maximum number of given trajectories is reached, the program stops

**extrapolation warnings** when a NNP is used, a maximum number of extrapolation warnings will stop the program to prevent simulating unphysical behavior

A complete list of available output formats and different types of outputs can be found on [170]. The final version is considerably faster as only less than a minute is needed on average for a single trajectory. With the incidence conditions of  $E_I = 1.92$  eV,  $\theta_I = 50^\circ$ ,  $\phi_I = 0^\circ$ , the projectile starting 3.5 Å above the surface plane and a maximum time length of 200 ps at 300 K surface temperature, only 45 seconds per trajectory are needed averaging over 10 000 trajectories. This is not only much faster compared to the slow version, but also compared to the previous used REBO potential. Although no proper benchmark was done, a rough estimation was around 1 minute per trajectory on average. But it is unfortunately not clear, if this average was for a specific incidence condition or averaged over multiple conditions. Despite all this, the main point was an estimation being on the order of a minute more or less. The most fundamental statement here is, that the latest version is performing faster, but at least on the same level compared to the previous used REBO function.

As a final remark, it is also possible to perform RPMD simulations using a neural-network potential. Assuming the information of the density is given in a proper and readable way to the neural-network, it is in principle also possible to perform non-adiabatic simulations, i.e. molecular dynamics simulation with electronic friction at the local density electronic friction approximation. [200–202] But preparing the data and make it structurally dependent so that a neural network is able to reproduce the wanted property is an ongoing task, but nevertheless a very interesting topic for future applications in other systems of interest.

What seems more likely is the description of electrostatic interactions and also considering non-local effects in neural network potentials. In the current implementation, there is no such treatment of electrostatics, but the necessary steps to extend the framework are still there. In the future, this will be a rather easy and fast task to update features in the program as well as the potential.

### 3.7 Improvements of MDT2

The use of an HDNN-PES in our simulation suite was made available. The use of a force-field based approach drastically reduces the time needed to perform molecular dynamics simulations but keeping the accuracy of AIMD simulations. These are improvements of the performance based on the PES used. Another point is the technical realization. I spent some more time not only to make the use of a new PES available, but also to improve the performance of the MDT2 code. Without going too much into detail, a potential point to improve is the way how to use a random number generator. There are two options available determining which type of random number generator is used in the program. When using the *traj\_id* option, roughly 20 seconds are needed to calculate random numbers for 2.5 million trajectories. In each trajectory, before the actual numbers are generated, 100 numbers are calculated but never used (dummy numbers). This should result in uncorrelated numbers to ensure a uniform distribution. For each trajectory, 4 numbers are calculated and used. This is because in typical simulations performed in this work, it has to be determined, which structure of the projectile as well as the surface has to be chosen as initial conditions. Furthermore, the initial position of the projectile inside the simulation cell has to be determined. Since the initial distance to the surface is set manually, the  $x$  and  $y$  coordinates of the projectile in the plane spanned by the lattice vectors parallel to the surface plane has to be defined.

In a small Benchmark test, no dummy numbers are used. In this case, there was not even a uniform distribution anymore, smaller numbers were favored, which will result in a bias of underlying structures used in the simulation, artificially pronouncing early-taken structures from previous NVT simulations. It turned out that calculating dummy numbers before the actual used numbers is crucial to get a uniform distribution of used numbers. Although 10 dummy numbers are sufficient to not bias the structures anymore, the distribution converges best to a uniform distribution when at least 100 dummy numbers are calculated. The second option is *global*, where a fixed seed is used and random numbers are calculated according to the current trajectory number. Here, also 100 dummy numbers are calculated but for all trajectories beforehand for each new trajectory. This means for trajectory with ID 1, 100 numbers have to be calculated, for trajectory with ID 2, 200 dummy numbers have to be calculated in addition to the 100 from before and so on. The scaling is tremendous. With the *global* option, more than 14 days are needed purely to calculate the random numbers needed to initialize the trajectories, which is a huge loss of valuable computational time. This is especially astonishing, because most of the CPU time is wasted to calculate numbers not even used.

In contrast to that, with the *traj\_id* option a higher quality uniform distribution is offered and the time demand will only scale linear with increasing numbers of trajectories.

I made it possible to re-run a single trajectory in a series of trajectories to get the exact same trajectory. Beforehand, there was a bug preventing this valuable insight into a single trajectory. The purpose is to analyze trajectories with specific conditions. Because of performance reasons, not every information is written in each step to save an overload of common hard discs. We therefore just save the initial and final information of a trajectory. But to get insight into the scattering events, it is necessary to check single trajectories in all detail in each step to extract data needed to understand the mechanism taking place for specific conditions. Therefore, it is crucial to get the exact same trajectory independent if it is calculated in a series or single. Otherwise, it would not be possible to see what is going on the surface during the scattering event and to really understand the elementary steps involved.

To further increase the workflow speed and make things easier, I also added several new structure output formats. A full list can be found in the project, but at least very common formats shall be mentioned here. A structure can be taken directly from simulations in VASP, AIMS and RuNNer to save conversion steps, saving time and accuracy.

Velocities have also been added for initial and final conditions of the projectile. Now, they can also be followed in each step for the total system, if requested.

Recently, the analysis tools have been updated to not only look at forward, but also backward scattering of the projectile.

Additionally, the time where the projectile has its closest approach with the surface will now also be written to the trajectory information file.

To further increase the performance of the simulations, I managed to check in the initialization part of the program if and how many output options are needed, saving valuable time during the main loop of the program over the steps in the simulations.

In case of ring-polymer molecular dynamics simulations, I also updated all output formats to write the centroid position of the polymer. It is now possible to request single beads, when writing down geometries. Since this would require a lot of checks during the simulation and the available disc space can be easily overrun, by default this is disabled and should only be used for a minor amount of trajectories, but this depends on the user and available resources.

The implementation has been done in the most general manner as possible. The use of a NNP is not restricted to the H-atom scattering from graphene system. It is not even restricted to use a single atom, molecules can be used as well. If it is possible to come up with a HDNN-PES that can adequately describe atom and surface scattering, from the technical site there are no drawbacks. Although I implemented 2G-HDNNP, it should be an ease to implement newer

generations, which can include electrostatics as well as non-local interactions.

### 3.8 Reference Data Set

The reference data set was generated in an iterative procedure. This procedure is explained in detail in [122]. In each step, energies and forces of new structures are added to the already established data set. This is always done if the current fit does not show the desired accuracy or the configuration space is not fully covered by the PES in progress. By comparing the results of several NNPs with different architectures, these geometries can be accounted for. By adding the new structures to the already existing data set, the number of underlying structures is constantly increased. This procedure is repeated until convergence is reached. For the initial data set, approximately  $6 \cdot 10^4$  reference geometries were created, which were picked from several approaches.

- (i) Ab initio molecular dynamics (AIMD) trajectories for an H-atom with 1.9 eV incidence energy and incidence angles of  $34^\circ$  and  $52^\circ$  scattering from a graphene slab at 300 K and 600 K surface temperature are used.
- (ii) Geometries from and close to the minimum energy path (MEP) to adsorption are taken. Here, the H-atom was put at the lateral position of the C-atom and the z-coordinates were varied over a range of  $-0.8 \text{ \AA} \leq z_H \leq 5.8 \text{ \AA}$  and  $-0.8 \text{ \AA} \leq z_C \leq 1.0 \text{ \AA}$ , respectively. The step size is  $0.025 \text{ \AA}$  and structures with  $r_{CH} \leq 0.6 \text{ \AA}$  are excluded. The remaining C-atoms are kept at their equilibrium positions.
- (iii) Further geometries from AIMD trajectories with the H-atom randomly placed over the thermalized graphene surface at 300 K are chosen. The position of the H-atom is allowed to range over the whole simulation cell with the z-coordinate ranging from 1 to 6  $\text{\AA}$ .

For the asymptotic energy reference the configuration with a C–H distance of 6  $\text{\AA}$  and a fully relaxed graphene surface was used. This structure is the energy zero point. Energies and forces of all structures in the data set are obtained from DFT calculations. The HDNN-PESs was created by fitting to the initial reference data set. About  $1.5 \cdot 10^4$  configurations obtained from MD simulations of H-atom scattering from a graphene sheet at incidence energy of 1.9 eV in the wide range of incidence angles (from  $0^\circ$  to  $90^\circ$  in  $10^\circ$  step) are added. Furthermore, structures from scattering trajectories with incidence energy of 6 eV and normal incidence angle with surface temperatures of 0 K and 600 K starting over high-symmetry sites shown in Fig. 3.2 are included as well. Moreover, configurations from equilibrium MD simulations of the graphene surface in the wide range of temperatures from 0 K to 2000 K are taken. Because the surface can locally being heated during the scattering in the proximity of the collision site, these structures are useful. All in all, 75 945 configurations form the reference data set, which the final HDNN-PES was trained on.

As mentioned before, different architectures using the same data set are used for the training and cross checked to check for holes in the configuration space of the underlying data points. In Fig. A.3, the used 15-15 architecture is compared to a 20-20 architecture. Because the RMSE values for energies and forces are very close for those different architectures, there is no indication of missing structures in the covered configuration space of the used data points for the fit to come up with a HDNN-PES. Although not explicitly shown here, but the difference between two different architectures is an order of magnitude smaller than the difference of the fit with respect to the DFT data. The fit accuracy of the HDNN-PES compared to the DFT data points is 15 meV for energy of the total system and  $\approx 2$  meV energy difference between like structures predicted by the two different NNs. The same counts for the forces. The reason

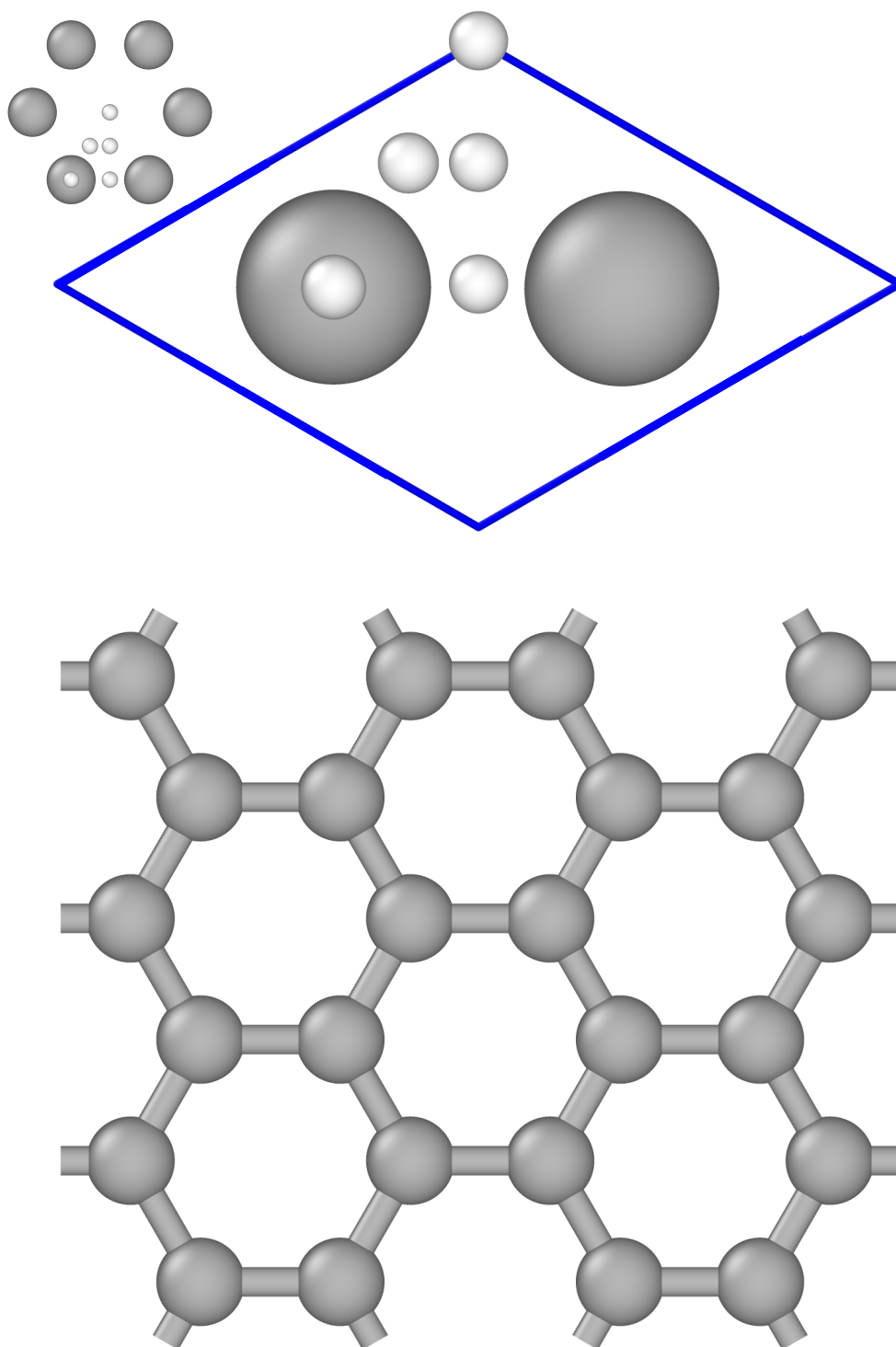


Figure 3.2: The primitive cell of graphene contains two C-atoms represented as gray spheres. Points of high symmetry are shown as white spheres. The cell is converted from hexagonal to orthogonal representation, which is then used to create the  $3\times 4$  surface sheet. Here, the bonds between adjacent atoms are shown including bonds to periodic image atoms. This figure and the ones showing surface structures of graphene are created using OVITO version 2.9.0 [203]. Reproduced from Ref. [204] with permission from the Royal Society of Chemistry.

why only two different architectures are shown and not more is that in the iterative process, several more architectures have been tested and it could be reduced to an architecture, which is able to accurately reproduce the underlying data points to our desired accuracy of less than 1 meV / atom. Only a 20-20 architecture was used for later fits to account for possible problems in the configuration space when adding newly generated structures and not anymore to find the best architecture.

This is also supported by our collaborationist Fabien Gatti and Lei Shi. Within the MCTDH framework, there are some tools available to find even subtle holes in the PES. At least in the region, where a chemical bond is formed between the impinging atom and the surface carbon atom and as shown in Fig. 4.6, no significant holes could be found, indicating that the configuration space of interest is well covered.

### 3.9 Molecular Dynamics Simulations

The presented framework MDT2, which is described in detail in Sec. 3.5 is used to simulate the scattering of projectiles from graphene surface in MD simulations.

To set up the H on graphene system, the equilibrium structure from DFT calculations is used and heated up to the desired temperature by using the Andersen thermostat in the *NVT* ensemble. The structure closest to the desired temperature is manually selected and used in the *NVE* ensemble to reach equilibrium condition. This condition is used as the starting point in a single 100 ps long trajectory, from which the initial structures are selected with a period of 100 fs to offer 1000 uncorrelated structures. By this, the sampling of slab geometry and velocities is more sufficient compared to structures directly taken from *NVT* ensemble, which can be distorted due to random collisions with the thermostat. The structures are typically saved in the mxt format. We apply a RNG to choose one of the given geometries in a random fashion. The procedure stays the same and has to be repeated for each sub-system.

The MD scattering simulations for H- and D-atoms have been carried out in the *NVE* ensemble using the velocity verlet algorithm, which is described in Chp. 2.4. The timestep is 0.1 fs, which has been confirmed to conserve the energy in the simulations. An analysis is shown in Fig. A.8. Although it not explicitly shown, but a timestep of 0.01 fs was tested as well, but there are no significant changes in the characteristics of the trajectories. This is even the case for the scattering with 2 eV incidence kinetic energy along the surface normal.

The particle was launched 3.5 Å above the surface plane and its initial position in the *xy*-plane was estimated using a RNG. The trajectories are stopped either if the distance of the projectile to the surface is larger than 3.6 Å or the duration of the trajectory exceeded 200 fs. This was done to decrease the computational demand. The energy difference of the projectile at the distance of 3.5 Å compared to 6.0 Å is less than 4 meV. Considering the high initial kinetic energy of the projectile and its high velocity, there are only subtle differences in the starting position.

It will be explicitly stated, where the projectile was launched 6.0 Å above the surface in the interaction free region and here trajectories are stopped again if the trajectory exceeded 200 fs or the projectile surface distance surpassed 6.1 Å.

The total number of trajectories carried out for different isotopes, angles, energies and at different surface temperatures are shown in Chp. A for each condition separately.

### 3.10 Ring Polymer Molecular Dynamics Simulations

In ring polymer molecular dynamics (RPMD) simulations, nuclear quantum effects (NQE) such as tunneling and zero point energy can be accounted for. Again, the presented framework

MDT2 is used to perform such simulations, which is described in detail in Sec. 3.5.

To include quantum effects in classical MD simulations, one can extend the configuration space by copies of the system in an imaginary space connected by ring polymers, also called beads. The procedure is described in Ch. 2.4.4.

The procedure to generate usable input structures is the same as in preparing classical MD simulations. To prepare the simulations, the starting structure have to be generated. The starting point is again a relaxed structure from DFT. The positions of the atoms in the extended space are generated automatically, based on the number of beads requested. The procedure is the same as before, the system is heated up to the temperature of 300 K using the *PILE* thermostat to account for the bead temperature as well, a snapshot from the equilibrated geometry containing positions and velocities is used in *NVE* ensemble as starting structure. From a single, 2 ps long trajectory, from which the initial structures are selected with a period of 200 fs to offer 1000 uncorrelated surface structures. For the projectile, 1000 initial structures are extracted from a single 200 ns long trajectory with a period of 20 fs. Because of the beads used for the projectile and the surface, the procedure of generating different initial structures has to be applied to the projectile, too.

In the following, the necessary steps to estimate the number of beads that has to be assigned

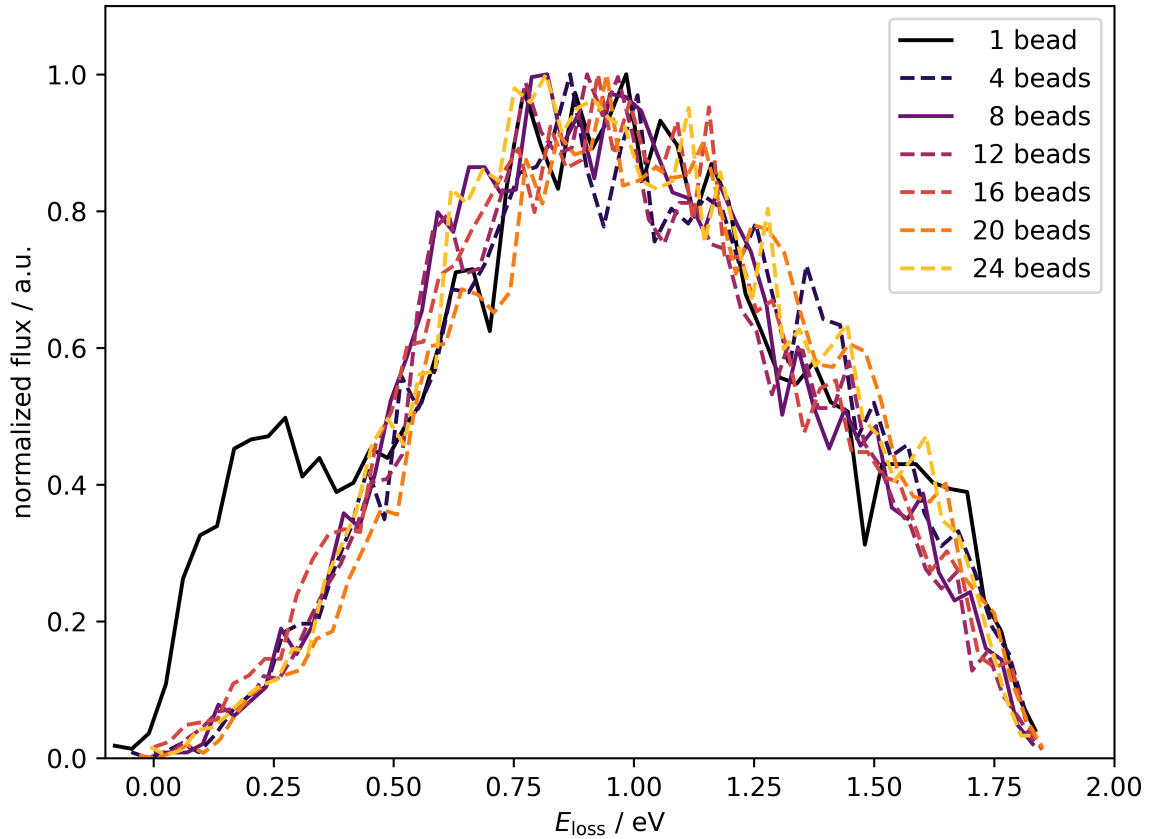


Figure 3.3: The normalized energy loss distribution is shown for all scattered trajectories depending on the number of beads assigned in RPMD simulations (dashed lines). The results shown here based on 10 000 trajectories each. The results based on classical MD simulations and are given as reference value in black solid line (1 bead). When comparing to classical results, in RPMD the quasi-elastic component is not present anymore (peak in black solid line around 0.2 eV).



in RPMD simulations to obtain meaningful results are shown. Like the basis set and many more properties in electronic structure calculations, the number of beads has to be estimated when performing RPMD simulations to make sure, the prediction of desired properties have converged. In this case, the average energy loss and the sticking probability depending on the number of beads is followed until convergence is reached.

To find an appropriate number of beads, several number of beads have to be tested beforehand. Some annotations to best decide on the number of beads follows. A single bead is equivalent to classic simulations, thus starting with 2 beads is constructive. Previous knowledge show that 2 beads are by far not enough and at least 4 beads make sense and odd numbers should be avoided. Therefore, the number of beads is constantly increased by 4 up to 24 beads. For each number of beads, 10 000 trajectories were generated to compare energy loss distributions as well as sticking coefficients.

In Fig. 3.3 the normalized energy loss distribution is shown for all beads assigned in RPMD simulations. Here, 1 bead shows the results obtained from classical simulations as a reference. Here, the projectile was launched 6.0 Å above the surface. Interestingly, the classical distribution has a peak around 0.2 eV, but all simulations including NQE doesn't show this peak. This behavior can be explained in the following way. Minor energy loss refers to quasi-elastic scattering at the middle of a six-membered carbon ring. When we introduce the beads, the volume of the projectile becomes much larger and it is rather unlikely that the middle of the ring is hit directly. In this case the extended projectile in form of the polymer is very likely to perform inelastic scattering leading to a higher energy loss.

Additionally, in Fig. 3.4 in the top panel the average energy loss of all scattered trajectories is shown depending on the number of beads used in RPMD simulations. Again, 1 bead represents the results obtained from classical MD simulations. An inset is shown as well to better follow the trend. On the large scale, the average energy loss seems to be rather constant and the number of beads does not have a significant influence. The inset is given to highlight that although on the large scale the value seems converged, there is an drastic increase at 20 beads. There are actually two things to consider here. First, the number of trajectories might not be statistically enough to well sample the average energy loss. Second, because of time restrictions, no higher numbers for the beads have been tested. This was also not the case, because to further increase the number of beads will drastically increase the time needed to run simulations. Since a large number of trajectories is needed to compare to experiment, this is not beneficial anymore speaking in terms of computation power.

Fig. 3.4 shows the sticking probabilities of 10 000 trajectories depending on the number of beads assigned in RPMD simulations. Like before, 1 bead shows the results obtained from classical MD simulations for reference. Again, an inset is shown to better follow the trend.

To conclude, at least 4 beads are enough to account for quantum effects in RPMD simulations. But considering the average energy loss as well as the sticking coefficient, convergence seems to be reached for at least 8 beads. Additionally, RPMD simulations are more demanding, and thus 8 beads seems to be a good compromise between convergence and performance. This is especially important, because for statistical reasons a high number of trajectories is needed for prediction and drastically increasing the demand is not beneficial anymore.

Bottom line, the number of beads is set to 8 when RMPD simulations are performed to account for tunneling and zero point energy in the scattering simulations.

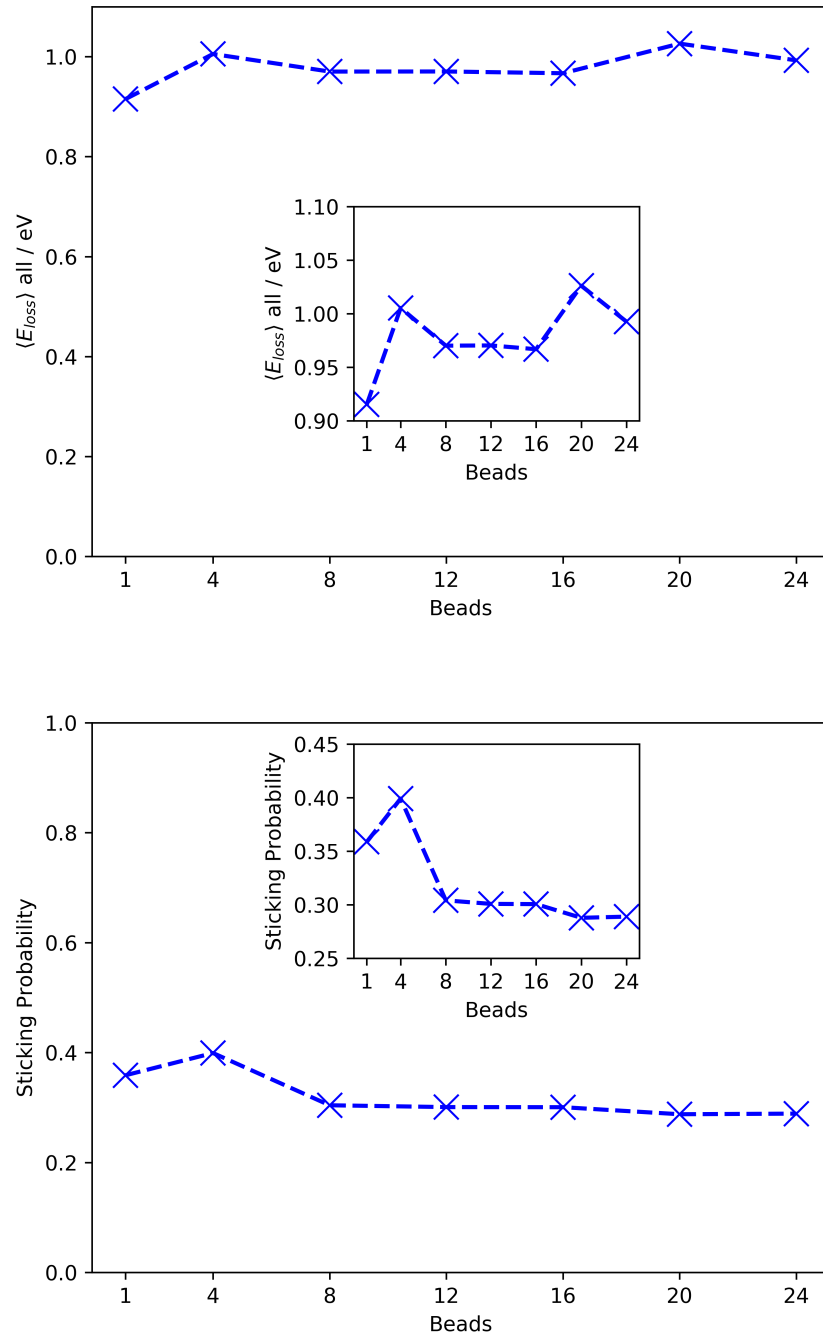


Figure 3.4: In the picture the convergence test in order to perform RPMD simulations is given. The average energy loss (top panel) of all scattered trajectories is given in meV depending on the number of beads assigned in the simulations. The estimated sticking coefficients are given depending on the beads in the bottom panel. At 1 bead the results obtained from classical simulations is given as a reference value, respectively. The insets show the same plot, but on a smaller range for y-values to emphasize the trend and highlight the behavior.

---

---

# Studying the C–H bond formation by analyzing scattering experiments

In this chapter I will present studies of H- and D-atoms scattering from graphene. Accurate first-principles dynamics simulations are used to view the atomic-scale motion and energy dissipation pathways involved in forming a covalent bond. The purpose, why we compare the results obtained from the to experiment is to validate its usability and test, if it is able to reproduce experimentally found results. If it is validated, analysis can be done rather easy and fast for different initial conditions compared to very expensive and long experiments. Furthermore, in theory it is even possible to analyze microscopic events and dynamics like backward-scattering along the incidence beam, which can not directly detected in experiment. This combination of experiment and theory is often referred to as the "worlds largest microscope". Processes too fast to be seen and to follow can be analyzed by simulations after it has been validated to experimental results. However, in the last years, very recent developments have been carried out from experimental point of view to get better insights into the microscopic world. Whereas in theory, although there are still limitations speaking of computing power, there were great efforts in describing bigger systems and increasing time scales to analyze the microscopic world.

I will start to show previous studies of the graphene surface and will give the knowledge we obtained so far from analyzing scattering experiments performed in our group by using an atomistic potential, developed in our group as well. This is followed by a presentation of the necessary steps to get a validated PES, that is able to reproduce experimental findings better compared to the previous used PES.

After that, I will show results from molecular dynamics simulations utilizing the developed PES simulating the scattering behavior depending on the incidence conditions. The incidence energy is varied in order to follow the bimodal feature in the experiment. At an incidence energy of  $\approx 2$  eV both peaks are present and the incidence polar angle is screened to follow the bimodal feature as well. Scattering simulations have been additionally carried out at different temperatures and also the isotope effect of the scattered particle as well as of the surface are

analyzed.

In our group, we achieved experimental results from two independent experiments. The first experiment uses the Rydberg-atom-tagging (RAT) machine and detects angular resolved scattered hydrogen atoms using high resolution time-of-flight (HR-TOF) technique for detection [24]. H-atoms scattering from epitaxial graphene have been studied depending on the incidence energy, incidence angle and surface temperature, respectively. The isotope effect of the projectile has been analyzed by scattering D-atoms from the surface as well. In the second experiment, H-atoms scattering from epitaxial graphene has been studied along the surface normal and depending on the incidence kinetic energy. The HBEAM experiment uses the velocity map imaging (VMI) technique for detection [29].

A part of the results presented here is already published in [204].

## 4.1 Previous Studies

In this section, first some general properties of graphene are given followed by the motivation, why the scattering of H-atoms from a graphene surface is studied. In the latter, I will also give the knowledge and insights we got so far from comparing experimental to theoretical results in order to figure out the underlying mechanisms and processes involved in the dynamics.

### 4.1.1 Graphene

Diamond and graphite are known since ancient times. Both consists only of carbon atoms and graphite — one of the softest materials known and primarily used as lubricant — can be structurally characterized as a compound of several graphene layer only weakly bound to each other due to van der Waals interactions. The discovery can be dated back to 3750 BC [205]. They consist of only a single element: Carbon. The Latin name carbo can be best translated with charcoal, which seems to be the origin of the word.

Graphene is the thinnest material known, but has a large mechanical stability [206]. It is the strongest compound discovered, the best heat conductor at room temperature and also the best conductor of electricity known so far. The highest carrier mobility was measured in free-standing graphene.

Graphene completes the list of known carbon allotropes in every dimension. Three-dimensional allotropes are diamond and graphite, graphene is a two-dimensional form, nanotubes [207] can be categorized as one-dimensional and fullerenes [208, 209] as zero-dimensional. Graphene can be seen as a building block of all  $sp^2$ -hybridized allotropes. Fullerenes are formed by wrapping, nanotubes are formed by rolling whereas graphite is formed by stacking. For this reason, they all share many electronic and vibrational properties.

Although long missing in this list, graphene is ironically the best studied carbon allotrope theoretically. The first theoretical analysis date back to the middle of last century applying the tight-binding method to describe properties of graphene [210, 211]. Carbon was first described by a many-body potential in 1988 by Tersoff [212] to reproduce experimentally estimated energies and bulk properties of various carbon allotropes. The reactive empirical bond order (REBO, REBO-II) potentials were built on the original Tersoff formulation including a wider range of parameters and data in the fit. Additionally, other reactive potentials are used to describe its properties like the carbon ReaxFF potential [213].

Machine-learning based descriptions have been used to describe numerous systems. This includes graphene and its allotropes [214, 215] as well. Free-standing graphene [216, 217] as well as multi-layer graphene [218] have been investigated. Bigger systems have been treated as well, not only graphite [218–220] but also amorphous carbon [221].

Atomistic simulations have played a major role in developing our understanding of carbon materials.

Despite fundamental theoretical investigations, numerous attempts only produced nanometer-size crystallites. A single sheet, which corresponds to a monolayer of atoms, was extracted from graphite using a technique called micromechanical cleavage. By this approach (topdown), which starts from three-dimensional crystals, the issues with the stability of small crystallites could be avoided. Identified in 2004, graphene is a promising candidate to revolutionize electronics, because it is conductive and extremely stable [222]. Geim and Novoselov earned the Nobel prize in 2010 for their production of free-standing graphene [223]. Graphene has been the subject of extensive investigation since it was first isolated.

Graphene is a one-atom thick thin layer (monolayer) of carbon atoms, all carbon atoms are ordered in a two-dimensional hexagonal honeycomb lattice, the crystal structure can be determined as simple hexagonal. All carbon atoms in this highly symmetrical structure form an angle of  $120^\circ$  to adjacent atoms, all atoms are  $sp^2$  hybridized and all atoms have the same C–C bond distance, which is 1.42 Å. The lattice constant of graphene was estimated to be 2.464 Å.

Each carbon atom forms a  $\sigma$ -bond to its three nearest neighbors and contributes a single electron to the valence band, which is delocalized over the sheet. The same bonding situation is present in carbon nanotubes, polycyclic aromatic hydrocarbons, partially in fullerenes and glassy carbon [224, 225].

Because the conduction band touches the valence band makes graphene a semimetal with unusual electronic properties [226]. The high electron mobility is due to half filled bands, which have a linear dispersion at the Dirac point, which is the reason for an observed quantized hall effect [227, 228]. This can be seen not exclusively in graphene, but in general in two-dimensional electron systems, for example in transition metal dichalcogenides [229].

It has also been found that a bilayer of graphene under the "magic angle" of  $1.1^\circ$  becomes a superconductor [230–232]. Trilayer graphene has been investigated [233] as well and recently, in mirror-symmetric twisted-trilayer graphene superconductivity could be observed. Stacking of the layers in a specific angle influences the bands, leading to an efficient treatment. What is new by using three layers is a combination of two points. First, it can be tuned very easily by applying a perpendicular displacement field. Second, it shows strong and reproducible superconductivity [233, 234].

Graphene foam has been used in battery technology [235] and also in electrically powered explosions. An electrically powered repeatable air explosion has been developed using microtubular graphene assemblies interconnected to a macroscopic framework, which are based on free-standing graphene layers of nanoscale thickness [236].

Graphene can also be used as small scale membrane, because it could be shown, that it is impenetrable to small atoms and ions [237]. It has been applied further in proton-deuteron separation [238, 239] as well as gas impermeability [240].

Graphene and bilayer graphene are both zero-gap semiconductors, which can also be referred to as zero-overlap semimetals [241]. Graphene can be transformed from a semimetal to a semiconductor [241]. Therefore, it is of interest in materials design for nanoelectronic, mechanical, and optical research [242, 243].

Mechanical exfoliation as well as chemical vapor dissociation (CVD) are prominent methods to produce high quality graphene. CVD is used to create epitaxial graphene, grown on metal substrates in high quality.

## Functionalization

As mentioned in the previous section, graphene is well studied. Even the functionalization and especially molecular hydrogen formation as well as dissociative adsorption [244] have been

investigated in experimental and theoretical studies [245]. Graphene is a zero band-gap material, but the conduction and valence band are only touching each other in the K and K' points in the reciprocal lattice. Theoretical predictions show that hydrogen and Fluorine are suitable to functionalize graphene by introducing a band-gap, utilizing graphene as two-dimensional semiconductor in electronic and spintronic devices [246–248]. Because of its properties and application possibilities, especially molecular hydrogen adsorption has been studied. The adsorption energy can be obtained as difference from calculations directly, by solving the Schrödinger equation of the gas molecule and the surface alone [249]. Diffusion, recombination as well as double H-atom adsorption on graphite surfaces have been studied [250, 251] and several potential energy surfaces have been developed [252, 253]. On the other hand it was also demonstrated that if the incidence kinetic energy of the impinging atom is high enough, it is even possible to penetrate the graphene sheet, where the experimental setup [254] has been reported as well as theoretical analysis [255].

H-atom adsorption is relevant in the catalytic formation of molecular hydrogen in the interstellar medium [256–263] governed by graphene and is discussed as in reversible hydrogen storage [264–268]. As mentioned before, the adsorption of H-atoms can induce a band gap in graphene [269–274]. When a hydrogen atom is added to graphene, it binds to the  $p_z$ -orbital of a carbon atom, which can induce a band-gap and opens applications as a two-dimensional semiconductor material. By atomic adsorption, the semimetal can be converted into a semiconductor [269, 270, 272, 275]. Organic light emitting diodes (OLED) [276], transparent and very flexible monitors are only a very few examples for electronic, spintronic and organoelectric applications. It was also reported that applications can be found in fusion technologies [277].

However, there is a lack of experiments studying the adsorption of a single atom. However, the patterned adsorption of H-atoms on graphene from the experimental site is well studied.

This means, a profound understanding of the underlying chemical reactions, dynamics and mechanism to functionalize graphene forms the basis to overcome this obstacles and open the pathway to future applications. A suitable benchmark system is the scattering of H-atoms from a well oriented graphene surface, therefore the next section will focus on the dynamics of H-atom scattering from a graphene surface, which has been investigated experimentally and theoretically in our group.

#### 4.1.2 Atom Scattering Experiments

It is a continuous challenge in scattering experiments to view the motion on the atomic scale to figure out the energy dissipation pathways involved when a covalent bond is formed.

Free-standing graphene is preferably used in theoretical investigations. In order to provide a benchmark system in experiment, graphene is put on a substrate. The substrate is chosen in a way that interactions with graphene are preferably small.

In performed experiments, the graphene surface was grown on a Pt(111) metal surface using CVD, which is in general used to produce a high-quality monolayer of graphene grown on metal substrates. This generated epitaxial graphene can be seen as quasi free-standing, because the phonon modes of graphene are barely influenced [278–281], because there are only small interactions due to weak dispersion forces between platinum and graphene [282].

Graphene has a very small density of states (DOS) at the Fermi level, which means that there is only a small number of occupied as well as unoccupied states. This explains, why non-adiabatic dynamics do not play any role at least on the energy range of scattered particles used in experiment. Therefore, a single electronically adiabatic PES is sufficient to describe the scattering of a single atom from graphene, which has been reported before [25].

When an H-atom scatters from a graphene surface, a bimodal translational energy loss distribution is observed. In the angular resolved energy loss distributions, we see two separated

signal peaks. H-atom scattering resolves into a quasi-elastic and a strongly inelastic scattering behavior, depending if the barrier to chemical bond formation has been overcome. The barrier arises from a rehybridization during bond formation.

The quasi-elastic scattering is referred to as the fast channel, because the impinging atom only loses a small fraction of its initial kinetic energy.

The slow channel describes inelastic scattering of an incoming atom, where the barrier to chemisorption is involved, where the particle loses a large fraction of its initial kinetic energy. The signal of this channel is shifted to smaller angles, indicating a transient bond formation of the impinging atom with a surface carbon atom.

Fig. 4.1 shows graphically the two types of scattering events that might occur when H-atoms are scattering from a graphene sheet and it was created using Inkscape version 0.92.5 [283]. In **A**, an example trajectory of the fast channel is shown, where the projectile is reflected before crossing the barrier to chemisorption, because it has not enough energy to cross the barrier. **B** shows an example trajectory, where the impinging H-atom has enough energy to overcome the barrier, can form a C–H bond and will be trapped on the surface.

If the impinging projectile can overcome the barrier to chemisorption, which involves an out-of-surface movement of a single carbon atom, a transient C–H bond is formed and the corresponding C-atom undergoes a re-hybridization from  $sp^2$  as it is in the graphene sheet to  $sp^3$ . The H-atom comes from the gas phase and can stick to the surface if it manages to distribute enough of its initial kinetic energy to the internal DOF of the graphene sheet. By this, surface phonons are excited and kinetic energy is transferred from the projectile to the surface atoms, heating locally the graphene sheet because of the excess kinetic energy. The temperature is related to the average kinetic energy, which itself depends on the distribution of velocities of atoms.

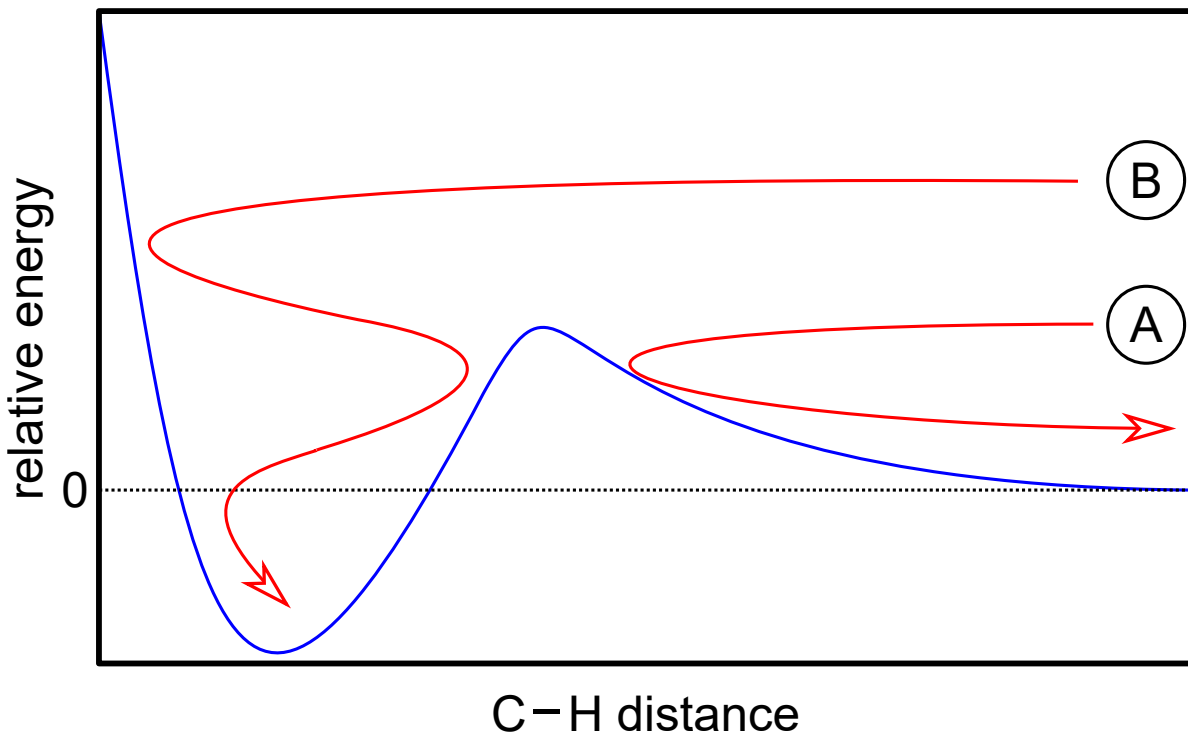


Figure 4.1: Possible channels for an H-atom scattering from graphene, where the barrier to chemisorption is involved. In **A** scattering before crossing the barrier to chemisorption is shown whereas **B** shows a possible path to chemisorption of the impinging projectile.

If the energy cannot be efficiently distributed to make sticking available, the projectile will lose a fraction of its initial kinetic energy and after a single or multiple bounces, it will be released to the gas phase again.

The unperturbed graphene structure can be seen as aromatic, but the aromaticity is different compared to e.g. benzene. It could be shown that graphene has only a local aromatic property resulting from two  $\pi$ -electrons located over every hexagon ring and no global delocalization was found [284]. In graphene, every carbon atom has a bond order of  $\frac{4}{3}$ .

The barrier is the energy needed to initialize the rehybridization of the involved carbon surface atom. Rehybridization in terms of geometry means a change from two-dimensional hexagonal (trigonal planar) to three-dimensional tetrahedral geometry, in which the H-atom points along the surface normal in equilibrium position. Rehybridization structurally means that one carbon atom is moving out of the surface plane. This process is called puckering of the C-atom. Adsorption of H-atoms on the graphene surface locally forms a diamond-like bonding situation. This also explains that the minimum energy pathway (MEP) to adsorption of an H-atom with a surface C-atom couples the movement of the H- and C-atom perpendicular to the surface plane. Here, adsorption takes place via a synchronized motion of both collision partners.

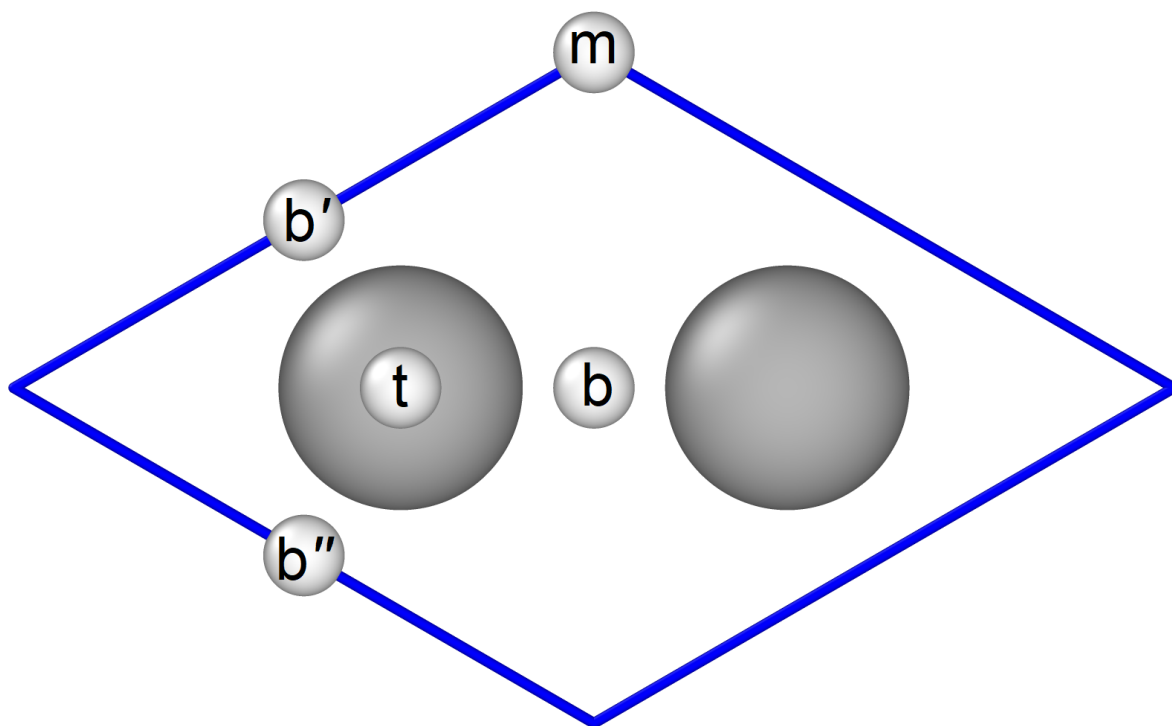


Figure 4.2: High symmetry points in the primitive cell of graphene. The top (t) point is directly on top of a C-atom, the middle point is the middle of a six-membered carbon ring and labeled mid (m). There are three different bridge points, named bri (b), bri' (b') and bri'' (b''), respectively. This figure and the following ones showing surface structures of graphene are created using Ovito version 2.9.0 [203] if not stated otherwise. Note, in the literature, the mid point can also be labeled as hollow point.



To be more specific, in previous performed AIMD simulations, for the H-atom scattering with  $E_I = 1.92$  eV incidence kinetic energy with an incidence polar angle of  $\theta_I = 52^\circ$ , both channels are present. By analyzing the closest approach of the projectile with respect to the surface, the fast and slow channel can be separated. Scattering before the projectile surface distance of  $d_{\min} = 1.44$  Å describe the small energy loss (fast) channel, whereas scattering smaller than  $d_{\min} = 1.33$  Å describes the high energy loss (slow) channel.

A full-dimensional PES was reported [25] using first principles energies obtained from Embedded Mean-Field Theory (EMFT) [285–287] to parameterize a second generation Reactive Empirical Bond Order (REBO) potential [288–290]. From previous performed accurate first principles dynamics simulations using this REBO-EMFT PES, it could be shown that the quasi-elastic channel is from scattering events, where the physisorption well is involved. Collision sites are near the center of a six membered carbon ring, which is referred to as the middle (mid) point and labeled m. This is shown in Fig. 4.2 and 4.3. Both figures are created using Ovito version 2.9.0 [203]. The atom feels the repulsive wall of delocalized  $\pi$ -electrons from a six membered carbon ring.

The second channel originates from transient C–H bond formation, where the single occupied  $s$ -orbital of the hydrogen atom overlaps with the  $p_z$ -orbital of a single carbon atom. Here, the chemisorption barrier is involved and the projectile will lose a high fraction of its initial kinetic

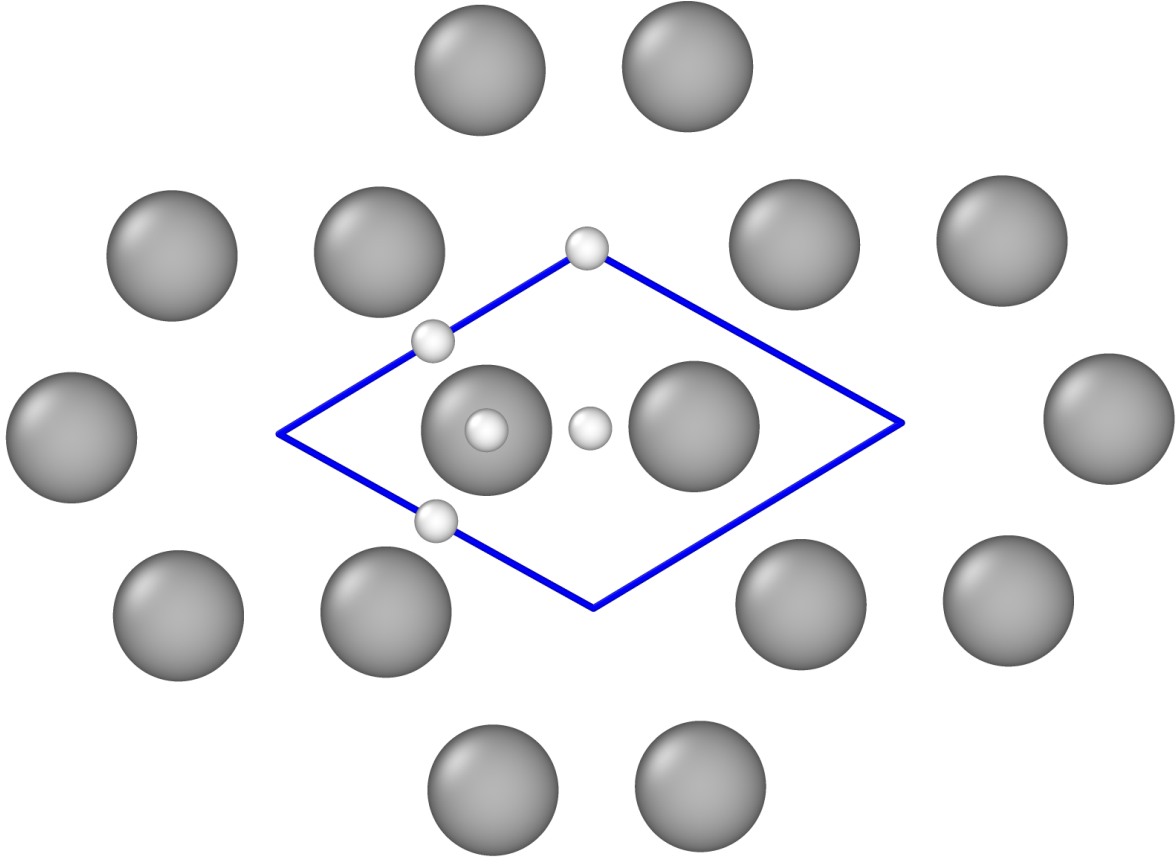


Figure 4.3: Surface structure of graphene. The primitive cell of graphene containing two carbon atoms shown as gray colored spheres from Fig. 4.2 is shown as well and again white colored spheres show high symmetry points in the primitive cell. Here, the location of the primitive cell according to four considered six membered carbon rings inside the honeycomb structure of graphene is shown.

energy. In this scattering event, one or more carbon atoms are involved in one or more collisions of the projectile with surface atoms. This happens on top of a single C-atom or between two C-atoms, depending how many atoms are involved. The top position is labeled t and crossing the barrier to chemisorption means coming close to a single carbon atom. Interactions are not restricted to a single atom, it could also be that several atoms are involved. This is indicated by the bridge (bri) point labeled b.

Within a 10 femtosecond long interaction time, the H-atom loses 1 to 2 electron volts before leaving the surface via transient bond formation. Complete distribution of the initial kinetic energy of the projectile might also happen. The shells around the C-atom, with which the H-atom collides are involved and they have an in-plane and out-of plane movement [25]. The collective influence of surrounded carbon surface atoms enables the efficient sticking, explaining the high sticking probability. The rehybridization leads to a remarkable rapid intramolecular vibrational relaxation, which is responsible for the high sticking probability. Sticking of H-atoms happens remarkable fast on the order of 10 femtoseconds, and it is reported that adsorption will create a sonic wave with a velocity of  $\approx 18.6 \text{ km s}^{-1}$  [25], which is in good agreement with experimentally measured graphene’s in-plane speed of sound of  $22.0 \text{ km s}^{-1}$  [291]. This was determined by longitudinal acoustic (LA) phonon branch analysis.

If the impinging atom can manage to distribute its initial kinetic energy completely to the surface, it will form a chemical bond with a single carbon atom. Diffusion could not be seen and the barrier to diffusion was calculated to be more than 1 eV [26, 27].

Because the scattered particles from the graphene sheet are light and there is a barrier involved, quantum effects might play a role and had to be accounted for. It was reported that accounting for tunneling and zero point energy (ZPE) in ring polymer molecular dynamics simulations when simulating the scattering of H- and D-atoms with an incidence kinetic energy of  $\approx 1 \text{ eV}$  from free-standing graphene, the influence of nuclear quantum effects seem to be small [28, 252].

In summary, the quasi-elastic channel comes from trajectories that fail to cross the barrier to chemisorption, whereas the high energy loss channel arises from trajectories that passed through the chemisorption well forming a transient C–H bond and subsequently returned to the gas phase. Because of the synchronized movement of the H- and C-atom and the equilibrium tetrahedral geometry of the adsorption complex, the transient C–H bond is efficiently formed with normal kinetic energy.

So far, H-atom scattering from epitaxial graphene have been carried out for multiple substrates. As mentioned, epitaxial graphene on Pt(111) can be seen as quasi free-standing. Graphene has also been grown on Iridium, where the graphene has a stronger interaction with the metal. The strongest interactions however, can be seen for epitaxial graphene grown on Ni(111). Here, due to strong interactions a chemical bond can be formed between graphene and the metal substrate, drastically changing the scattering dynamics.

## 4.2 HDNN-PES

In the following section, it will be explained why I have chosen a high-dimensional neural network potential to describe the system and which benefits it has compared to previous used potential energy surfaces already reported. The challenge is to develop a potential, which is able to accurately describe the dynamics, where a great number of degrees of freedom are involved. Simultaneously, energies and forces must be predicted fast to get better statistics in a reasonable time frame. Since the range of the incidence kinetic energy of the impinging atom covers several eV, a potential covering this range without re-fitting is preferable.

In 1988, the first many-body interatomic potential for modeling carbon was published [212]. To date, there exist a variety of bond-order potentials including the Brenner [292], AIREBO [293] and ReaxFF [294], which are available in the literature. Amongst others, they have been used to describe adsorption, beneath formation of  $H_2$  on graphene [295]. Their accuracy is limited by their functional forms. Typically, they are manually constructed and a set of parameters has to be found for each system. There can be hundreds of parameters, which can be challenging to determine. In most cases, the essential features seem to be reasonably described, but these potentials represent a compromise between accuracy and efficiency.

On the other hand, using AIMD simulations are computationally very demanding. Thus they are restricted to a few hundred atoms and short simulation times.

Although in ML based potentials, there are at least an order of magnitude more parameters, but fitting is less demanding. The choice of ML based potentials is because they are developed to fill the gap between mentioned accuracy and efficiency. To fit the HDNN-PES presented here, it only took one to two days, depending on the number of iterations and the fit was restarted after half the iterations, which slightly increases the demanding time.

In ML based potentials, the available descriptors can be arbitrarily combined with the method. Currently, there are a few prominent combinations of those. This is not about compatibility reasons, but the personal preferences of the developers [83]. The reason, why the method of HDNNP is chosen to be part of our framework is that the symmetry function descriptors are commonly used and offer a linear dependence for larger system sizes. What makes NNPs interesting for us is their long history and the largest diversity in terms of methods and concepts [84] and also the fact that the framework containing the description of the neural networks was also programmed in Fortran, which was highly beneficial for us from a technical point of view.

In order to come up with a full-dimensional potential energy surface that can describe the scattering dynamics of H-atoms from a free-standing graphene surface sheet, the method of high-dimensional neural network potentials was fitted to accurate density functional theory data using the Perdew Burke Ernzerhof functional with Grimme D2 dispersion correction. To develop a full-dimensional neural network potential energy surface, the iterative procedure as shown in Fig. 2.1 and described in Chp. 2 was applied. In the following, the procedure to come up with a PES that fulfills all needs to properly describe atom-surface scattering is discussed.

### 4.2.1 Evaluation of the quality of the PES

The reference data set generated to develop a high-dimensional neural network function to come up with a full-dimensional potential energy surface (HDNN-PES) is described in detail in Sec. 3.8. I found out that using two hidden layers with 15 neurons per layer for the atomic neural network's architecture is sufficient to accurately reproduce the energies and forces from electronic structure data. In short, the architecture has been estimated to be 15-15-1.

In this section I will focus on the validation of the generated PES to check if the developed PES is able to describe the properties of our system and to properly describe the dynamics of the scattering events taking place, because we are very much interested to get an insight into

the processes taking place on the surface. The processes are too small to be seen and too fast to follow, which makes a theoretical accurate description inevitable to study surface processes.

In experiment, when an H-atom scatters from an epitaxial graphene sheet grown on Pt(111), a bimodal translational energy loss distribution of the scattered atom is observed. This corresponds to the fast and slow channel, depending if scattering takes place before or after crossing the barrier to chemisorption. This has been shown and discussed in detail in Sec. 4.1.2.

As already mentioned, the physisorption well is involved in the fast whereas the barrier is involved in the slow channel. In the latter I have already explained that the minimum energy pathway to adsorption is influenced by a synchronized motion of both collision partners. Therefore, these two regions are of most interest and will be inspected in detail in the following, before describing the dynamics of the scattered projectile.

The global physisorption well is located over the mid (m) point, so over the middle of a six-membered carbon ring. A comparison between DFT data and the HDNN-PES can be found in Fig. 4.4. The physisorption well in the DFT data on the PBE-D2 level is estimated to be -26 meV at the lateral position of the H-atom of  $z_H = 2.87$  Å. The physisorption well was also estimated to be 47 meV located at the same position using PBE-D3. In the HDNN-PES,

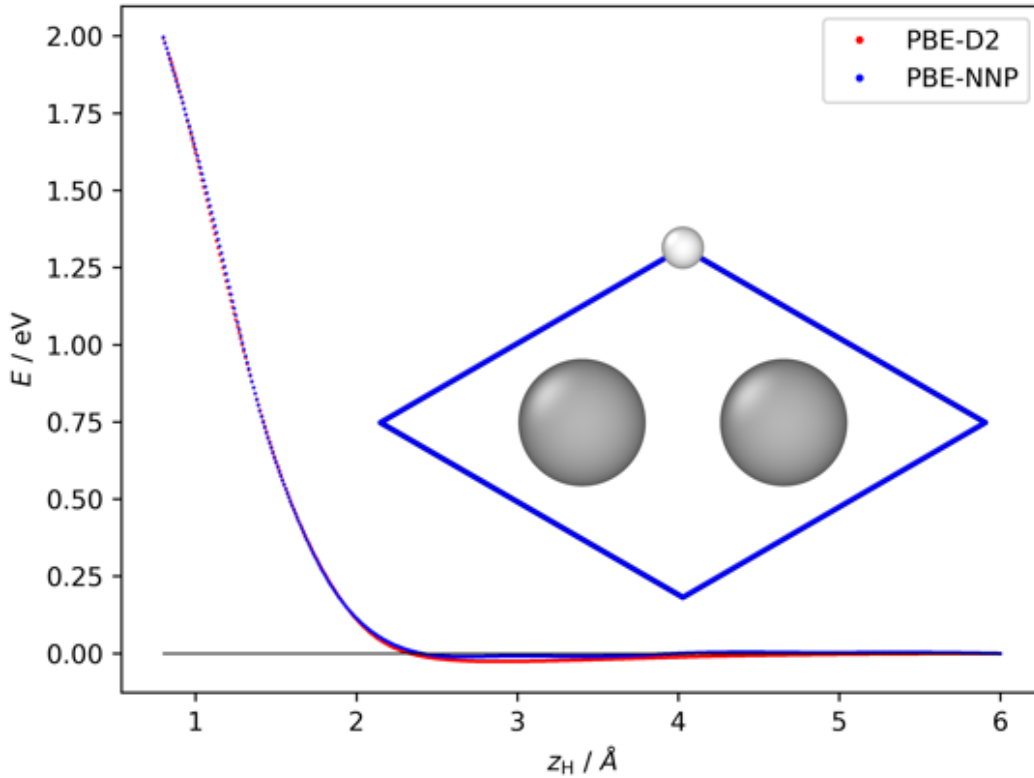


Figure 4.4: Following the  $z$ -coordinate of the H-atom over the mid point of a six-membered carbon ring, which goes over the global physisorption well. The physisorption well is -25.87 meV at  $z_H = 2.87$  Å (PBE-D2) and -10.76 meV at  $z_H = 2.67$  Å (PBE-NNP). The results from HDNN-PES is labeled PBE-NNP to highlight that the underlying data points of the fit are compared to the points from the fit. This picture and the following showing graphs are created using python 3 [296–298] and the matplotlib library [299].

the physisorption well is -11 meV and located at the position of the H-atom of  $z_H = 2.67$  Å. In Fig. 4.4 the results from the HDNN-PES are labeled PBE-NNP to highlight that the HDNN-PES was build up by fitting to DFT data on the PBE level of theory. It should be demonstrated that the comparison is between data points and the fit.

The experimentally derived physisorption well depth is estimated to be 40 meV, which was reproduced by a counterpoise corrected wave function calculation of the hydrogen-coronene system [302], with the minimum at  $z_H = 2.93$  Å. The previous used REBO-EMFT function had no physisorption well.

Although there is a difference of about 15 meV between the physisorption well predicted by DFT and the physisorption well predicted by the HDNN-PES, this does not have a big influence to the scattering, because the  $\approx 2$  eV incidence kinetic energy is two orders of magnitude higher compared to the well depth. One has to also consider that a difference of 15 meV is exactly the fit accuracy of the underlying data to the developed PES. Still, the DFT data is in good agreement and although the fitted well depth is four times smaller, there is an increased accuracy compared to the previous PES.

Because I want to study the formation of a chemical bond between the impinging hydrogen atom with a surface carbon atom, during the scattering it has to cross the barrier to chemisorption. This region, where the barrier is fully or partially involved, was investigated in more detail. Compared to before, now the slow channel is investigated in detail, where a transient bond is formed in the high energy loss region. This has been done because of two reasons. The RMSE gives a hint of the overall quality of the fit, but does not say anything

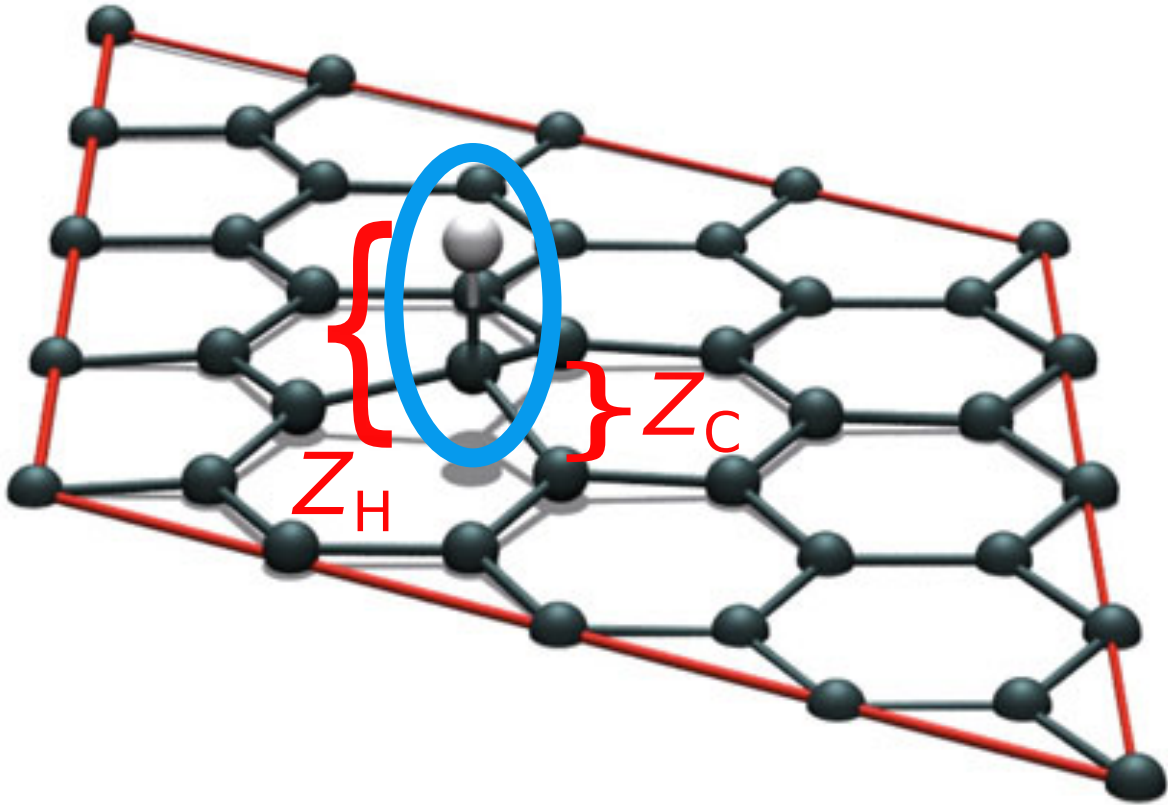


Figure 4.5: Parameters used in 2D cut of PES. The two most important DOF involved in the formation of a transient bond (blue circle) are the  $z$ -coordinate of the H-atom and the C-atom, where the projectile impinges, respectively. This figure was created using Inkscape [283].

about the region or configuration space of most interest, where the formation of the chemical bond takes place. This is, as already mentioned, the synchronized movement of both collision partners. This is foremost the distance between the H-atom and the C-atom. Therefore, the two degrees of freedom who were mostly involved in the formation of the chemical C–H bond are the  $z$ -coordinates of the H-atom and the C-atom, respectively. The minimum energy path to chemisorption (MEP) involves both DOF and is visualized in Fig 4.5, where the blue circle shows the bond formation and the two parameters involved.

A two-dimensional cut of the full-dimensional PES showing exactly the mentioned two DOF is shown in Fig. 4.6. Important to mention here is that only the  $z$ -coordinates of the H- and corresponding C-atom are changed, but no structure geometry optimization was carried out. To actually bind to the surface, the projectile has to overcome the barrier. The barrier is the energy needed to move the C-atom out of the surface plane in the process called puckering, that is mostly involved in the scattering event and that has the strongest interaction with the impinging projectile. The puckering of the C-atom, electronically is the rehybridization process of the corresponding carbon atom from  $sp^2$  to  $sp^3$  configuration, which was mentioned before. According to the heat map shown in the contour plot, the movement starts in the high-interaction region, when the projectile atom is roughly  $2.2 \text{ \AA}$  away from the surface plane. To form the chemical bond, the carbon has to move around  $0.3 \text{ \AA}$  out of the surface plane. The plot is generated by changing the lateral position of the H-atom above a fully relaxed graphene surface sheet at 0 K. The barrier height has been estimated in this grid to be 172 meV whereas DFT predicts the barrier to be 160 meV, which is reproduced well. The barrier represents

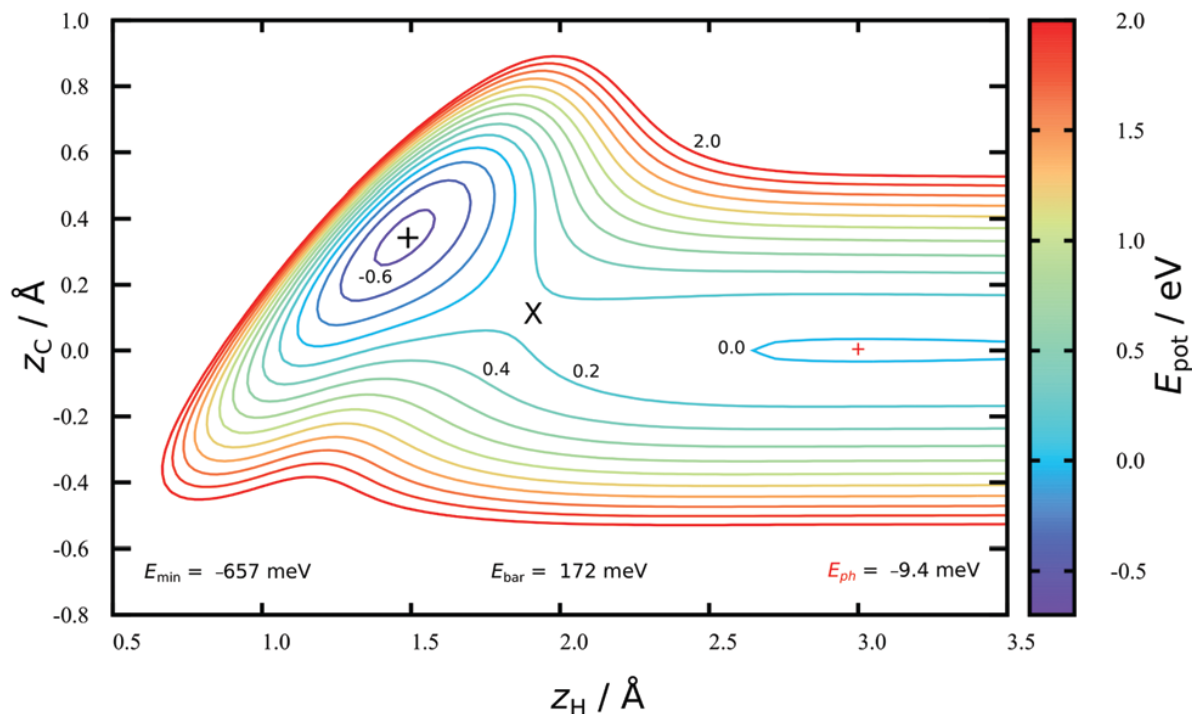


Figure 4.6: 2D cut of the HDNN-PES near the minimum energy path to chemisorption. The H-atom is constrained to be directly above a C-atom.  $z_C$  and  $z_H$  is the distance of the C- and H-atom to the surface plane, respectively. The physisorption (+) and chemisorption (+) minima have depths of 9 and 657 meV, respectively. The barrier (×) height to chemisorption is 172 meV. This picture was generated using gnuplot in version 5.2 [300]. Reproduced from Ref. [204] with permission from the Royal Society of Chemistry.

the transition state to chemisorption and is located at  $z_C = 0.10 \text{ \AA}$  and  $z_H = 1.88 \text{ \AA}$ . Previous theoretical simulations performed on free-standing graphene determines the barrier to be in the range from  $0.13 \text{ eV} - 0.44 \text{ eV}$  [303–305]. However, more recent results give a range of  $0.15 \text{ eV} - 0.37 \text{ eV}$  [306–308]. The barrier seems at least be in the most probable range estimated so far.

Comparing the preliminary results from MCTDH to experimental finding, also indicates that the experimental final velocity distribution is better reproduced if a higher barrier is considered. A detailed analysis is beyond the scope of results presented in this work, the main point here is just that we have justifications from our collaborators to consider data that will estimate the barrier height to chemisorption more accurate in future studies. However, when analyzing the scattering from epitaxial graphene, due to interactions the Pt substrate effectively lowers the barrier height to chemisorption, which promotes the reproduction of experimental results, since the PES under-estimates the barrier. The aspect of this error-compensation has to be considered.

The well depth of the chemical bond has been estimated to be  $657 \text{ meV}$ , which agrees with the minimum found in DFT that is  $676 \text{ meV}$ . The minimum is located at  $z_C = 0.35 \text{ \AA}$  and  $z_H = 1.48 \text{ \AA}$ . The local physisorption well depth was estimated to be  $9 \text{ meV}$ , which corresponds to  $z_H \approx 3.03 \text{ \AA}$  and compares well with the DFT energy of  $22 \text{ meV}$  calculated for the same

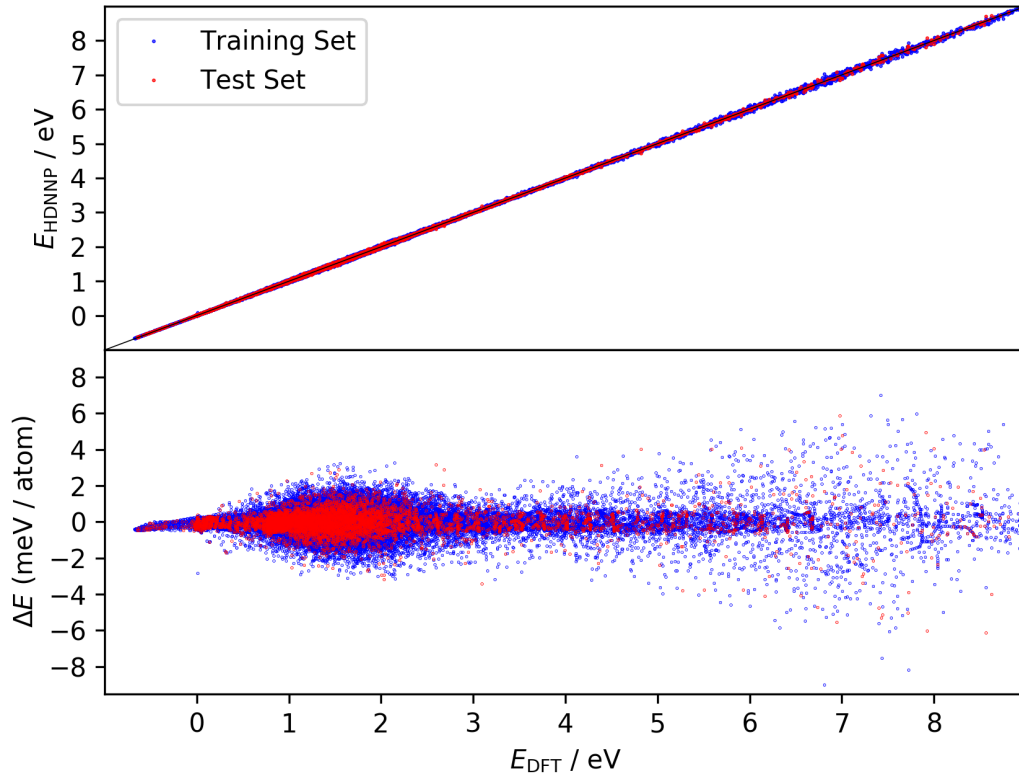


Figure 4.7: Comparison of reference DFT ( $E_{\text{DFT}}$ ) and predicted energies by HDNNP ( $E_{\text{HDNNP}}$ ) is in the upper panel. The lower panel shows the signed error. Training set is shown in blue and test in red, respectively. Zero energy scale of DFT energy corresponds to a relaxed graphene sheet configuration at  $T = 0 \text{ K}$  with an H-atom  $6 \text{ \AA}$  away from the plane of the surface. Reproduced from Ref. [204] with permission from the Royal Society of Chemistry.



geometry. The chemical well depth is shown as black plus, the barrier — which is the transition state of C–H formation — as black cross and the local physisorption well is shown as a red plus. The C-atom is partially re-hybridized at the shown transition state, because it is found only 0.1 Å above the surface plane.

The previous used REBO-EMFT PES predicted the chemisorption well of 610 meV, which is more shallow compared to the HDNN-PES and DFT. The barrier, however with 260 meV is much higher, but in better agreement compared to previous studies and experiment.

So far, the important regions, which can be related to the two channels seen in experiment and previously investigated have been analyzed.

The generation of structures used to fit a HDNN-PES is described in detail in Sec. 4.1.2. The configuration space of interest has a range of  $\approx 10$  eV, which has to be covered by the PES. The range is because of energies and temperatures respected in the data set.

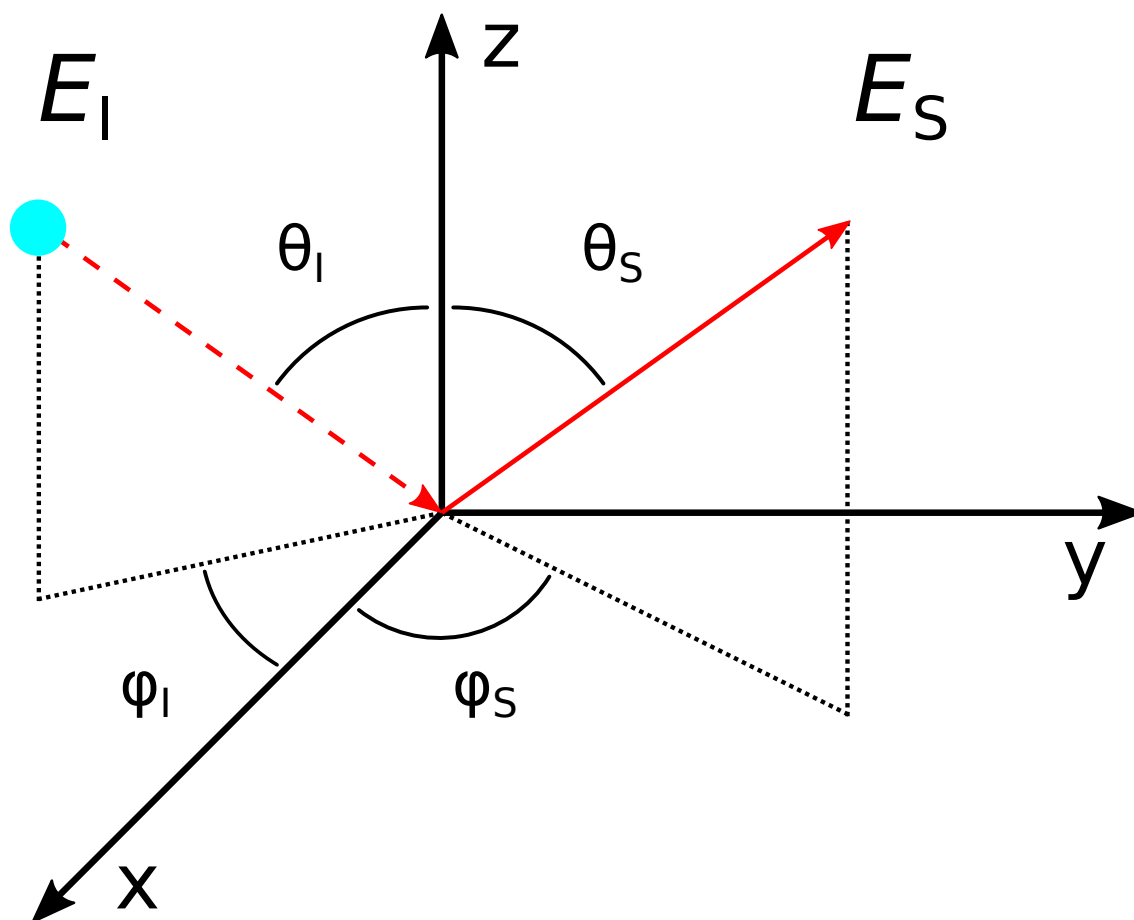


Figure 4.8: Definition of Parameters used in thesis. Here,  $\theta$  and  $\phi$  represent the polar and azimuthal angle, respectively.  $E$  is the kinetic energy of the projectile drawn as a cyan colored sphere. The incidence parameters are indexed with I and the parameters with index S indicate conditions of the projectile after its interaction with the surface. The red dotted line shows the incidence trajectory and the red solid line the scattered trajectory of the projectile. The surface geometry is considered to lie in the  $xy$ -plane and  $z$  is parallel to the surface normal. This figure was created using Inkscape [283].



The architecture of the HDNN-PES that is able to accurately reproduce the electronic structure data has been estimated to be two layers with 15 neurons each, making a 15-15-1 architecture. The parameters for the atom-centered symmetry functions can be found in Tab. A.1 (radial type) and Tab. A.2 (angular type). RMS fitting errors for different atomic neural network architectures to account for holes in the configuration space can be given in Fig. A.3.

The RMSE of the HDNN-PES to the DFT data is  $\approx 0.6$  meV per atom for energies in both the training and the test set, which corresponds to a fit accuracy of  $\pm 15$  meV for the total system. The RMSE for the forces is  $\approx 90$  meV  $\text{\AA}^{-1}$  in the training and test set, respectively.

Using a different architecture of NN to account for holes in the configuration space by comparing the predicted energies of both architectures, we observe the same RMSE for both architectures and the difference between energies predicted by both are less compared to the difference to the underlying DFT data, which has already been mentioned in Chp. 3.

The RMSE fitting error of the REBO function to DFT-EMFT data was reported to be  $\approx 7$  meV per atom, which corresponds to an error of 175 meV for the total system. Again, the REBO function does not include a physisorption well.

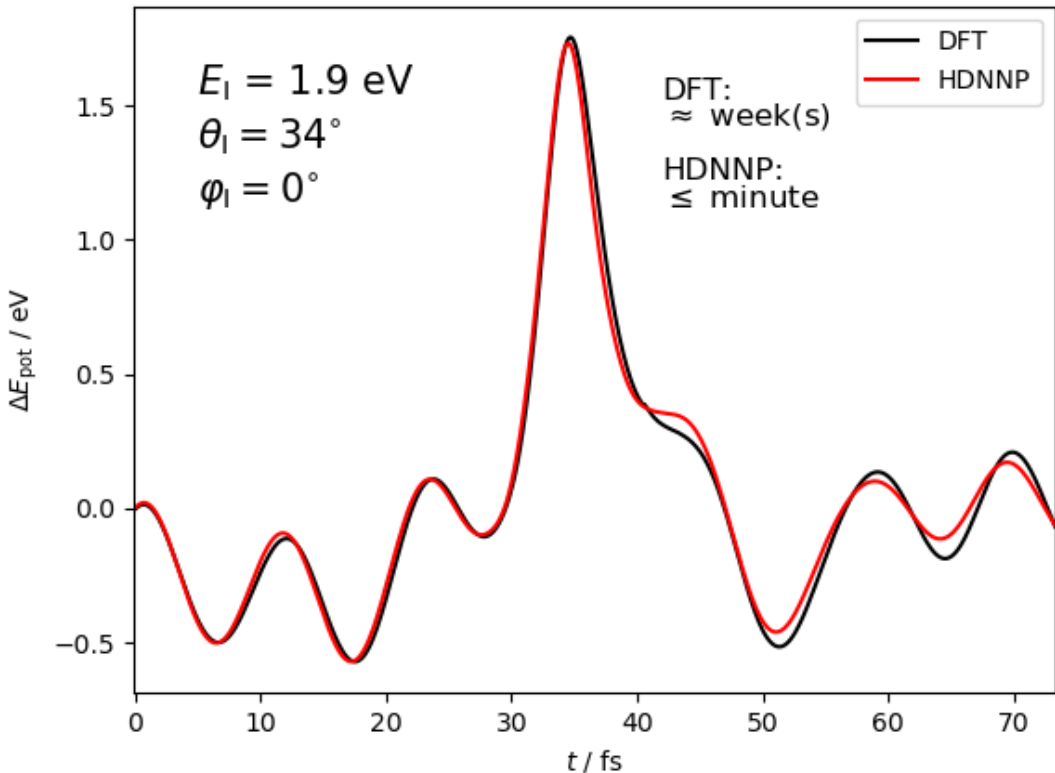


Figure 4.9: Potential energies obtained from AIMD (black) and MD simulations using HDNN-PES (red). The initial conditions are given in the plot and are the same for both trajectories. Both trajectories traverse the chemisorption well before returning to the gas phase after a single bounce. The distance of closest approach is below  $r_{\text{CH}} = 1.4 \text{ \AA}$ . Movies of the two trajectories are offered in the supporting material [301]. Remarkable are the different times to get a single trajectory. Reproduced from Ref. [204] with permission from the Royal Society of Chemistry.

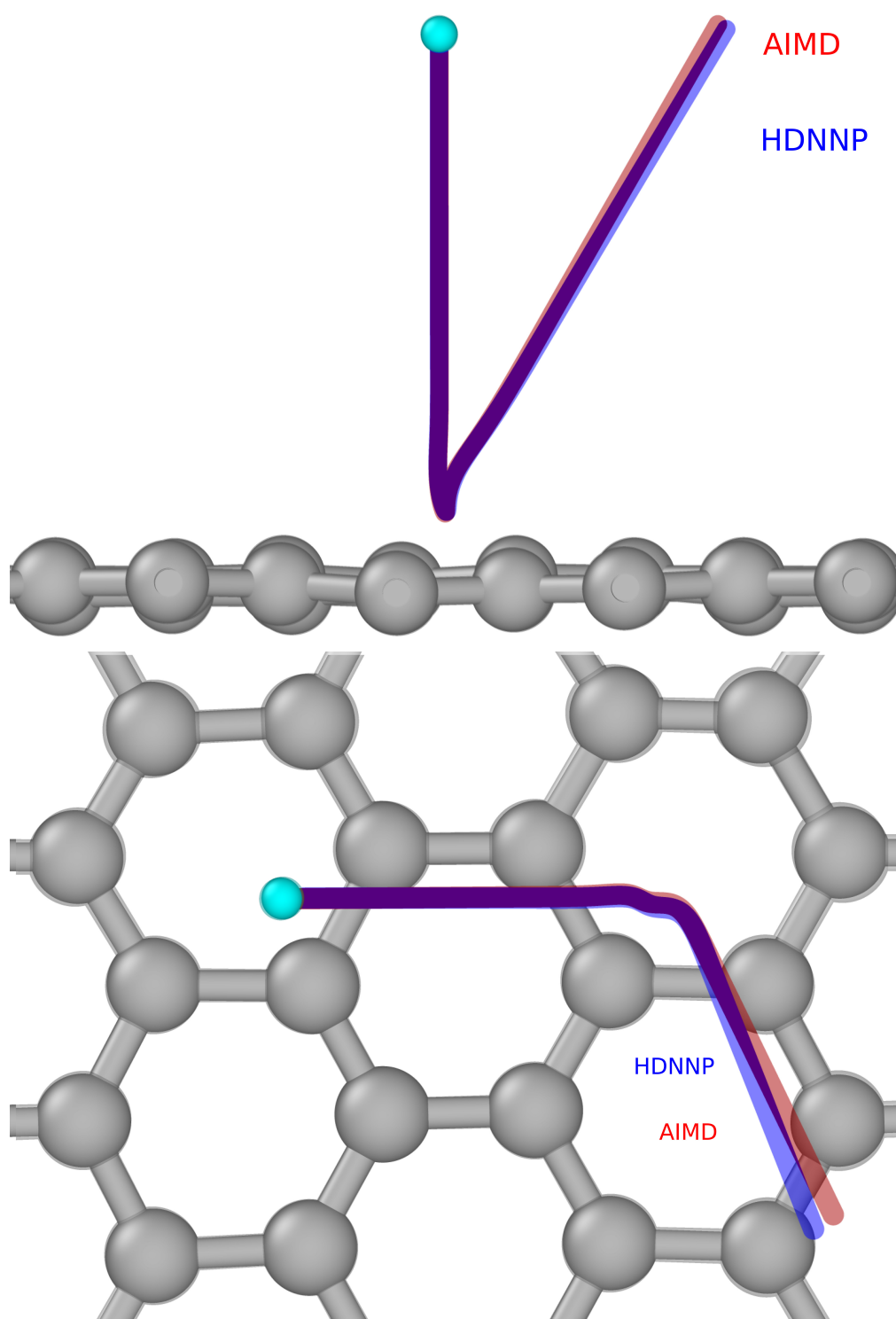


Figure 4.10: The same two trajectories as in Fig. 4.9 – AIMD (red) and HDNN-PES (blue). The trajectory is shown as "side view" and "top view". The H-atom's initial position is shown as a cyan colored sphere. Because of residual error of the NN fit to DFT data, the two trajectories diverge. This figure was created using Inkscape version 0.92.5 [283] and Ovito version 2.9.0 [203]. Reproduced from Ref. [204] with permission from the Royal Society of Chemistry.

In Fig. 4.7, the fitting error to all used DFT data is shown graphically. In the figure, the correlation between reference energies from DFT ( $E_{\text{DFT}}$ ) and predicted energies by HDNNP ( $E_{\text{HDNNP}}$ ) is shown in the upper panel. The energetic difference of reference and predicted structures depending on the energy of the structure compared to our zero energy reference structure is shown. The reference structure corresponds to an H-atom placed 6.0 Å above a fully relaxed graphene surface plane. In both panels, not only the training data set is shown (blue data points), but also the structure from the test set, which is used as validation data (red data points). Independent of the data set and even at higher energies, no random distribution can be seen. Therefore, there is no reason to suspect systematic problems by the fitting procedure to come up with a PES over the energy range of 10 eV.

From cuts through the full-dimensional PES the overall capability of the PES can be tested to reproduce electronic structure data. The next step is to further test, if real-time dynamics are reproduced as well, which in the end are compared to experimental results. To do this, the scattering of a projectile crossing the chemisorption barrier in the scattering event to subsequently traverse back into the gas phase is simulated in AIMD and MD simulations, because this is a typical trajectory with a transient bond formation. The latter utilizes the HDNN-PES.

The parameters defined in our simulations and commonly used in our group are the incidence polar angle  $\theta$ , the azimuthal angle  $\varphi$  and the kinetic energy  $E$  of the projectile. Initial conditions of the impinging atom have index I whereas final conditions of the projectile after the scattering event are indexed with S. The definition of these parameters is shown in Fig. 4.8, where the incidence position of the projectile is shown as a cyan colored sphere.

Unlike it was the case generating the reference data set, no snapshots from MD simulations are calculated with electronic structure codes, but a single trajectory from AIMD simulations is compared to a trajectory from HDNN-PES using the exact same initial conditions. Comparison was done by following the potential energy of H-atom scattering with the graphene surface. The change of potential energy along the trajectories from classical simulations is shown in Fig. 4.9. The impinging projectile was released 3.5 Å above the surface with an initial polar angle of 34° and azimuthal angle of 0°, which corresponds to scattering along a C–C-bond. The initial kinetic energy of the impinging atom was set to  $E_{\text{I}} = 1.9$  eV. The atom comes from the gas phase, traverse the chemisorption well and after a single bounce return to the gas phase again. In the simulations, the C–H distance of closest approach is smaller than  $r = 1.4$  Å, indicating that the atom crosses the barrier.

By following the potential energy, one can get a hint of the structure. The collision of the impinging atom with the surface is around  $t = 35$  s. Before, there are only minor differences in the potential energy, whereas after the scattering the trend stays the same, but there are larger differences in the energies. To better follow the scattering event shown in Fig. 4.9, the two trajectories have been visualized. A "top" and "side" view of the two trajectories can be found in Fig. 4.10. For a better understanding, movies of the corresponding trajectories from different angles of view are also offered in the supporting material [301], namely in "top" and "side" view as already mentioned and to further support the understanding, also a movie showing a "perspective" view has been added. All structure files as well as movies were created using OVITO version 2.9.0 [203].

This Figure highlights at the same time the importance of using force fields in our simulations. In AIMD, the time needed for a single trajectory is on the order of weeks. It was mentioned before that in the latest implementation — depending on the incidence conditions — the time needed to simulate a single trajectory is on the order of a minute. Even if a couple of minutes are needed for a single trajectory, there is still a benefit that drastically increase the performance. This is especially of importance if we consider that 100,000 up to 1,000,000 trajectories are needed for each condition to get comparable statistical results.

Good statistics are needed when comparing the results from theory to experiment. This means, a very large number of trajectories is needed to get meaningful results. This will be discussed later in detail, but also the fact that mostly in-plane scattering can be detected in experiment, there is an even higher need for a large number, because not all generated trajectories can be used when comparing to experiment.

Compared to the previous used REBO-EMFT PES, the time on average needed for a single trajectory could be reduced from  $t \geq 1$  minute to  $t \approx 45$  seconds, which is discussed in detail in Sec. 3.6 and Sec. 3.7.

#### 4.2.2 Discussion of the underlying DFT data

In order to analyze the scattering simulations, the hexagonal lattice representation of graphene surface as shown in Fig. 4.2 was converted to an orthogonal lattice as shown in Fig. 4.11 when building the system to perform electronic structure calculations. The orthogonal primitive cell contains 4 carbon atoms, shown as gray colored spheres. Although the PES represents the DFT data quite well, it was not discussed if the DFT data itself contains all properties of the system we want. The question is if the way of converting the hexagonal to an orthogonal cell still describes the symmetry of the graphene sheet. In the end of my PhD, I found out some discrepancies. In the orthogonal cell if we change the lateral position of a single H-atom along the high-symmetry bridge (bri) points labeled b, b' and b'' in the simulation cell as shown in Fig. 4.2 and compare the energies at the same  $z$ -coordinate for all bridge points. In the region between  $1 \leq z \leq 6$  Å, b' and b'' result in the exact same energy (on the order of requested accuracy in the electronic structure calculations, which was  $10^{-5}$  eV), but not b! The maximum in difference is at  $z = 1.2$  Å, which is 96 meV compared to b' and b''. This huge energetic difference might lead to the assumption, that it is a structural problem. However, I did some checks of the symmetry of the structure by checking C–C bond lengths and the angles between adjacent carbon atoms, which are all the same. This assumption was confirmed by using the symmetry function descriptors, which also take the geometry into account.

In the following, several checks to figure out the exact reason for the high energetic difference of seemingly symmetric bridge points are given.

Despite the fact, that taking dispersion corrections into account, they could not be responsible for such large energy difference, but intrinsically, they also check for nearest neighbors and are structurally dependent, they are used as an additional tool to check for the structure. Energies are compared on the GGA-DFT level of theory using PBE functional. By using different schemes as dispersion corrections, we end up at the same energetic differences for Grimme correction D2 and D3 as well as Tkatchenko Scheffler (TS). This is shown in Fig. 4.12 in the top panel. As expected, independent of the level, both D2 and D3 predict the exact same energetic difference of the two seemingly inequivalent bridge sites. TS follows this trend but fluctuates more, which is as expected, since it is a numerical expression compared to Grimme corrections, which are analytical expressions. As can be seen, independent of the correction scheme, all predict the different bridge points as structurally the same.

To check if the energetic difference might be according to the PBE functional used, the hybrid-level DFT functional B3LYP was used to repeat the scan of the  $z$ -coordinate of the H-atom approaching the surface C-atoms. The results are dispersion corrected by Grimme on the D2 level when using the PBE functional and TS together with B3LYP. TS was chosen, because it is easily accessible in the FHI-aims electronic structure code. Alongside the results from two different functionals, the results from the HDNN-PES based on the PBE-D2 data is shown as well in Fig. 4.12 in the bottom panel. Independent of the functional, there is an energetic difference between two inequivalent bridge points. The difference is even more pronounced when utilizing the B3LYP functional. Here, the largest deviation is  $\approx 115$  meV.

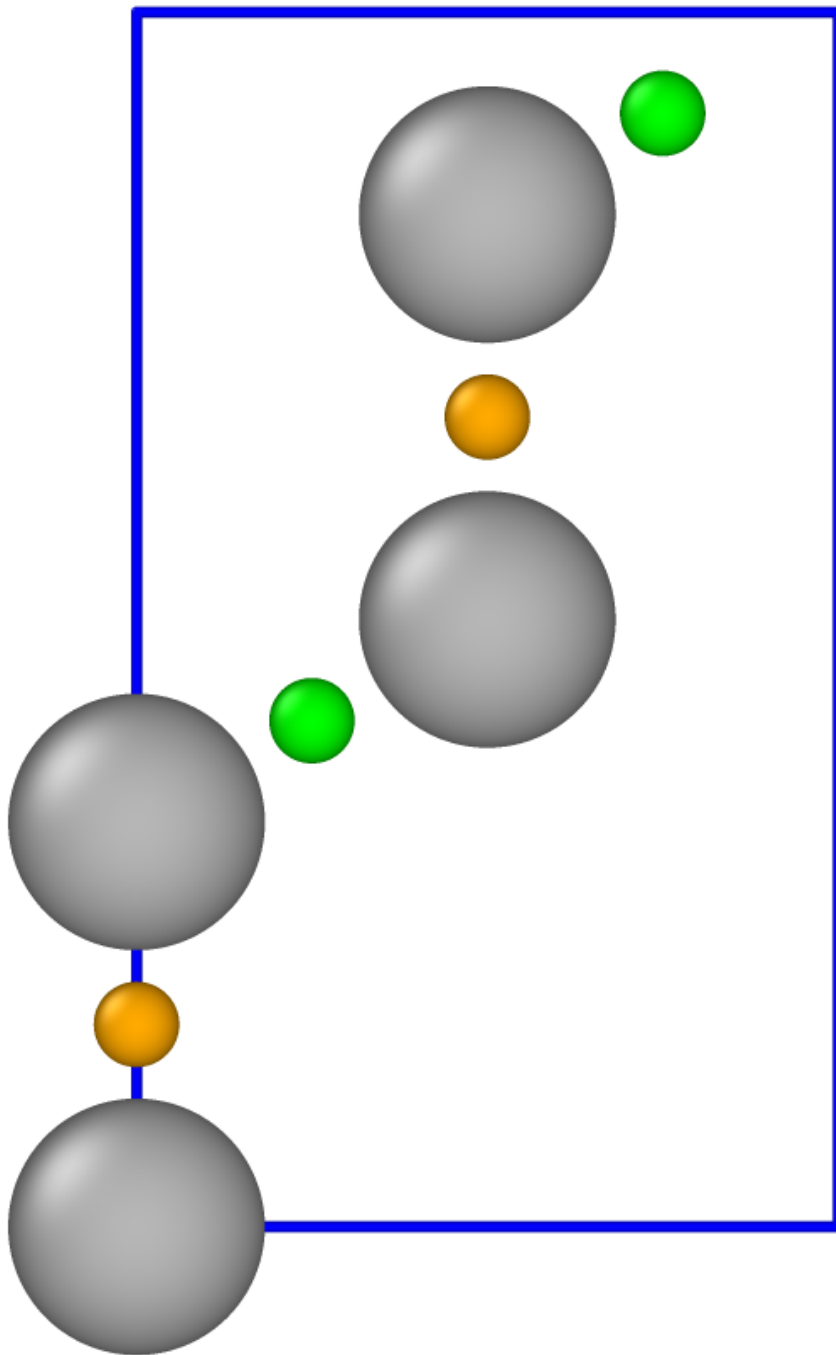


Figure 4.11: The orthogonal primitive cell of graphene contains 4 carbon atoms, shown as gray colored spheres. To account for the hydrogen coverage in the hexagonal lattice, the interaction energy of two different structures are compared. Both structures contain two hydrogen atoms at symmetrical equivalent bridge points. The first structure contains H-atoms at positions marked with green colored spheres and the second structure has H-atoms at positions marked with orange colored spheres. This cell is labeled *orthogonal (2 H)*.

This indicates that using a different and seemingly more accurate functional does not solve this problem. From the figure it can also be seen that although the energetic difference is less pronounced compared to the underlying data, the HDNN-PES learns the features present in the data set.

Interestingly, in case of the HDNN-PES there is a small artificial barrier of  $\approx 5$  meV introduced for the H-atom being between 2 Å and 3 Å away from the surface atoms, which is not seen in the underlying DFT data at this region but between 1 Å and 2 Å and being  $\approx 20$  meV. There is also not the big oscillation of energies when the H-atom approaches the two surface carbon atoms. It seems, the HDNN-PES tries to average over the high-interaction region. Although the energetic difference between the bridge points is reduced to be  $\approx 65$  meV, it is still present and a multiple of the fit accuracy of the potential. This makes sense since the HDNN-PES can only learn from data, which it is based on. If there is some contradicting or wrong data, the NN will learn the problems, too. The other way around this more promising, because if correct data is used to fit the NN, the fitted PES will be correct as well.

The two bridge points with the same  $y$ -coordinate have essentially the same energy, but the energetic difference between bridge points with a different  $y$ -coordinate is more than 100 meV, which is more than a factor of 6 compared to the fit accuracy of the fit of the HDNN-PES with respect to the underlying DFT data. Depending on the  $\Gamma$ -centered  $k$ -point mesh (KPOINTS), the energy ranges from 211 meV to 132 meV, when using a bigger basis set (1000 eV cutoff for the kinetic energy labeled ENCUT). The energetic difference seems to be independent or only small influenced by the size of the grid. The results for the two primitive cell types depending on the basis set and  $k$ -point grid can be found in Tab. A.4. One would immediately think, that this difference arise from a non-symmetrical structure. The symmetry of the structure was therefore carefully checked, by screening the bond length and angles. Even the symmetry functions as used as structural fingerprints for the HDNNP and also the structural check used when applying dispersion corrections predict the three bridge points as geometrically equivalent. Even using a different way to generate the structures does not change this issue. Before, the structure was generated manually by my predecessor Marvin Kammler and I repeated the generation of the graphene structure in orthogonal representation by using the atomic simulation environment (ASE) python library.

Two plots further supporting the analysis are given in the appendix. The Grimme dispersion correction D2 and D3 alone are shown in Fig. A.4, next to the difference of the energies for each  $z$ -coordinate. Independent of the level, both schemes predict the exact same dispersion correction energy for both bridge sites. Furthermore, in Fig. A.5 it was tested, if the electronic structure code used has an influence. It can be seen, that independent of the used electronic structure code and with that even the type of basis set has no influence on the energetic difference, it is present in all considered calculations.

The cell type of the primitive unit cell is converted from hexagonal to orthogonal to simplify the analysis. In the hexagonal cell, two atoms are in the primitive unit cell and the lattice vectors have the same length. After conversion, in the orthogonal cell there are four atoms. The lattice vectors have not the same length in  $x$ - and  $y$ -direction. In Fig. 4.12 in both panels it can be seen that the largest difference of the energies is when the H-atom is 1.2 Å away from the surface plane, meaning in the high-interaction region and close to the equilibrium C–H bond length of 1.1 Å. Therefore, in the following presented calculations, the  $z$ -coordinate of the H-atom was always set to 1.2 Å to specifically look at the largest deviations.

Although the performed checks predict the geometry to be fully symmetric, it seems that the coverage of the hydrogen atoms changed, which may be the reason for the energetic difference. This is because the number of carbon atoms in the primitive cell in orthogonal representation is doubled compared to the primitive cell in hexagonal representation, but still a single hydrogen atom is included, changing the coverage. To confirm this assumption, calculations have been

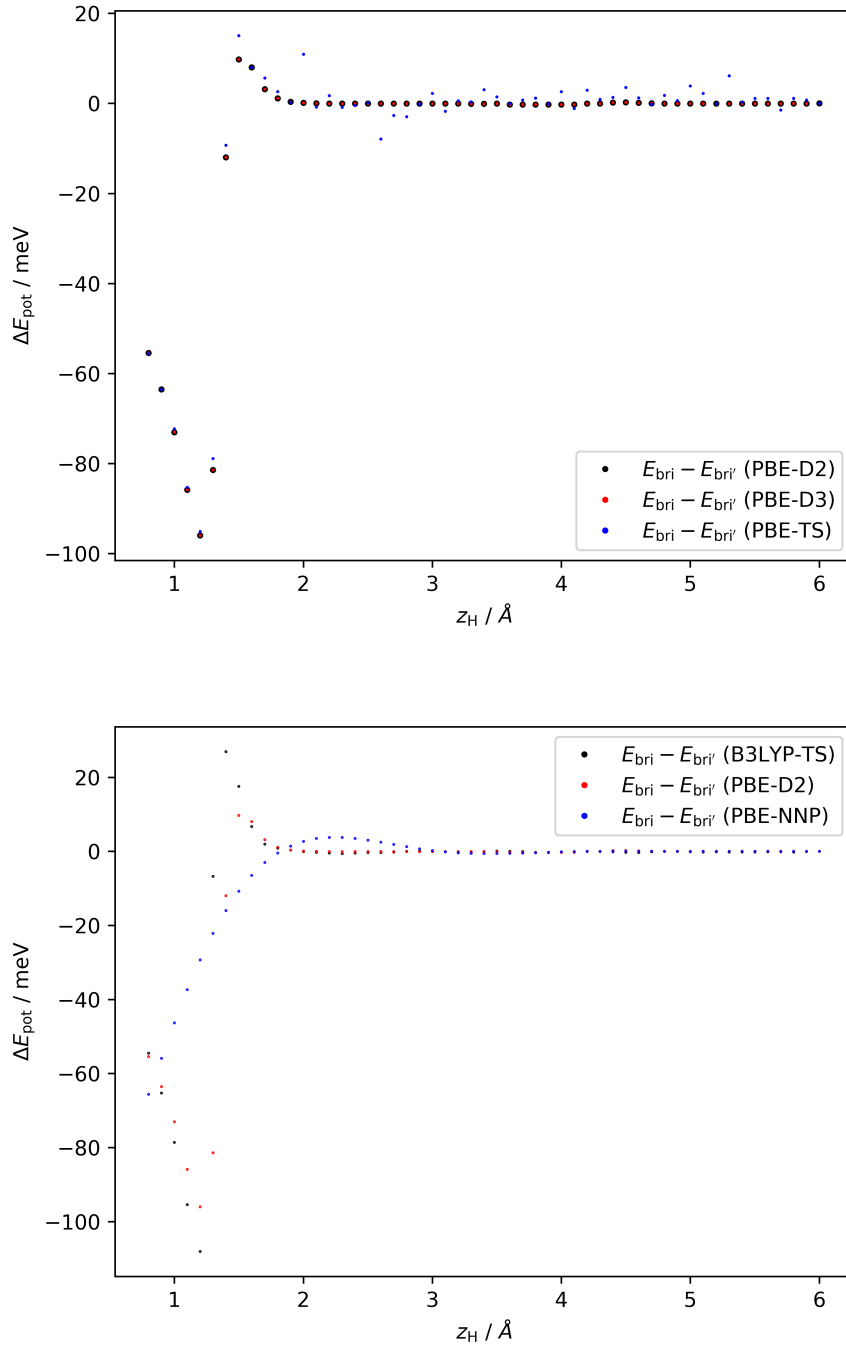


Figure 4.12: Top: Energetic difference of inequivalent bridge sites depending on different dispersion correction schemes by Grimme and Tkatschenko Scheffler. The energetic difference is largest for an H-atom at the lateral position of 1.2 Å with 96 meV. Note, the results from D2 and D3 are exactly the same and only the size of the data points was adjusted to highlight their visibility. Bottom: Energetic difference of inequivalent bridge sites depending on different functionals with vdW corrections and the results from the NNP. Again, the results from HDNN-PES is labeled PBE-NNP to highlight that the underlying data points of the fit are compared to the points from the fit.

done in an orthogonal cell, but this time two hydrogen atoms are included but at symmetrically equivalent bridge points. Since two bridge points are still the same because of the argument with the same  $y$ -coordinate, a second structure containing two hydrogen atoms as well but at a different bridge point was carried out, too. By comparing the energies of these two structures, we account for the same hydrogen coverage in the orthogonal cell compared to the hexagonal primitive cell. This is shown in Fig. 4.11, where a structure containing two hydrogen atoms at the positions shown as green colored spheres is compared to a structure containing two hydrogen atoms at the positions shown as orange colored spheres.

In Tab. A.4 the results are shown labeled with *orthogonal* ( $2H$ ). In there, the energetic difference is higher compared to the hexagonal cell type, but on the order of a tenth of an meV, which is our desired accuracy. These results are independent from the basis set, simply the  $k$ -point mesh has to be large enough to account for this case.

In order to still use the orthogonal cell, because it will make the analysis of the scattering easier in MD simulations, I also started to analyze the interaction energy of the hydrogen atom with the graphene surface depending on its size. By constantly increasing the number of atoms,

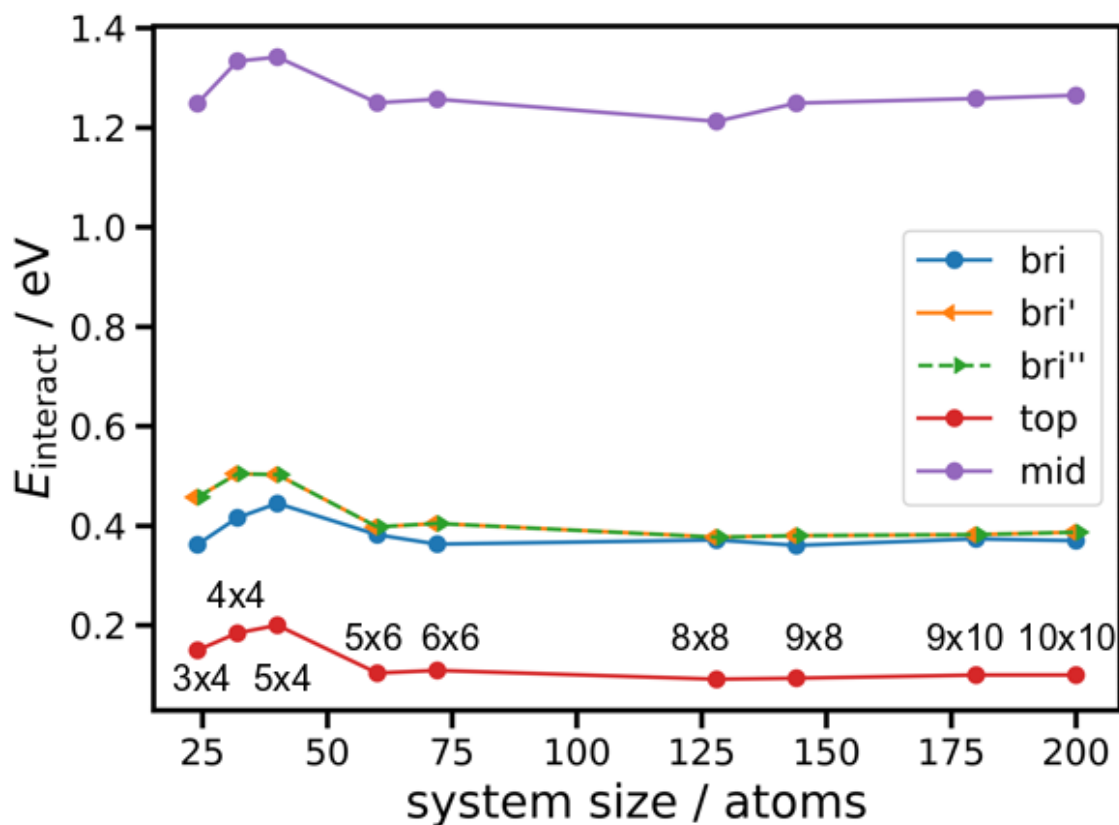


Figure 4.13: Surface size dependence of the interaction energy of an H-atom with the graphene sheet at three different high symmetry points (HSP) bridge (bri), middle (mid) and top as shown in Fig. 4.2. The dependence of two other structurally equivalent bridge points bri' and bri'' are shown as well. The lateral position of the H-atom was always 1.2 Å above the HSP, zero energy is the H-atom 6 Å away from the surface plane. The reason for the difference in interaction energies become clear if following the H-atom approaching the surface plane along HSP, which is shown in Fig. A.6 and A.7.



the difference of the interaction energies at different bridge sites decreases up to a surface size of  $8 \times 8$  containing 128 atoms. However, in bigger systems we see oscillations, but no drastic decrease in the interaction energies. It seems, the interaction energies are converging and the difference in the bridge sites is slowly vanishing. To rationalize this assumption, bigger system sizes as well as more accurate data is needed to support this hypothesis. The goal is to find the size of the surface and with it the number of atoms needed to be in the system when performing electronic structure calculations. This will increase the fit accuracy of the HDNN-PES further and maybe is a key to quantitatively describe the H-atom scattering from graphene to get a fundamental understanding.

The dependence of the interaction energy with respect to the surface size is shown in Fig. 4.13. The interaction energy is given as difference of the H-atom at different high symmetry sites at 1.2 Å and 6.0 Å, between high and zero interaction region. The reason for the different interaction energies can be explained, when following the H-atom approach to the surface at the different high symmetry points. Since here, the difference of only two lateral positions is considered, because at this distance to the surface normal, the deviations are at most. In Fig. A.6 and A.7, the H-atom approach to the surface plane is shown at the mid, top and bri points, respectively. The size of the graphene surface is  $3 \times 4$ . A full scan of bigger system sizes could not have been carried out due to time restrictions. At 1.2 Å, It can be seen that from a  $6 \times 6$  surface size onward, the interaction energies seemingly converges. However, the difference between the different bridge sites is not constantly decreased but oscillating. At least it is indicated, that even the difference seems to be converging, but slowly.

It is worth to discuss if using systems of this sizes in the orthogonal representation is still beneficial, because DFT will reach the limit of atoms considered in electronic structure calculations. In order to fit an accurate potential, it has also been shown that the reference data set has to contain a large number of structures to sample the configuration space of interest. Accurate calculations of so many structures will be computationally very demanding, giving rise to the question if maybe using the representation in the hexagonal lattice make more sense, although this would require adjusting the treatment in our program and following analysis.

To clarify, in the following Sections, the results are shown using a HDNN-PES with a 15-15-1 architecture that contains 24 carbon atoms and has the issue with the difference in energy of the bridge points.

### 4.3 Classical MD Simulations

This section is organized as follows. First, I will give some general aspects of classical simulations performed. The results from MD simulations using the HDNN-PES are compared to two experiments. Before showing any analysis, I will give some general remarks how the analysis was done. Furthermore, I will show some example trajectories of the fast and slow channel as well as the adsorption, which has been discussed in detail in Sec. 4.1.2. For each experiment, I will give the specific setup and how the comparison of experiment and theory has been achieved. General computational details are given in Chp. 3, but for each experiment the specific computational details are given in the corresponding sections as well.

In the following, the results from classical molecular dynamics (MD) simulations using the high-dimensional neural network potential energy surface (HDNN-PES) are compared to two different experiments, first to the RAT [24] followed by the HBEAM experiment [29], as mentioned before. Previous to this work and as mentioned before, a full-dimensional PES was generated by fitting a second generation Reactive Empirical Bond Order (REBO) potential to

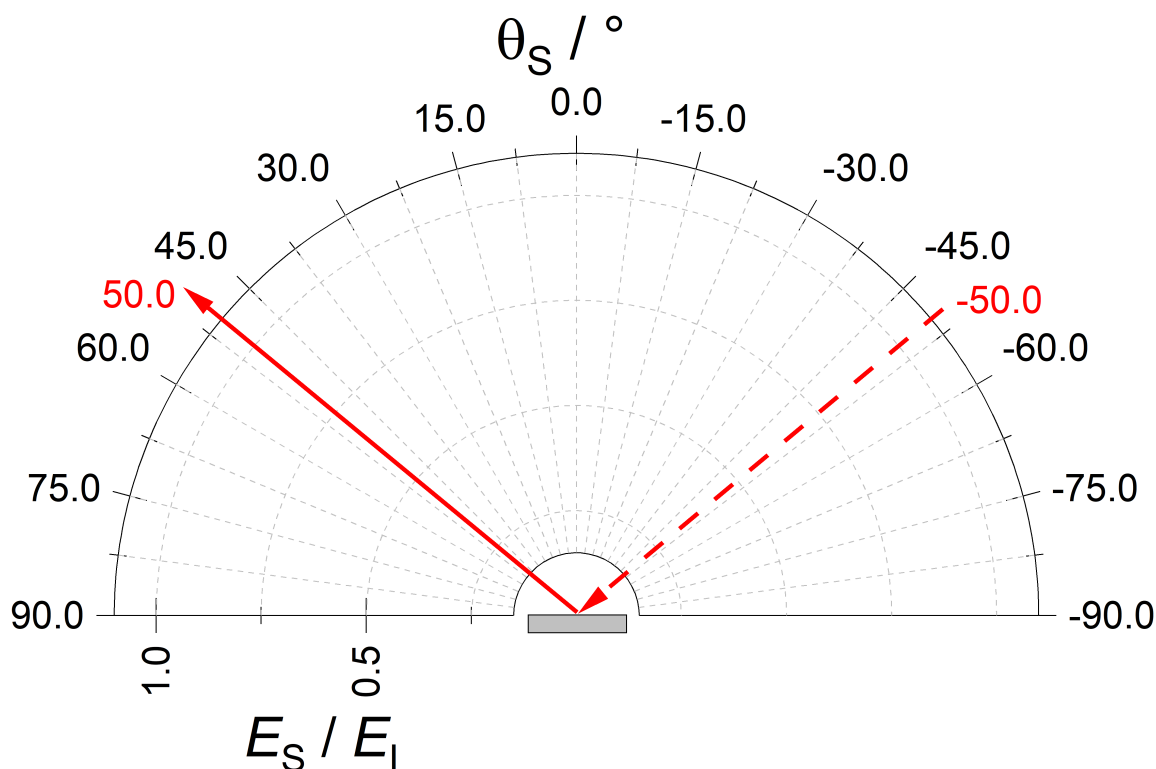


Figure 4.14: Scheme for the distribution of scattering angle and translational energy of H-atom scattering from free-standing graphene. The red dashed arrow represents the incidence angle whereas the long solid arrow represents the specular angle. Here, the gray bar indicates the graphene sheet. The translational energy of the projectile after the scattering event ( $E_S$ ) is normalized to its initial kinetic energy ( $E_I$ ) and is shown on the radial axis. The scattering angle  $\theta_S$  is shown on the polar axis and the probability density ( $P(E_S; \theta_S)$ ) in the next figures will be represented by the color coding. The two-dimensional distribution is normalized to the integrated area. Positive values for  $\theta_S$  indicate forward and negative values backward scattering. This figure and the ones showing distributions of the translational energy are created using OriginPro version 2022 [309].

energies obtained from Embedded Mean-Field Theory (EMFT) [25]. This will be referred to as the REBO-EMFT PES. The H-atom scattering depending on the incidence angle will not only be compared to experiment but also to results obtained from previously used REBO-EMFT PES.

The details of the channels seen and previous investigations on the scattering dynamics are given in Sec. 4.1.2. The notation of initial and final conditions of the projectile is defined and shown in Fig. 4.8. The kinetic energy of the impinging atom is denoted  $E$ ,  $\theta$  and  $\varphi$  represent the polar and azimuthal angle, respectively. The incidence parameters are indexed with I and parameters of the projectile after its interaction with the surface are indexed with S. Here, the red dotted line shows the incidence trajectory of the projectile represented as a cyan colored sphere. The red solid line shows the trajectory of the projectile after the collision with the surface. The graphene surface is assumed to lie in the  $xy$ -plane and  $z$  is parallel to the surface normal. Because of the adsorption complex geometry and as already mentioned in Sec. 4.1.2, a transient C–H bond is efficiently formed with normal kinetic energy. The normal kinetic energy  $E_N$  can be estimated considering the incidence kinetic energy  $E_I$  and the incidence polar angle  $\theta_I$  according to

$$E_N = E_I \cdot \cos^2(\theta_I). \quad (4.1)$$

In Fig. 4.14 an overview of the analysis in the following sections is given. The scheme shows the translational energy and scattering angle distribution of H-atoms from graphene. The red dashed arrow represents the incidence whereas the red solid arrow indicates the trajectory of the atom after its collision with the graphene surface, represented as a gray colored bar. The red number on the negative scale shows the incidence angle and the red number at the positive scale indicates the specular angle of the scattered atom. Note, comparing theoretically derived results with those from experiment, only forward scattering is considered. From  $0^\circ$  to  $90^\circ$ , forward-scattering of the projectile is shown, whereas the negative scale shows backward-scattering events, which cannot be seen in experiment, but in the simulations. These regions are therefore not confirmed by experiment. Although, only trajectories have been used that fulfill the mentioned detector geometry, this has also been applied when backward-scattering is shown.

To better understand the scattering, in Fig. 4.15 and 4.16 example trajectories of the two different channels as well as the adsorption of the H-atom are given. The trajectories have also been visualized and can be found in the supporting information as videos [301]. Again, different angles of view for the same trajectories are offered to better follow the dynamics during the scattering events.

What has not been discussed yet is the energy transfer in the opposite direction. What can be seen in experiment and is supported by previously performed molecular dynamics simulation using the REBO-EMFT PES is an inelastic scattering, where energy is transferred from the graphene surface to the impinging atom. Energy transfer is from transversal surface phonons of the graphene sheet to the projectile, increasing its initial kinetic energy. The increase of the translational energy of the scattering atom depends on several factors. For the same incidence angle, at smaller incidence energies, it is more likely that the surface can distribute its kinetic energy to the projectile, because it is less likely that the impinging atom will cross the barrier. In case of D-atom scattering off graphene, it is also more likely that the energy flow will be away from the surface. This is due to the higher inertia of the D-atom compared to its isotope. This will be discussed in detail in the following sections.

An example of this mechanism is shown in Fig. 4.15 in the bottom. In the bottom left panel, the initial position of the surface as well as the H-atom in the trajectory is shown. On the right, the final positions of the system are shown and the arrow indicates the surface movement along the trajectory. Like before, the impinging H-atom is again shown as a cyan colored sphere and

carbon atoms are shown as gray colored spheres. The red colored circle highlights the area of the surface that will change from a convex-shaped curvature (left picture) to a concave-shaped curvature after the scattering event. The terminology of the shape is used according to the shape of mathematical functions. To better follow the mechanism, a movie showing the same trajectory from different angles of view is offered in the supporting material as well [301].

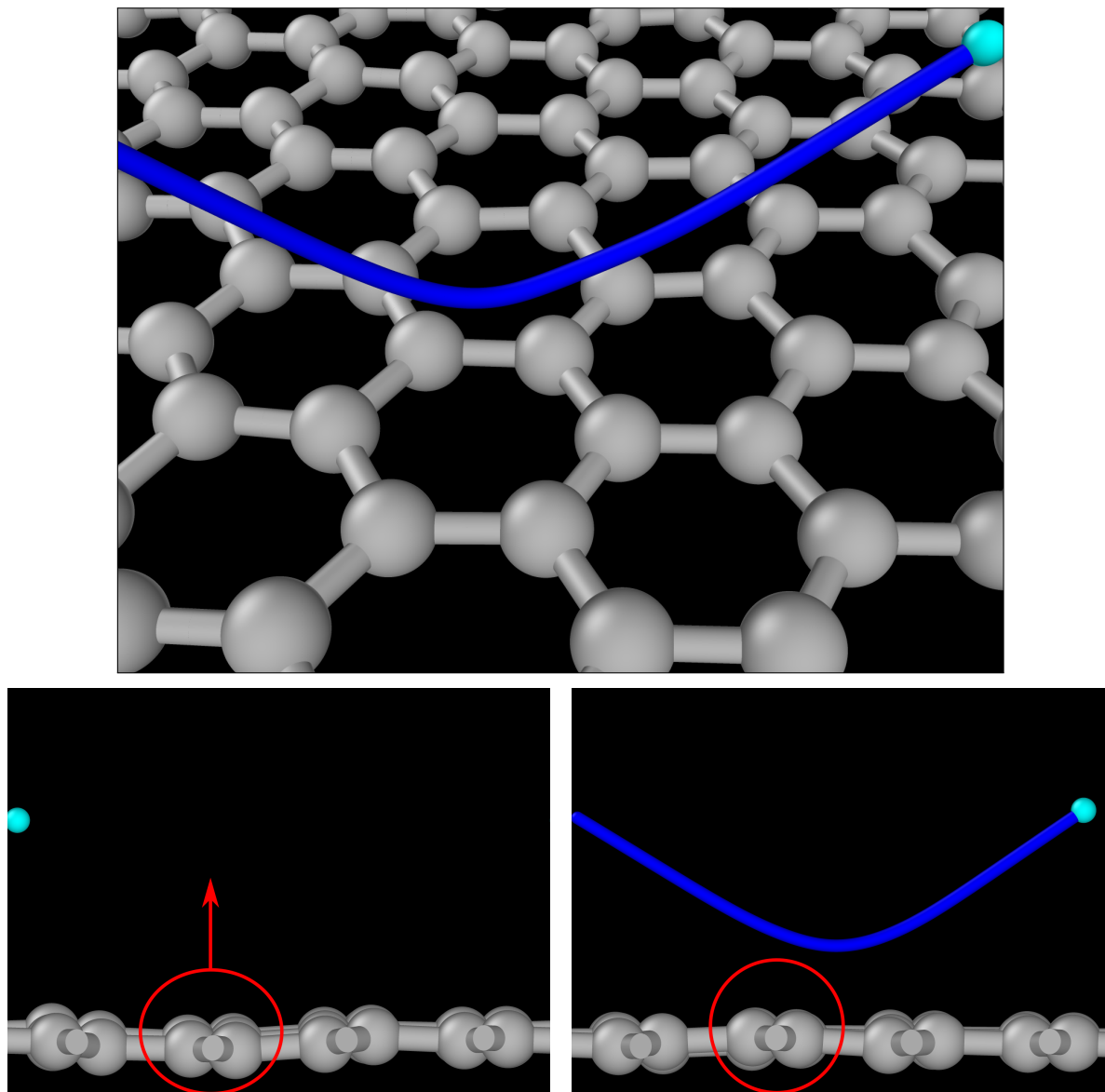


Figure 4.15: Top: Example trajectory showing the fast channel in a "perspective view". Bottom: Mechanism of energy transfer from surface transversal phonons to the impinging atom in an inelastic scattering event. The change of the curvature of the surface from convex to concave during the scattering trajectory is highlighted via the red circle and the arrow indicates the surface movement from the start to the end of the trajectory. The left picture shows the initial and the right picture the final position of the impinging H-atom. The trajectory of the H-atom is shown in dark-blue and the H-atoms final position is shown as a cyan colored sphere. The carbon surface atoms are represented as gray colored spheres and the chemical bonds to adjacent atoms are shown as well.

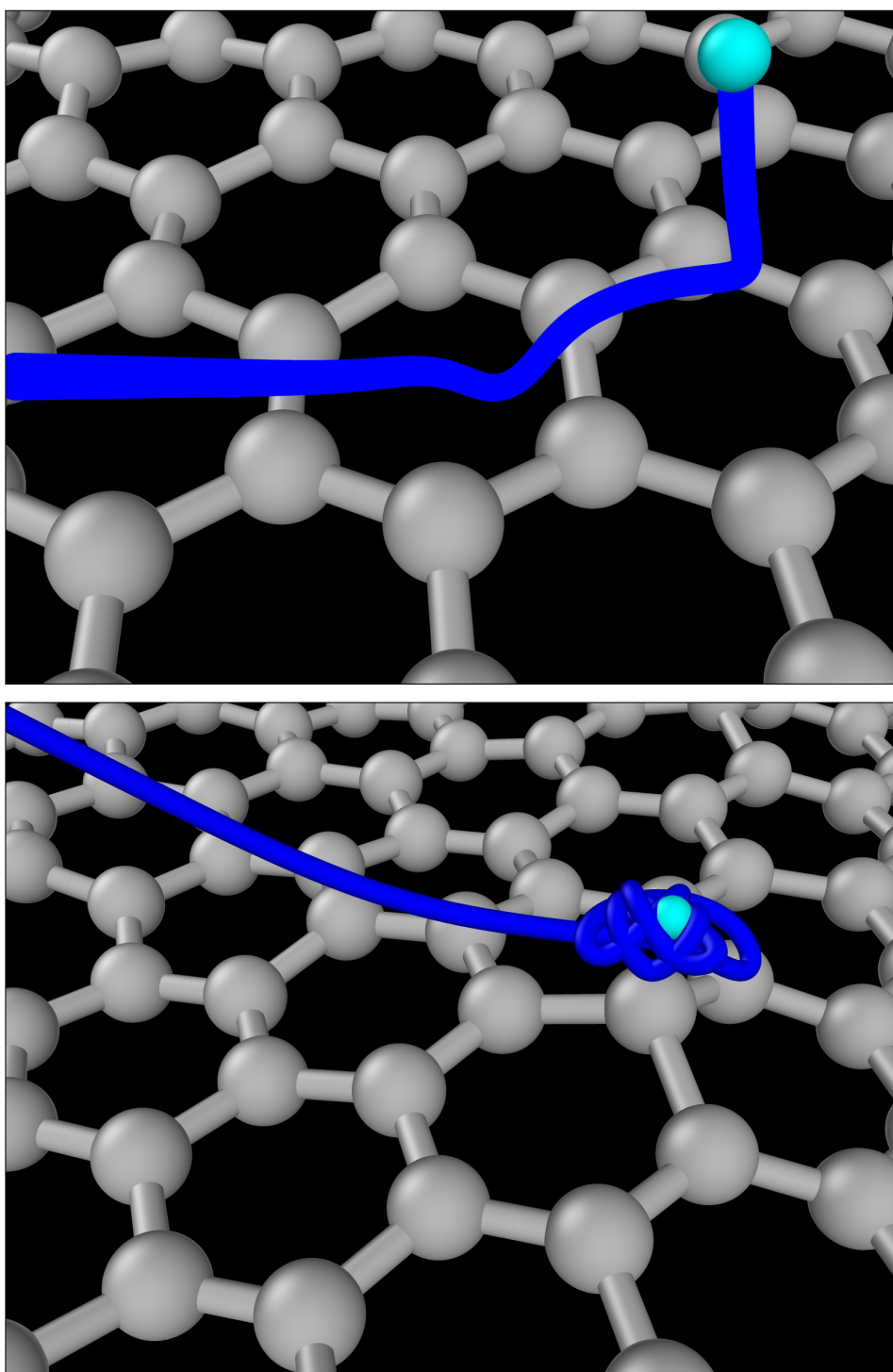


Figure 4.16: Top: Example trajectory showing the slow channel in a "perspective view". Bottom: Example trajectory showing the adsorption in a "perspective view". The trajectory of the H-atom is shown in dark-blue and the H-atoms final position is shown as a cyan colored sphere. The carbon surface atoms are represented as gray colored spheres and the chemical bonds to adjacent atoms are shown as well.

### 4.3.1 Comparison to RAT Experiment

It was reported that H-atom scattering from epitaxial graphene has a strong dependence on the initial conditions [25]. The incidence kinetic energy of the atom interacting with the surface shows a difference in the dynamics depending if the adsorption barrier is crossed or not. From studies before and as mentioned in Sec. 4.1.2, a bimodal feature can be seen in translational energy loss distributions from RAT experiment. The two separated signals are the quasi-elastic and inelastic scattering events, which are referred to as fast and slow channel, as already mentioned. In Fig. 4.17 the two channels as seen in the translational and energy loss distributions are shown. The fast channel is close to the specular angle of the scattering atom whereas the slow channel is shifted to smaller angles and much broader in shape. Visualizations of the different scattering dynamics are offered in the beginning of Sec. 4.3.

It has already been reported and mentioned, that graphene on Pt(111) can be seen as quasi-free standing graphene, which will simplify the comparison. Using a single PES seems to be fine, because the density of states around the Fermi level give no indication, that the scattering has

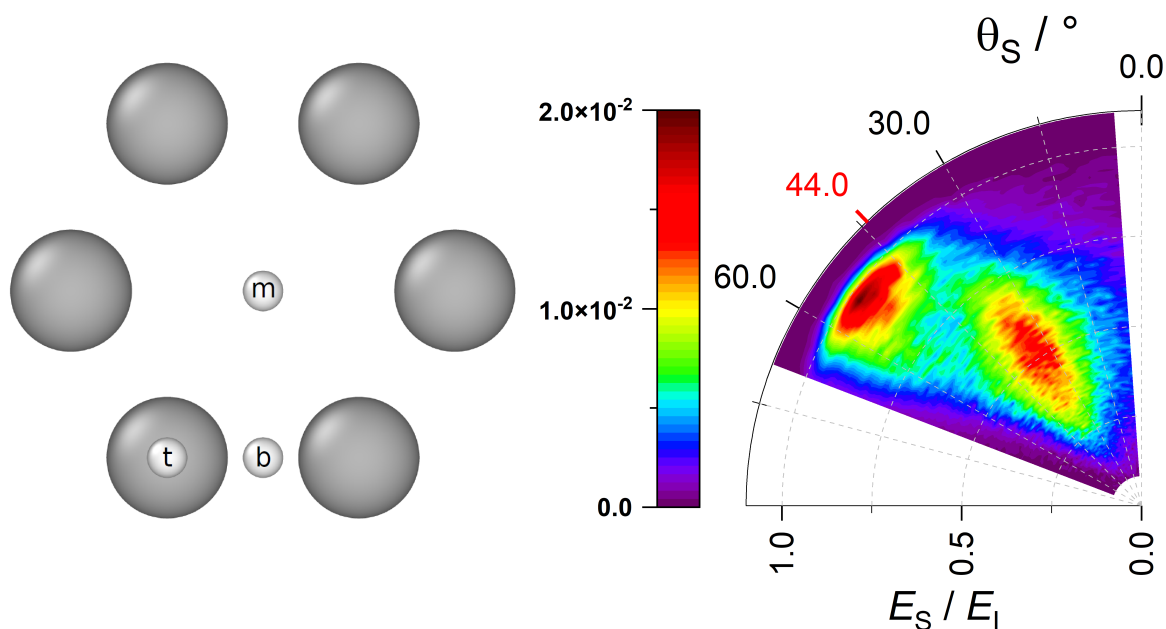


Figure 4.17: Bimodal translational energy loss distribution showing two channels. The fast channel is close to the specular angle (right panel, red label) and because there is only minor energy loss it can be seen as quasi-elastic scattering, where the global physisorption well is involved. Structurally, this corresponds to H-atom scattering close to the mid point (middle of a six-membered C-ring, labeled m). The slow channel is shifted to smaller angles and because of the high energy loss, this corresponds to inelastic scattering. This channel arises from scattering around the top point (labeled t), so where the H-atom hits directly a single C-atom. Here, the chemisorption barrier is involved, indicating a transient C–H bond formation. The transient bond formation also explains the shift to smaller angles, because the corresponding carbon atom changes its hybridization from  $sp^2$  to  $sp^3$ . The structural change is from trigonal planar to tetrahedral, with the H-atom pointing along the surface normal.

to be considered as non-adiabatic. In short, assuming an adiabatic behavior seems valid, which has been mentioned and done before [25].

In order to achieve a one-to-one comparison from theoretical obtained results to experimental data, the parameters from the experimental setup have to be respected. In LEED experiments it can be seen, that graphene is not a single crystal but a composition of equally abundant orientational domains. These two domains of the graphene sheet grown on the Pt(111) substrate are shifted by an angle of  $27^\circ$  with respect to each other and have a rotational distribution with a Gaussian width of  $5^\circ$ . This results in an H-atom velocity vector that is oriented symmetrically with respect to the two domains. In the molecular dynamics simulations, this circumstance is respected by averaging over two different initial azimuthal angles of the impinging atom with respect to a C–C bond. By construction, the azimuthal angle of  $0^\circ$  is along a C–C bond. The two domains are considered by applying an initial azimuthal angle of  $\pm 13.5^\circ$  to the impinging atoms. The two domains have to be treated differently when comparing to the setup of the detector used in the experimental setup. To mimic the detection geometry, only trajectories scattered within  $3^\circ$  of the in-plane direction are considered in the plots showing the distribution of scattering angle and translational energy of H-atom scattering from the graphene surface.

The most common isotope of hydrogen is deuterium, which mass is twice compared to hydrogen. The reason is that the isotope effect of the incidence atom is most pronounced when changing from H- to D-atoms scattering because of the factor two in the mass, which is the highest for the considered isotopes.

In the following sections, the scattering of H-atoms as well as D-atoms depending on the incidence energy, angle and temperature is shown, respectively. Furthermore, the isotope effect of the surface sheet is investigated for both projectiles. For H-atom scattering from graphene depending in the incidence angle, the results have been additionally compared to previous used REBO-EMFT potential. In case of D-atom scattering, also the isotope effect of the projectile will be analyzed as well.

I analyze the dependence on initial conditions in the following way. First, I will compare the measured translational energy and scattering angle distributions from H-atoms scattering from graphene grown on a Pt(111) metal surface to results from classical molecular dynamics (MD) simulations using a HDNN-PES and will also show the improvement compared to the previous used REBO-EMFT PES. Showing only the results from HDNN-PES, the figures are all arranged in the same manner. In each comparison, the distribution measured in experiment is shown in the top left panel. The predicted distributions from MD simulations using a HDNN-PES matching experimental conditions are shown on the top right. Additionally, in the bottom the distribution also taking backward-scattering into account is shown as well. Here, trajectories have been chosen that also match the geometry of the detector from experiment.

For the different dependence, there are also statistics of the scattering dynamics offered in the corresponding tables in the appendix, which will be given explicitly for each initial condition in the corresponding sections.

### **H-atom scattering depending on the incidence polar angle**

This section is organized as following: First, the polar angle incidence of the scattering atom is compared to the previous reported REBO-PES as well as experimentally measured energy loss and scattering angle distributions for three different angles. The angles have been selected where only the fast channel ( $\theta_S = 59.5^\circ$ ), only the slow channel ( $\theta_S = 40^\circ$ ) and where both channels are present ( $\theta_S = 50^\circ$ ). Note, no angular shift is applied to the results from REBO-PES to highlight the improvements of the theoretical description when changing the PES. After that I will scan the incidence angle and by that the normal energy of the impinging H-atom. Experimental findings will be compared to the HDNN-PES and it will be estimated, how good

experiment can be reproduced for different incidence angles.

The parameters used in the simulations to describe the scattering are defined in Fig. 4.8, an overview of the analysis is shown in Fig. 4.14 and the definition of the channels is given in Fig. 4.17, respectively.

Although the processes and dynamics involved in the scattering have already been determined as shown in Sec. 4.1.2, the prediction of the correct branching for the same incidence conditions when comparing to experiment could not be achieved by using the previous mentioned REBO-EMFT PES. By changing the incidence conditions and compare them to experimental findings, I want to make a statement, if the newly developed HDNN-PES can describe the correct branching and if reproduction of energy loss distributions estimated in experiment is improved.

**Comparison to REBO-PES** Previous to this work and as mentioned in Sec. 4.2, a full-dimensional PES was reported [25] using first principles energies obtained from Embedded Mean-Field Theory (EMFT) [285–287] to parameterize a second generation Reactive Empirical Bond Order (REBO) potential [288–290]. The procedure to generate such PES is reported in detail in the SI of [25] and in [192].

The translational energy and scattering angle distribution for H-atom scattering with  $E_S = 0.99$  eV could be well reproduced by the REBO-PES. The scattering for H-atom with  $E_S = 1.92$  eV could only reproduce the bimodal feature by applying an offset to the angles, which has been reported in [25].

Here, only three incidence conditions are compared, where one can see either the fast or the slow channel alone, and one condition in between to get a major overview of the scattering process.

The statistics of experiment for H-atom scattering from graphene and results from MD simulations using a HDNN-PES as well as an REBO-EMFT PES are given in Tab. A.6. The number of simulated trajectories, scattered trajectories within detection limit compared to experimental setup, the incidence angle as well as kinetic energy, its normal component and sticking coefficients are given. The normal component of the incidence kinetic energy is given as well, because the transient C–H bond is efficiently formed with normal kinetic energy, which is discussed in detail in Sec. 4.1.2. The scaling factors for the drop of flux is given as well for experiment and both theories. This is done to use the same color code in the shown distributions in experiment.

In Fig. 4.18 the comparison between experiment and theory is shown. The flux measured in experiment of the H-atom scattering from epitaxial graphene on Pt(111) is shown in panels A–C. The red numbers indicate the specular angle of the scattering H-atom. The signal is normalized to the integrated area. The incidence kinetic energy is  $E_S = 1.92$  eV for all conditions at the surface temperature is  $T = 300$  K, which is shown in the gray boxes. In panels D–F, the distribution from HDNN-PES are shown and results from the REBO-EMFT function can be seen in panels G–I. With the developed HDNN-PES, the correct branching of the two channels is reproduced for the exact same incidence conditions comparing to experiment. In case the REBO-EMFT, as mentioned, only by applying the shift in incidence polar angles of the projectile, the branching of the two channels match experimental conditions. This can be seen, when panels B and I are compared.

Compared to the previous used REBO-EMFT function, the branching can now be reproduced for the same initial conditions and the trend of the flux as seen in experiment can be reproduced well. Thus, there is a better agreement with experiment when using a HDNN-PES compared to the REBO-EMFT PES.

From these comparisons and analysis, it can be concluded that the HDNN-PES is able to correctly predict the change of ratio as seen in the experiment of the fast and slow channel. The newly developed PES is able to predict the correct branching and thus is in much better



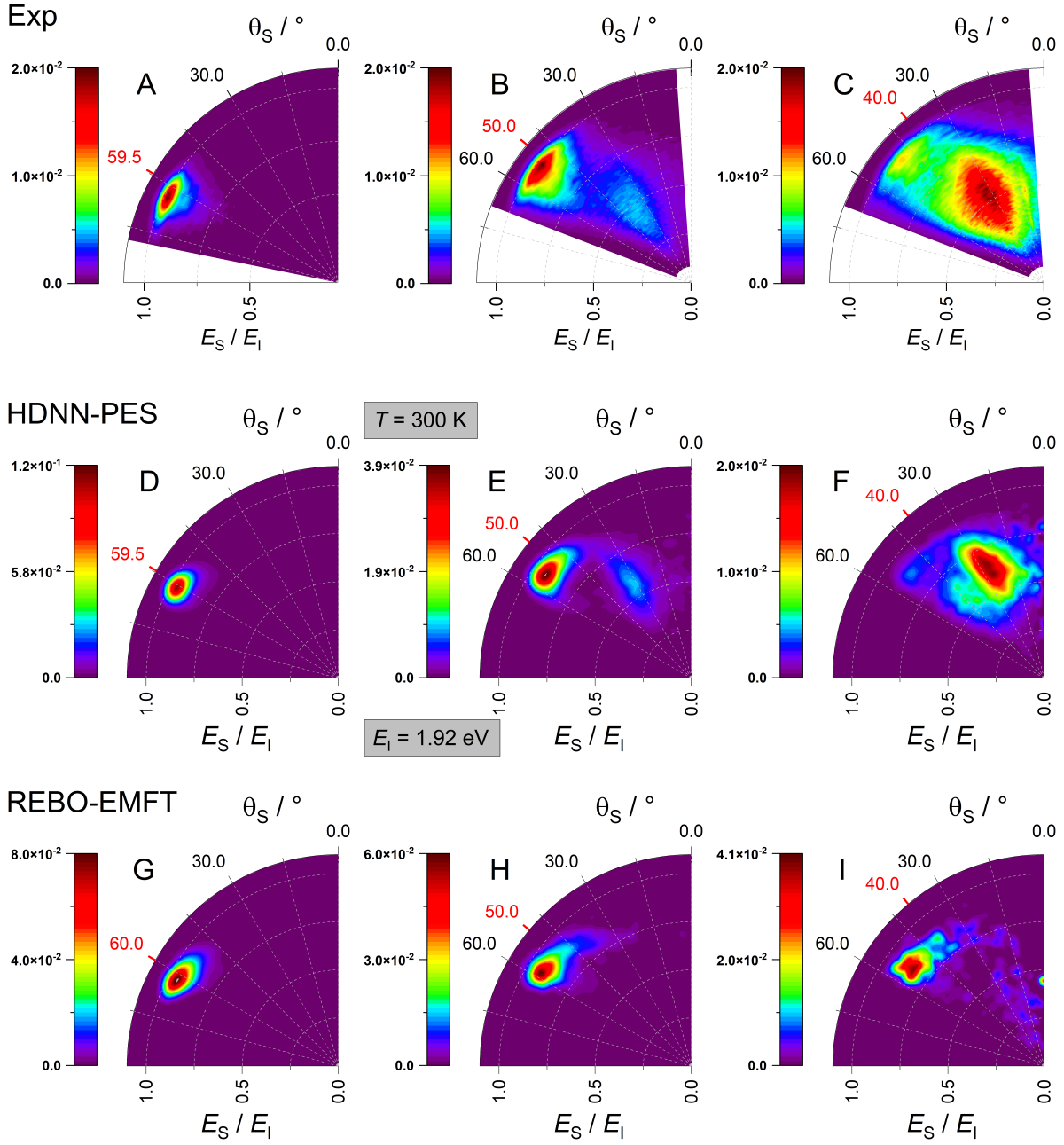


Figure 4.18: Comparing theory with experiment for H-atom scattering from graphene at given incidence kinetic energy  $E_I$  and surface temperature  $T$ . The fraction of the kinetic energy of the projectile before ( $E_I$ ) and after its hit with the surface ( $E_S$ ) is shown. Experimental distribution are shown in panels A–C next to theoretical results. Panels D–F show the results from MD simulations using HDNN-PES, whereas panels G–I show the results from MD simulations utilizing the REBO-EMFT PES [25]. The red labeled ticks indicate the incidence and specular scattering angles. The distribution is normalized to the integrated area. Statistics and further analysis of trajectories are given in Tab. A.6. The presented distributions here and in the following sections are generated using OriginPro version 2022 [309].

agreement with experimental results compared to the previous used REBO-EMFT function.

In the following, the translational energy and scattering angle distributions are shown for different incidence polar angles from experiment are compared to results from MD simulations using the HDNN-PES.

The incidence polar angle, the incidence kinetic energy and its normal component for H-atom scattering from graphene on Pt(111) in the RAT experiment are given in Tab. A.7. The scaling factors for the drop of flux is given as well to use the same color code in the shown distributions.

The statistics of H-atom scattering from free-standing graphene from MD simulations using a HDNN-PES are given in Tab. A.8. The number of simulated trajectories, scattered trajectories within detection limit compared to experimental setup, trajectories also considering backward scattering, the incidence angle as well as kinetic energy, its normal component and sticking coefficients are given. The normal component of the incidence kinetic energy is given as well, because the transient C–H bond is efficiently formed with normal kinetic energy. The scaling factors for the drop of flux is given as well, normalized to the smallest incidence angle for H-atom scattering.

Fig. 4.19 – 4.28 show the translational energy loss distribution of H-atom scattering from a free-standing graphene sheet with  $\theta_I$  ranging from  $30^\circ$  to  $59.5^\circ$ . Simulations have been carried out for more incidence angles and the results obtained are shown in Tab. A.8.

The observed scattering flux decreases rapidly as the incidence angle approaches the surface normal. The scaling factors from experiment and HDNN-PES are given in the respective tables, as mentioned before. The flux is decreasing, because at higher normal kinetic energy of H- and D-atoms, the passage over the barrier to chemisorption is promoted. Thus, a higher sticking probability is observed at smaller incidence polar angles. In experiment, only scattered atoms can be observed that are within a plane defined by the direction of the atomic beam and the normal to the surface. Changing the incidence angle affects the fraction of atoms scattered within that plane. The drop in flux due to the decrease of the incidence angle is respected in the plots. This is quantitatively indicated by the multiplying factors given in the corresponding tables.

In Fig. 4.19 only the slow channel is present but close to the specular angle. Here, the normal kinetic energy with, which is calculated via  $E_I \cos^2 \theta_I$ , is  $E_N = 1.44$  eV. In the simulations, the closest approach to the surface atoms can be followed. If the projectile comes closer than  $1.4$  Å, it has overcome the barrier to adsorption. This is a structural fingerprint to determine, if a projectile crossed the barrier, which is discussed in detail in Sec. 4.1.2. At this incidence angle, more than 99% of all in-plane trajectories were scattered after crossing the barrier. This means, their normal kinetic energy was enough to cross the barrier to adsorption, they scattered at a single carbon atom and managed to cross the barrier again, to re-emerge into the gas-phase. Simultaneously, this explains the small sticking coefficient of  $\approx 4\%$ .

When considering forward and backward scattering as shown in the bottom panel in Fig. 4.19, minor signal intensities can be seen for backward scattering.

In Fig. 4.20 the distribution is shown for H-atoms with  $\theta_I = 38^\circ$ . In the distribution from experiment a minor intensity of the fast channel can be seen, which is only marginally present in the distributions from simulations. Starting from this incidence angle, the fast channel is present and its intensity compared to the slow channel is rising. Although the ratio of intensities found in simulations does not exactly reproduce the ones in the experiment, at least the trend can be reproduced when going to higher incidence polar angles. By applying a small shift in the incidence polar angle, the experiment can be reproduced better. This can be seen, if we compare the distribution of HDNN-PES from Fig. 4.23 with the experimental one shown in Fig. 4.21.

Compared to  $\theta_I = 30^\circ$ , at  $\theta_I = 38^\circ$  (Fig. 4.20), the intensities for back-scattering events are more pronounced. This trend follows up to  $\theta_I = 46^\circ$ , where the signal intensities reach a

maximum. For bigger incidence angles, the signal intensities drastically drops and at  $\theta_I = 54^\circ$ , no significant signal intensities for backward scattering can be seen and even the slow channel is only marginally present. At  $\theta_I = 59.5^\circ$ , neither the slow channel nor backward scattering is observable anymore. This and studies from following the dynamics of the H-atom scattering with this incidence conditions indicate that inelastic scattering is involved in the mechanism for backward scattering events.

For all shown distributions in this chapter it is very important to mention that for those conditions, where a smaller number of trajectories is used, the statistics are maybe not enough for a direct comparison to experiment and this might explain, why there is a larger discrepancy. This is especially the case for those conditions, when only 100,000 trajectories are used and only a fraction contributes to the shown plots. For the angles of  $\approx 40^\circ$ ,  $\approx 50^\circ$  and  $\approx 60^\circ$ , a tenfold number is used to improve the statistics. In these cases, the bimodal feature and with that the correct branching of the fast and the slow channel is better reproduced, but not exactly. For smaller incidence angles it seems applying an angular shift of at least  $2^\circ$  better match the branching seen in experiment. This is analog to the previous reported REBO-EMFT PES, but less pronounced.

In Fig. 4.29 and 4.30, the energy loss distributions for the different incidence polar angles are shown and compared to experiment. Like discussed before, for H-atom scattering with smaller incidence polar angle and therefore with higher normal kinetic energy there is an increased mismatch between experiment and theory. In Sec. 4.2, the barrier height in the PES used has already been discussed. Higher incidence energy make crossing the barrier more likely. Especially at smaller incidence angles, the comparison of theoretical and experimentally obtained energy loss distributions shows significant differences of the average energy loss and shape of the distribution. And from the two dimensional translational energy and angular distributions it was mentioned, that applying an angular shift improves reproduction of experimentally found ratios of the fast and slow channel. With the indication, that the barrier height seem to be underestimated, this explains the trend of the shown distributions and the larger mismatches for smaller incidence angles.

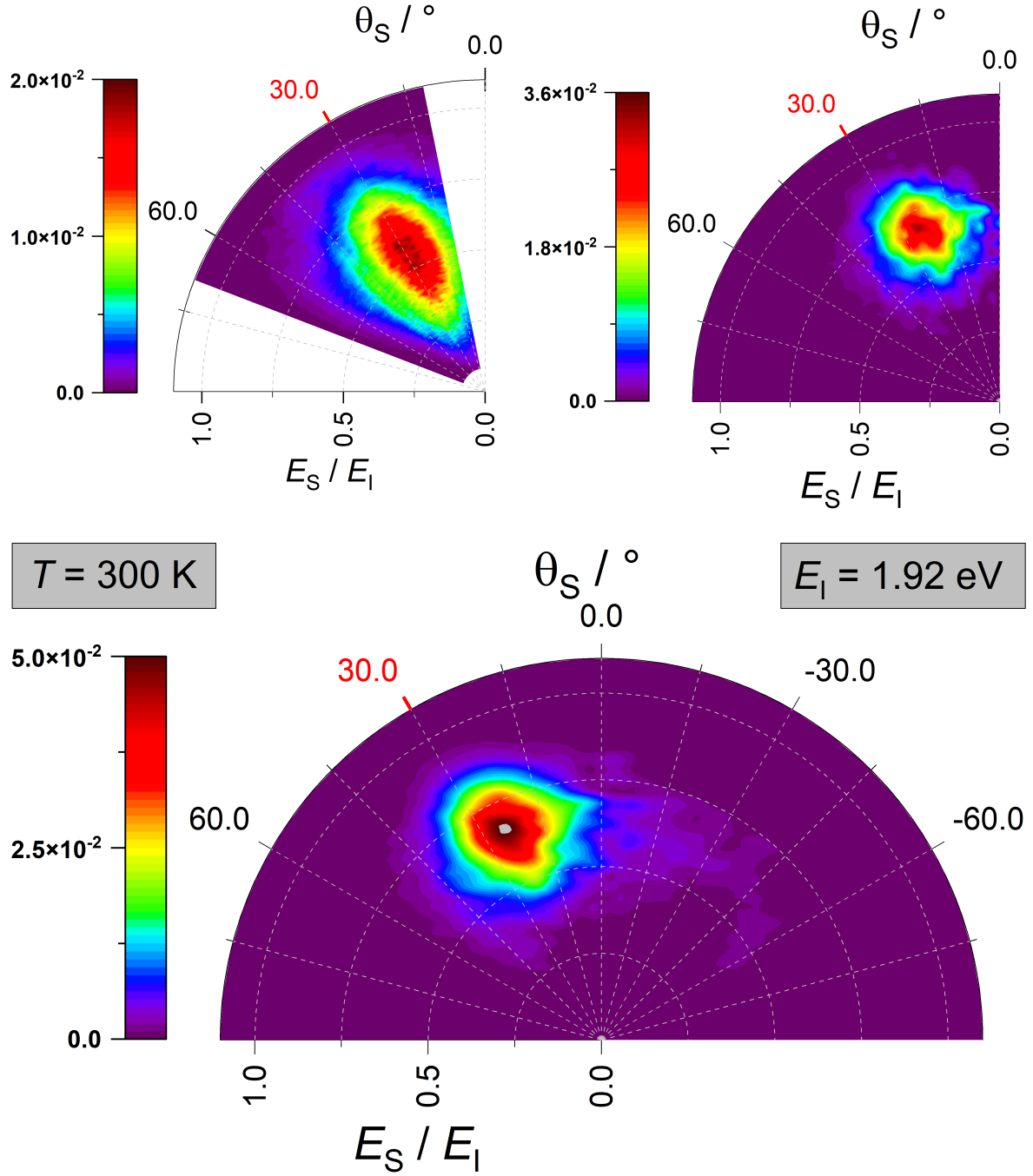


Figure 4.19: Comparing translational energy and scattering angle distribution from experiment (top left) with classical simulations using the HDNN-PES (top right) for H-scattering from graphene. The bottom panel also shows backward-scattering. The incidence kinetic energy  $E_I$  and surface temperature  $T$  are given in gray boxes. The incidence as well as specular polar angle  $\theta_I$  is shown in red. Statistics and further analysis of trajectories are given in Tab. A.7 and A.8.

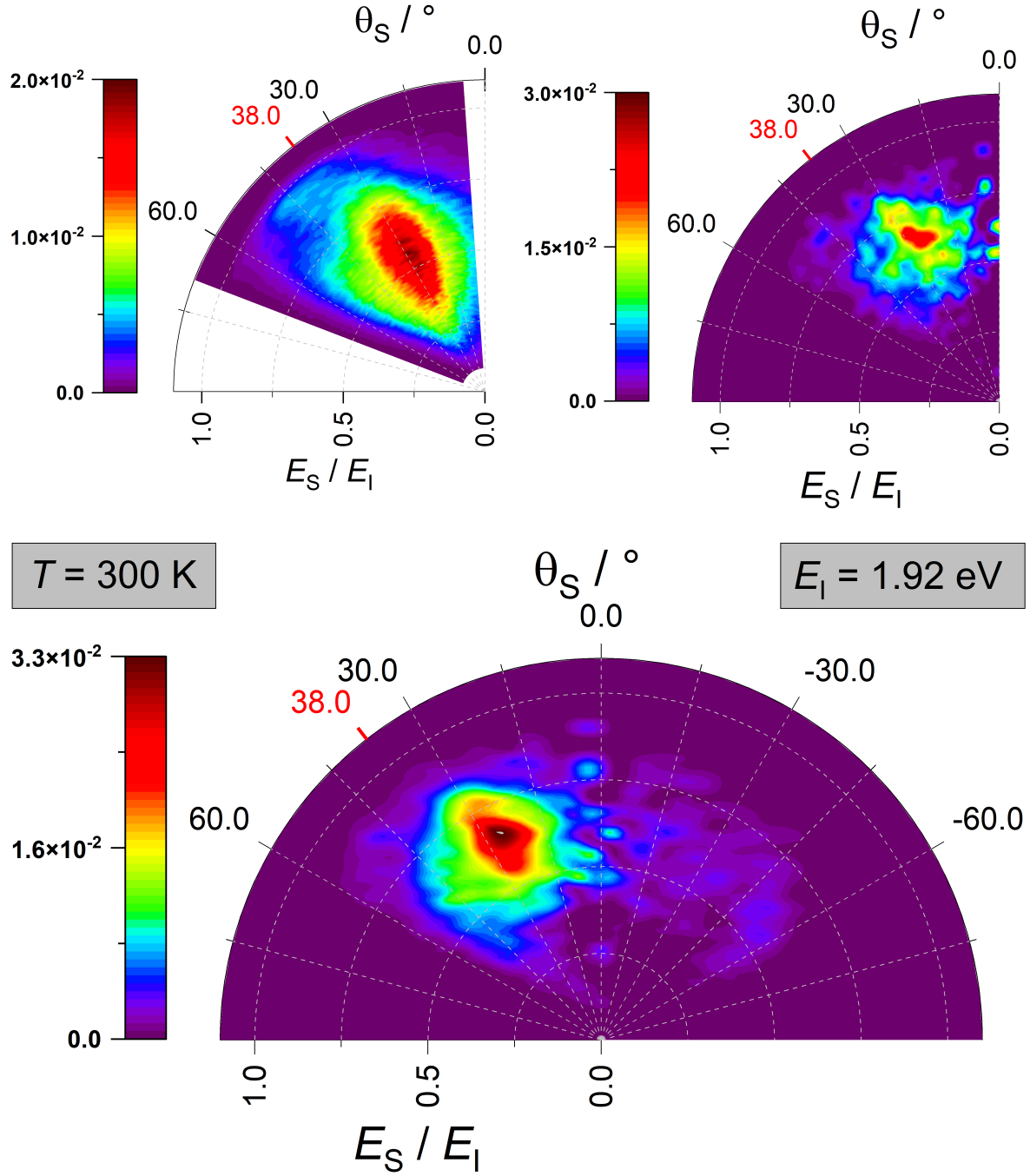


Figure 4.20: Comparing translational energy and scattering angle distribution from experiment (top left) with classical simulations using the HDNN-PES (top right) for H-scattering from graphene. The bottom panel also shows backward-scattering. The incidence kinetic energy  $E_I$  and surface temperature  $T$  are given in gray boxes. The incidence as well as specular polar angle  $\theta_I$  is shown in red. Statistics and further analysis of trajectories are given in Tab. A.7 and A.8.

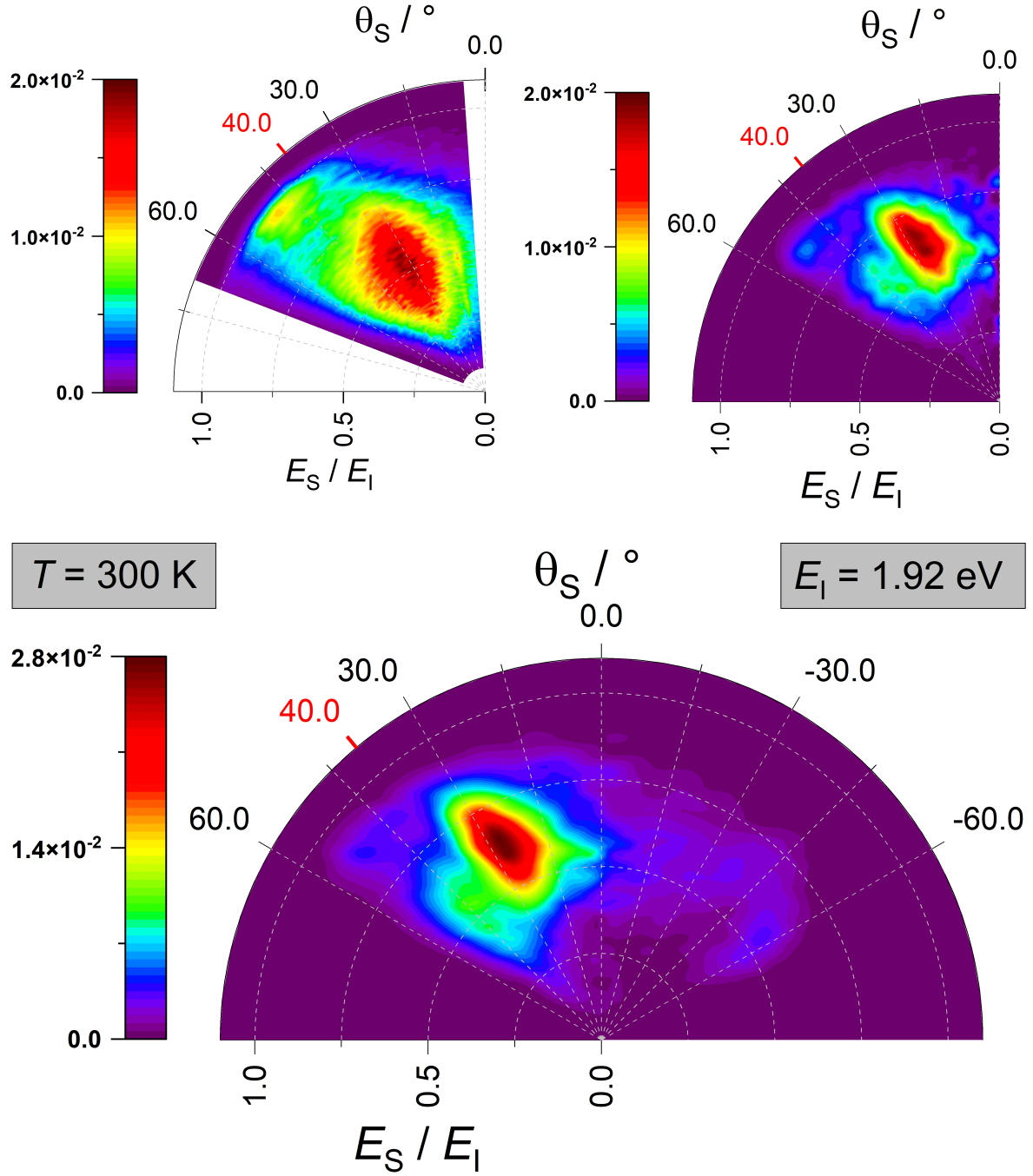


Figure 4.21: Comparing translational energy and scattering angle distribution from experiment (top left) with classical simulations using the HDNN-PES (top right) for H-scattering from graphene. The bottom panel also shows backward-scattering. The incidence kinetic energy  $E_I$  and surface temperature  $T$  are given in gray boxes. The incidence as well as specular polar angle  $\theta_I$  is shown in red. Statistics and further analysis of trajectories are given in Tab. A.7 and A.8.

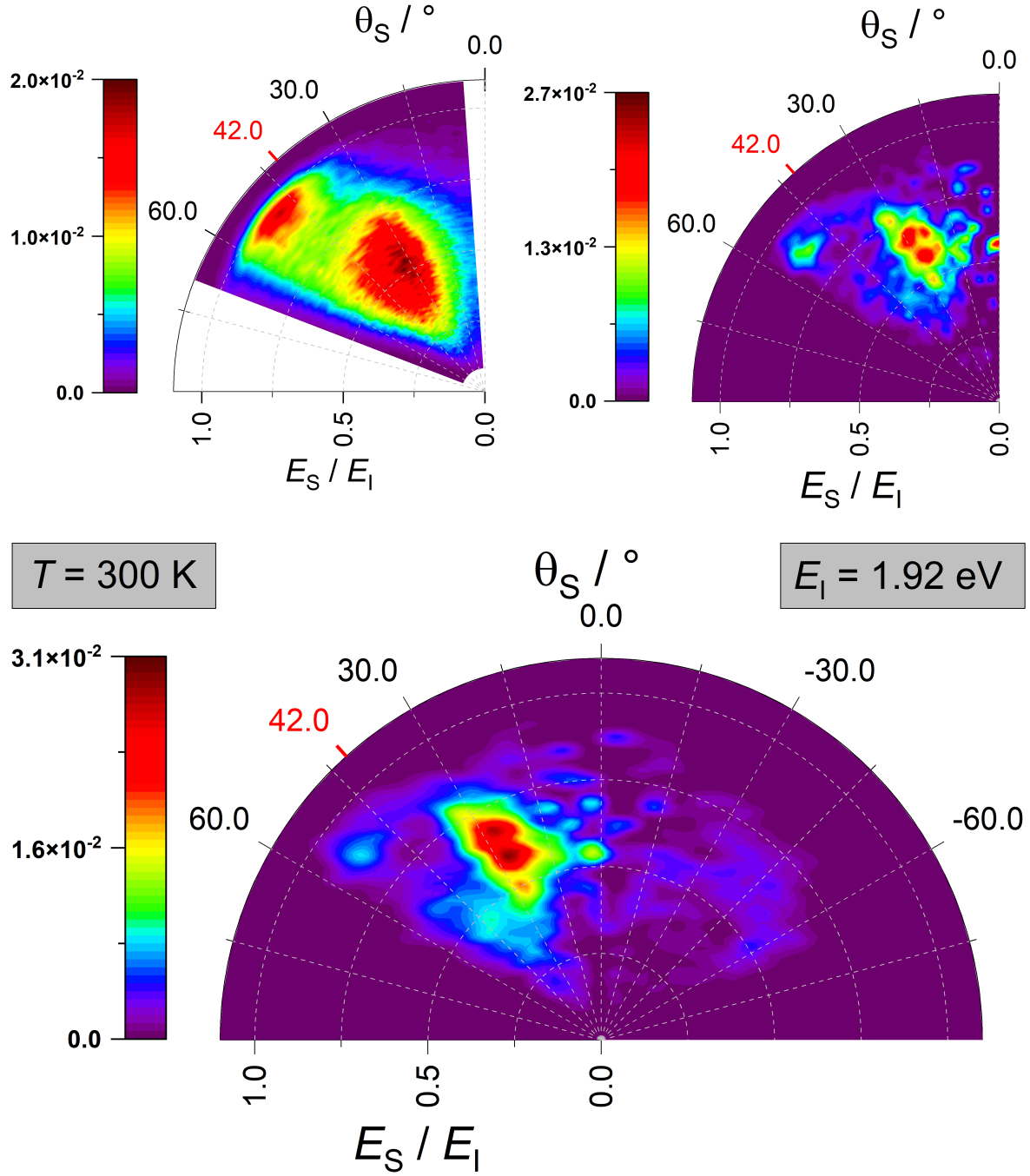


Figure 4.22: Comparing translational energy and scattering angle distribution from experiment (top left) with classical simulations using the HDNN-PES (top right) for H-scattering from graphene. The bottom panel also shows backward-scattering. The incidence kinetic energy  $E_I$  and surface temperature  $T$  are given in gray boxes. The incidence as well as specular polar angle  $\theta_I$  is shown in red. Statistics and further analysis of trajectories are given in Tab. A.7 and A.8.

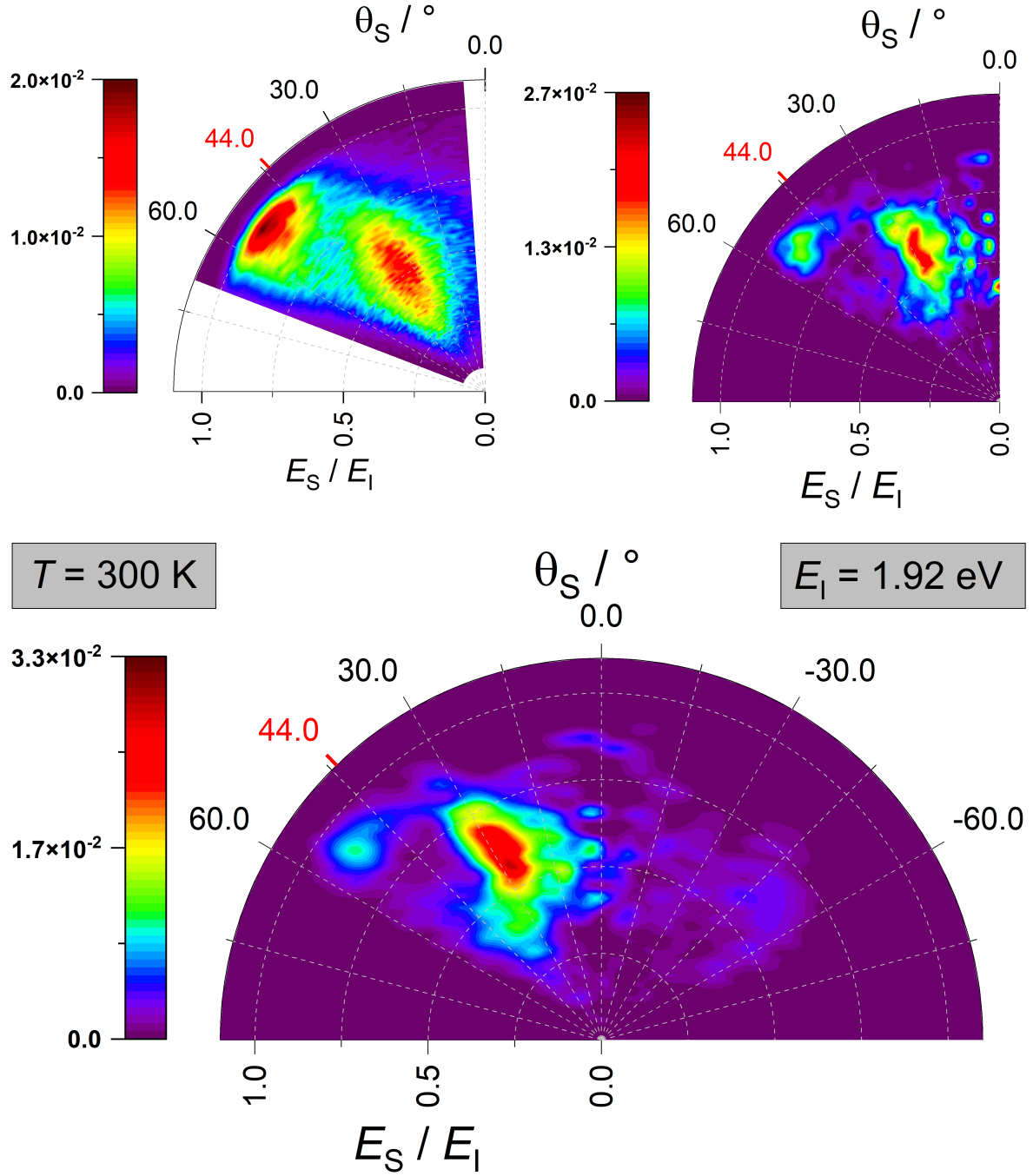


Figure 4.23: Comparing translational energy and scattering angle distribution from experiment (top left) with classical simulations using the HDNN-PES (top right) for H-scattering from graphene. The bottom panel also shows backward-scattering. The incidence kinetic energy  $E_I$  and surface temperature  $T$  are given in gray boxes. The incidence as well as specular polar angle  $\theta_I$  is shown in red. Statistics and further analysis of trajectories are given in Tab. A.7 and A.8.



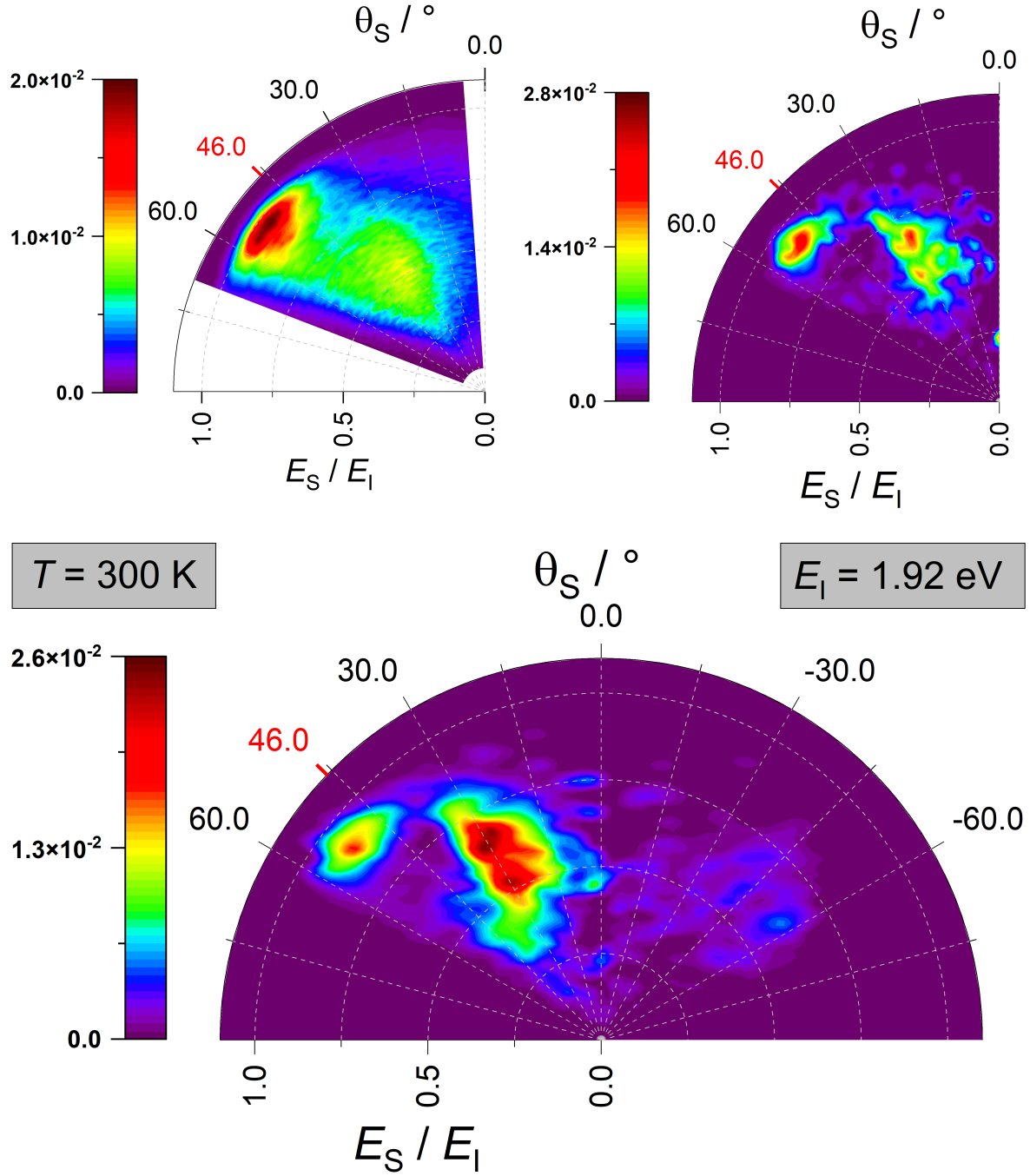


Figure 4.24: Comparing translational energy and scattering angle distribution from experiment (top left) with classical simulations using the HDNN-PES (top right) for H-scattering from graphene. The bottom panel also shows backward-scattering. The incidence kinetic energy  $E_I$  and surface temperature  $T$  are given in gray boxes. The incidence as well as specular polar angle  $\theta_I$  is shown in red. Statistics and further analysis of trajectories are given in Tab. A.7 and A.8.

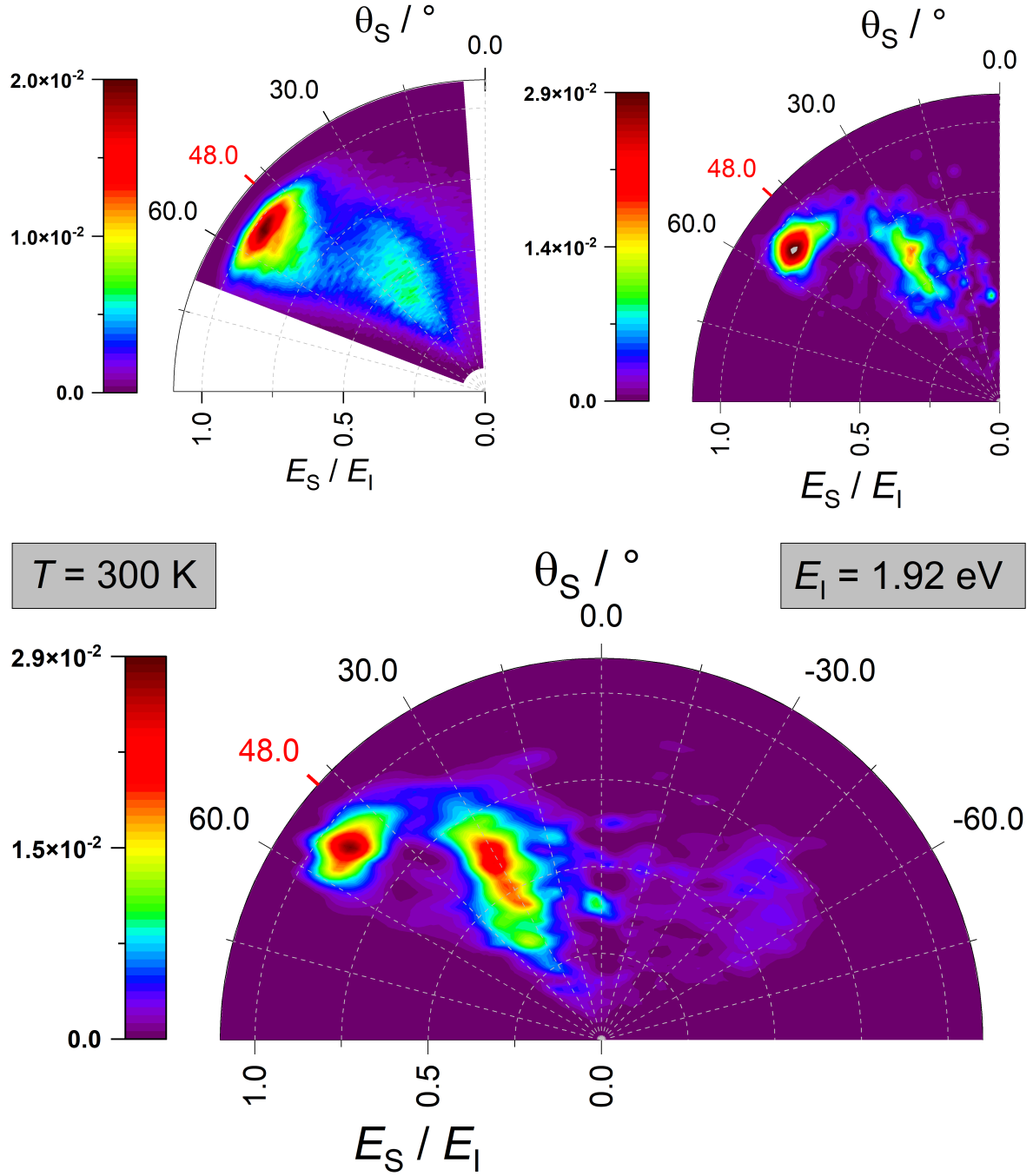


Figure 4.25: Comparing translational energy and scattering angle distribution from experiment (top left) with classical simulations using the HDNN-PES (top right) for H-scattering from graphene. The bottom panel also shows backward-scattering. The incidence kinetic energy  $E_I$  and surface temperature  $T$  are given in gray boxes. The incidence as well as specular polar angle  $\theta_I$  is shown in red. Statistics and further analysis of trajectories are given in Tab. A.7 and A.8.

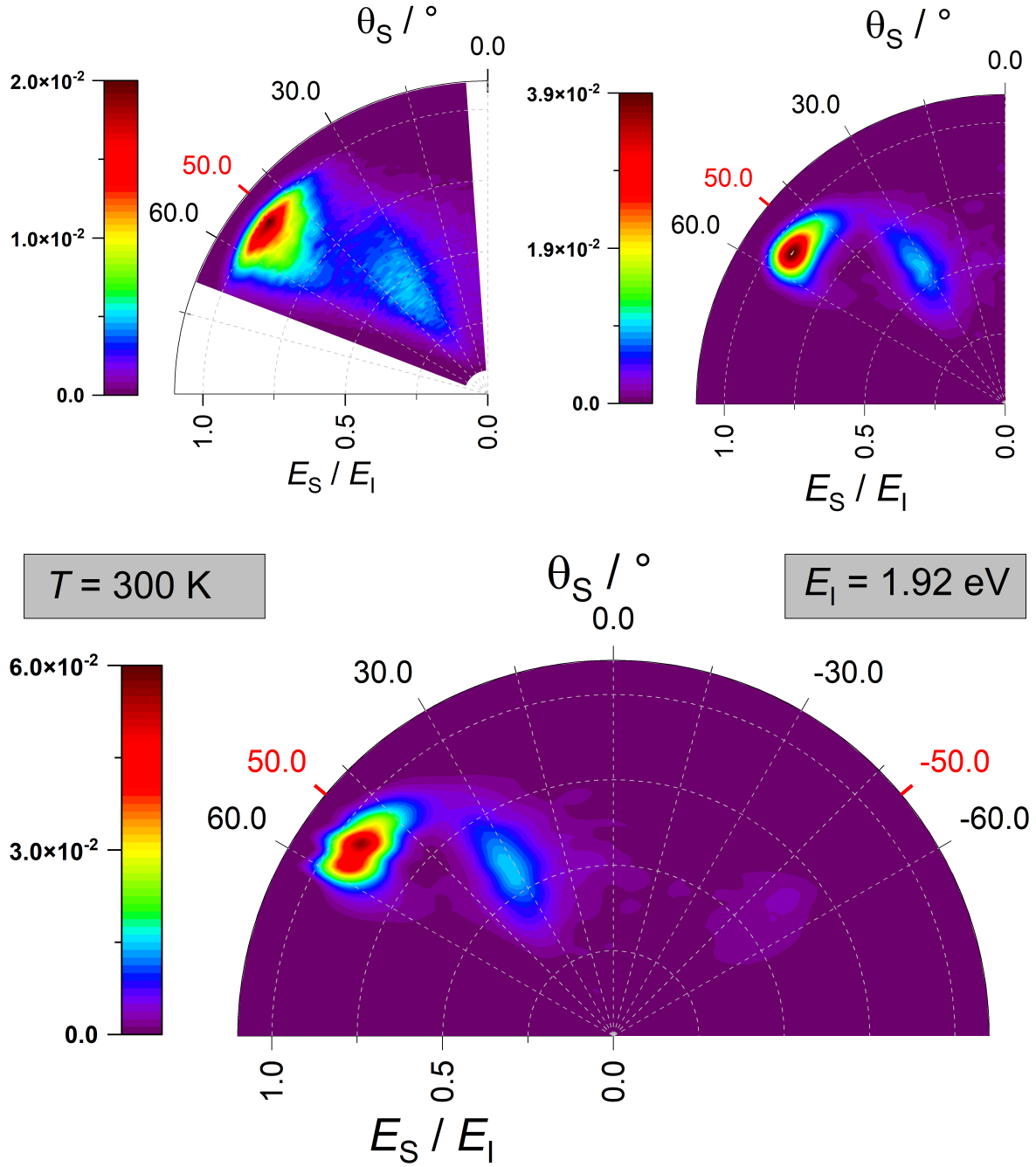


Figure 4.26: Comparing translational energy and scattering angle distribution from experiment (top left) with classical simulations using the HDNN-PES (top right) for H-scattering from graphene. The bottom panel also shows backward-scattering. The incidence kinetic energy  $E_I$  and surface temperature  $T$  are given in gray boxes. The incidence as well as specular polar angle  $\theta_I$  is shown in red. Statistics and further analysis of trajectories are given in Tab. A.7 and A.8.

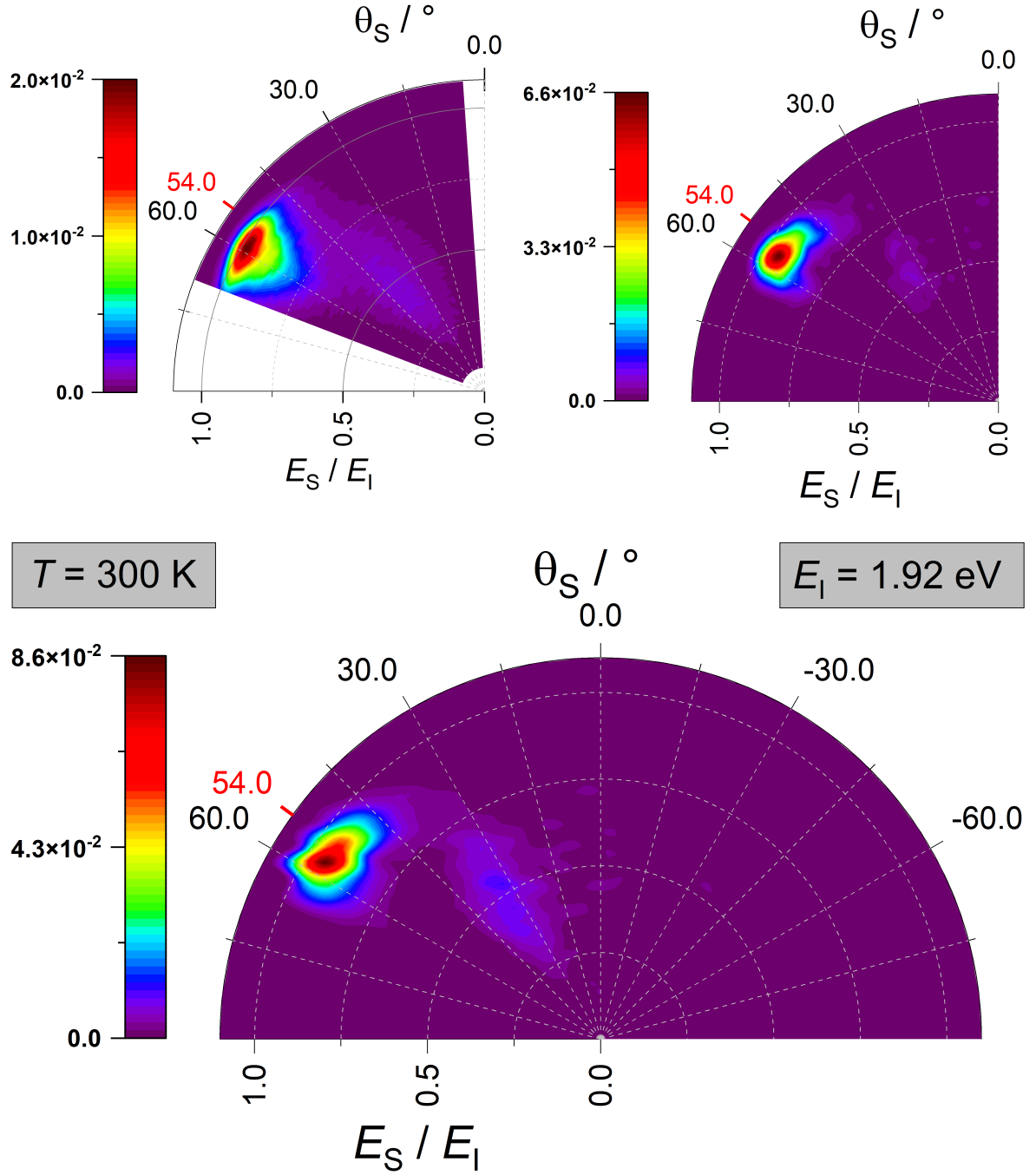


Figure 4.27: Comparing translational energy and scattering angle distribution from experiment (top left) with classical simulations using the HDNN-PES (top right) for H-scattering from graphene. The bottom panel also shows backward-scattering. The incidence kinetic energy  $E_I$  and surface temperature  $T$  are given in gray boxes. The incidence as well as specular polar angle  $\theta_I$  is shown in red. Statistics and further analysis of trajectories are given in Tab. A.7 and A.8.

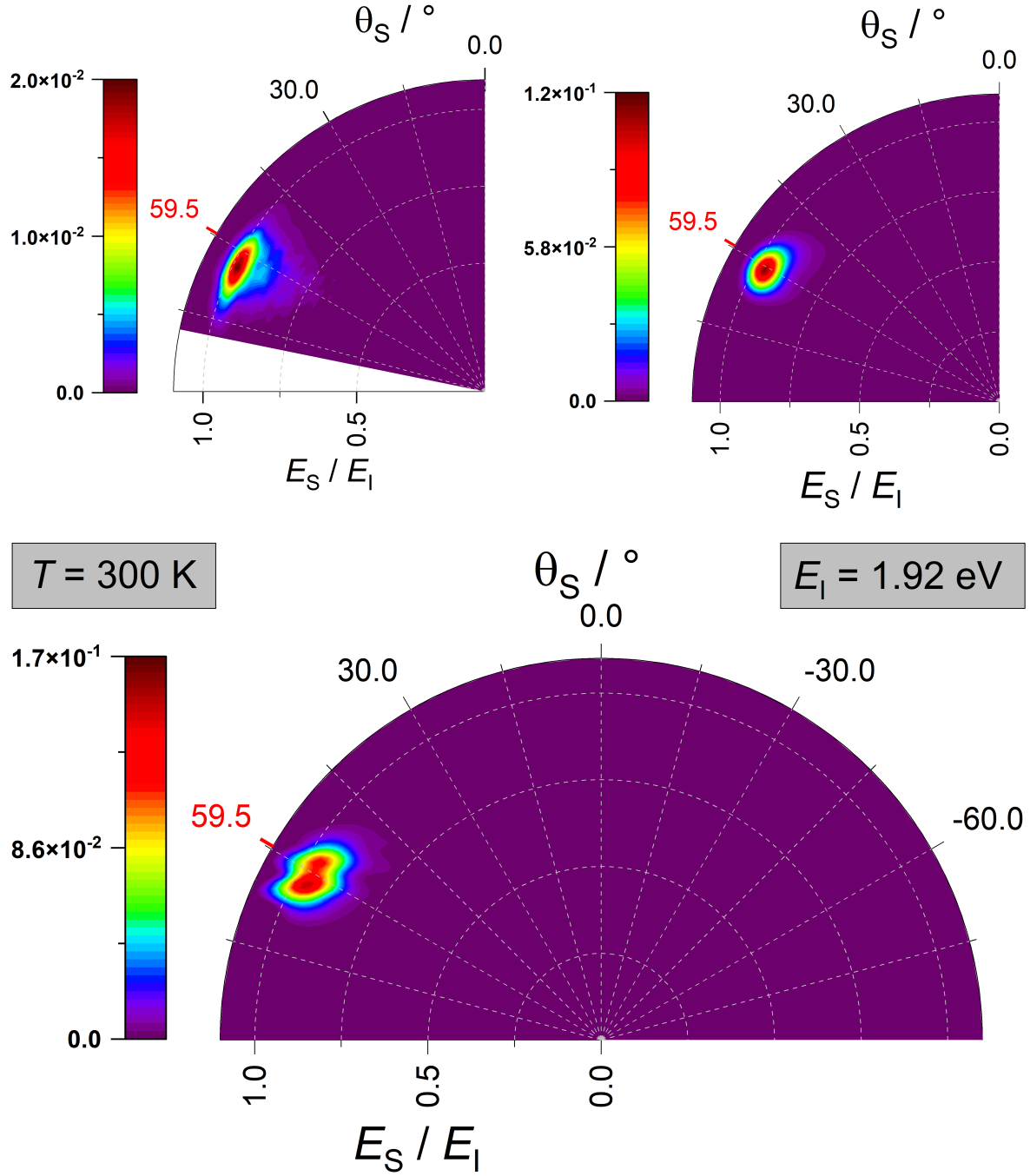


Figure 4.28: Comparing translational energy and scattering angle distribution from experiment (top left) with classical simulations using the HDNN-PES (top right) for H-scattering from graphene. The bottom panel also shows backward-scattering. The incidence kinetic energy  $E_I$  and surface temperature  $T$  are given in gray boxes. The incidence as well as specular polar angle  $\theta_I$  is shown in red. Statistics and further analysis of trajectories are given in Tab. A.7 and A.8.

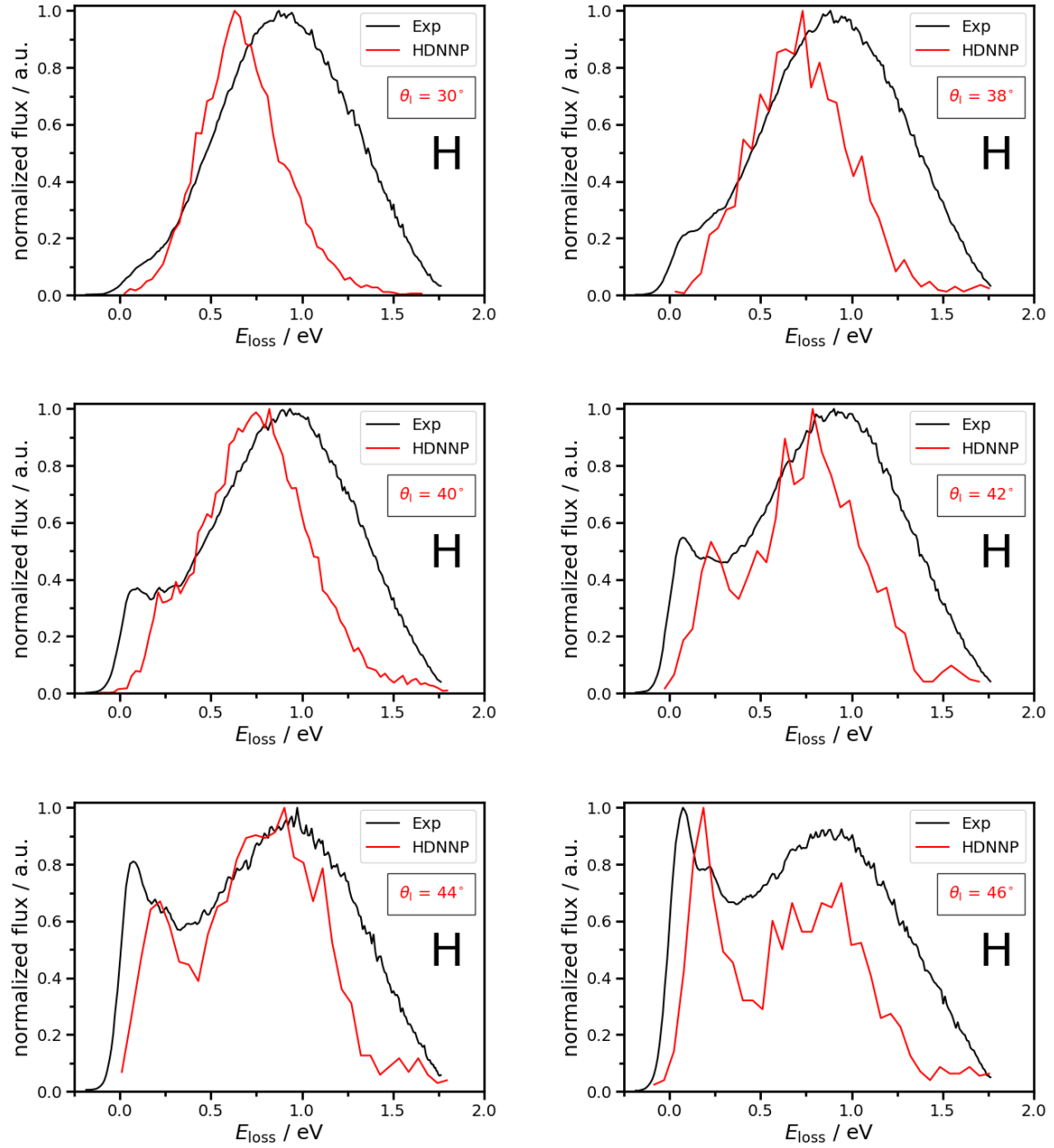


Figure 4.29: The same as Fig. 4.30, but the incidence angles are different. Energy loss distributions from the experiment shown in black and from HDNN-PES shown in red. The red number in the boxes indicate the incidence and specular angle of the D-atom. Other than in the translational energy and angular distributions, the flux is normalized to the maximum value. The incidence energy  $E_1 = 1.92$  eV and the surface temperature  $T = 300$  K are given as well.

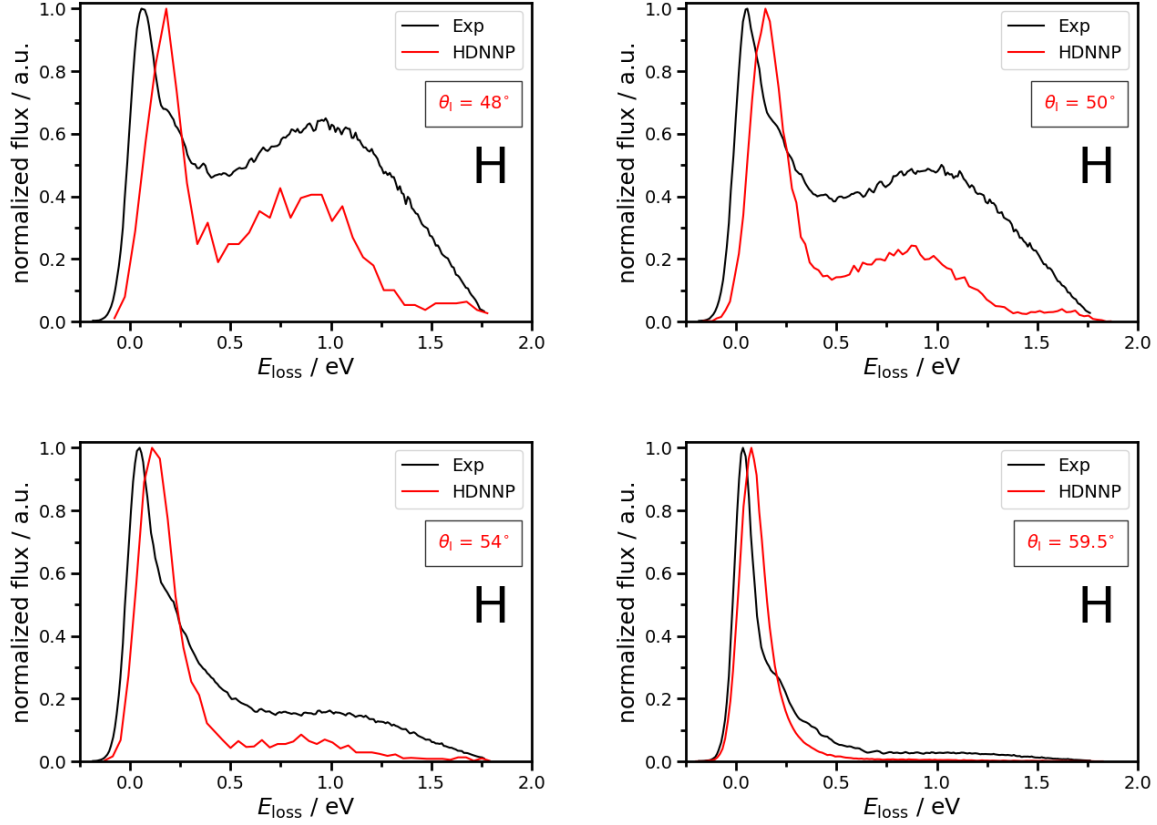


Figure 4.30: The same as Fig. 4.29, but the incidence angles are different. Energy loss distributions from the experiment shown in black and from HDNN-PES shown in red. The red number in the boxes indicate the incidence and specular angle of the D-atom. Other than in the translational energy and angular distributions, the flux is normalized to the maximum value. The incidence energy  $E_I = 1.92$  eV and the surface temperature  $T = 300$  K are given as well

### H-atom scattering depending on the incidence kinetic energy

In this section, the H-atom scattering from a graphene surface depending on the incidence kinetic energy is analyzed. In order to analyze the energy dependence of the scattering of H-atoms from a free-standing graphene sheet, the incidence angle of the impinging particle is kept fixed and the atom was launched with an initial kinetic energy  $E_I$  of 0.99 eV, 1.92 eV, 2.18 eV, 2.62 eV and 3.31 eV, respectively. The incidence polar angle of the scattered atom is kept fixed at  $\theta_I = 50^\circ$  and the surface temperature is  $T = 300$  K for all different incidence energies. Here, the projectile was launched 6.0 Å above the surface.

The parameters used in the simulations to describe the scattering are defined in Fig. 4.8, an overview of the analysis is shown in Fig. 4.14 and the definition of the channels is given in Fig. 4.17, respectively.

The incidence polar angle, the incidence kinetic energy and its normal component for H-atom scattering from graphene on Pt(111) in the RAT experiment are given in Tab. A.11.

The statistics of H-atom scattering from free-standing graphene from MD simulations using a HDNN-PES are given in Tab. A.12. The number of simulated trajectories, scattered trajectories within detection limit compared to experimental setup, trajectories also considering backward scattering, the incidence angle as well as kinetic energy, its normal component and sticking coefficients are given. The normal component of the incidence kinetic energy is given as well, because the transient C–H bond is efficiently formed with normal kinetic energy.

The translational energy and scattering angle distribution for H-atoms is shown in Fig. 4.31 – 4.35. By comparing to experiment, the results could be reproduced speaking in terms of the correct branching of the slow and fast channel. Note that the initial polar angle of the impinging atom considered in the simulations is shifted by  $4^\circ$  compared to the results from experiment. Here, not the direct comparison to a specific angle in the experiment was of interest, but how the ratio of intensities of the two channels change with incidence energy. It is tested, if the HDNN-PES can reproduce the mentioned energy dependence. The main data of the underlying PES is for scattering at 1.92 eV, but here it should be analyzed, if the PES is also able to capture the correct trend of the energy dependence. The dependence of the incidence kinetic energy should give a hint, if the PES can capture the trend seen in experiment as additional check of quality.

At 0.99 eV incidence energy, only the fast channel is present (Fig. 4.31), indicating the only quasi-elastic scattering is present and the barrier is not crossed. At 1.92 eV incidence energy both the fast and the slow channel are present (Fig. 4.32). At this incidence energy, there is a small signal intensity around the specular angle, but in the direction of the incoming beam. This means backward scattering can be seen in theory. This is even more pronounced for scattering at 2.18 eV, where the intensities of the fast and slow channel are inverse. The slow channel has a much larger intensity compared to the fast channel, which can be reproduced by the HDNN-PES. The signal around the surface normal is due to a release of the impinging atom after forming a transient bond with surface carbon atoms. The incoming beam has enough energy to cross the barrier and is released in analog to a swing-by maneuver to leave the surface. Here, the release can happen in forward-scattering direction or backward-scattering direction, but preferably in forward direction. Increasing the incidence kinetic energy of the projectile even further to 2.62 eV, the fast channel is completely vanished, indicating all scattered atoms can overcome the barrier. Simultaneously, the signal becomes much broader in angular as well as energetic range. The broadening in angles continues when the H-atom has 3.31 eV incidence energy, but the energy loss is more localized. Since now all particles have enough energy to cross the barrier and are not anymore able to distribute a large fraction of their initial kinetic energy due to decreased interaction time. In experiment, there is a less range of energy loss, but this is more pronounced in the simulations. Here, the HDNN-PES seems to reach its limit in terms of reproduction of experimental translational and scattering angle distributions.



To get an impression, how the backward scattering might look like, in Fig. 4.36 an example trajectory is shown in a side view.

The quality of the results can be more clearly seen in angle integrated energy loss distributions. To better compare the energy loss for different energies, in Fig. 4.37 the normalized energy loss of the scattering atom with different incidence kinetic energies is shown. In the plot, the peak around  $E_{\text{loss}} \approx 0$  eV corresponds to the fast channel whereas the peak at  $E_{\text{loss}} \approx 0.5$  eV indicates the slow channel and has a much broader shape like before in the translational energy and scattering angle distributions. When increasing the incidence kinetic energy of the H-atom, the signal of the fast channel drops and eventually vanishes if the energy is high enough. This behavior reproduces the experimental findings and indicates a change in the dynamics, as found before. Even here, it seems the HDNN-PES can at least predict the correct trend. But since not the same incidence angles are compared, it is harder to determine, if the HDNN-PES is able to reproduce energy loss distributions from experiment. The PES was mainly fitted to scattering data with 1.92 eV. With the energy dependence I just want to check, if the trend can be predicted, which seems to be the case.

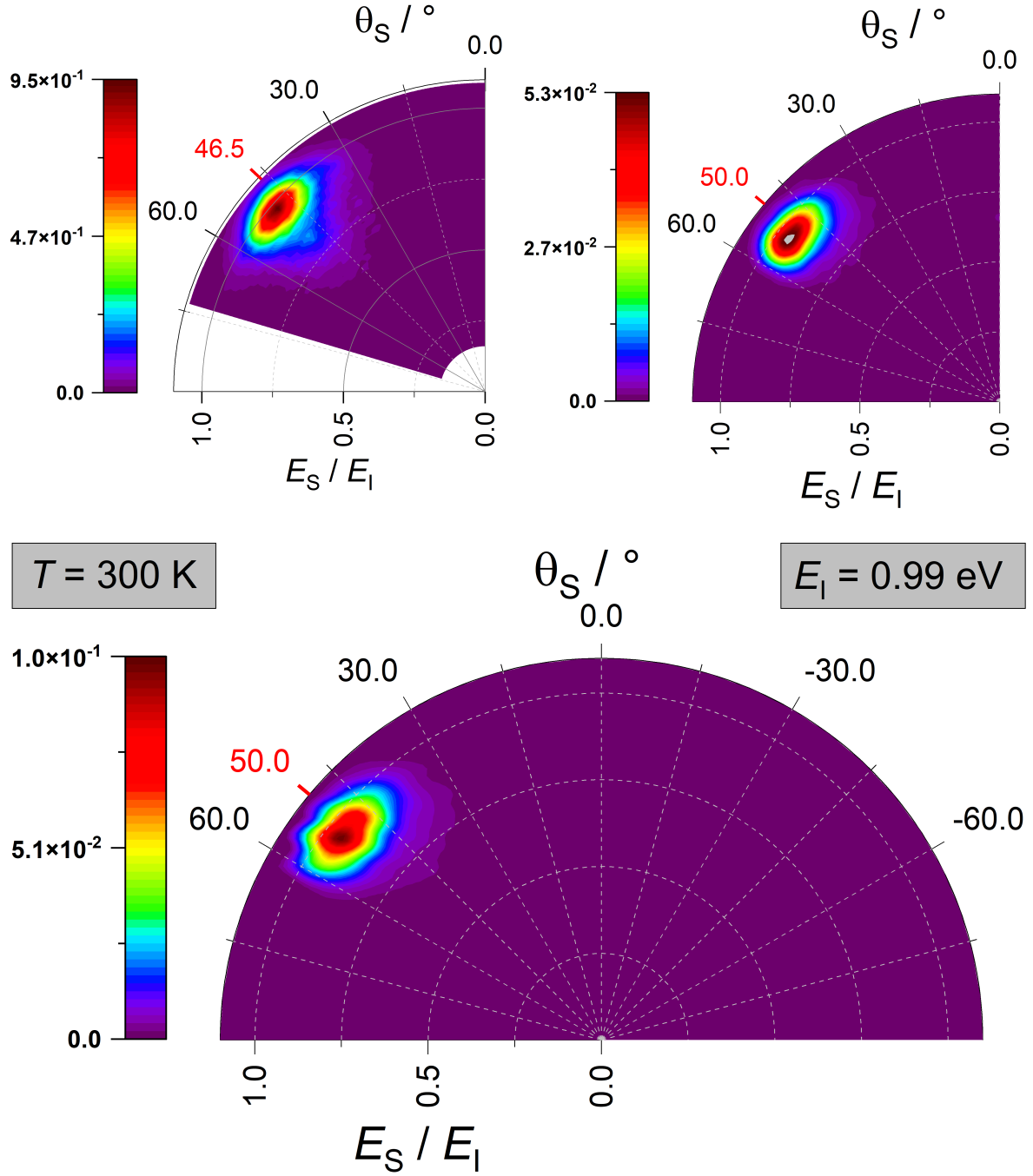


Figure 4.31: Comparing translational energy and scattering angle distribution from experiment (top left) with classical simulations using the HDNN-PES (top right) for H-scattering from graphene. The bottom panel also shows backward-scattering. The incidence kinetic energy  $E_I$  and surface temperature  $T$  are given in gray boxes. The incidence as well as specular polar angle  $\theta_I$  is shown in red. Statistics and further analysis of trajectories are shown in Tab. A.11 and A.12.

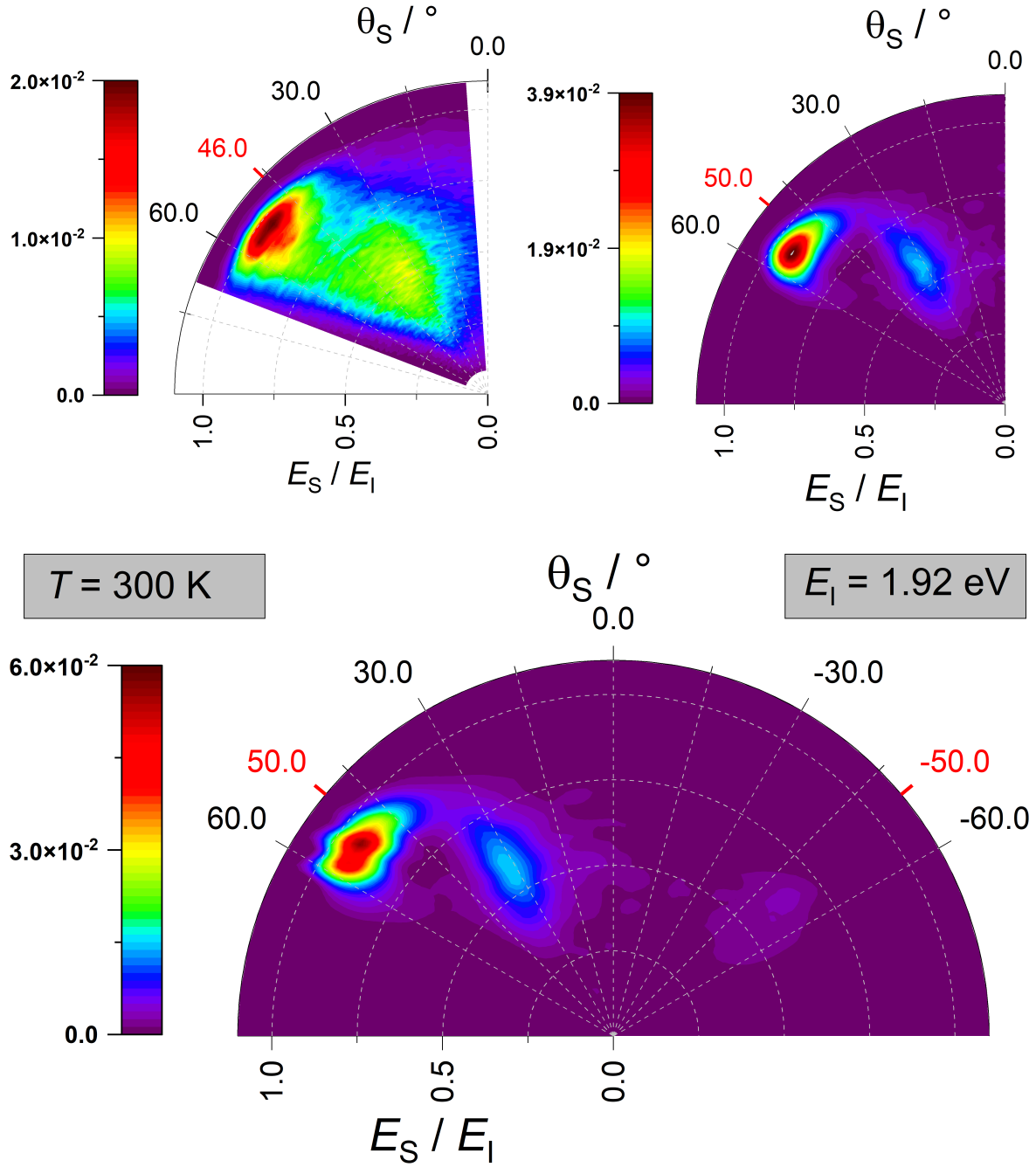


Figure 4.32: Comparing translational energy and scattering angle distribution from experiment (top left) with classical simulations using the HDNN-PES (top right) for H-scattering from graphene. The bottom panel also shows backward-scattering. The incidence kinetic energy  $E_I$  and surface temperature  $T$  are given in gray boxes. The incidence as well as specular polar angle  $\theta_I$  is shown in red. Statistics and further analysis of trajectories are given in Tab. A.11 and A.12.

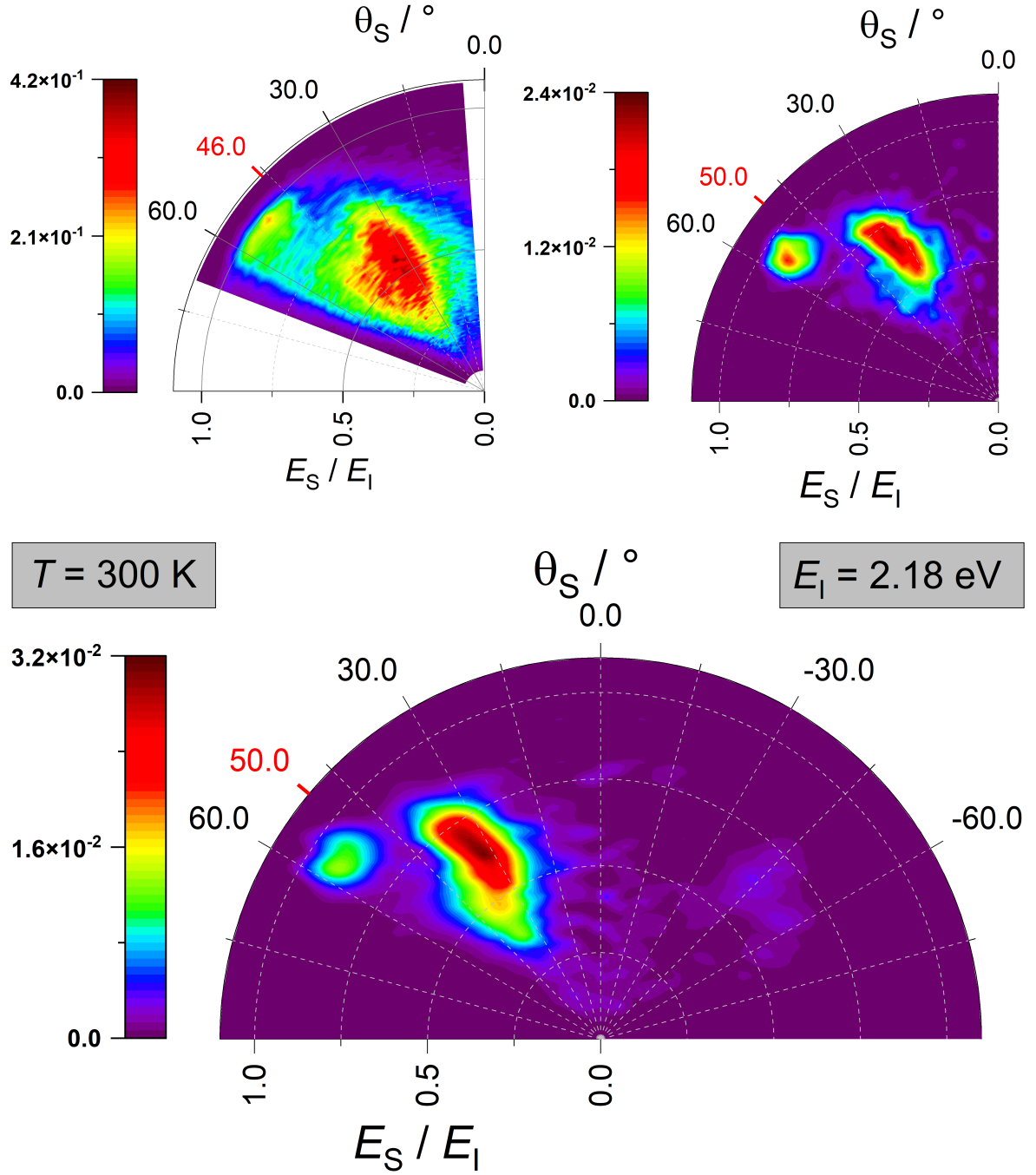


Figure 4.33: Comparing translational energy and scattering angle distribution from experiment (top left) with classical simulations using the HDNN-PES (top right) for H-scattering from graphene. The bottom panel also shows backward-scattering. The incidence kinetic energy  $E_I$  and surface temperature  $T$  are given in gray boxes. The incidence as well as specular polar angle  $\theta_I$  is shown in red. Statistics and further analysis of trajectories are given in Tab. A.11 and A.12.

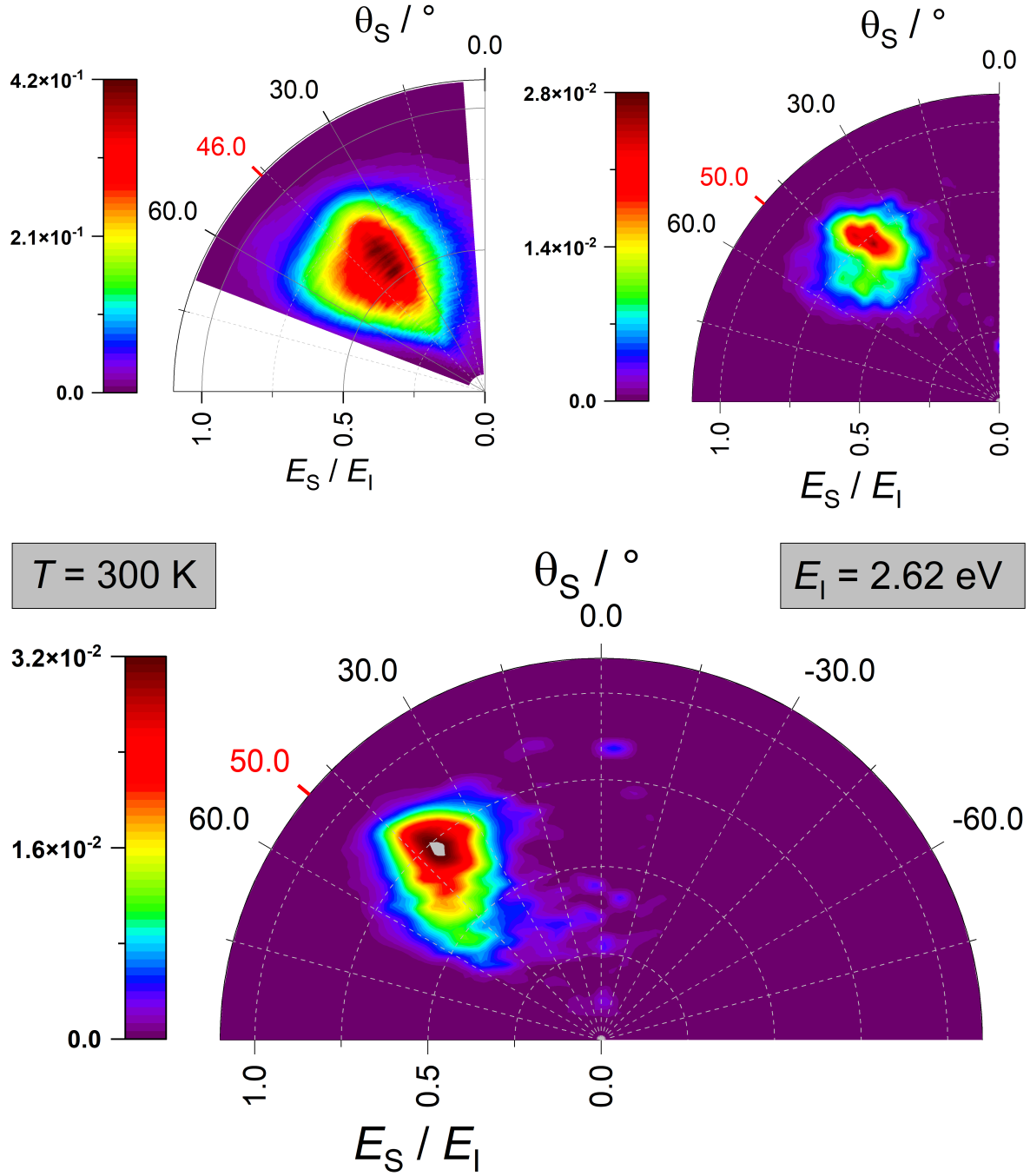


Figure 4.34: Comparing translational energy and scattering angle distribution from experiment (top left) with classical simulations using the HDNN-PES (top right) for H-scattering from graphene. The bottom panel also shows backward-scattering. The incidence kinetic energy  $E_I$  and surface temperature  $T$  are given in gray boxes. The incidence as well as specular polar angle  $\theta_I$  is shown in red. Statistics and further analysis of trajectories are given in Tab. A.11 and A.12.

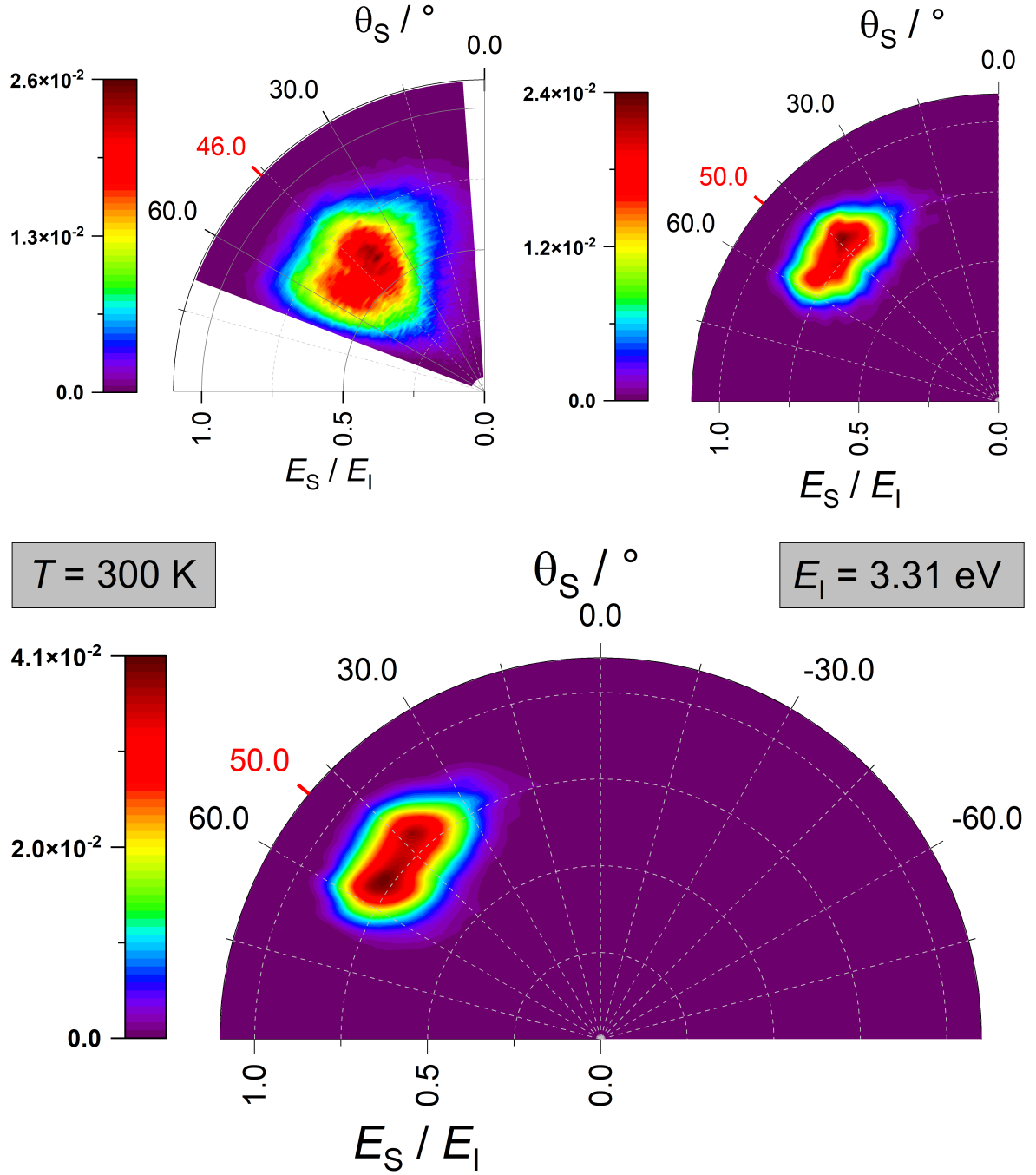


Figure 4.35: Comparing translational energy and scattering angle distribution from experiment (top left) with classical simulations using the HDNN-PES (top right) for H-scattering from graphene. The bottom panel also shows backward-scattering. The incidence kinetic energy  $E_I$  and surface temperature  $T$  are given in gray boxes. The incidence as well as specular polar angle  $\theta_I$  is shown in red. Statistics and further analysis of trajectories are given in Tab. A.11 and A.12.

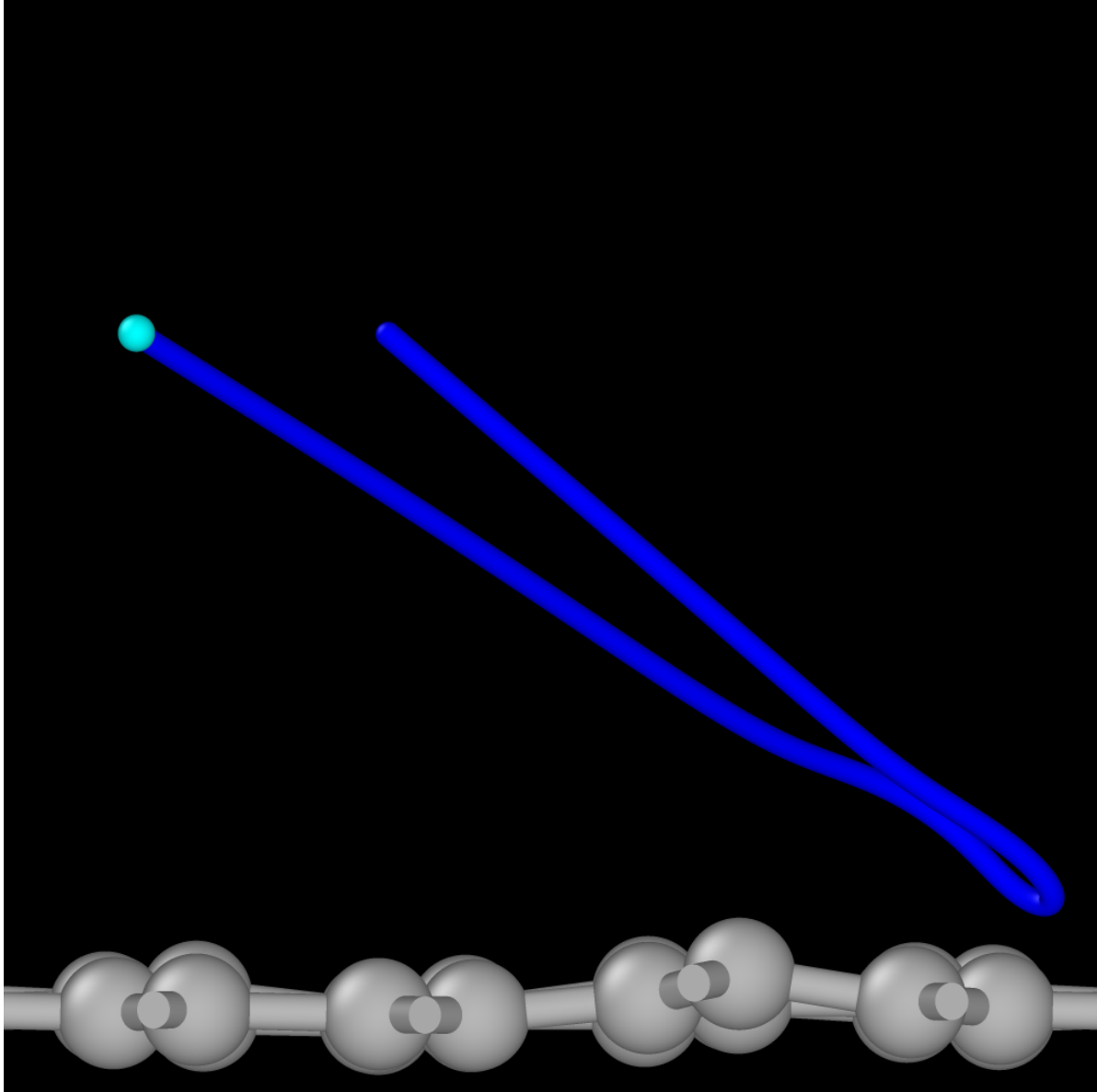


Figure 4.36: Side view of a trajectory showing backward-scattering of an H-atom from graphene with  $E_I = 2.18$  eV and  $\theta_S = 50^\circ$ . The final conditions are  $E_S = 1.21$  eV and  $\theta_S = 63^\circ$ . The final position of the scattered H-atom is shown as a cyan colored sphere.

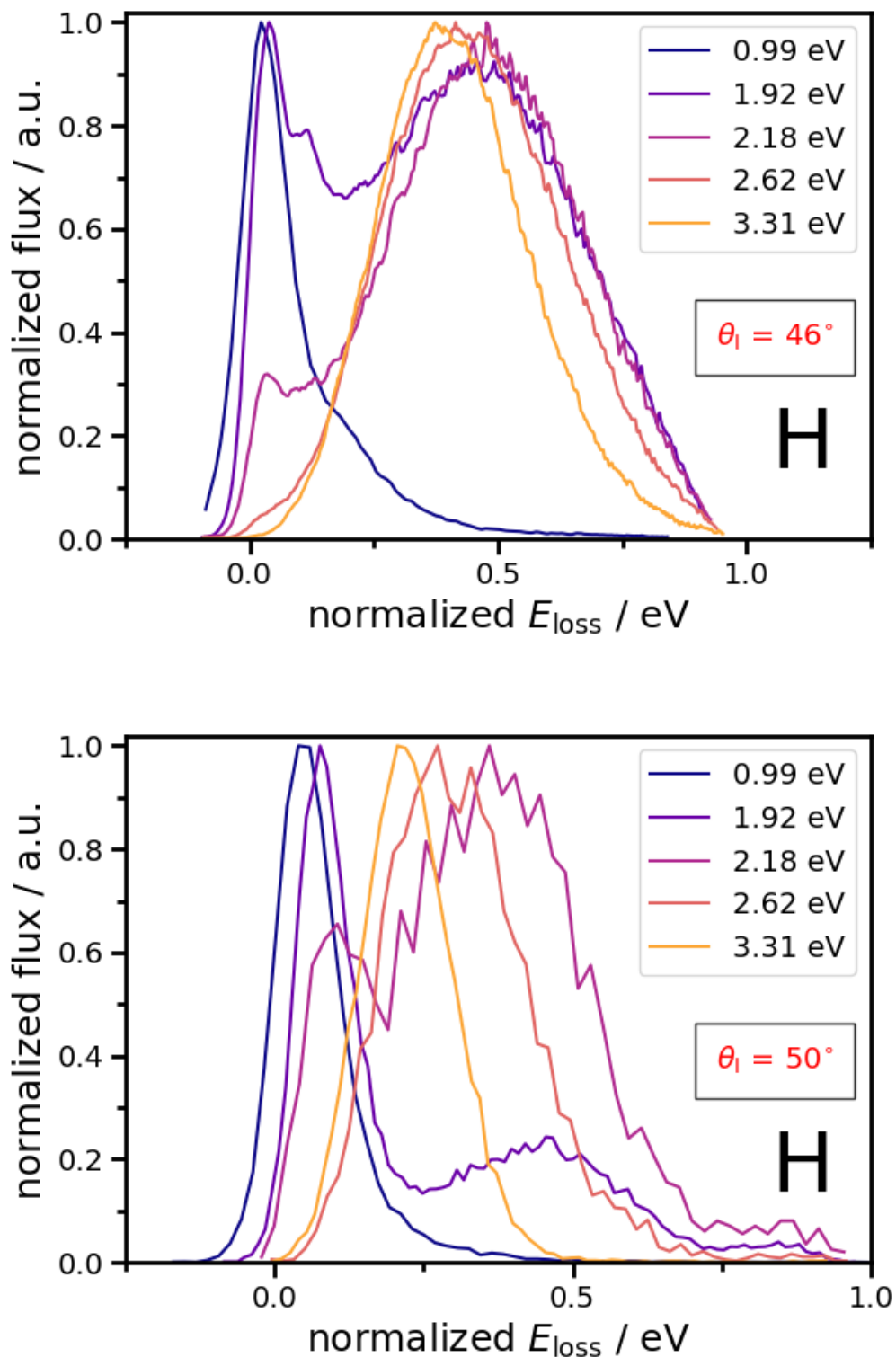


Figure 4.37: Comparing normalized angle integrated energy loss distributions from experiment (top) with classical simulations using the HDNN-PES (bottom) for H-atom scattering from graphene. The incidence polar angle  $\theta_I$  and the different incidence kinetic energies  $E_I$  are given as labels.



### H-atom scattering depending on the surface temperature

In this section, the temperature dependence on the scattering processes should be analyzed. Therefore, H-atom scattering was performed with  $E_I = 1.92$  eV with  $\theta_I = 50^\circ$  at 77 K, 300 K and 600 K. Note, at 77 K, there are no experimental results yet. Here, the projectile was launched 6.0 Å above the surface.

The parameters used in the simulations to describe the scattering are defined in Fig. 4.8, an overview of the analysis is shown in Fig. 4.14 and the definition of the channels is given in Fig. 4.17, respectively.

The surface temperature, the incidence polar angle, the incidence kinetic energy and its normal component for H-atom scattering from graphene on Pt(111) in the RAT experiment are given in Tab. A.9.

The statistics of H-atom scattering from free-standing graphene from MD simulations using a HDNN-PES are given in Tab. A.10. The number of simulated trajectories, scattered trajectories within detection limit compared to experimental setup, trajectories also considering backward scattering, the surface temperature as well as kinetic energy, its normal component and sticking coefficients are given. The normal component of the incidence kinetic energy is given as well, because the transient C–H bond is efficiently formed with normal kinetic energy.

In Fig. 4.38 – 4.40 the signal of the slow channel rises with increasing surface temperature. At  $T = 600$  K, the signals of the fast and slow channel are coming closer in intensity. Although the incidence angles of the H-atoms are not the same when comparing to experiment directly, here it is the same as in Sec. 4.3.1 for the energy dependence: The surface temperature should give a hint, if the PES can capture the trend seen in experiment as additional check of quality.

Previous studies demonstrated, that the puckering of the C-atom influences the adsorption barrier height. The pre-puckering (movement out of the surface plane) of the carbon atom, that is involved in the transient bond formation is less pronounced at smaller surface temperatures. The effective barrier is smaller at higher surface temperatures, explaining the rise in signal for the slow channel, because more H-atoms can cross the barrier. At higher surface temperatures, more vibrational states are excited and energy dissipation is less efficient, which can be seen when following the trend of sticking coefficients estimated and shown in Tab. A.9. However, due to the higher thermal in-plane movement of surface C-atoms, the atoms can easier rearrange when the sonic wave that is created by C–H bond formation whereas out-of-plane movement also decrease the barrier. The intensity for back-scattering rises with the surface temperature, which further indicates a change in the effective barrier height. Previous, it was stated that a higher surface temperature increases the chance of H-atoms crossing the barrier, but the energy transfer mechanism is not changed. Considering the peak of flux in the simulations, the trend found in experiment can be reproduced reasonable well. It seems, the contributions to the energy dissipation channels change, but they balance each other so that the effective energy distribution is stable.

The decreasing sticking coefficients for higher surface temperatures, the effective barrier and efficiency of the energy dissipation explains the change of the ratios of the fast and slow channel seen in experiment. The simulations are reasonable well reproducing the experimental findings.

A further analysis was done of the angle integrated energy loss distributions, which can be seen in Fig. 4.41 showing the results from RAT experiment (top) in comparison to results obtained from using HDNN-PES in MD simulations (bottom). Again, here not a direct comparison of the found intensities is compared, but the change in the ratio of the fast and slow channel. The fast channel can be seen as a peak around 0 eV, whereas the slow channel has a broader peak around 0.5 eV. In the experiment (top), the fast channel decreases in intensity and the slow channel increases, when H-atoms scattering from graphene at higher surface temperatures. This trend can be reproduced by theory.

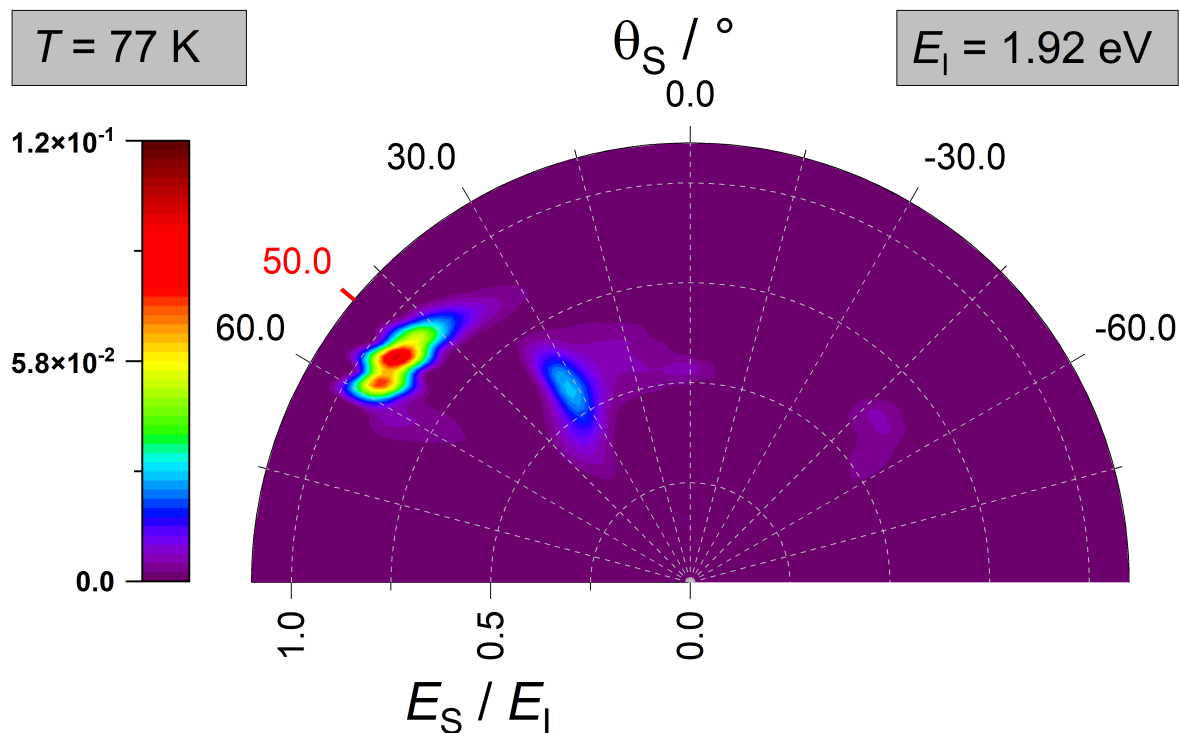


Figure 4.38: Showing translational energy and scattering angle distribution from classical simulations using the HDNN-PES (top right) for H-scattering from graphene. The incidence kinetic energy  $E_I$  and surface temperature  $T$  are given in gray boxes. The incidence as well as specular polar angle  $\theta_I$  is shown in red. Statistics and further analysis of trajectories are given in Tab. A.9 and A.10.

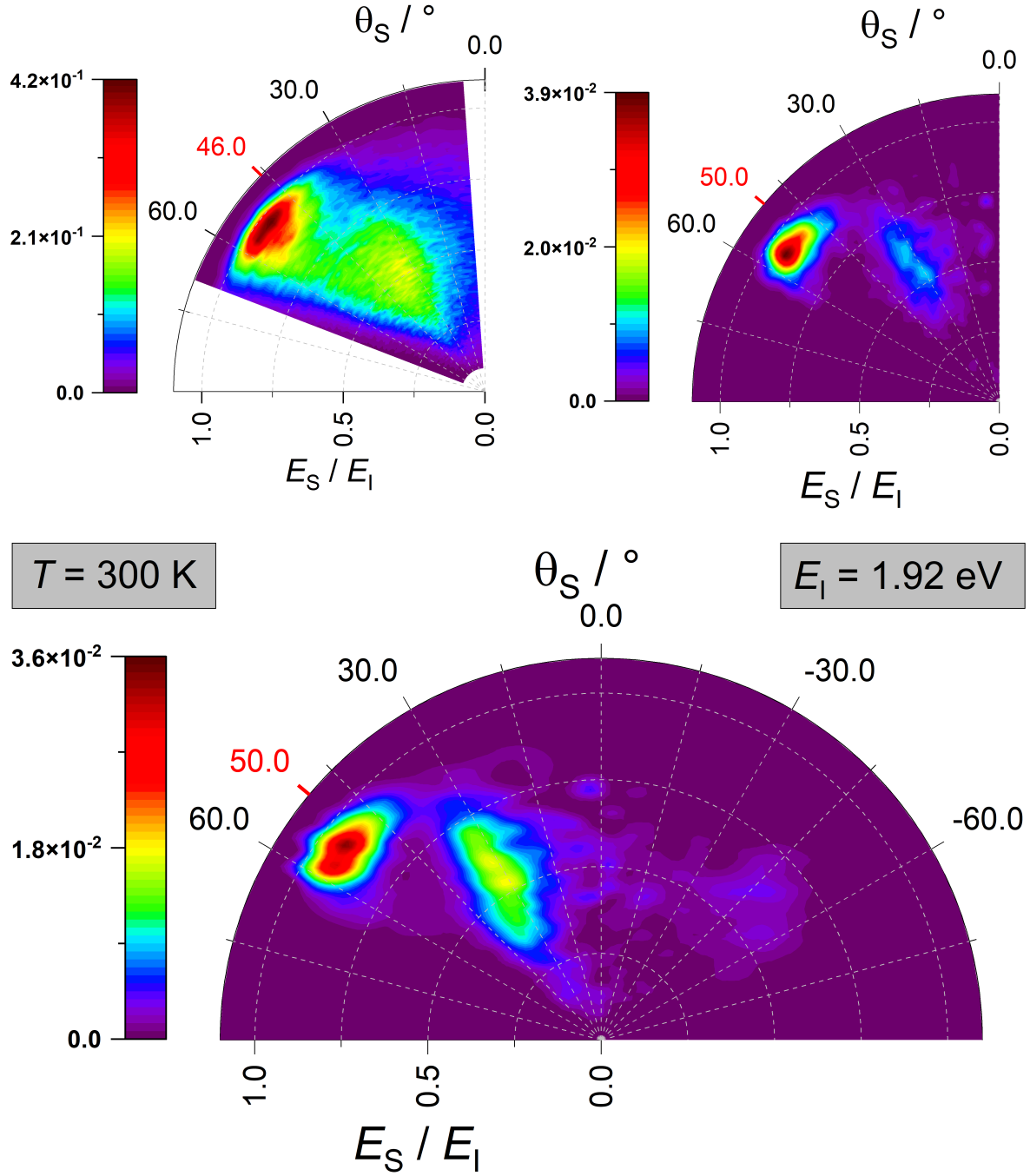


Figure 4.39: Comparing translational energy and scattering angle distribution from experiment (top left) with classical simulations using the HDNN-PES (top right) for H-scattering from graphene. The bottom panel also shows backward-scattering. The incidence kinetic energy  $E_I$  and surface temperature  $T$  are given in gray boxes. The incidence as well as specular polar angle  $\theta_I$  is shown in red. Statistics and further analysis of trajectories are given in Tab. A.9 and A.10.

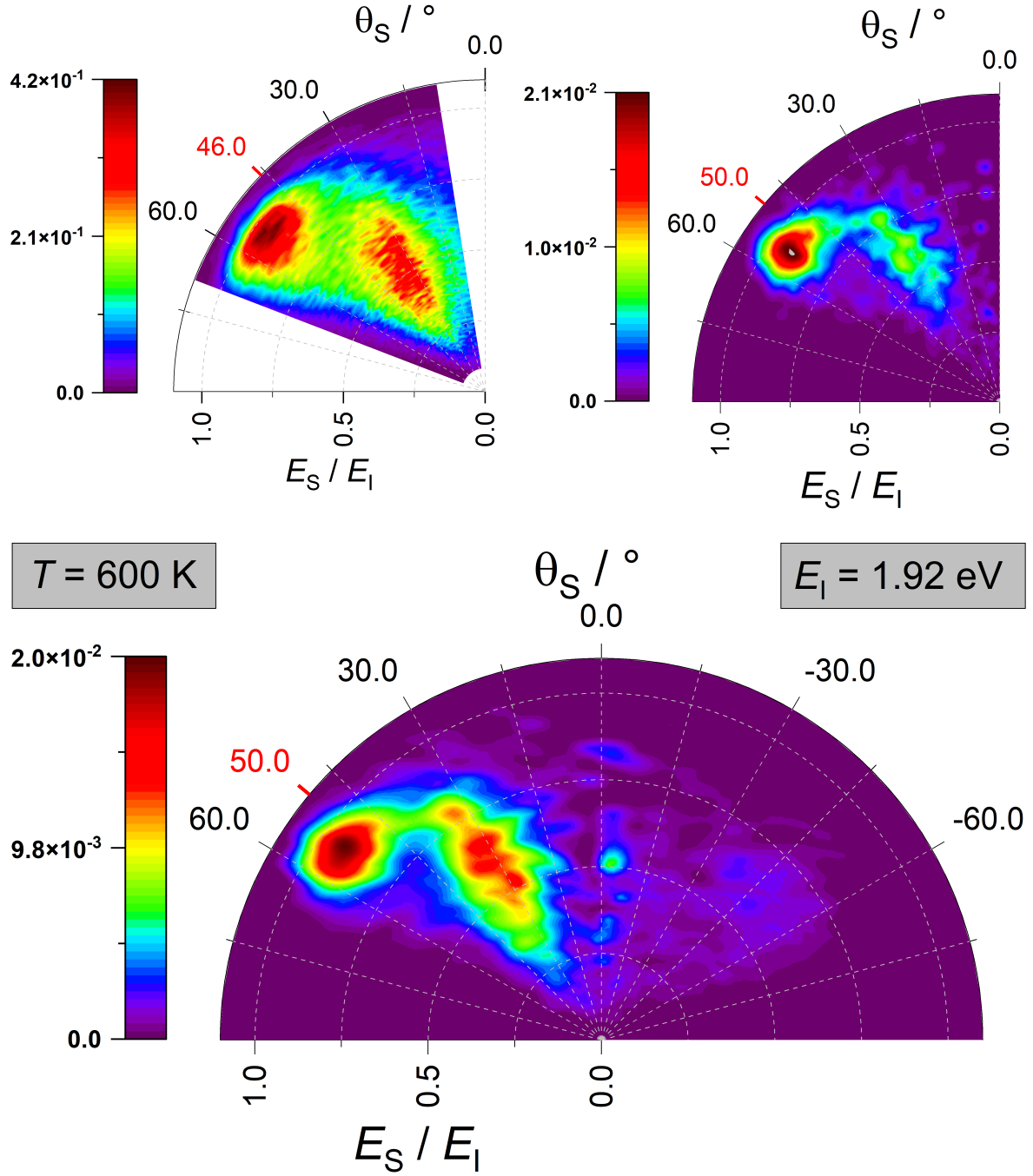


Figure 4.40: Comparing translational energy and scattering angle distribution from experiment (top left) with classical simulations using the HDNN-PES (top right) for H-scattering from graphene. The bottom panel also shows backward-scattering. The incidence kinetic energy  $E_I$  and surface temperature  $T$  are given in gray boxes. The incidence as well as specular polar angle  $\theta_I$  is shown in red. Statistics and further analysis of trajectories are given in Tab. A.9 and A.10.

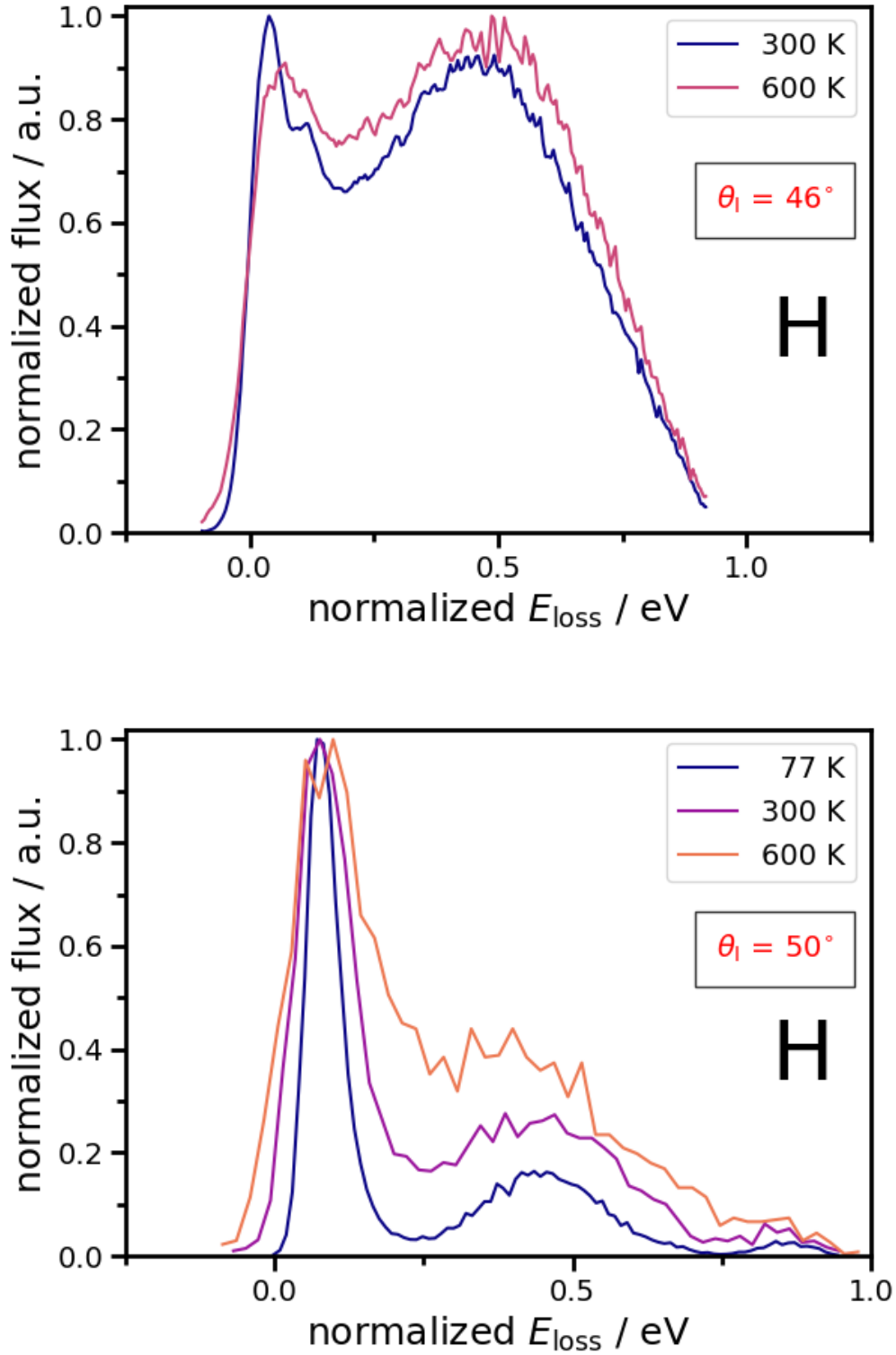


Figure 4.41: Energy loss distribution for H-atom scattering with  $\theta_i = 50^\circ$  and incidence kinetic energy of  $E_i = 1.92$  eV from the experiment (top) and obtained from MD simulations using a HDNN-PES (bottom). The surface temperature  $T$  is given as labels.

### H-atom scattering depending on the surface isotope effect

In the following, the H-atom scattering angle depending on the surface isotope effect of the free-standing graphene sheet will be analyzed. The influence of isotopic substitution on the energy loss spectra can serve as an additional test to validate the accuracy of the HDNN-PES. As before, the slab consist fully of  $^{12}\text{C}$  carbon atoms but here a slab of fully  $^{13}\text{C}$  carbon atoms is investigated as well. The same argumentation is applied as for the isotope of the projectile. Isotopes share the same electronic structure, therefore the same PES can be used. The only difference compared to the projectile is that because of the different masses, in order to set up the simulations, the snapshots from structures from *NVT* simulations has to be performed again, because the changed masses lead to a different relaxed surface geometry, which has to account for the changed inertia of the surface atoms. The procedure stays the same compared to before, but the generation of surface geometries has to be repeated.

The incidence angle, the number of trajectories used for the comparison, the normal kinetic energy and estimated sticking coefficients are shown in Tab. A.13.

The energy loss distributions from H-atom scattering from graphene will be analyzed. H-atom scattering from a fully  $^{13}\text{C}$  graphene sheet is compared to a fully  $^{12}\text{C}$  graphene sheet. The scattering has been simulated for H-atoms at six different incidence angles from  $\theta_1 = 10^\circ$  to  $\theta_1 = 60^\circ$  in steps of  $10^\circ$  and is shown in Fig. 4.42. Unlike before, here all trajectories are used in the energy loss distributions, because there are no distributions accessible from experiment. Therefore, the geometry of the detection does not have to be considered and together better statistics are achieved. Note that in this sections only theoretical energy loss distributions are compared, which both based on the HDNN-PES. The purpose of this section is not to predict, what might be possible to see in experiment, but considering the isotope effect the surface can give a hint, if the HDNN-PES is able to predict even smaller effects.

Changing the mass of the surface by introducing carbons most common isotope only slightly changes the average energy loss of the impinging atom to smaller energy losses due to the higher inertia of the graphene surface. The surface isotope effect does not have a significant influence on the scattering events. This can be explained by considering the increased inertia of the surface, making forming a transient bond and energy dissipation via phonon excitation less likely.

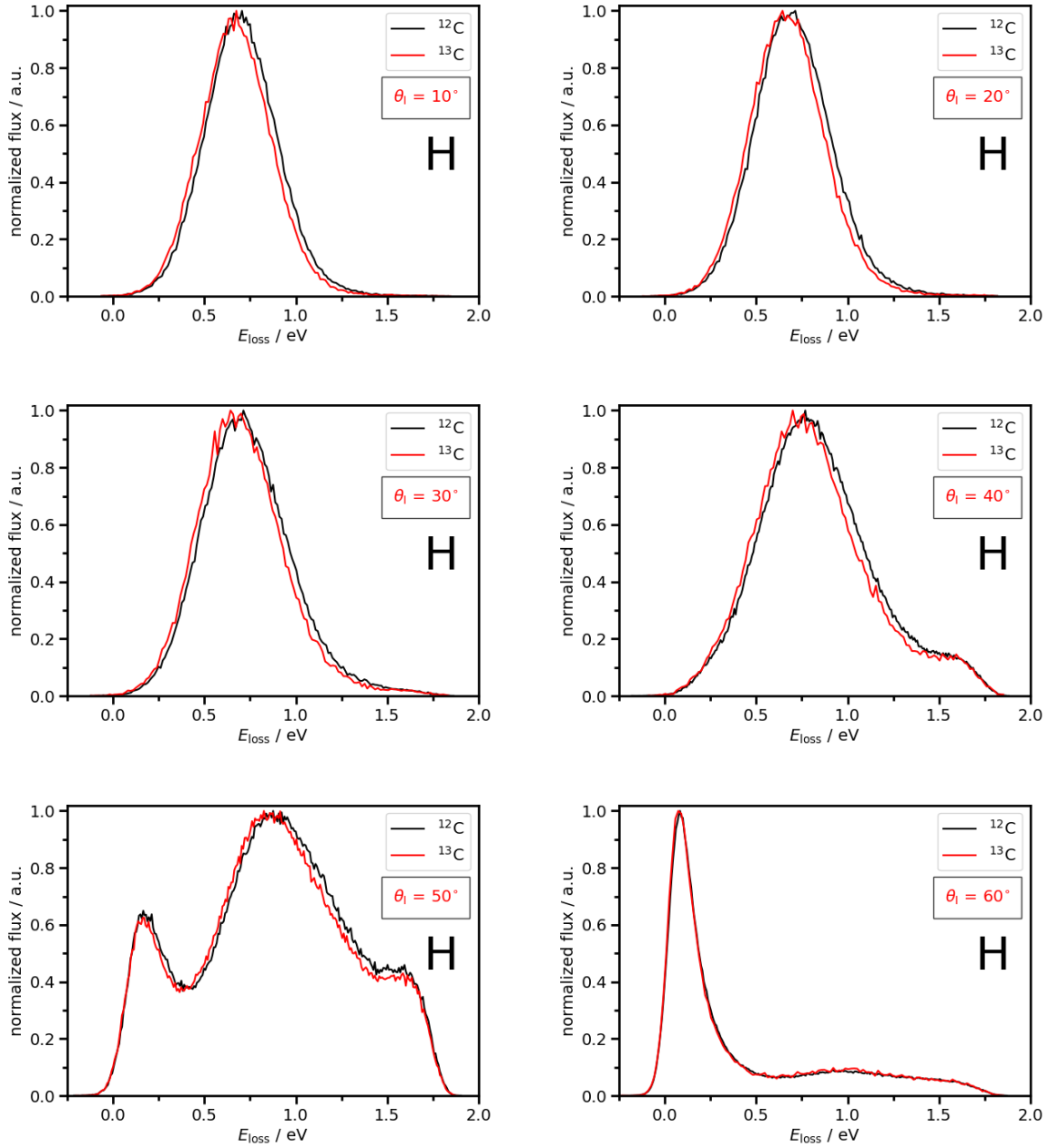


Figure 4.42: Energy loss distribution for H-atom scattering with incidence kinetic energy of  $E_I = 1.92$  eV for given incidence angle  $\theta_I$  depending on the mass of the surface (surface isotope effect). The scattering is shown for a fully  $^{12}\text{C}$ - and fully  $^{13}\text{C}$ -graphene surface. Statistics and further analysis of trajectories are given in Tab. A.13.

### D-atom scattering depending on the incidence polar angle

Before this work, theoretical analysis of D-atom scattering and the influence of the isotope on the scattering dynamics has been reported, but only for incidence energies of 1 eV [28].

Independent of the isotope used as scattering particle, a bimodal feature corresponding to the fast and slow channel can be seen in translational energy and scattering angle distributions. However, the high energy loss channel has a lower intensity simply due to the higher inertia of D-atoms compared to H-atoms and resulting longer interaction times with the surface. Therefore, efficient energy distribution is more likely. The influence of isotopic substitution on the energy loss spectra can serve as an additional test to validate the accuracy of the HDNN-PES. In this section and the following, I present studies of D-atom scattering from free-standing graphene and compare my results to experimentally found translational energy and scattering angle distributions in order to estimate, if the HDNN-PES can reproduce the found isotope effect of the impinging atom when going from H- to D-atoms. The analysis is given in the same manner as done before in case of H-atoms. Like before, the same different initial conditions have been analyzed. Additionally for D-atom scattering, also the isotope effect of the projectile is analyzed by comparing the estimated distributions from D-atom scattering to H-atom scattering. With this, not only the reproduction of experiment can be estimated but also if the HDNN-PES can capture subtle differences in angle resolved energy loss distributions as found in experiment.

Because isotopes have the same electronic structure at least treated classically, the same HDNN-PES was used for D-atom scattering. Only the mass of the impinging particle was changed in classical simulations. Like in case of H-atom scattering from the surface, the same geometric parameters for the detector are used. Not only the mass but also the incidence kinetic energy was adjusted to account for the different inertia of the D-atom.

Like before for H-atom scattering from graphene, the incidence kinetic energy of the scattered atom is set to  $E_I = 1.87$  eV. The surface temperature is  $T = 300$  K for all incidence conditions.

The analysis for D-atom scattering from free-standing graphene is done in the manner of the already shown H-atom scattering depending on the incidence polar angle. The following sections will present the data from experiment for each different incidence angle in the top left panel. Next to it in the right panel, the estimated translational and angular distribution from HDNN-PES is shown. The translational and angular distribution containing forward and backward scattering of the projectile is shown in the bottom panel. The parameters are defined in Fig. 4.8, an overview of the analysis is shown in Fig. 4.14, the definition of the channels is given in Fig. 4.17, like mentioned in the previous section for H-atom scattering.

The D-atom scattering depending on the incidence polar angle  $\theta_I$  is shown in Fig. 4.43 – 4.51. Like in case of H-atoms, the calculated trajectories, those who fulfill the geometry of experiment and used for the plot are given in A.8. Beside the incidence polar angle  $\theta_I$ , the normal kinetic energy  $E_N = E_I \cos^2 \theta_I$  is given and estimated sticking coefficients for this conditions are offered, too. The conditions from the experiment like the incidence polar angle, the incidence kinetic energy and its normal component as well as the scaling factors for the flux are given in Fig. A.7.

The translational energy and scattering angle distributions for H-atom scattering with incidence polar angle  $\theta_I = 43^\circ$  is shown in Fig. 4.43. In the distribution from experiment, the fast and the slow channel are present. The signal intensity of the slow channel is higher compared to the fast channel (left panel). The results from HDNN-PES can reproduce the branching of the channels, although the slow channel is more pronounced for these incidence angle (right panel). When considering also backward scattering events, there is a very broad spreading from  $0^\circ$  to  $-60^\circ$ . Compared to H-atom scattering with  $\theta_I = 42^\circ$  as shown in Fig. 4.22, the intensities of backward scattering are higher. Backward scattering are very inelastic bounces and are even more pronounced with the interaction time, which is higher in case of D-atoms compared to H-atoms simply because of the higher mass, the smaller incidence energy and



with that smaller velocities. This explains, why backward scattering is more pronounced for D-atoms with  $E_I = 1.87$  eV compared to H-atom with  $E_I = 1.92$  eV. The mentioned precession of the impinging atom around a single surface atom explains the different releases and with that angles of the projectile both for the azimuthal and the polar angle.

In Fig. 4.52 and 4.53, the energy loss distributions for the different incidence polar angles are shown and compared to experiment. Like discussed before for the angle dependence of H-atoms, D-atom scattering with smaller incidence polar angle corresponds to scattering with higher normal kinetic energy. In Sec. 4.2, the barrier height in the PES used has already been discussed. Higher incidence energy make crossing the barrier more likely. Especially at smaller incidence angles, the comparison of theoretical and experimentally obtained energy loss distributions shows significant differences of the average energy loss and shape of the distribution. And from the two dimensional translational energy and angular distributions it was mentioned, that applying an angular shift improves reproduction of experimentally found ratios of the fast and slow channel. With the indication, that the barrier height seem to be underestimated, this agrees well with the shown distributions.

In Fig. 4.52 and 4.53, the energy loss distributions for the different incidence polar angles are shown and compared to experiment. Like discussed before for the angle dependence of H-atoms, for D-atom scattering with smaller incidence polar angle and therefore with higher normal kinetic energy there is an increased mismatch between experiment and theory. In contrast to H-atom scattering and because incidence angles not smaller than  $43^\circ$  are compared to experiment, the overall mismatch seems less pronounced. But smaller angles have not been compared, where more differences compared to experimental distributions is expected. Like before, we see a drop in flux when considering only in-plane scattering. In Sec. 4.2, the barrier height in the PES used has already been discussed. Higher incidence energy make crossing the barrier more likely. Especially at smaller incidence angles, the comparison of theoretical and experimentally obtained energy loss distributions shows significant differences of the average energy loss and shape of the distribution. And from the two dimensional translational energy and angular distributions it was mentioned, that applying an angular shift improves reproduction of experimentally found ratios of the fast and slow channel. With the indication, that the barrier height seem to be underestimated, this explains the trend of the shown distributions and the larger mismatches for smaller incidence angles. The drop of flux in case of D-atom scattering is even more pronounced. This can be seen in Tab. A.6, when comparing the flux scaling factors estimated for H- and D-atom scattering to experiment.

On the other hand, the distributions estimated using a HDNN-PES are at least following the trend of the isotope effect of the projectile. A better comparison to experiment analyzing the isotope effect will be given in the following.

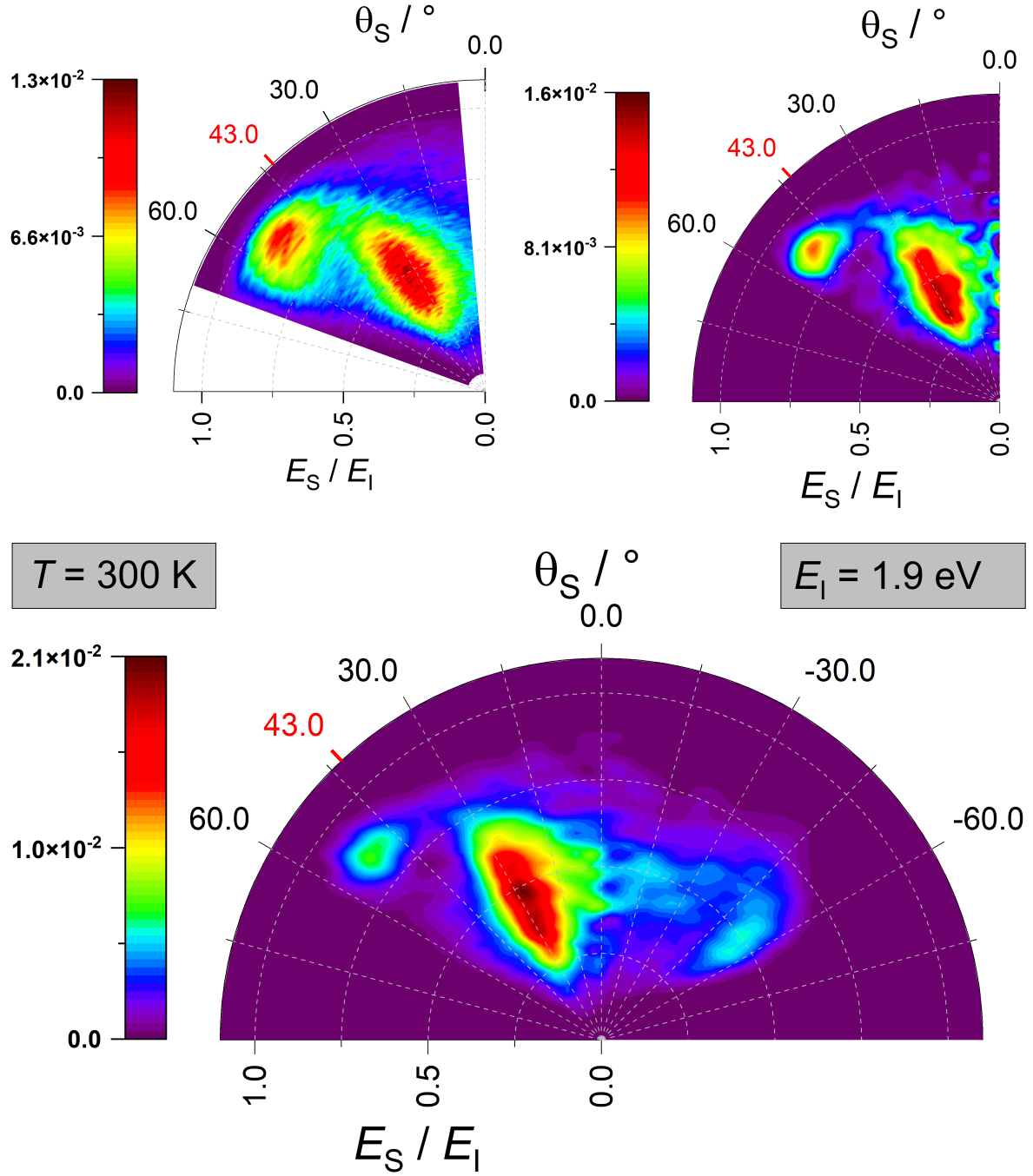


Figure 4.43: Comparing translational energy and scattering angle distribution from experiment (top left) with classical simulations using the HDNN-PES (top right) for D-scattering from graphene. The bottom panel also shows backward-scattering. The incidence kinetic energy  $E_I$  and surface temperature  $T$  are given in gray boxes. The incidence as well as specular polar angle  $\theta_I$  is shown in red. Statistics and further analysis of trajectories are given in Tab. A.7 and A.8.

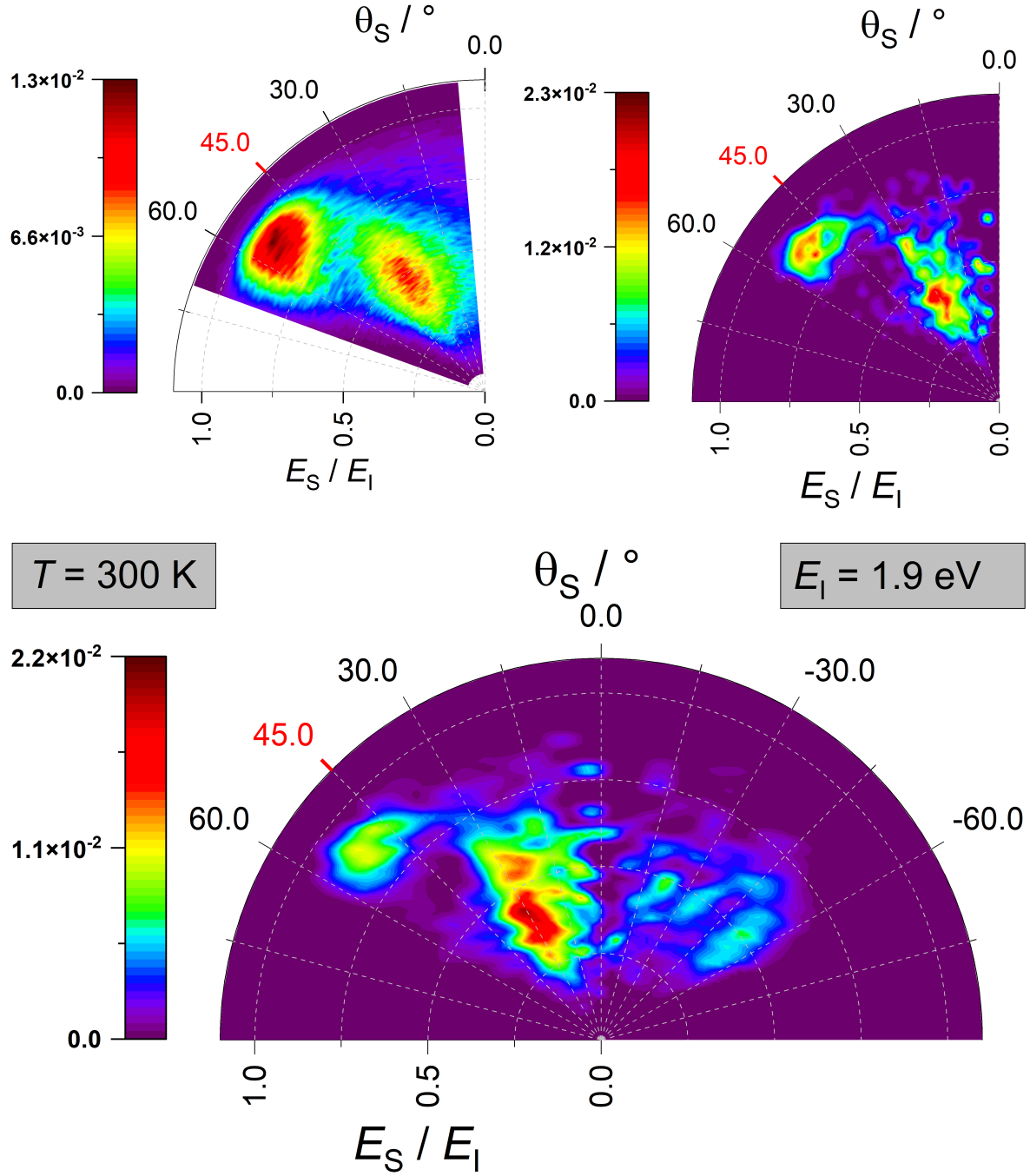


Figure 4.44: Comparing translational energy and scattering angle distribution from experiment (top left) with classical simulations using the HDNN-PES (top right) for D-scattering from graphene. The bottom panel also shows backward-scattering. The incidence kinetic energy  $E_I$  and surface temperature  $T$  are given in gray boxes. The incidence as well as specular polar angle  $\theta_I$  is shown in red. Statistics and further analysis of trajectories are given in Tab. A.7 and A.8.

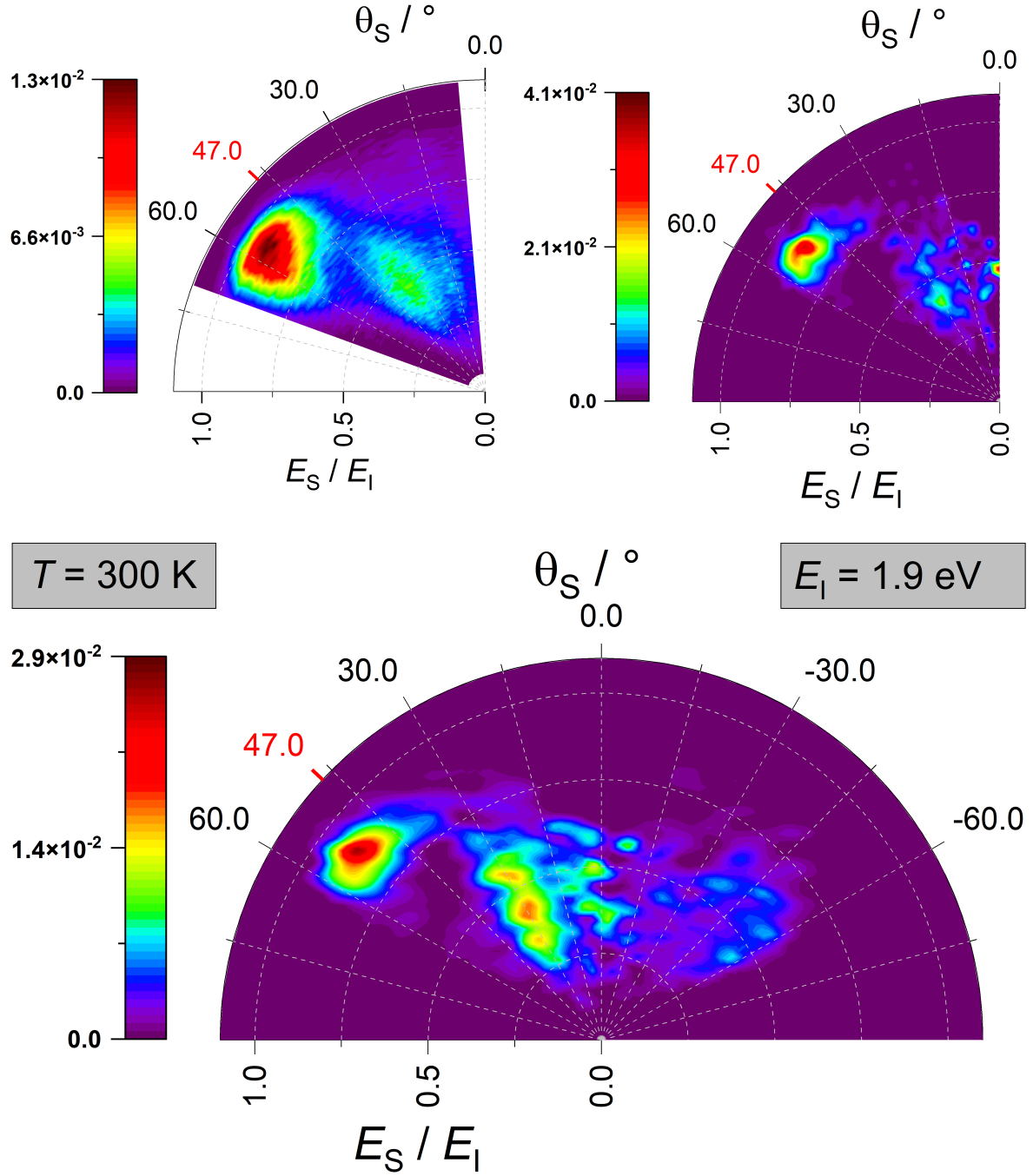


Figure 4.45: Comparing translational energy and scattering angle distribution from experiment (top left) with classical simulations using the HDNN-PES (top right) for D-scattering from graphene. The bottom panel also shows backward-scattering. The incidence kinetic energy  $E_I$  and surface temperature  $T$  are given in gray boxes. The incidence as well as specular polar angle  $\theta_I$  is shown in red. Statistics and further analysis of trajectories are given in Tab. A.7 and A.8.

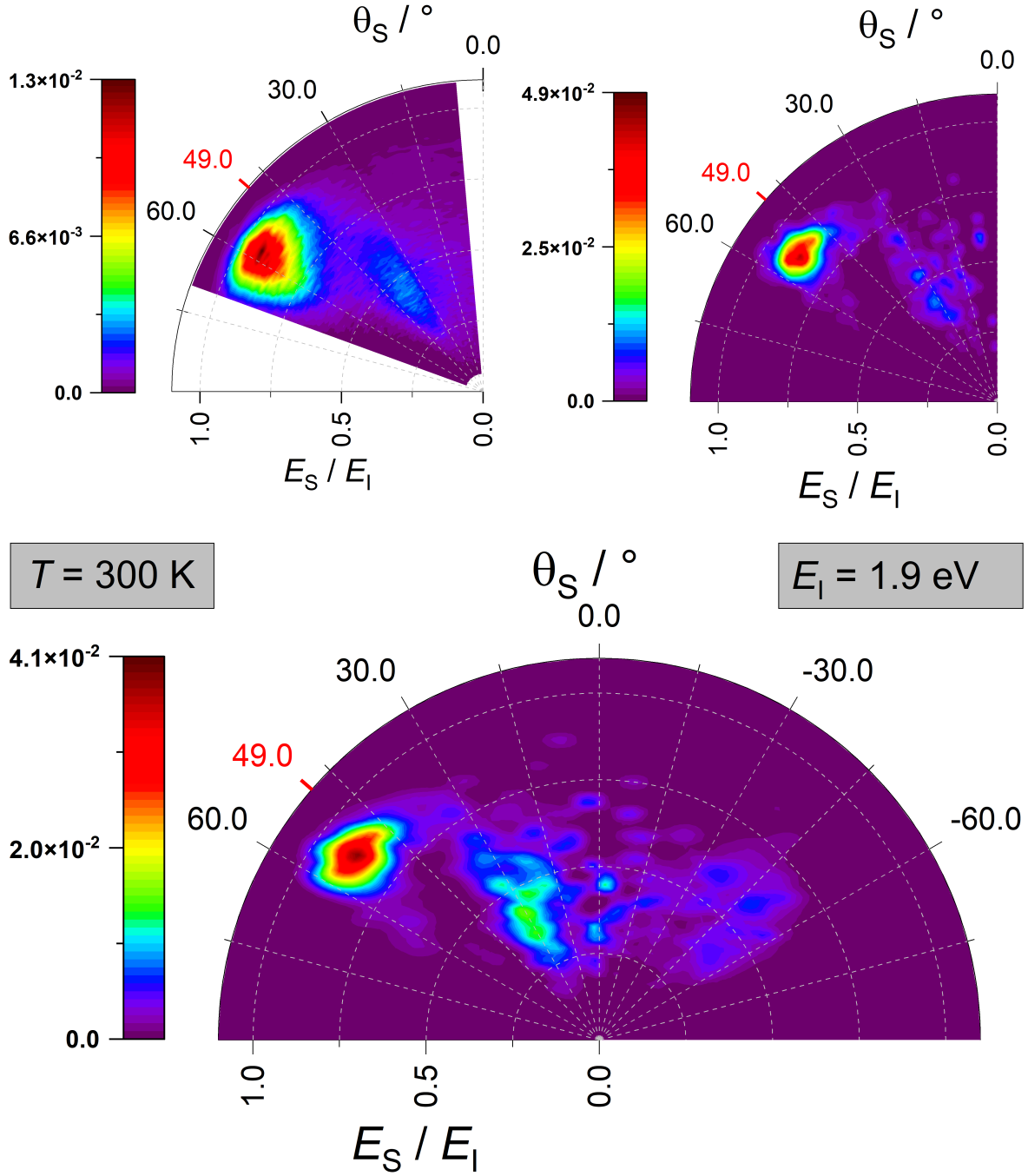


Figure 4.46: Comparing translational energy and scattering angle distribution from experiment (top left) with classical simulations using the HDNN-PES (top right) for D-scattering from graphene. The bottom panel also shows backward-scattering. The incidence kinetic energy  $E_I$  and surface temperature  $T$  are given in gray boxes. The incidence as well as specular polar angle  $\theta_I$  is shown in red. Statistics and further analysis of trajectories are given in Tab. A.7 and A.8.

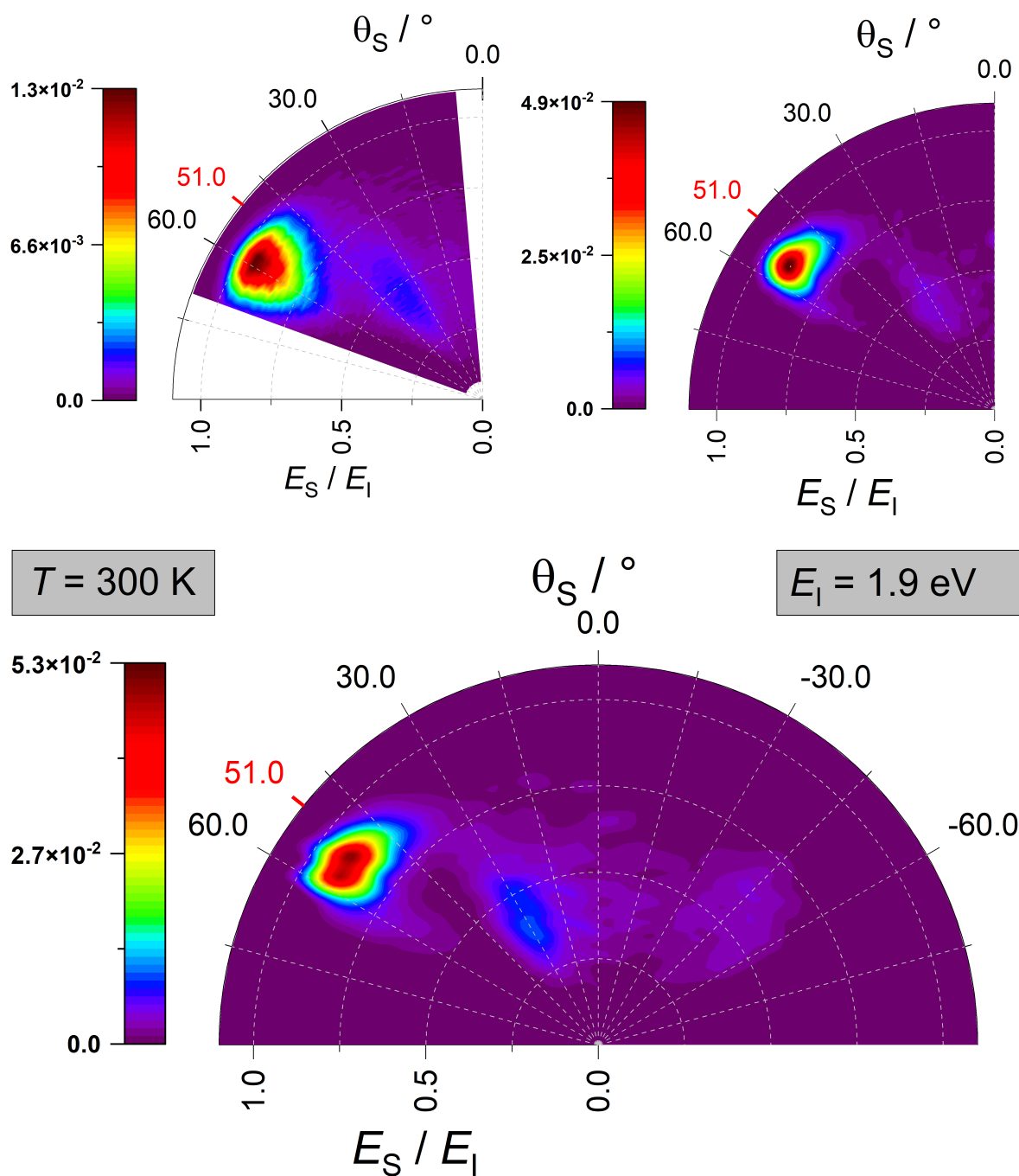


Figure 4.47: Comparing translational energy and scattering angle distribution from experiment (top left) with classical simulations using the HDNN-PES (top right) for D-scattering from graphene. The bottom panel also shows backward-scattering. The incidence kinetic energy  $E_I$  and surface temperature  $T$  are given in gray boxes. The incidence as well as specular polar angle  $\theta_I$  is shown in red. Statistics and further analysis of trajectories are given in Tab. A.7 and A.8.

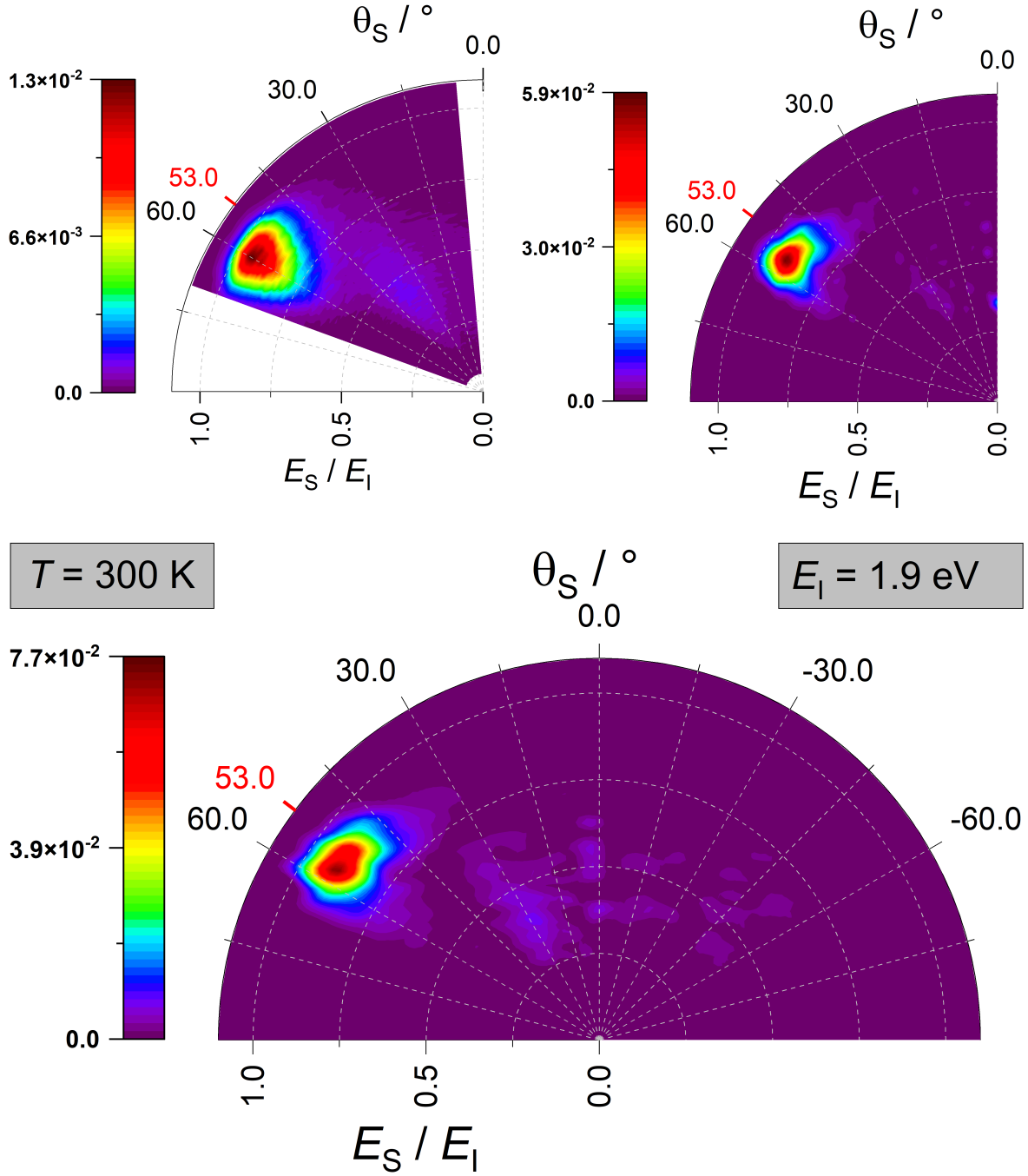


Figure 4.48: Comparing translational energy and scattering angle distribution from experiment (top left) with classical simulations using the HDNN-PES (top right) for D-scattering from graphene. The bottom panel also shows backward-scattering. The incidence kinetic energy  $E_I$  and surface temperature  $T$  are given in gray boxes. The incidence as well as specular polar angle  $\theta_I$  is shown in red. Statistics and further analysis of trajectories are given in Tab. A.7 and A.8.

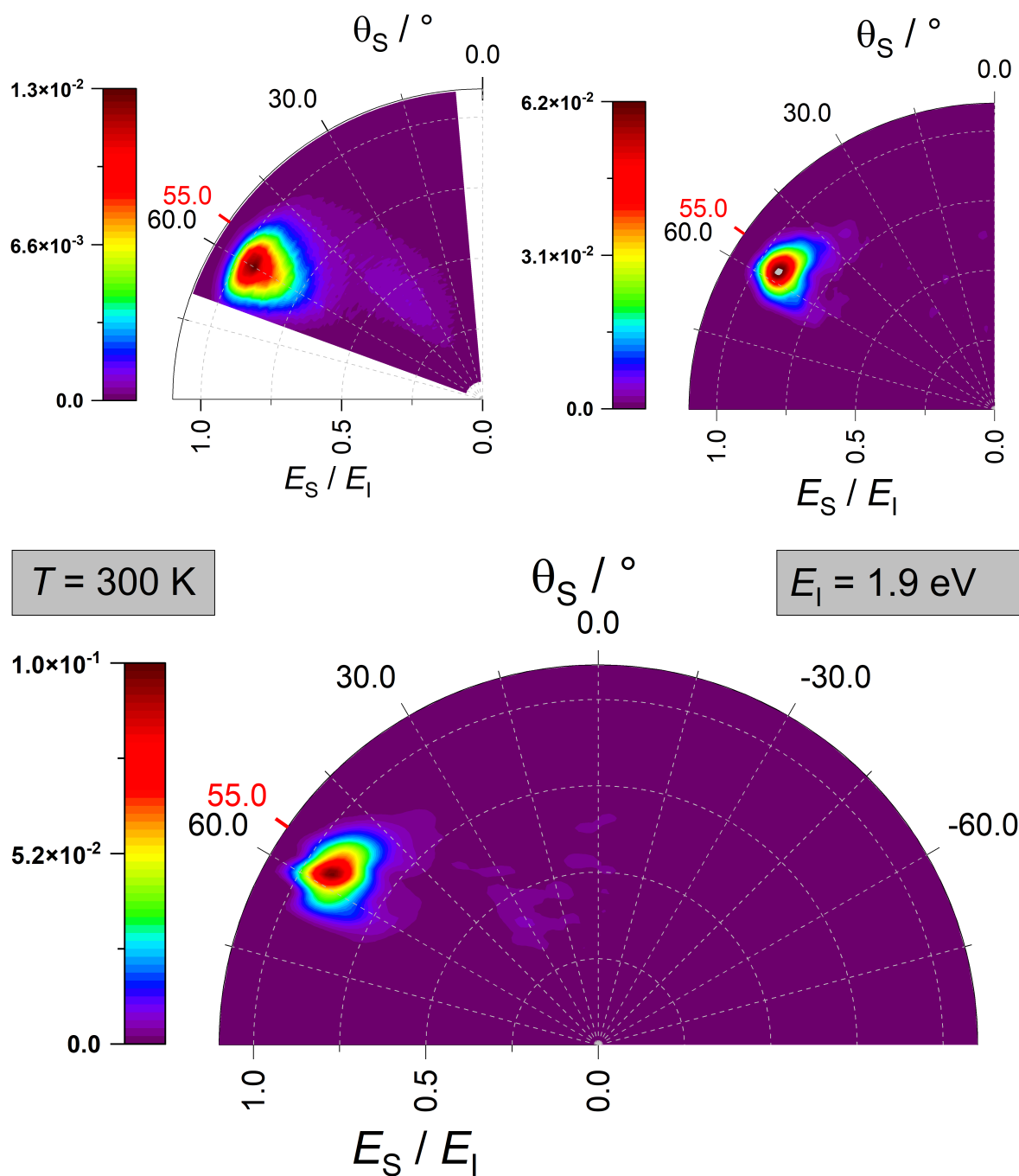


Figure 4.49: Comparing translational energy and scattering angle distribution from experiment (top left) with classical simulations using the HDNN-PES (top right) for D-scattering from graphene. The bottom panel also shows backward-scattering. The incidence kinetic energy  $E_I$  and surface temperature  $T$  are given in gray boxes. The incidence as well as specular polar angle  $\theta_I$  is shown in red. Statistics and further analysis of trajectories are given in Tab. A.7 and A.8.



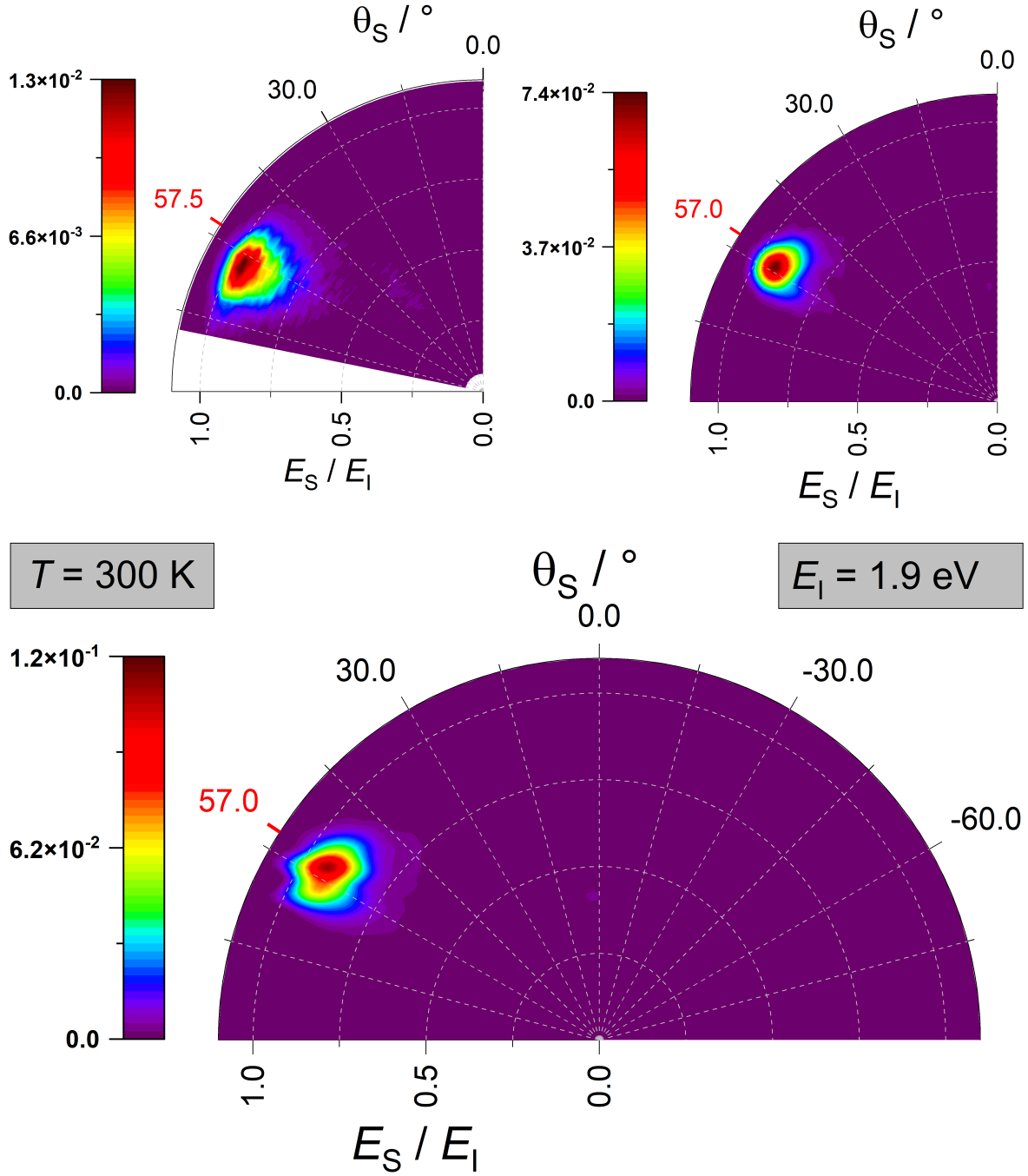


Figure 4.50: Comparing translational energy and scattering angle distribution from experiment (top left) with classical simulations using the HDNN-PES (top right) for D-scattering from graphene. The bottom panel also shows backward-scattering. The incidence kinetic energy  $E_I$  and surface temperature  $T$  are given in gray boxes. The incidence as well as specular polar angle  $\theta_I$  is shown in red. Statistics and further analysis of trajectories are given in Tab. A.7 and A.8.

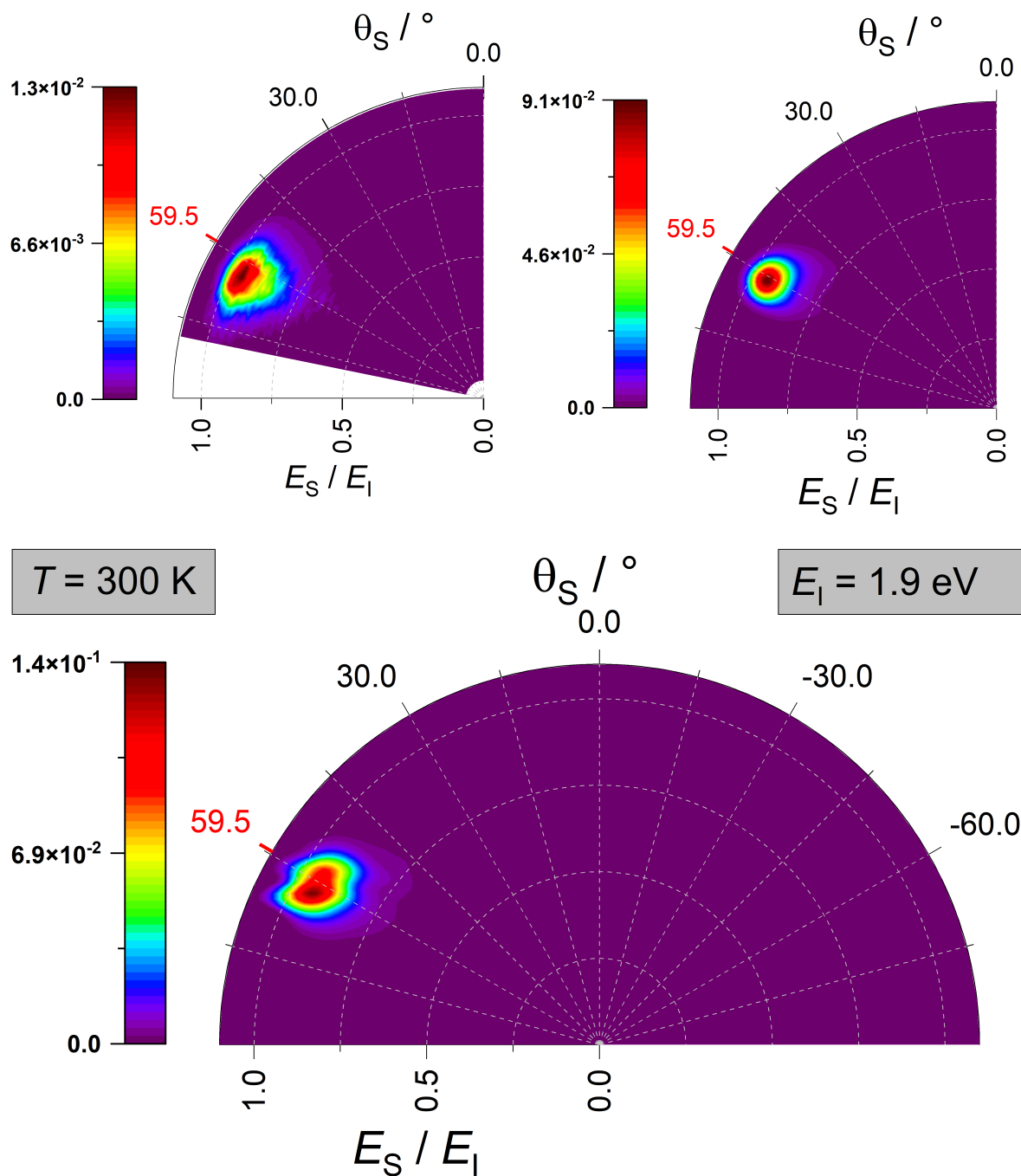


Figure 4.51: Comparing translational energy and scattering angle distribution from experiment (top left) with classical simulations using the HDNN-PES (top right) for D-scattering from graphene. The bottom panel also shows backward-scattering. The incidence kinetic energy  $E_I$  and surface temperature  $T$  are given in gray boxes. The incidence as well as specular polar angle  $\theta_I$  is shown in red. Statistics and further analysis of trajectories are given in Tab. A.7 and A.8.

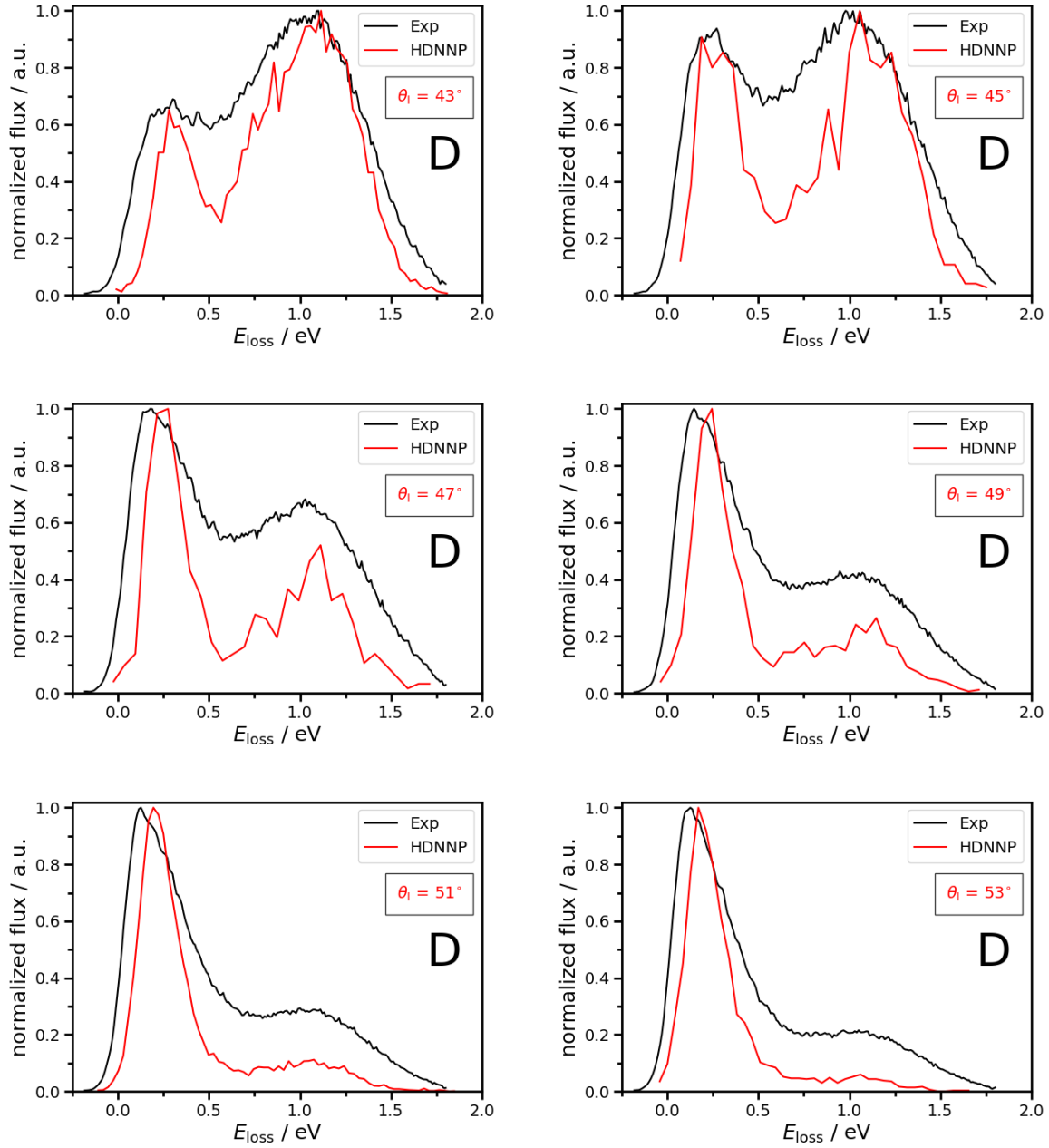


Figure 4.52: The same as Fig. 4.53, but the incidence angles are different. Energy loss distributions from the experiment shown in black and from HDNN-PES shown in red. The red number in the boxes indicate the incidence and specular angle of the D-atom. Other than in the translational energy and angular distributions, the flux is normalized to the maximum value. The incidence energy  $E_I = 1.9$  eV and the surface temperature  $T = 300$  K are given as well.

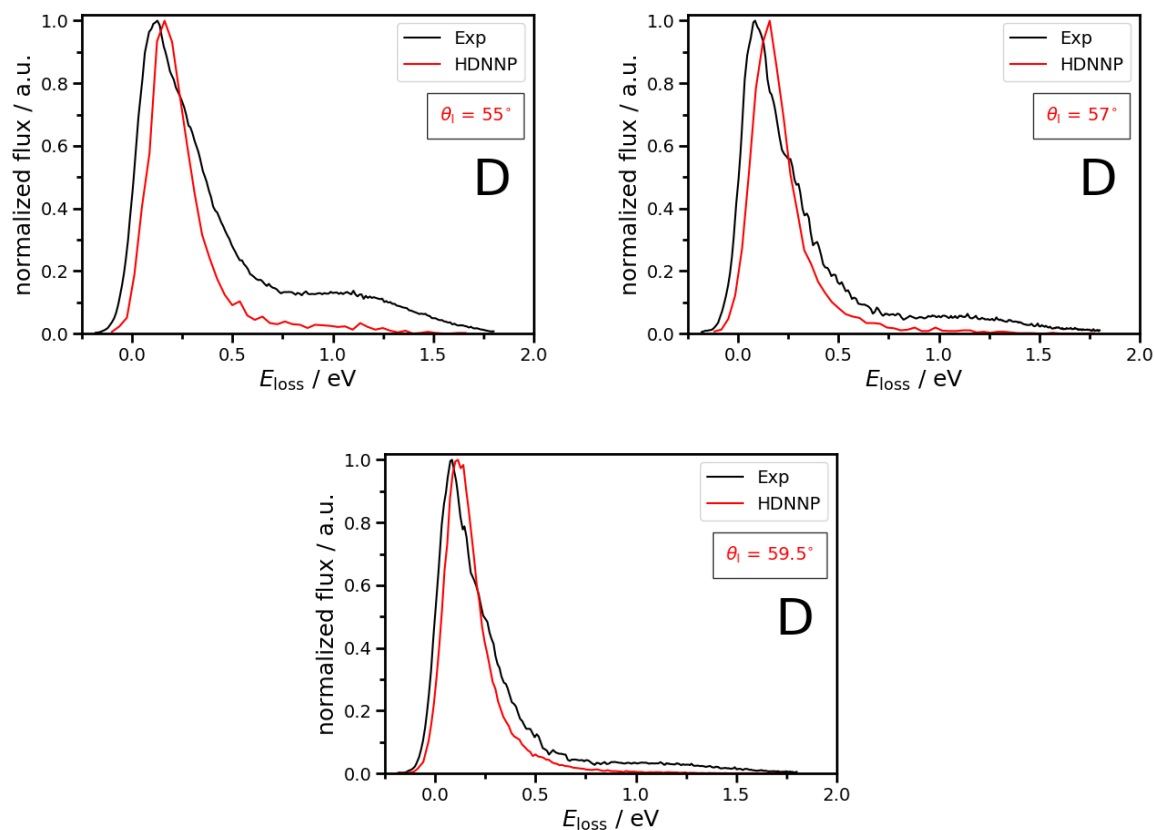


Figure 4.53: The same as Fig. 4.52, but the incidence angles are different. Energy loss distributions from the experiment shown in black and from HDNN-PES shown in red. The red number in the boxes indicate the incidence and specular angle of the D-atom. Other than in the translational energy and angular distributions, the flux is normalized to the maximum value. The incidence energy  $E_I = 1.9$  eV and the surface temperature  $T = 300$  K are given as well.

**Isotope effect of projectile depending on the incidence angle** To analyze the isotope effect of the impinging projectile, for three different incidence polar angles  $\theta_I = 59.5^\circ$ ,  $\theta_I = 50^\circ$  and  $\theta_I = 40^\circ$ , the one-dimensional energy loss distribution from H- and D-atoms are compared to experiment to check, if the HDNN-PES is able to predict the changes in the ratio of the fast and slow channel depending on the isotope effect of the projectile. This is shown in Fig. 4.54. In the comparison, one can see the difference in the mass of the impinging projectile from experiment by comparing the peak intensity ratio of the fast channel (peak around  $E_{\text{loss}} = 0.0$  eV) with respect to the slow channel (peak around  $E_{\text{loss}} = 1.0$  eV). At  $\theta_I = 59.5^\circ$  incidence angle, there are only minor deviations from the predicted compared with the estimated energy loss distribution for H- and D-atoms. At  $\theta_I = 50^\circ$  for H- and  $\theta_I = 51^\circ$  for D-atoms, the slow channel has a smaller peak for the slow channel. It was discussed before, that the correct ratio compared to experiment could not be reproduced, but at least the trend when going to the heavier isotope can be reproduced. The same argumentation can be applied for the distributions at  $\theta_I = 40^\circ$  for H- and  $\theta_I = 43^\circ$  for D-atoms. Again, the rise in intensity for the fast channel can be predicted quite well, although a direct comparison to experiment seems to be shifted to smaller  $E_{\text{loss}}$  in case of H- and underestimated  $E_{\text{loss}}$  range in case of D-atoms.

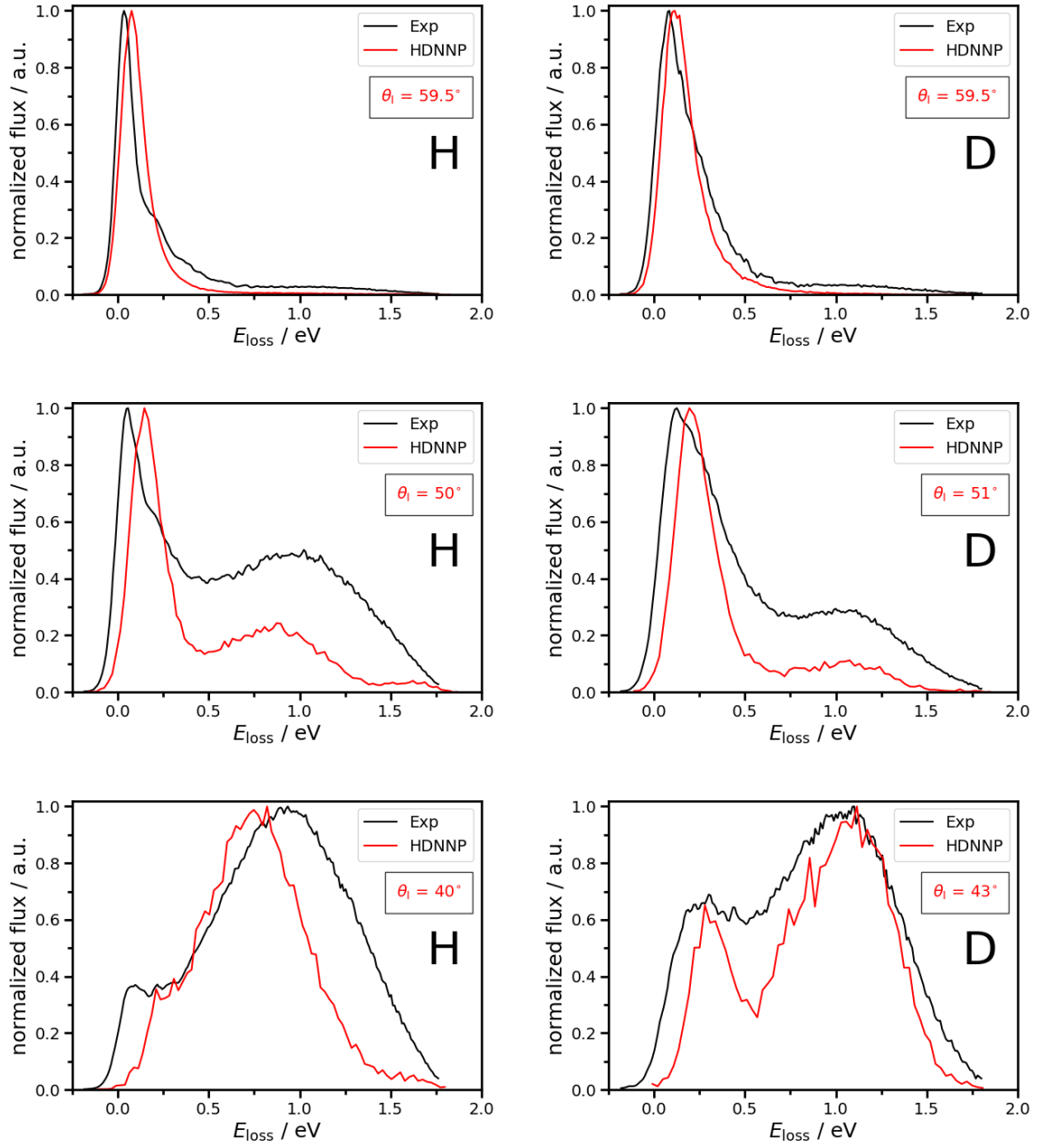


Figure 4.54: Comparing energy loss distributions from experiment (black) and from HDNNPES (red) for H- (left) and D-atom scattering from graphene. The red number in the boxes indicate the incidence and specular angle  $\theta_1$  of the atom. The flux is normalized to the maximum value. The incidence energy is  $E_I = 1.9$  eV for H- and D-atoms. The surface temperature is  $T = 300$  K.

### D-atom scattering depending on the incidence kinetic energy

In this section, the D-atom scattering from a graphene surface depending on the incidence kinetic energy is analyzed. Here, I present studies how well the HDNN-PES can describe the experimentally found dependence on the scattering when changing the initial kinetic energy of the scattering D-atom and will it compare to H-atom scattering depending on the incidence energy to check, if D-atom scattering reproduce experimental findings and with that the estimated isotope effect of the impinging atom. The incidence polar angles of the scattered D-atom are  $\theta_I = 47.5^\circ$ ,  $47^\circ$  and  $49.1^\circ$  with increasing incidence energy. The surface temperature is kept fixed at  $T = 300$  K for all incidence conditions.

The analysis for D-atom scattering from free-standing graphene is done in the manner of the already shown H-atom scattering depending on the incidence kinetic energy. The parameters used in the simulations are defined in Fig. 4.8, an overview of the analysis is shown in Fig. 4.14 and the definition of the channels is given in Fig. 4.17, like mentioned in Sec. 4.3.1 for H-atom scattering.

The D-atom scattering depending on the incidence kinetic energy  $E_I = 0.94$  eV,  $1.87$  eV and  $3.25$  eV is shown in Fig. 4.55 – 4.57. Like in case of H-atoms, the calculated trajectories, those who fulfill the geometry of experiment and used for the plot are given in A.12. Beside the incidence polar angle  $\theta_I$ , the normal kinetic energy  $E_N = E_I \cos^2 \theta_I$  is given and estimated sticking coefficients for this conditions are offered, too. The corresponding incidence conditions in experiment are given in Tab. A.11. The scaling factors of the flux needed to keep the same range of the color code in the distributions is given as well.

Note, like in the case of H-atom scattering depending on the incidence kinetic energy, here not a direct comparison to experiment is done, because the incidence angles are slightly different, but the trend, how the ratio of the fast and slow channel changes and if this trend can be reproduced by HDNN-PES.

D-atom scattering with  $E_I = 0.94$  eV is shown in Fig. 4.55. Here, only the signal of the fast channel is present. The normal component is not enough to efficiently cross the barrier to adsorption and only quasi-elastic scattering events can be seen. It was already mentioned, that backward scattering involves inelastic scattering events. This is the reason, why no signal intensity can be estimated. Even if the comparison is not done for exactly the same incidence polar angle, but overall the distribution follow the one found in experiment. Increasing the incidence kinetic energy of the D-atom to  $E_I = 1.87$  eV as shown in Fig. 4.56, the signal of the slow channel is present. Although, again, the ratios of the two channels cannot be compared to experiment because of the deviations in the incidence angle, but the HDNN-PES is able to reproduce the seen trend that going to higher energy, the slow channel is present. Going even higher to  $E_I = 3.25$  eV, which is shown in Fig. 4.57, like in the case of H-atoms scattering, for this energy, the fast channel completely vanishes and only the slow channel is present. Again due to the angular shift, the direct comparison is not possible, but the HDNN-PES correctly predicts the appearance of only the slow channel. This is further confirmed by considering the predicted sticking coefficients as given in Tab. A.12, which show an increasing sticking probability from 0.49 to 0.64 of the D-atom to the surface with its maximum at  $E_I = 1.87$  eV and drastic drop at higher energies to 0.12 at  $E_I = 3.25$  eV. From this it can be seen that at  $E_I = 0.99$  eV because of the high sticking and no signal of the slow channel that all impinging atoms that manage to overcome the barrier to adsorption will stick to the surface. Although the sticking probability reaches a maximum  $E_I = 1.87$  eV, this just means that because of the increased normal component of the kinetic energy makes a crossing of the barrier more likely, but also indicating, there are now also inelastic scattering events, in which the barrier is crossed again and the impinging atom will not stick to the surface, but will be scattered off the surface and reach the gas phase again, where it can be detected. This is the reason, why both the sticking coefficient is increasing and the signal of the slow channel.

The higher inertia of D-atoms compared to H-atoms explain the higher sticking coefficients. Because of the mentioned higher interaction time, distribution of kinetic energy to surface phonons is elevated.

Scattering of D-atoms with  $E_1 = 3.25$  eV happens exclusively after crossing the barrier, because the normal energy is enough to overcome the barrier. And from the estimated sticking coefficients we can see that sticking is less likely because of the higher energy, which cannot be distributed efficiently to enhance surface phonons on the time of interaction. Compared to H-atom scattering with higher energies, the slightly higher sticking coefficient makes sense. This is, again, due to the smaller velocities and with that higher interaction times of D-atoms with the surface carbon atoms and dissipation of energy is easier compared to H, but due to the high energy, the sticking itself is less likely compared to smaller incidence kinetic energies of the impinging atom.

As done before, in Fig. 4.58, the energy loss distributions from the experiment are shown in the top panel and the ones from HDNN-PES are shown in the bottom panel. Like in the distributions shown before, the trend for the change of ratios of the fast and slow channel is well reproduced by the HDNN-PES, but still there is not a one-to-one comparison possible due to the differences in the incidence polar angle  $\theta_1$ .

From the shown translational energy and scattering angle distributions it could be demonstrated, that the HDNN-PES is able to reproduce the correct dynamics as seen in the experiment when changing the mass of the incoming atom.

**Isotope effect of the projectile depending on the incidence energy** In Fig. 4.59, the change of ratios of the slow and fast channel are shown for H- and D-atom scattering from graphene depending on the incidence kinetic energy. Note, in the boxes showing the incidence polar angles of D-atom scattering, just the average angles are given to increase readability. By comparing the energy loss distributions for both isotopes of the projectile, we see the same trend for both isotopes, which is in good agreement with the trend seen in experiment. The energy loss distributions shown for D-atom scattering are broader in shape and shifted to higher energy loss. This makes perfectly sense, because of the higher mass and resulting less velocities of the projectile, the interaction time with the surface is increased and with that effective energy dissipation of the projectile to the surface is pronounced, leading to the found and predicted results.

From the isotope of the projectile we can conclude, that the results are reasonable, follow the correct trend and see differences in the scattering behavior as found in experiment. This indicates, that the HDNN-PES is able to reproduce translational energy and scattering distributions as well as energy loss distributions.



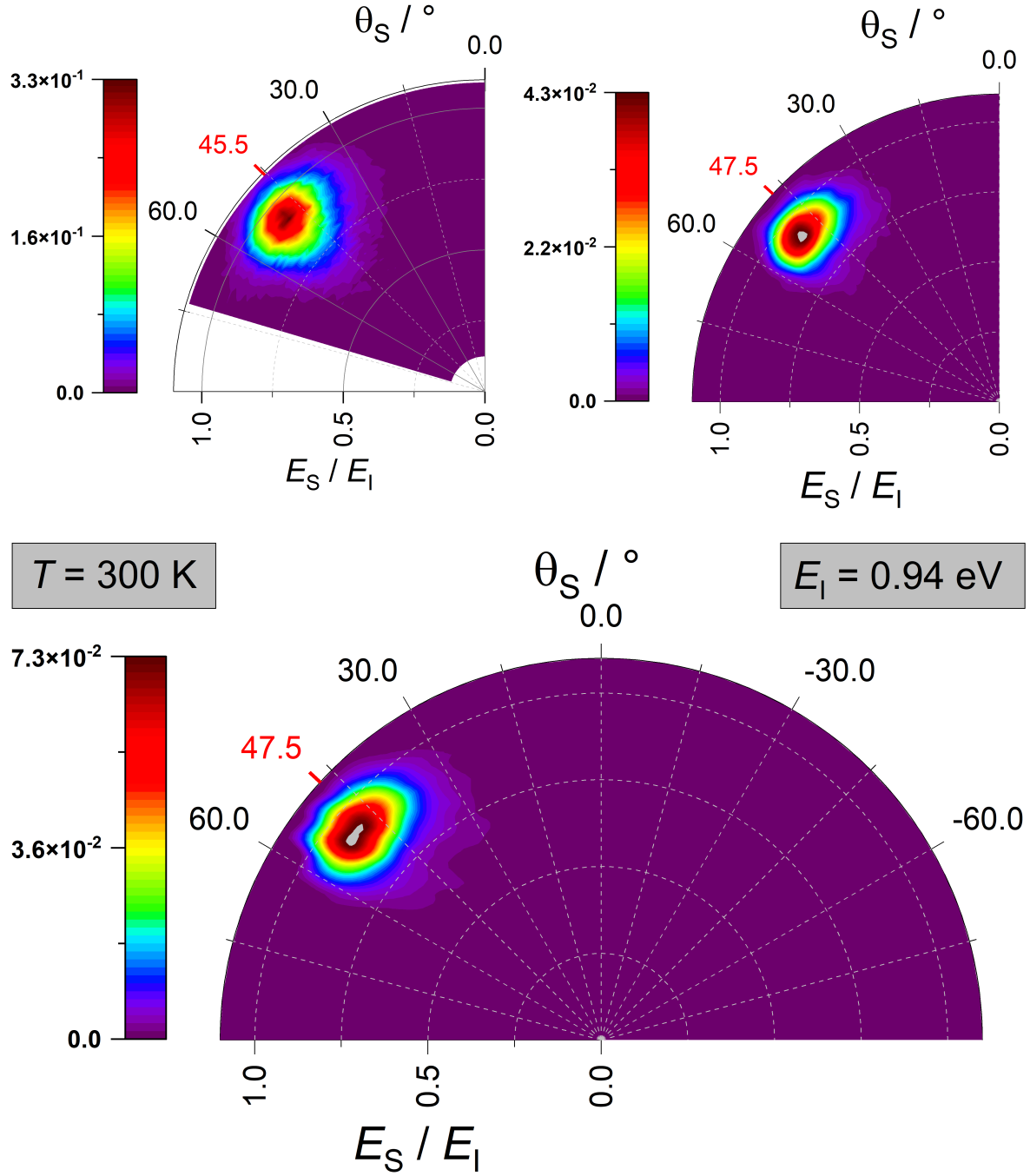


Figure 4.55: Comparing translational energy and scattering angle distribution from experiment (top left) with classical simulations using the HDNN-PES (top right) for D-scattering from graphene. The bottom panel also shows backward-scattering. The incidence kinetic energy  $E_I$  and surface temperature  $T$  are given in gray boxes. The incidence as well as specular polar angle  $\theta_I$  is shown in red. Statistics and further analysis of trajectories are given in Tab. A.11 and A.12.

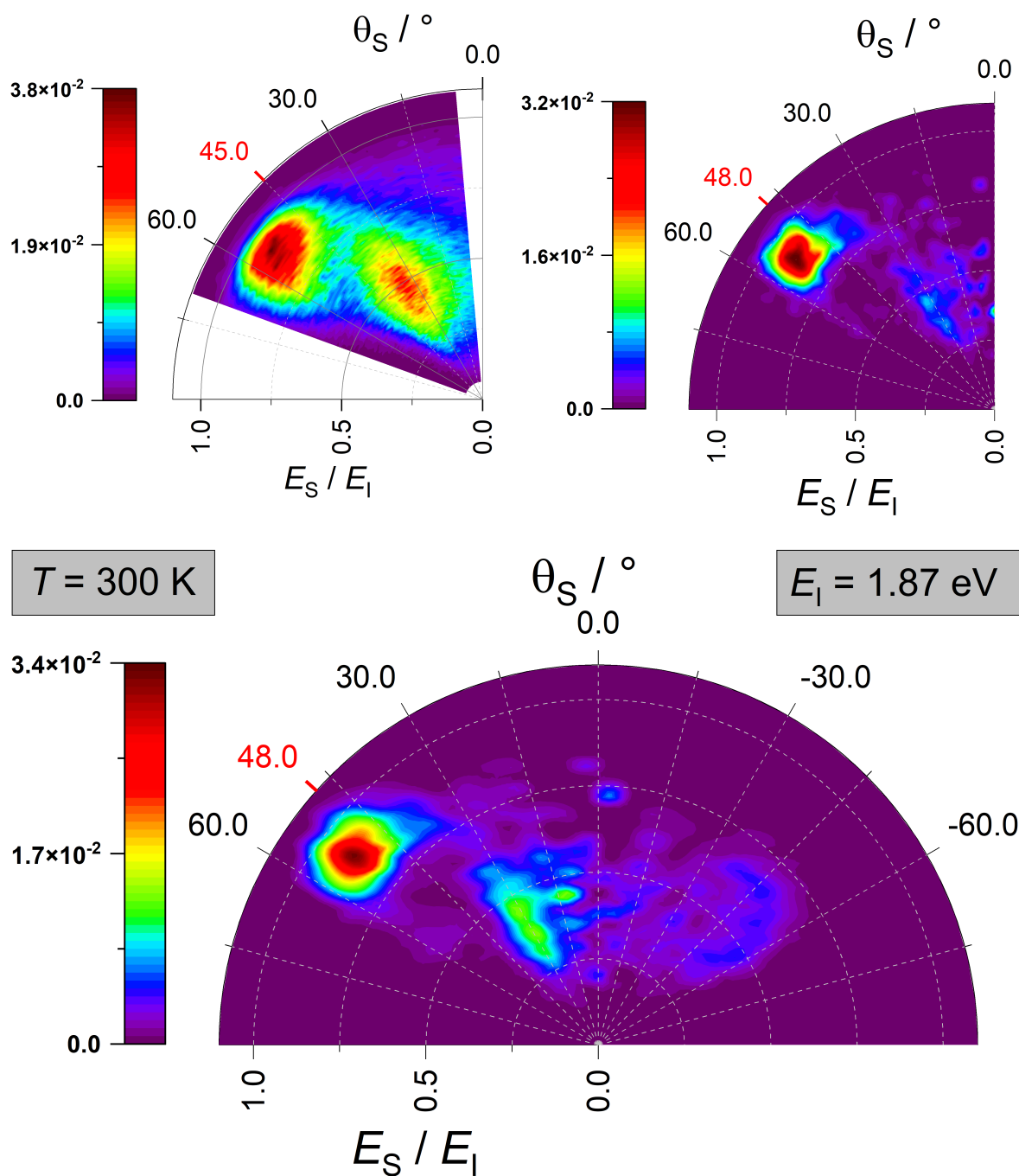


Figure 4.56: Comparing translational energy and scattering angle distribution from experiment (top left) with classical simulations using the HDNN-PES (top right) for D-scattering from graphene. The bottom panel also shows backward-scattering. The incidence kinetic energy  $E_I$  and surface temperature  $T$  are given in gray boxes. The incidence as well as specular polar angle  $\theta_I$  is shown in red. Statistics and further analysis of trajectories are given in Tab. A.11 and A.12.

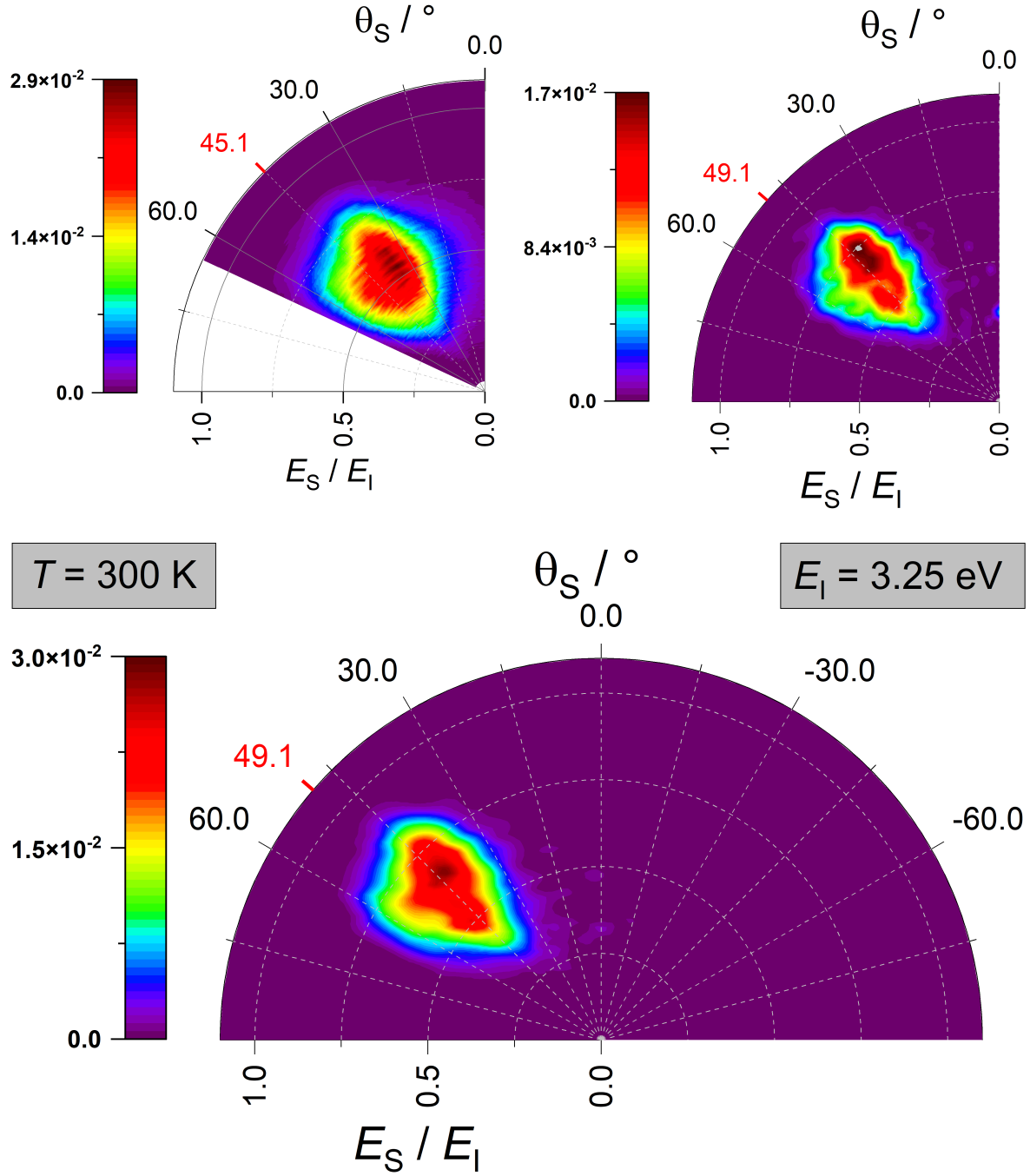


Figure 4.57: Comparing translational energy and scattering angle distribution from experiment (top left) with classical simulations using the HDNN-PES (top right) for D-scattering from graphene. The bottom panel also shows backward-scattering. The incidence kinetic energy  $E_I$  and surface temperature  $T$  are given in gray boxes. The incidence as well as specular polar angle  $\theta_I$  is shown in red. Statistics and further analysis of trajectories are given in Tab. A.11 and A.12.

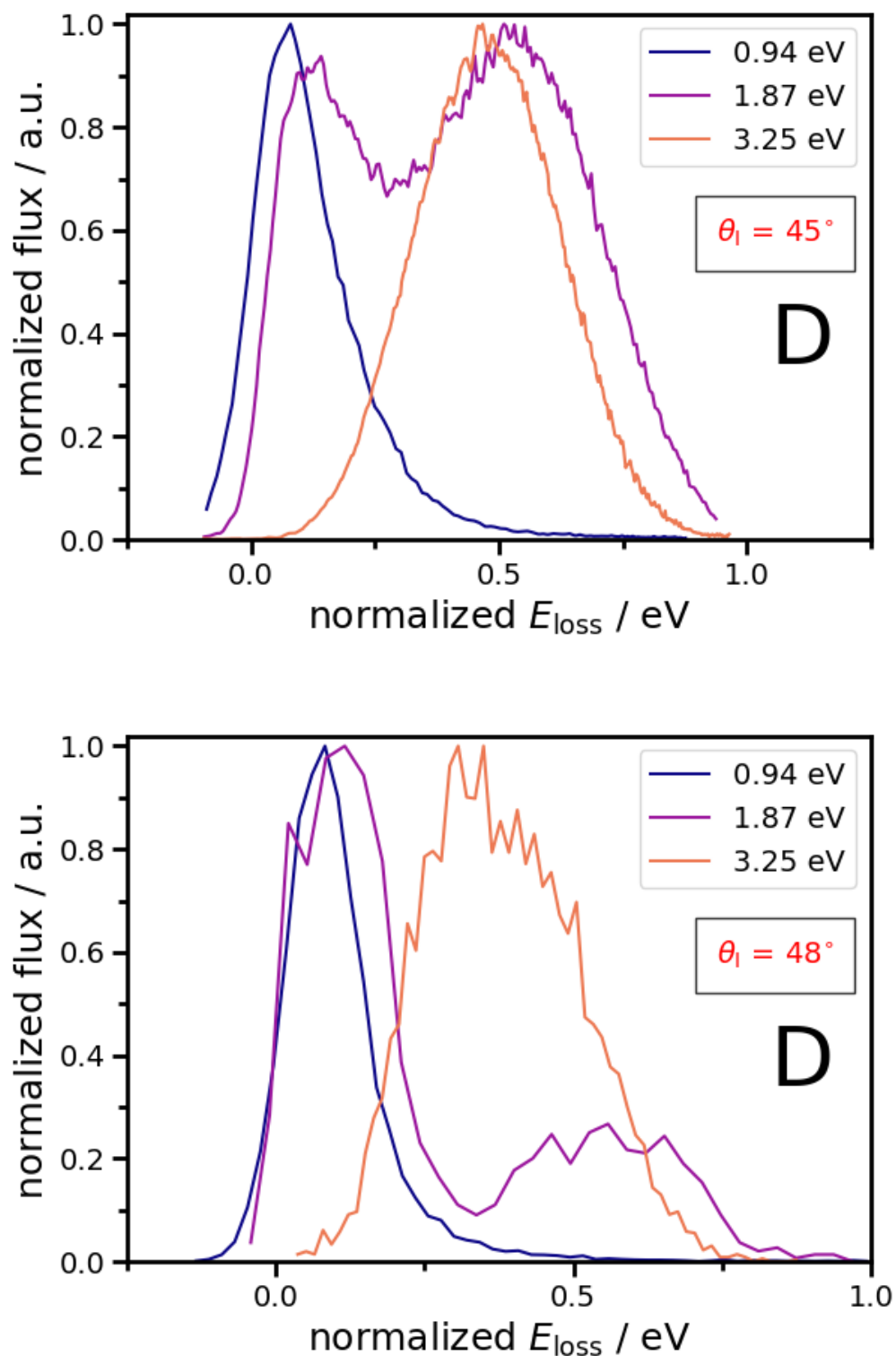


Figure 4.58: Comparing normalized angle integrated energy loss distributions from experiment (top) with classical simulations using the HDNN-PES (bottom) for D-atom scattering from graphene. The incidence polar angle  $\theta_i$  and the different incidence kinetic energies  $E_i$  are given as labels. Note, the incidence angle of simulated D-atom scattering with  $E_i = 3.25$  eV is  $\theta_i = 49.1^\circ$ . The surface temperature is  $T = 300$  K.

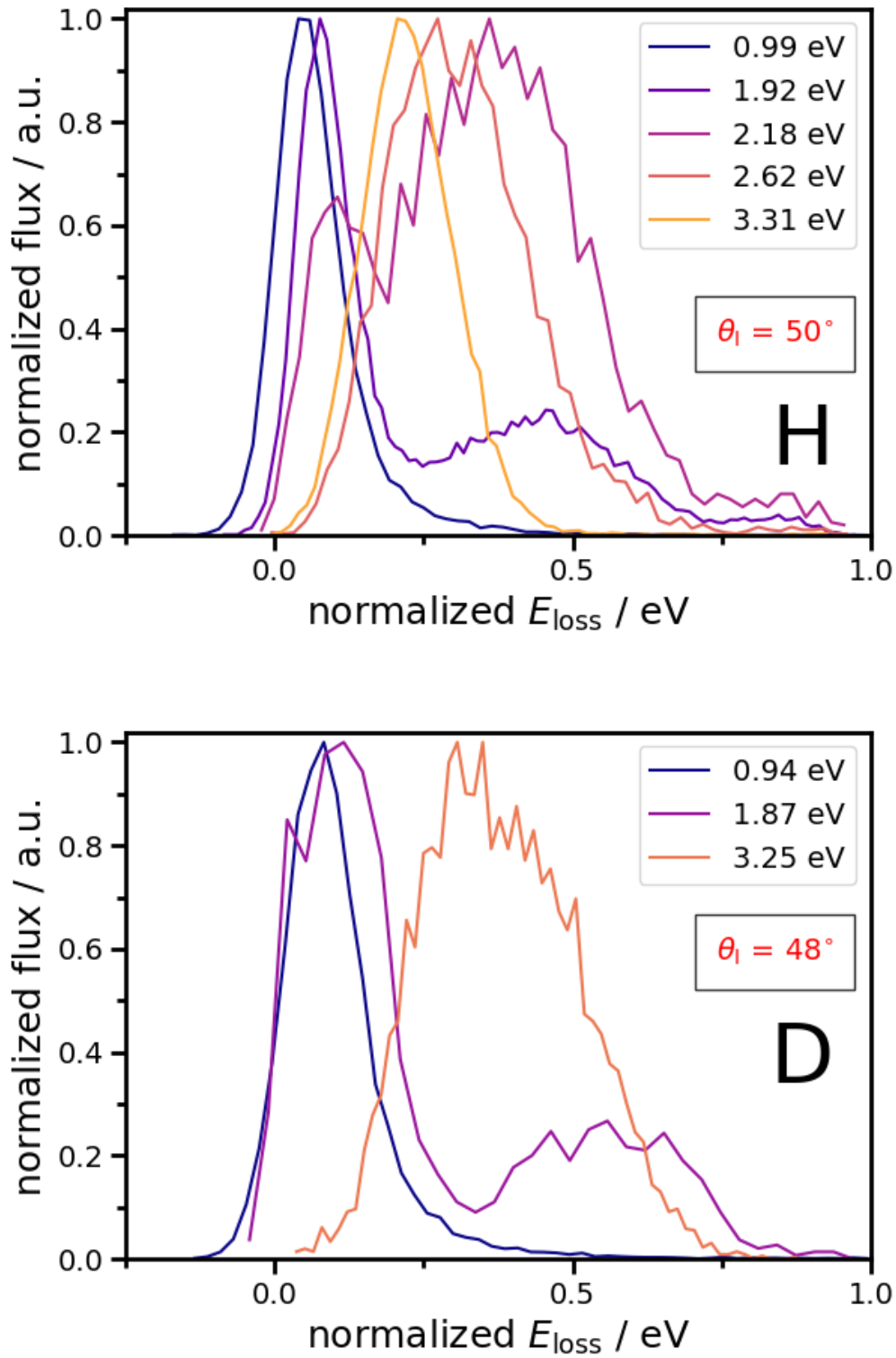


Figure 4.59: Comparing normalized angle integrated energy loss distributions from classical simulations using the HDNN-PES for H-atom (top) and D-atom (bottom) scattering from graphene. The incidence polar angle  $\theta_i$  and the different incidence kinetic energies  $E_i$  are given as labels. Note, the incidence angle of simulated D-atom scattering with  $E_i = 3.25$  eV is  $\theta_i = 49.1^\circ$ . The surface temperature is  $T = 300$  K.

### D-atom scattering depending on the surface temperature

In this section, the scattering of D-atoms depending on the surface temperature is analyzed. There are no experimental results the estimated translational energy and angular distributions can be compared to. Nonetheless, in this section the distributions estimated for D-atom scattering will be compared to theoretical results for H-atoms, which have been showed to reproduce the experimentally found results in a reasonable manner.

**Isotope effect of the projectile depending on the surface temperature** The scattering of D-atoms were performed with  $E_I = 1.92$  eV with  $\theta_I = 50^\circ$  at surface temperatures of 77 K, 300 K and 600 K.

The parameters are defined in Fig. 4.8, an overview of the analysis is shown in Fig. 4.14 and the definition of the channels is given in Fig. 4.17, like mentioned in Sec. 4.3.1 for H-atom scattering.

The total number of trajectories calculated and used for the plots for each temperature is shown in Tab. A.10. The normal component of the kinetic energy is given next to estimated sticking coefficients.

In Fig. 4.60, the translational energy and scattering angle distribution for H-atoms is shown in the top panel and for D-atoms in the bottom panel, respectively. As discussed before, puckering of the C-atom influences the adsorption barrier height. The pre-puckering (movement out of the surface plane) of the carbon atom, that is involved in the transient bond formation is less pronounced at smaller surface temperatures. The effective barrier is smaller at higher surface temperatures, explaining the rise in signal for the slow channel, because more H-atoms can cross the barrier. At higher surface temperatures, more vibrational states are excited and energy dissipation is less efficient, which can be seen when following the trend of sticking coefficients estimated and shown in Tab. A.9. Compared to H-atoms, D-atoms have an increased probability to be adsorbed. However, due to the higher thermal in-plane movement of surface C-atoms, the atoms can easier rearrange when the sonic wave that is created by C–H bond formation whereas out-of-plane movement also decrease the barrier. The intensity for back-scattering rises with the surface temperature, which further indicates a change in the effective barrier height. The signal intensity in backward scattering direction for D-atoms is higher compared to H-atoms. Previous, it was stated that a higher surface temperature increases the chance of H-atoms crossing the barrier, but the energy transfer mechanism is not changed. Like for H-atoms, the temperature does not alter the energy dissipation pathway, but the changed inertia of the projectile and the corresponding increased interaction time with the surface is enhancing the energy dissipation in case of D-atoms. That explains the difference in the ratios of the fast and slow channel and why the signal for the slow channel is smaller compared to H-atoms. The decreasing sticking coefficients for higher surface temperatures, the effective barrier and efficiency of the energy dissipation explains the change of the ratios of the fast and slow channel seen, which is analog to H-atoms. The simulations seem to be reasonable distinguish between H- and D-atom scattering depending on the surface temperature, but this has not been experimentally validated.

To better compare the change in the ratios of the fast and slow channel for both isotopes, in Fig. 4.63 only considering forward scattering is shown.

Again, also energy loss distributions are analyzed. In Fig. 4.64, the energy loss  $E_{\text{loss}}$  distribution of H-atoms are shown in the top panel and D-atom distribution is shown in the bottom panel for surface temperatures of  $T = 77$  K, 300 K and 600 K, respectively. For both isotopes, the incidence polar angles is  $\theta_I = 50^\circ$ . Again, the fast channel is the peak around 0 eV and the slow channel has a broader shape around  $E_{\text{loss}} = 0.5$  eV. Like before, the average energy loss in case of D-atoms is shifted to higher values and has a broader shape, which can

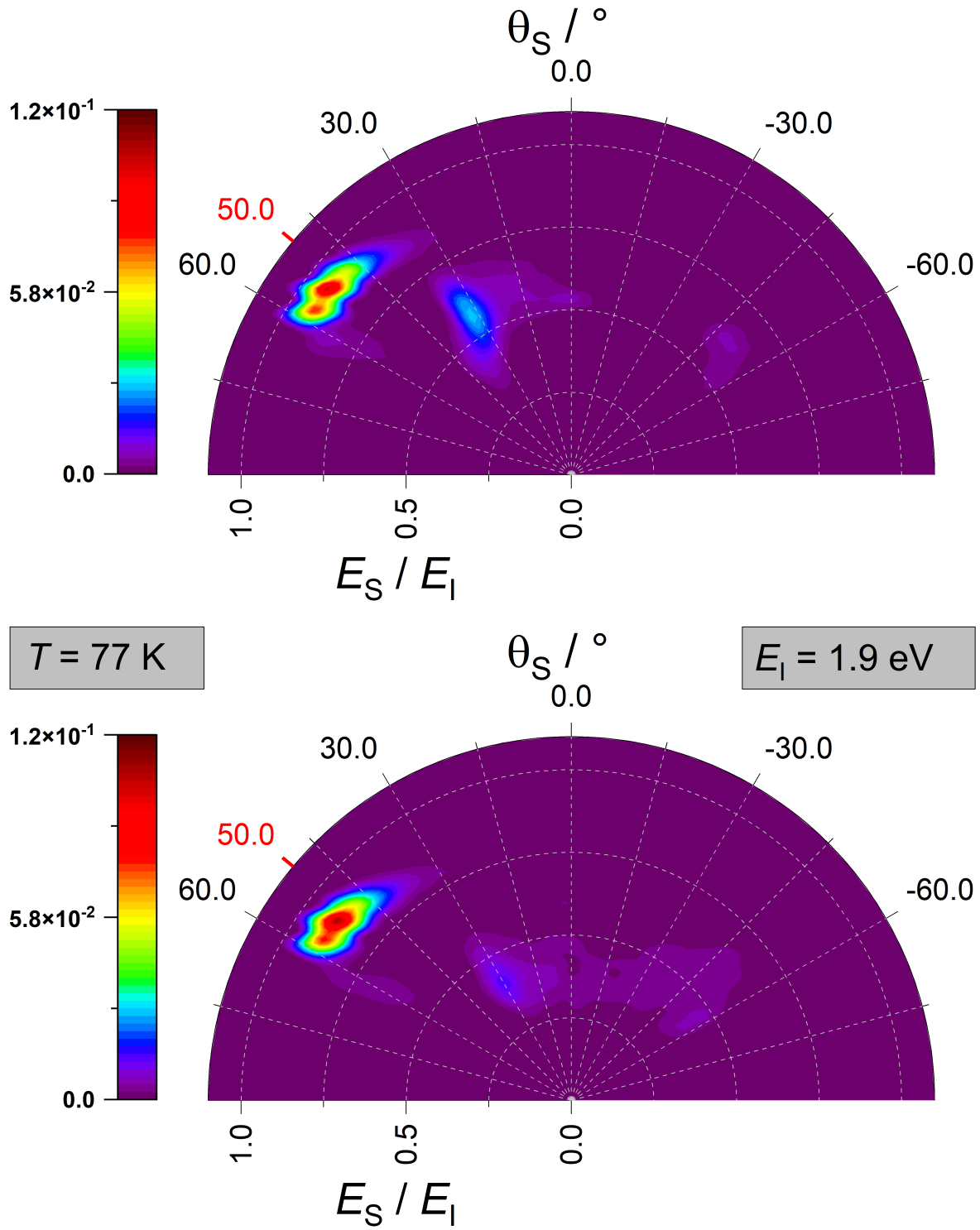


Figure 4.60: Comparing translational energy and scattering angle distribution from classical simulations using the HDNN-PES for H-atom (top) with D-atom (bottom) scattering from graphene. The incidence kinetic energy  $E_I$  and surface temperature  $T$  are given in gray boxes. The incidence as well as specular polar angle  $\theta_I$  is shown in red. Statistics and further analysis of trajectories are given in Tab. A.10.

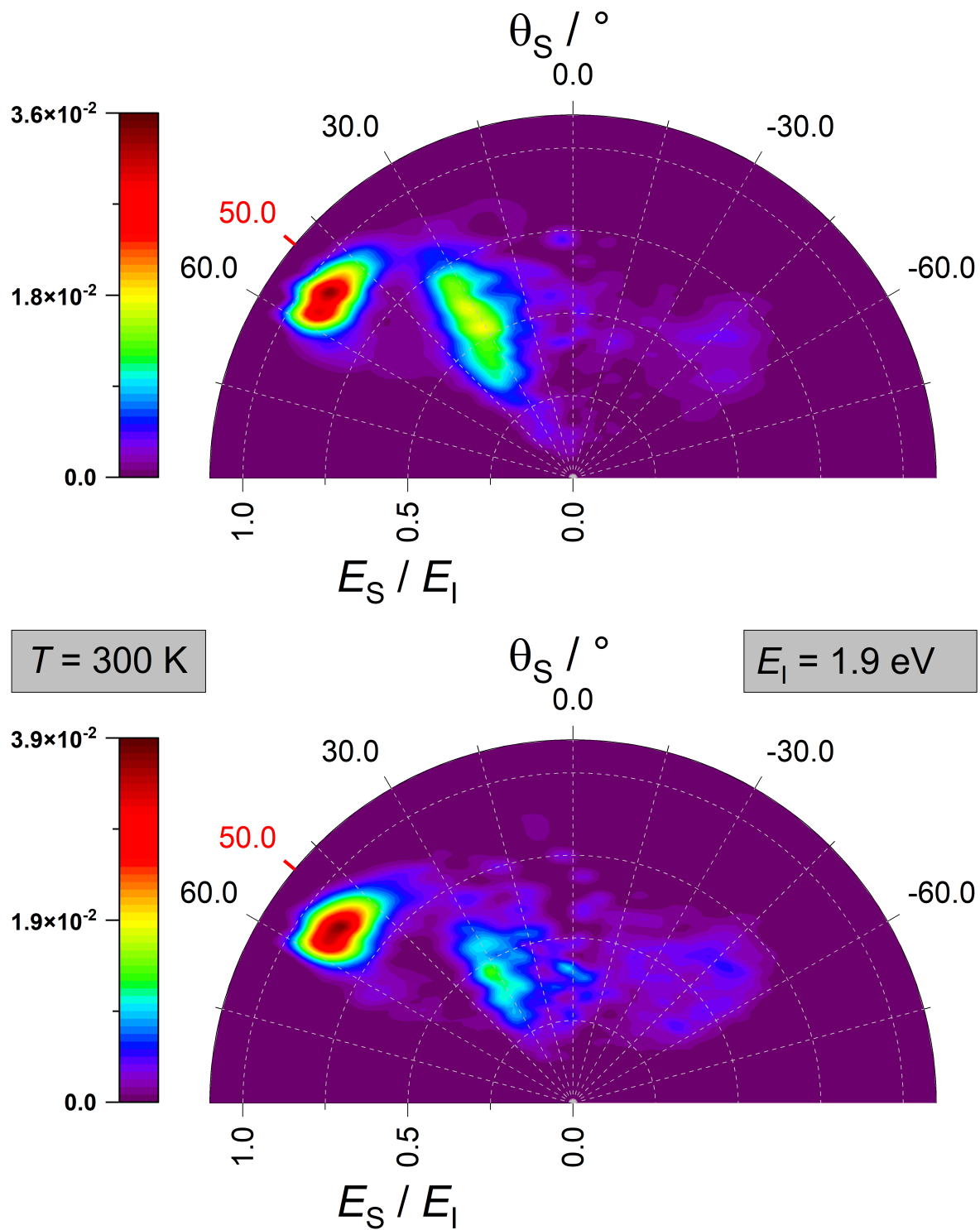


Figure 4.61: Comparing translational energy and scattering angle distribution from classical simulations using the HDNN-PES for H-atom (top) with D-atom (bottom) scattering from graphene. The incidence kinetic energy  $E_I$  and surface temperature  $T$  are given in gray boxes. The incidence as well as specular polar angle  $\theta_I$  is shown in red. Statistics and further analysis of trajectories are given in Tab. A.10.



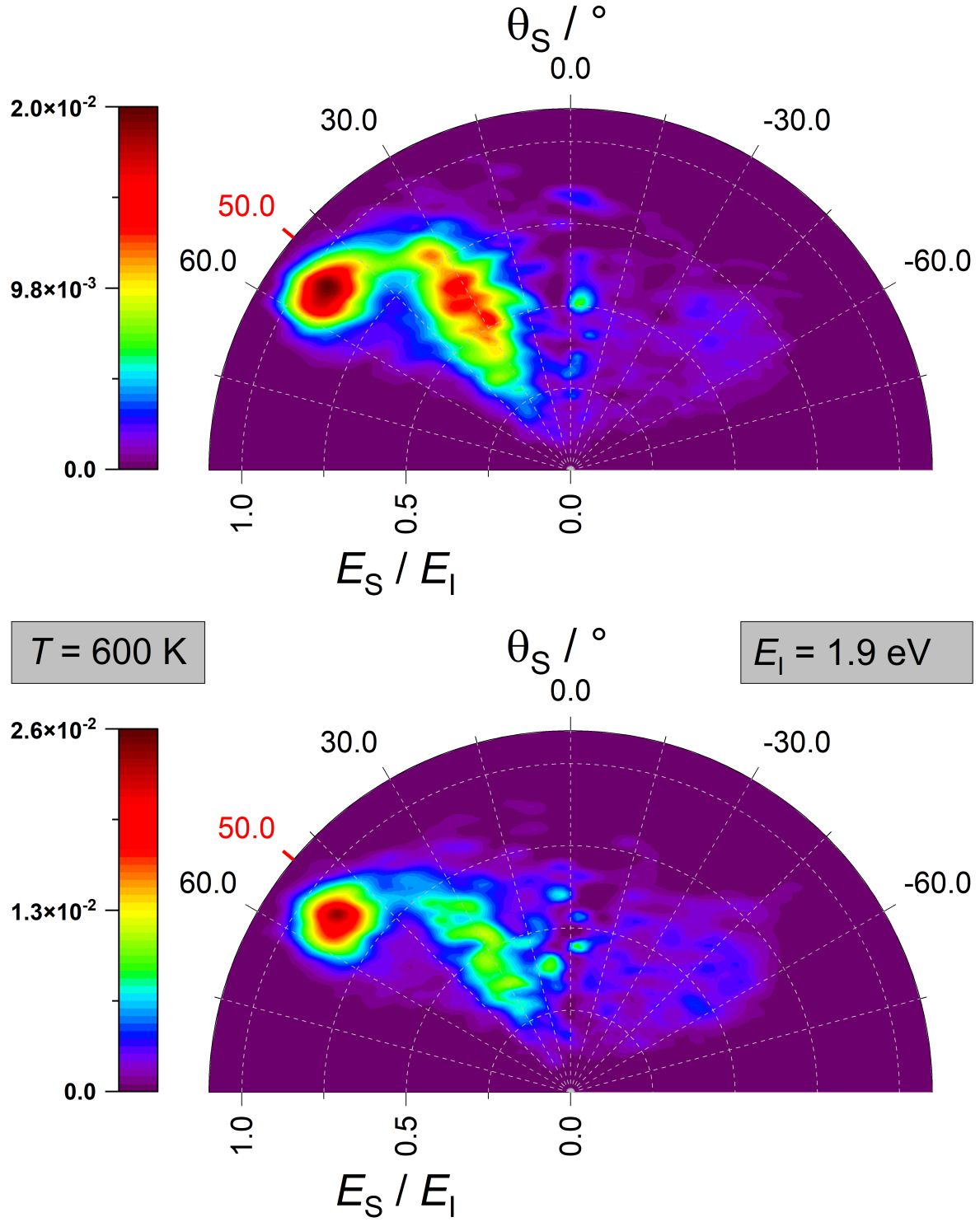


Figure 4.62: Comparing translational energy and scattering angle distribution from classical simulations using the HDNN-PES for H-atom (top) with D-atom (bottom) scattering from graphene. The incidence kinetic energy  $E_I$  and surface temperate  $T$  are given in gray boxes. The incidence as well as specular polar angle  $\theta_I$  is shown in red. Statistics and further analysis of trajectories are given in Tab. A.10.

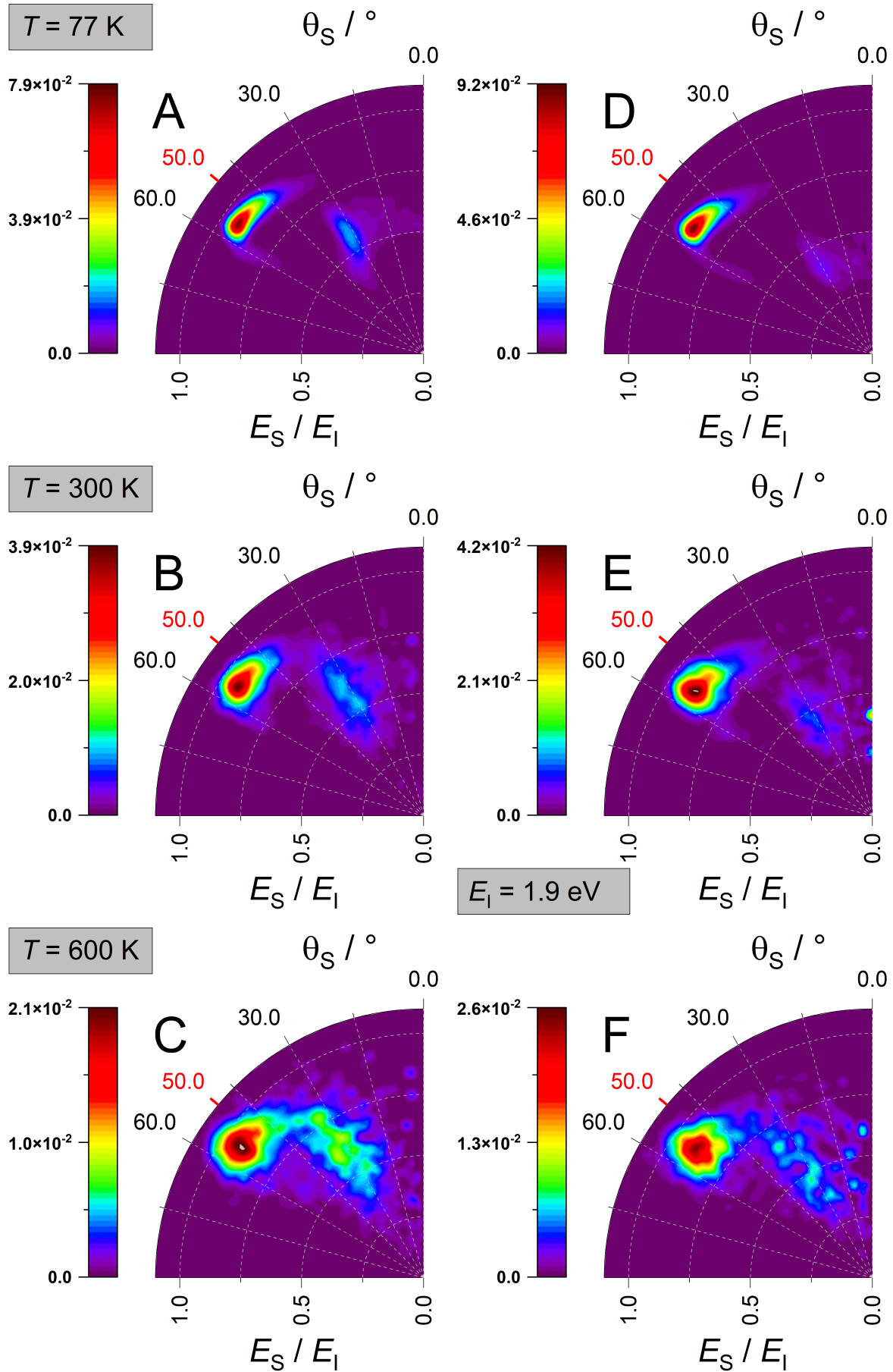


Figure 4.63: Comparing the translational energy and scattering angle distributions from classical simulations using HDNN-PES for H-atom (panels A–C) and D-atom (panels D–F) scattering from graphene. The incidence kinetic energy  $E_I$  and surface temperature  $T$  are given in gray boxes. The incidence as well as specular angle  $\theta_I$  is shown in red. Statistics and further analysis of trajectories are given in Tab. A.10.

be explained simply with the higher inertia of D-atoms compared to H-atoms. The ratio of the slow channel compared to the fast channel is increased at higher surface temperatures.

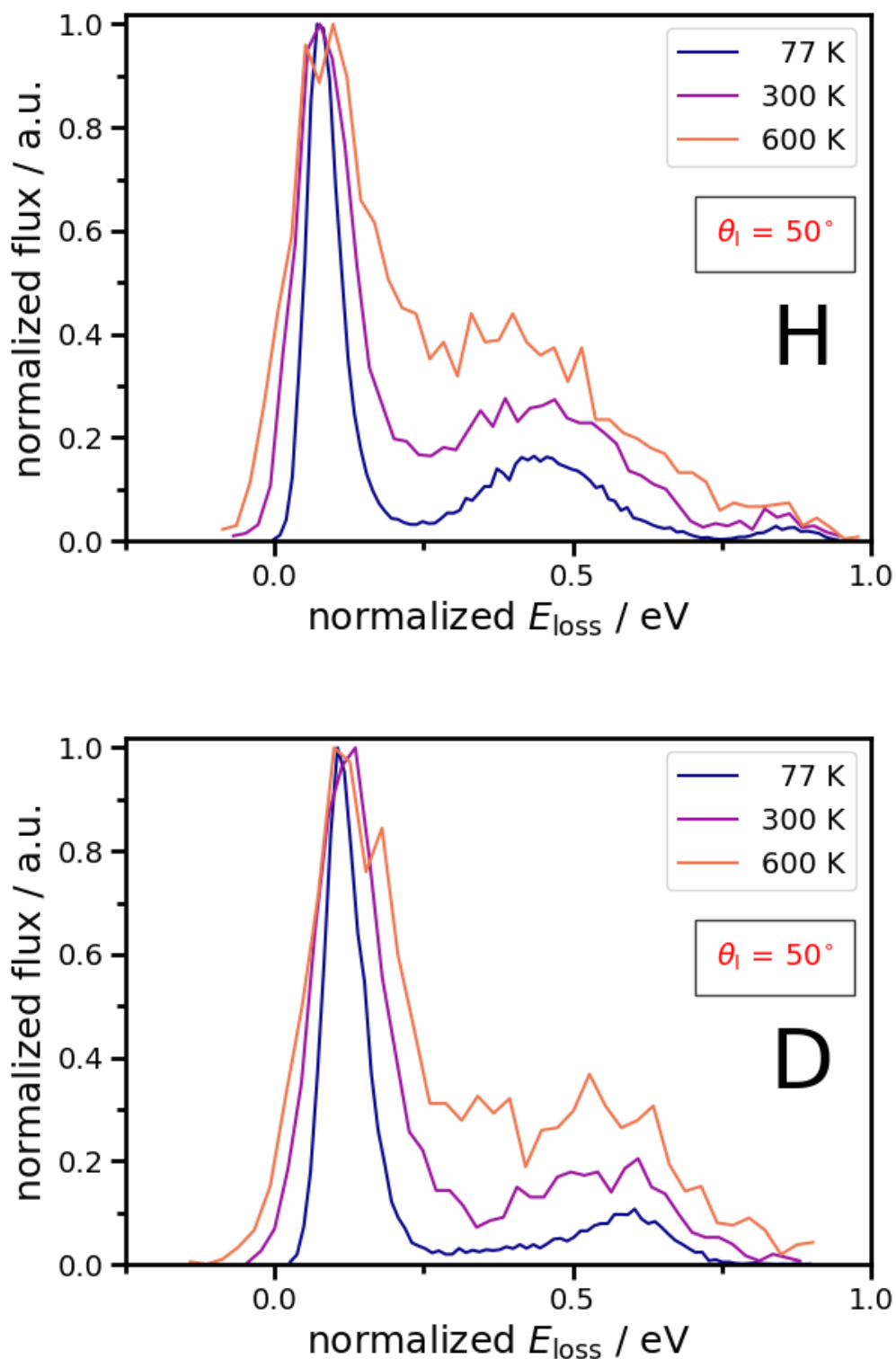


Figure 4.64: Comparing normalized angle integrated energy loss distributions from classical simulations using the HDNN-PES for H-atom (top) with D-atom (bottom) scattering from graphene. The incidence polar angle  $\theta_i$  and the different surface temperatures are given as labels. The incidence kinetic energy of H- and D-atoms is  $E_i = 1.9$  eV.

### D-atom scattering depending on the surface isotope effect

In the following section and as already done in Sec. 4.3.1 for H-atom scattering, the D-atom scattering angle depending on the surface isotope effect of the free-standing graphene sheet will be analyzed. As before, the slab consist fully of  $^{12}\text{C}$  carbon atoms but here a slab of fully  $^{13}\text{C}$  carbon atoms is investigated as well. Since the surface geometry is not changed when changing the mass of the projectile, the same structures generated in case of H-atom scattering from the surface with different masses can be used again, reducing the amount of preparation.

The incidence angle, the number of trajectories used for the comparison, the normal kinetic energy and estimated sticking coefficients are shown in Tab. A.13

The energy loss distributions from H-atom scattering from graphene will be analyzed. H-atom scattering from a fully  $^{13}\text{C}$  graphene sheet is compared to a fully  $^{12}\text{C}$  graphene sheet. The scattering has been simulated for H-atoms at six different incidence angles from  $\theta_1 = 10^\circ$  to  $\theta_1 = 60^\circ$  in steps of  $10^\circ$  and is shown in Fig. 4.65. Note, because there were the results already shown for  $\theta_1 = 43^\circ$  and  $51^\circ$ , those angles are used when changing the mass of the surface. Like done in Sec. 4.3.1 before, here all trajectories are used in the energy loss distributions, because there are no distributions accessible from experiment. Therefore, the geometry of the detection does not have to be considered and together better statistics are achieved. Note that in this sections only theoretical energy loss distributions are compared, which both based on the HDNN-PES. The purpose of this section is not to predict, what might be possible to see in experiment, but considering the isotope effect the surface can give a hint, if the HDNN-PES is able to predict even smaller effects.

Changing the mass of the surface by introducing carbons most common isotope only slightly changes the average energy loss of the impinging atom to smaller energy losses due to the higher inertia of the graphene surface. The surface isotope effect does not have a significant influence on the scattering events. This can be explained by considering the increased inertia of the surface, making forming a transient bond and energy dissipation via phonon excitation less likely.

By accident, I found out that especially for D-atoms if the incidence polar angle is only shifted by  $1^\circ$  to smaller angles, the signal of the slow component significantly drops off, indicating an ever stronger incidence angle dependence when simulating the D-atom scattering from the graphene surface.

For H-atom and D-atom scattering we get exactly the same results, changing the mass of the surface by introducing carbons most common isotope only slightly changes the average energy loss of the impinging atom to smaller energy losses due to the higher inertia of the graphene surface. The surface isotope effect does not have a significant influence on the scattering events. This can be explained by considering the increased inertia of the surface, making forming a transient bond and energy dissipation via phonon excitation less likely. The differences at D-atom scattering with  $\theta_1 = 60^\circ$  are very subtle and barely seen in the figure. At  $\theta_1 = 51^\circ$  however, the differences especially for the slow channel are most pronounced. As mentioned, here both channels are present and a change in inertia has a stronger influence of the scattering events.

To summarize the results of D-atom scattering from graphene shown so far, I could show that classical trajectories carried out using the HDNN-PES are able to describe the isotope effect as seen in experiment. Independent of the incidence conditions, the subtle differences as seen in experiment are captured by the PES. Even for conditions, where no experimental results are available, the trend is in agreement with the trend seen before and compared to experiment. Those results, which have not been experimentally validated at least are reasonable and fit to the understanding of previous investigations.

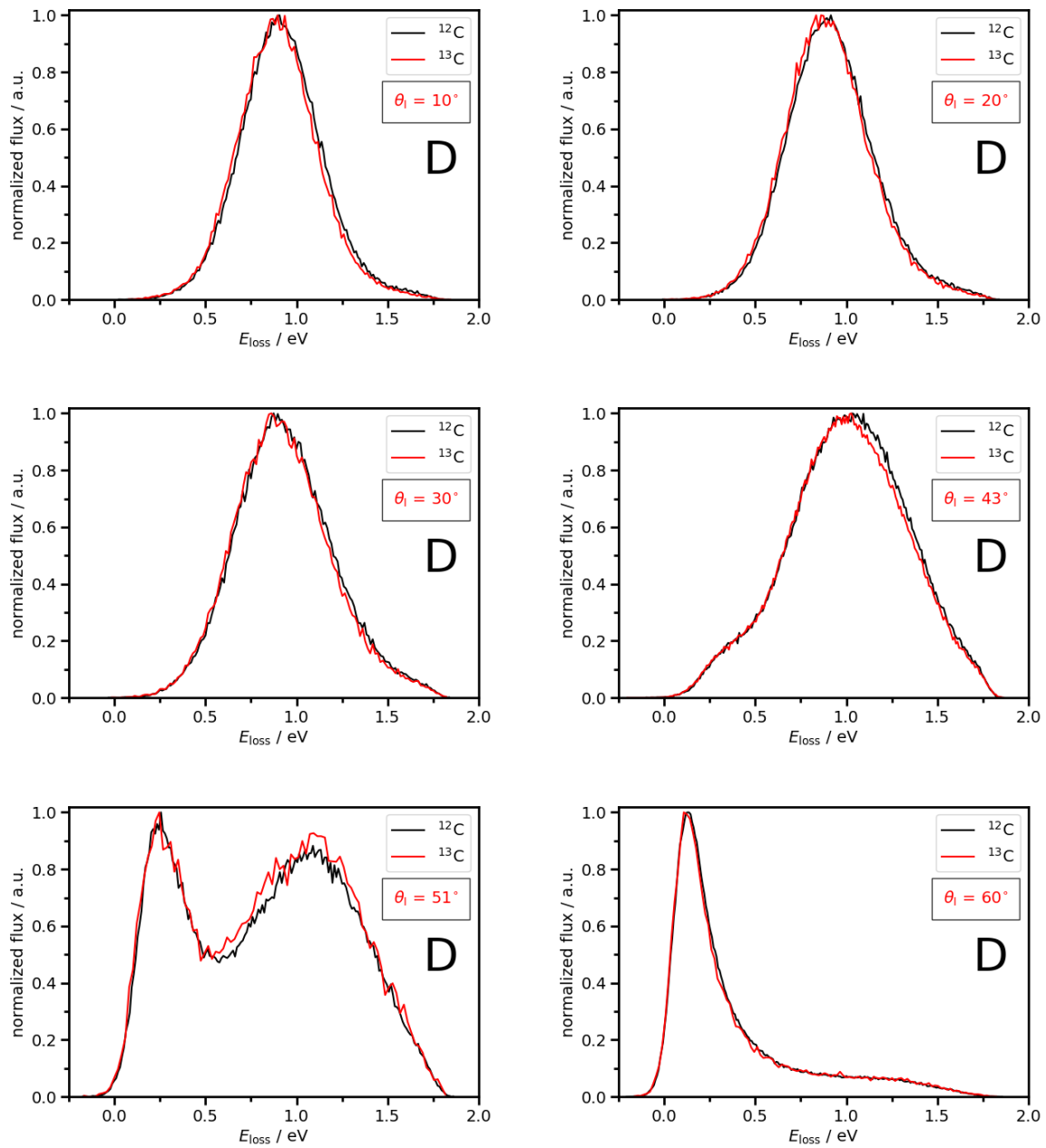


Figure 4.65: Energy loss distribution for D-atom scattering with incidence kinetic energy of  $E_I = 1.9$  eV for given incidence angle  $\theta_I$  depending on the mass of the surface (surface isotope effect). The scattering is shown for a fully  $^{12}\text{C}$ - and fully  $^{13}\text{C}$ -graphene surface.

### 4.3.2 Comparison to HBEAM Experiment

In comparison to the RAT experiment, in the HBEAM experiment, also epitaxial graphene is considered, but here it is grown on a Ir(111) surface. Platinum as well as Iridium have only weak interactions with the graphene sheet and again, the system can be seen as quasi-free standing graphene. Compared to RAT, here the system can be seen even more as free from interactions to the underlying substrate.

Unlike for H- and D-atom scattering before, when the incidence polar angle of the impinging particle is  $0^\circ$ , it is not necessary to consider different domains of the graphene sheet grown on the metal substrate anymore. But the rotation of the whole graphene sheet estimated in LEED experiment has to be accounted for. With the information from experiment, this has to be considered when analyzing trajectories. In HBEAM as well as in RAT experiment, also in-plane scattering has to be considered when analyzing the scattering. To create a one-to-one comparison of theory and experiment again, the setup of the HBEAM experiment has to be accounted for. This means, only trajectories scattering in between  $\pm 30^\circ$  polar angle and  $\pm 4.5^\circ$  azimuthal angle will be considered, because they match the detection geometry. From LEED, the analysis will take an overall rotation of  $\varphi = -42^\circ$  into account to match the geometry of the detector. However, even if out-of plane scattering is considered as well, the energy loss distribution is not affected. This is contrary when comparing the results to RAT experiment, where a large fraction of out-of plane scattering can be seen in the simulations. In the simulations, the projectile was launched  $6.0 \text{ \AA}$  above the surface.

It was mentioned before, that a transient C–H bond is efficiently formed with normal kinetic energy. Here, all of the initial kinetic energy of the impinging atom can contribute to the bond formation. Unlike before, the two different channels are not angle separated any more, which will be discussed in detail in the following.

In this section, only the translational energy and scattering angle distributions are compared. Because of the geometry of the experiment, the complete range of scattered angles is considered as already done when comparing to RAT experiment. But here, there is data for backward and forward scattering, because it is distributed along the surface normal. The further analysis of energy loss distribution is not offered here, but in the next section, where quantum effects are taken into account. I did this in order to highlight the change of distributions for different levels of theory. Again, the details of the scattering trajectories are given and the tables showing all information are mentioned.

#### H-atom scattering depending on the incidence energy

The H-atom scattering depending on the incidence kinetic energy  $E_I = 0.99 \text{ eV}$  and  $1.92 \text{ eV}$  will be analyzed. The surface temperature is  $T = 300 \text{ K}$  for all incidence conditions. The incidence polar angle of the H-atom is  $\theta_I = 0.0^\circ$ , which corresponds to scattering along the surface normal. Unlike before, the normal component is exactly the incidence energy meaning all of the incidence kinetic energy can contribute to the interaction with the barrier to adsorption. Here, the projectile was launched  $6.0 \text{ \AA}$  above the surface.

The parameters are defined in Fig. 4.8 and an overview of the analysis is shown in Fig. 4.14, like mentioned before.

The statistics of H-atom scattering from free-standing graphene along the surface normal from MD simulations using a HDNN-PES are given in Tab. A.15. The number of simulated trajectories, scattered trajectories within detection limit compared to experimental setup and sticking coefficients are given. Here, just the normal component is given, because it is exactly the incidence kinetic energy. Transient C–H bond is efficiently formed with normal kinetic energy.

Due to the geometry, there are no independent signals for the slow and fast component

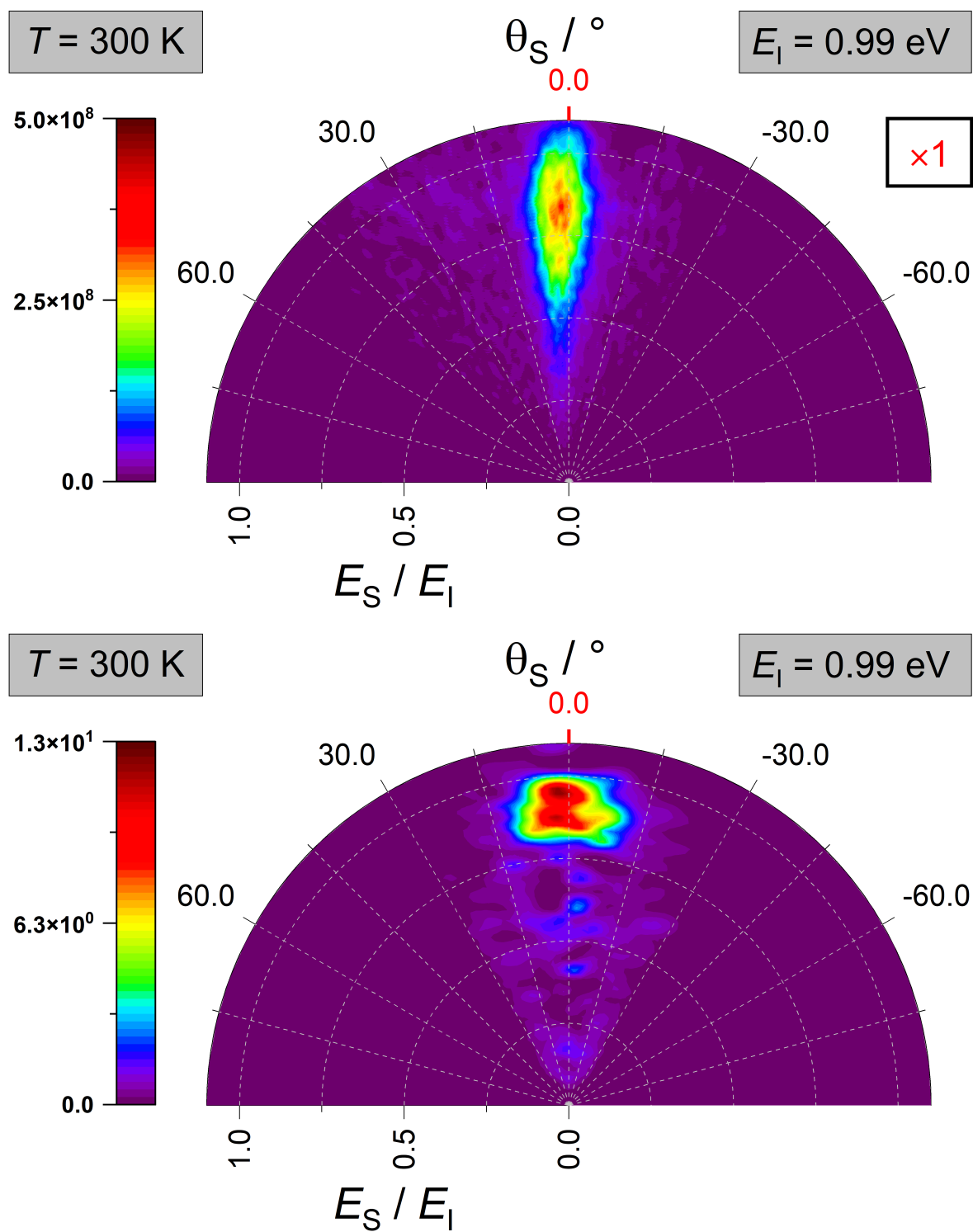


Figure 4.66: Comparing translational energy and scattering angle distribution from HBEAM experiment (top) with classical simulations using the HDNN-PES (bottom) for H-atom scattering from graphene. The incidence kinetic energy  $E_I$  and surface temperature  $T$  are given in gray boxes. The incidence as well as specular polar angle  $\theta_I$  is shown in red. Statistics and further analysis of trajectories are given in Tab. A.15.



anymore. In Fig. 4.66 the translational energy and scattering angle distribution is shown from experiment in the top panel and the estimated distribution from HDNN-PES is shown in the bottom panel. In the top panel, a single signal can be seen, but with a very broad shape. A lot of energy gain in kinetic energy can be observed as well as intensity ranging from former quasi-elastic scattering with nominal energy loss to  $\approx 0.5$  eV, which corresponds to inelastic scattering events. Because of the incidence angle, here is not a clear separation of the two channels according to the angle, as it was before in the distributions from RAT experiment. Here, the HDNN-PES predicts a nearly exclusive quasi-elastic scattering. Although there are some minor signal intensities found for smaller normalized final kinetic energies, it is not able to reproduce the correct shape. Although the broad angular spread of the signal is not fully reproduced, but in the HDNN-PES all seems to be more localized around the fast channel.

For this condition, scattering does not happen exclusively before crossing the barrier, but also there are moderate intensities observable of projectiles after crossing the barrier to adsorption. The dominant scattering is still quasi-elastic, which can be best seen in the bottom panel in Fig. 4.66. Interestingly a very coarse comparison only on the qualitative site at least seems to indicate the right direction, but unlike when comparing to RAT experiment, here the deviations are more pronounced.

Changing the incidence kinetic energy of the projectile to  $E_I = 1.92$  eV, again a single peak can be seen in the distribution obtained from experiment. This is shown in Fig. 4.67 in the top panel. In contrast to scattering with 0.99 eV, the peak is shifted to smaller normalized final kinetic energies, its signal intensities are more localized around the surface and have a larger range. Energy gain of the projectile is less pronounced ( $E_S/E_I > 1.0$ ). In contrast to that, the signal intensities with a larger angular spread are increased compared to  $E_I = 0.99$  eV. The red number in the black box indicates, that the found flux is decreased by a factor of 10 compared to the distribution of 0.99 eV.

The distribution from HDNN-PES is shown in Fig. 4.67 in the bottom panel. Like before, the signal is rather localized but now shows the slow channel exclusively. Analyzing the simulations, here scattering happens exclusively after crossing the barrier. Scattering before the barrier can be seen, but only a small fraction.

In the scattering with  $E_I = 0.99$  eV, the sticking coefficient is 0.53, more than half of the trajectories show adsorption events. Increasing the kinetic energy of the H-atom to  $E_I = 1.92$  eV, the sticking coefficient drastically drops to 0.01, adsorption events are highly unlikely. This makes total sense. At 0.99 eV, the normal energy is enough to overcome the barrier to adsorption. But crossing the barrier again only happens in half of the times. When comparing this to results from the RAT experiment, it makes sense that increasing the angle at this incidence kinetic energy will enhance crossing of the barrier again to finally get scattered back into the gas phase. Therefore, the sticking coefficient is reduced. But speaking of the energy, it still depends, how efficient the energy can be distributed to surface phonons. Therefore, it makes sense to still see adsorption. It is the exact same argumentation in case of 1.92 eV when comparing to RAT, the sticking coefficient decreases, because all of the projectiles kinetic energy is normal energy. It is therefore easy to cross the barrier and re-crossing again is enhance due to the high energy, that cannot be effectively distributed on the time scale of the interaction, resulting in minor adsorption events. The overall predicted trend of changed sticking coefficients is in total agreement with previous studies and are confirmed by the picture of the dynamical barrier.

To deepen the insights of the dynamical processes taken place on the surface, the scattering was performed at different conditions. By adjusting the initial conditions and analyze the distributions might help to understand the underlying dynamics even further.

For this reason, several conditions are investigated. First, the scattering for a particle with  $E_I = 1.50$  eV was investigated, too. The energy was chosen to be in the middle of the two others. This was done in order to see the dynamics in between, if there is a more energy dependent

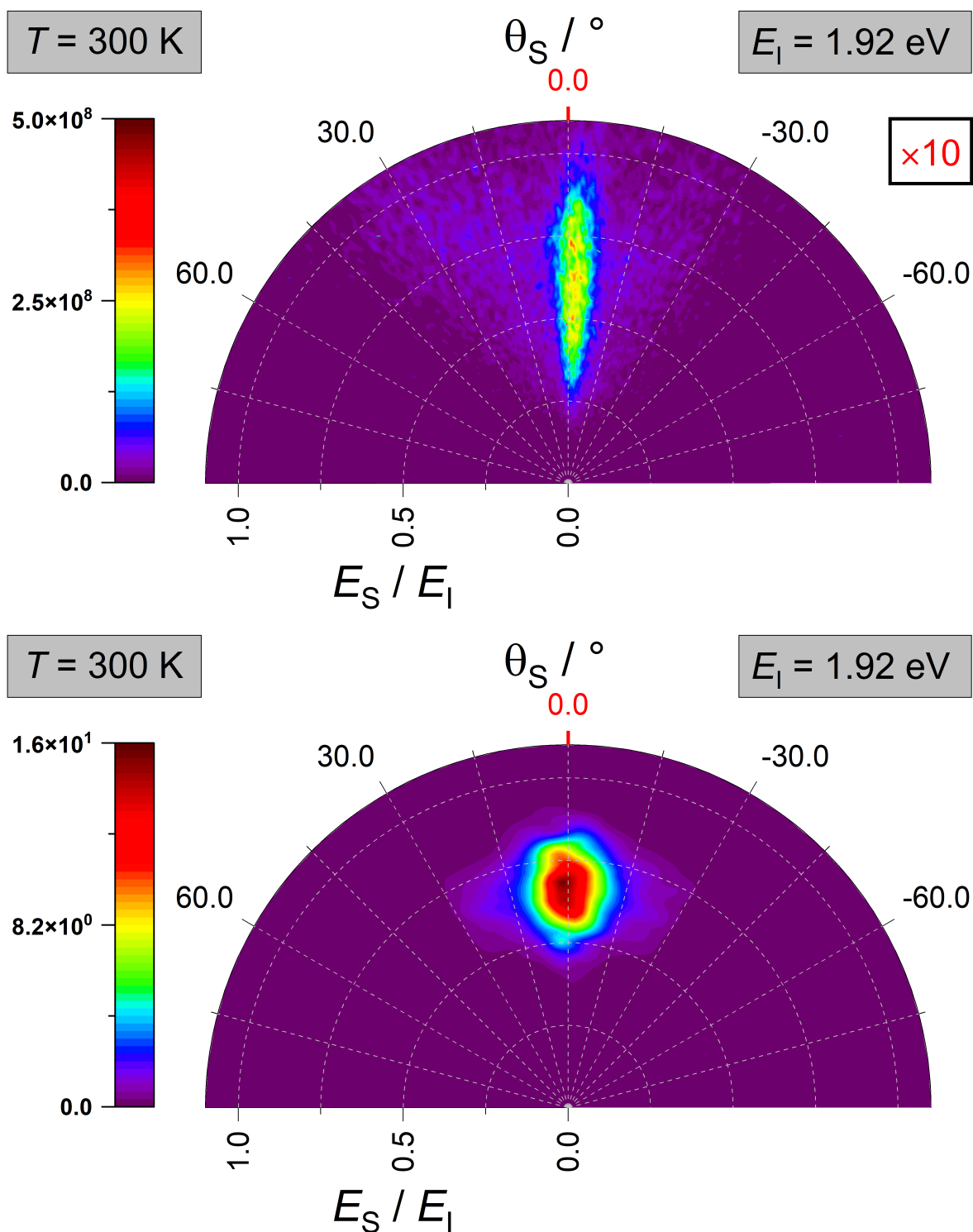


Figure 4.67: Comparing translational energy and scattering angle distribution from HBEAM experiment (top) with classical simulations using the HDNN-PES (bottom) for H-atom scattering from graphene. The incidence kinetic energy  $E_I$  and surface temperature  $T$  are given in gray boxes. The incidence as well as specular polar angle  $\theta_I$  is shown in red. Statistics and further analysis of trajectories are given in Tab. A.15. Note, the red number in the black box indicates the drop in flux compared to H-atom scattering with  $E_I = 0.99$  eV.

dynamic influence of the surface. This makes also sense because all of the incidence energy is normal energy and with this, the energy to efficiently overcome the barrier is reduced, in contrast to RAT experiment, where the normal energy depends on the angle and the initial kinetic energy of the projectile. Additionally, to determine if there is an isotope effect, scattering was also simulated for D-atoms. The incidence energies have been chosen to be  $E_I = 0.94$  eV, 1.50 eV and 1.87 eV, respectively. The number of trajectories, those who fulfill the geometry of the experiment, the normal energy and estimated sticking coefficients are given in Tab. A.15.

Note, since the results compared to our latest HBEAM experiment are rather new, a complete analysis is still missing and we just started to get insights, how to reproduce the experimental findings to understand the mechanisms contributing to the measured distribution of H-atom scattering from epitaxial graphene along the surface normal.

But, because of the visible discrepancies in the translational energy and angular distributions, the overall reproduction of found experimental results has to be improved. Although it was reported that nuclear quantum effects only have a small influence on the scattering behavior of H- and D-atoms scattering from graphene, scattering along the surface normal was neither measured nor investigated before. Here, the barrier to chemisorption is most pronounced. This might indicate, that nuclear quantum effects have a stronger influence for this incidence conditions. Therefore and because it was already mentioned that the comparison does not reproduce the experimental findings quite well, in the following section, quantum effects will be accounted for in the simulations.

## 4.4 Quantum Simulations

In Sec. 4.1.2 it was mentioned that because a barrier is involved, nuclear quantum effects might play a role. Although from previous studies it could be shown that quantum effects only have a minor influence for H- and D-atom scattering from free-standing graphene with incidence kinetic energy of 1 eV. However, from the comparison of translational energy and scattering angle distributions as shown in the previous section, there are indications that nuclear quantum effects might have a stronger influence at this incidence conditions, because the barrier to chemisorption is most pronounced. Reproduction of translational energy and scattering angle distributions is poor for H-atom scattering along the surface normal, therefore in the following sections, nuclear quantum effects will be accounted for in the simulations. This has already been done by using path integrals in ring polymer molecular dynamics simulations to account for tunneling and zero point energy. The computational details of path integral based molecular dynamics simulations is given in Sec. 3.10.

The theoretical background of QMD simulations when using MCTDH are given in [166]. I did not do QMD simulations, I am just showing the results from our collaborators [30]. For more technical details and theory applied, the interested reader might contact them.

With path integrals it is possible to account for tunneling and zero point energy (ZPE), but MCTDH can account for all nuclear quantum effects, which has already been mentioned. It is important to mention that unlike in classical simulations, in QMD the impinging atom does not have a single energy and angle. Instead, a distribution is used for the starting position of the projectile, it has an energetic distribution and also the initial angle has a width. At least for the energy, it seems possible to extract the distribution corresponding to a single incidence energy value. Here, it also of importance, that QMD only treats four carbon surface atoms, was performed for a single relaxed surface geometry at  $T = 0$  K. The exact procedure to extract this is not discussed here, because it is beyond the scope of this work.

As already mentioned before, in order to further increase the accuracy of simulations to finally better reproduce experimental measured translational energy and scattering angle distribution shown in Fig. 4.66 and 4.67, nuclear quantum effects will be accounted in the simulations by using ring-polymer molecular dynamics as described in 2.4.4. From a collaboration with Fabien Gatti and Lei Shi [30], I will also show preliminary results from quantum molecular dynamic simulations. MCTDH is used to propagate a wave package [310] and can offer a full treatment of nuclear quantum effects. The following section is not only about the change in the distributions, when accounting for NQEs in RPMD, but also to evaluate the quality of classical simulations in an extended space in comparison to QMD simulations.

In the following, the translational energy and scattering angle distributions from RAT as well as HBEAM experiment are compared to classical simulations, path integral molecular dynamics and to preliminary results using quantum molecular dynamics describing H-atom scattering from a free-standing graphene sheet.

When comparing to HBEAM experimental results, also the angle integrated energy loss distributions are considered for MD as well as RPMD.

### 4.4.1 Comparison to RAT Experiment

In classical simulations, the discrepancies to reproduce experimentally found translational energy and scattering angle distributions are more pronounced when comparing the distributions estimated by HDNN-PES to the latest distribution from HBEAM experiment. However, there is also an increased mismatch in the results when going to higher incidence angles when comparing the results to RAT experiment.

The parameters are defined in Fig. 4.8, an overview of the analysis is shown in Fig. 4.14.

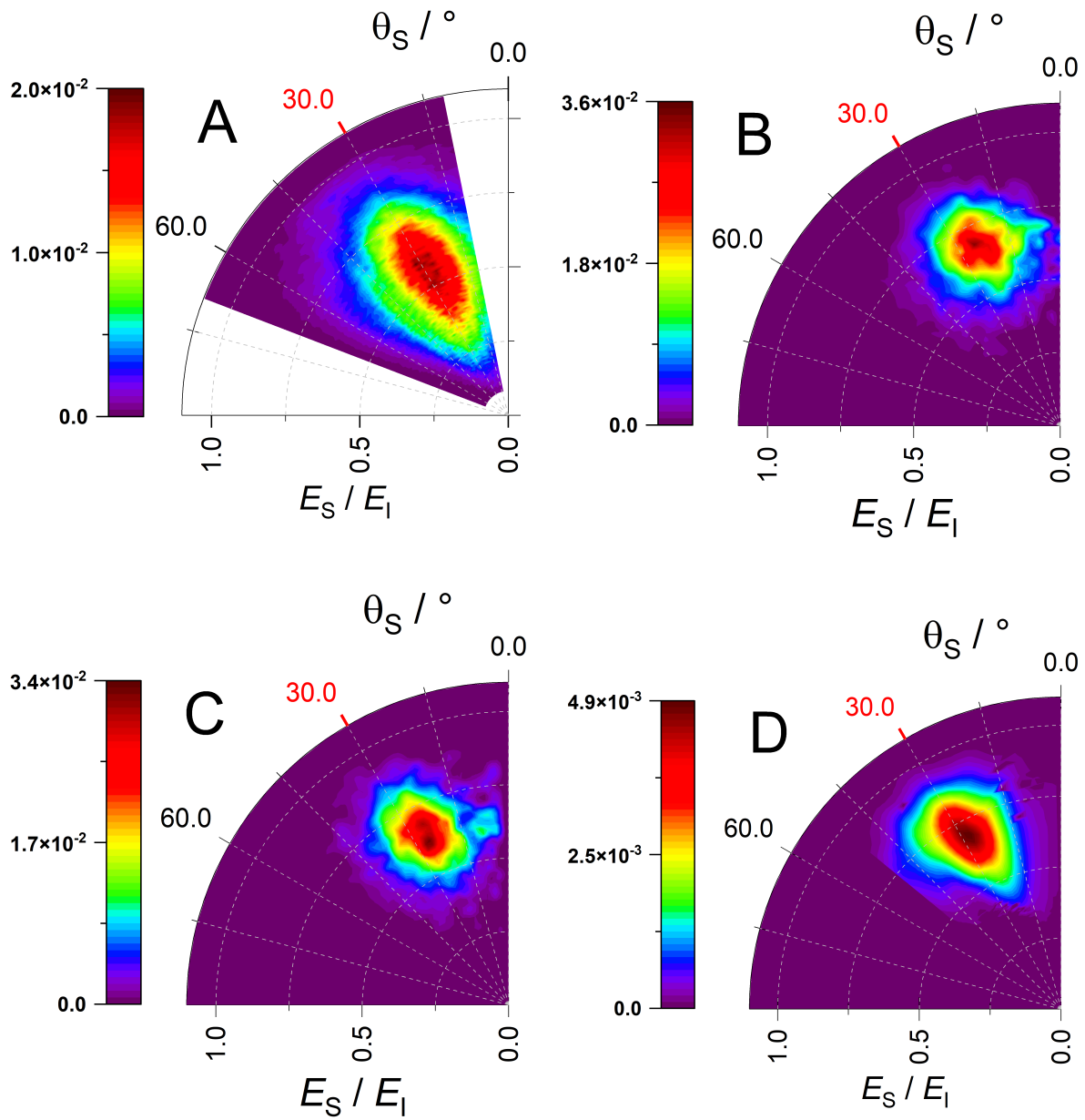


Figure 4.68: Comparing translational energy and scattering angle distributions from RAT experiment (A) with simulations based on the HDNN-PES. Shown are classical (B), RPMD (C) and QMD (D) simulations. The incidence as well as specular angle  $\theta_I$  is shown in red. Statistics and further analysis of trajectories are given in Tab. A.14.

The statistics of H-atom scattering from graphene from RAT experiment, MD, RPMD as well as QMD simulations based on a HDNN-PES are given in Tab. A.14. The number of simulated trajectories, scattered trajectories within detection limit compared to experimental setup, the incidence polar angle, the incidence kinetic energy and its normal component and sticking coefficients are given. The normal component of the incidence kinetic energy is given as well, because the transient C–H bond is efficiently formed with normal kinetic energy.

To better follow the trend, simulations have also been performed with an initial kinetic energy of 1.5 eV of the impinging H-atom. Important to mention is, that for this incidence kinetic energies, no experimental results are accessible.

In Fig. 4.68, the translational energy and scattering angle distributions obtained from experiment (panel A), from MD simulations (panel B), RPMD simulations (panel C) and QMD simulations (panel D) are shown. In the distribution from experiment, a single very broad peak showing the slow channel is present. A single peak can be seen in MD, RPMD and QMD simulations as well, but in MD it is more localized and signals for smaller final energies are not present. Accounting for NQEs in RPMD does not change this localized feature and even there, only marginal signal intensities can be seen. The overall shape seems a little bit elongated to higher and smaller energies, but this might also be due to statistical errors. The distribution from QMD simulations [30] is also more localized, but at least a tail towards smaller final energies can be seen. Here, it seems independent of the theory, there is no complete reproduction of the experimental findings, but from QMD we can conclude, that it seems to go in the right direction for a better description of the dynamic processes. Here, it also very important to mention, that QMD only treats four carbon surface atoms, was performed for a single relaxed surface geometry at  $T = 0$  K.

Considering the sticking coefficients shown in Tab. A.14, MD predicts a very small sticking coefficient  $s_0 = 0.04$ , RPMD predicts  $s_0 = 0.01$ . There are no results from QMD, yet. Because of the high normal kinetic energy, it is highly likely that the projectile can cross the barrier and is not able to efficiently distribute enough kinetic energy on the time scale of interaction to the surface in order to be adsorbed. This results in inelastic scattering events with a broad shape, which can be seen in experiment. This is also the case in MD simulations, as discussed before in Sec. 4.3.1. And it makes sense, that RPMD predict a lesser sticking coefficient, because of the treatment of tunneling and zero point energy, the barrier to adsorption is effectively reduced in its height and adsorption events become less likely. The full treatment of quantum effects also influence the barrier height to adsorption, but in both directions. The wave-like behavior of the projectile will result in scattering at a lower barrier compared to before, but because of the distribution in energy and angle, there is also a probability that the projectile will feel an increased barrier height, which will result in more sticking probability, but this has to be determined.

To summarize the comparison to RAT experiment, from the distributions alone, it seems there is only a small influence of quantum effects to the scattering, which is in good agreement with previous studies for H-atom scattering with  $E_i = 0.99$  eV. But the prominent difference in the sticking coefficients indicate that there could be much more influence from the quantum mechanically behavior of the projectile. So far, any more analysis to compare to experimental findings from RAT experiment have not been carried out. Since we see an seemingly increase of quantum effects for smaller incidence angles, the focus was more on the comparison to the latest results from HBEAM experiment, where scattering alongside the surface normal with the smallest possible incidence polar angle is of interest, which will be shown in the next section.

#### 4.4.2 Comparison to HBEAM Experiment

As already mentioned, the discrepancies to reproduce experimentally found translational energy and scattering angle distributions are more pronounced when comparing the distribution from simulations based on a HDNN-PES to the latest found distribution from HBEAM experiment using VMI detection. In the same manner as already done before by comparing to RAT experiment, in the following the H-atom scattering from graphene along the surface normal depending on the incidence energy is analyzed. Again, all simulations base on a HDNN-PES and results from classical simulations are compared to RPMD as well as QMD simulations, how well the experimental found results can be reproduced.

The H-atom scattering depending on the incidence kinetic energy  $E_I = 0.99$  eV and  $1.92$  eV will be analyzed, again. The surface temperature is  $T = 300$  K for all incidence conditions. The incidence polar angle of the H-atom is  $\theta_I = 0.0^\circ$ , which corresponds to scattering along the surface normal. In contrast to already shown results, here the focus is on the change in the translational energy and scattering angle distributions, when quantum effects (tunneling and zero point energy) are considered in RPMD simulations. The obtained results will be compared to already shown experimental results, classic simulations but furthermore to QMD simulations utilizing the MCTDH framework, where possible.

The parameters are defined in Fig. 4.8, an overview of the analysis is shown in Fig. 4.14, like mentioned before.

The statistics of H-atom scattering from free-standing graphene along the surface normal from MD, RPMD as well as QMD simulations based on a HDNN-PES are given in Tab. A.15. The number of simulated trajectories, scattered trajectories within detection limit compared to experimental setup and sticking coefficients are given. Here, just the normal component is given, because it is exactly the incidence kinetic energy. Transient C–H bond is efficiently formed with normal kinetic energy.

For H-atom scattering from graphene along the surface normal with  $0.99$  eV incidence kinetic energy and including nuclear quantum effects in RPMD simulations the translational energy and scattering angle distributions is shown in Fig. 4.69 in the bottom panel. The distribution measured is shown in the upper panel. Compared to classical results shown in Fig. 4.66 in the bottom panel, the results seem non-intuitive at first. As it was discussed before, the missing of a pronounced peak for the fast channel is due to the geometry of the underlying simulations. Although the reproduction of a single peak seemingly including the fast and slow channel is poorly, at least including quantum effects might explain the signal intensities off the specular angle. Considering the missing intensity for the quasi-elastic channel, the signal intensities would be less pronounced, which would at least lead to the experimental findings.

By comparing the final velocity and corresponding final kinetic energy distribution from MD and RPMD simulations with the measured distributions, which is shown in Fig. 4.70, it seems, classical simulations are not so far off the experiment. Although the distributions from RPMD seems at first non-intuitive, because the branching of the two channel is not in agreement with experiment. But with the background, that the fast channel, which corresponds to the signal around  $v = 14$  km s<sup>-1</sup> and  $E_S = 1.0$  eV is under-represented, this would scale the broad signal for the former slow channel down, which would be in better agreement with the experiment and even close to the classical distribution.

The comparison of the distribution of scattering angle and translational energy of H-atom scattering from graphene along the surface normal ( $\theta_I = 0.0^\circ$ ) with  $E_I = 1.92$  eV at  $300$  K is shown in Fig. 4.71. The measured distribution (top panel) is compared to simulations using RPMD (middle panel) and the fully quantum mechanically treatment using MCTDH in QMD simulations (bottom panel). In the experiment, the energy loss distribution has a broad shape and an energetic range of  $\approx 0.75$  eV. The main signal with highest intensity is along the surface normal but a lot of signals with very low intensity can be seen between  $\pm 30^\circ$  polar angle.

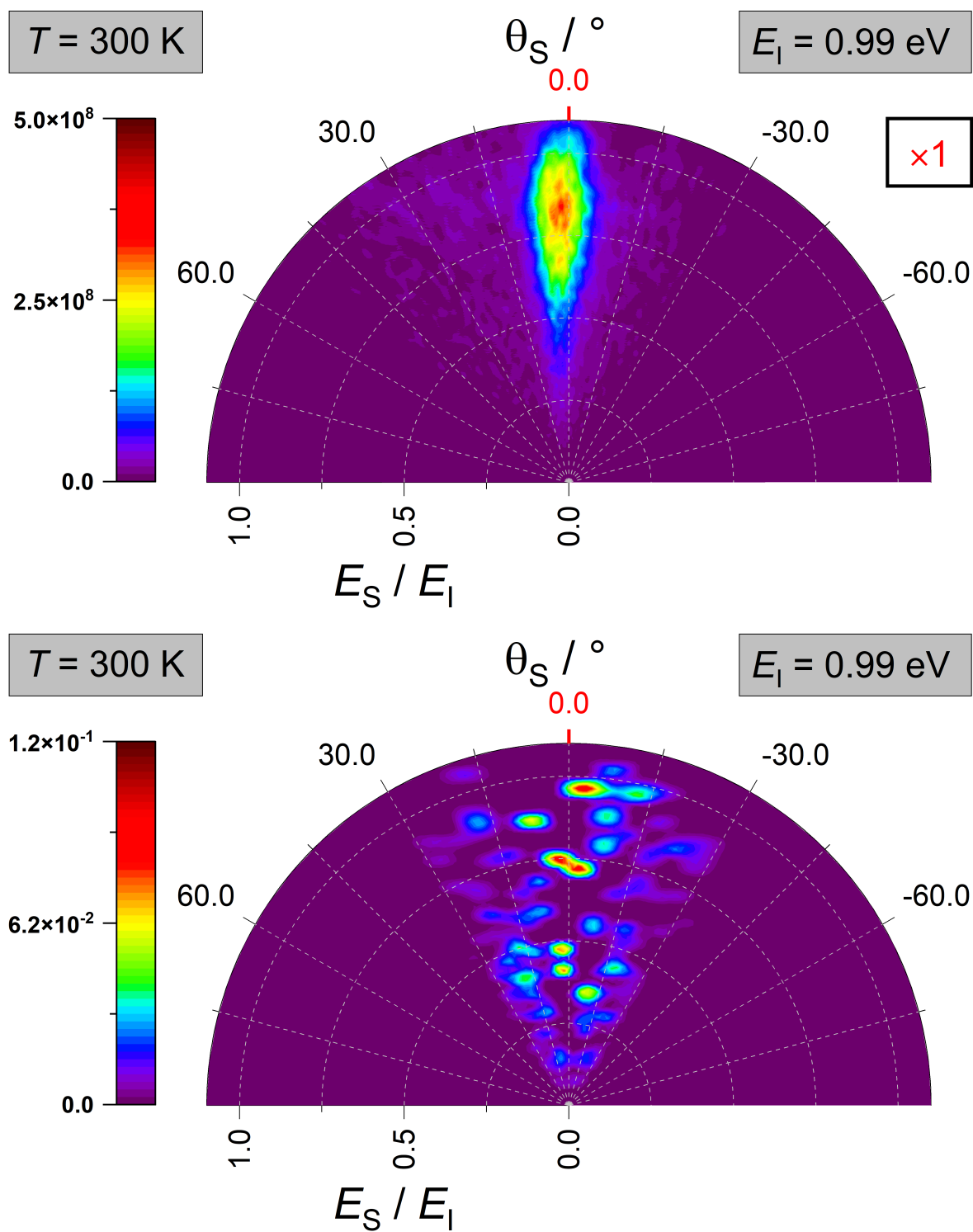


Figure 4.69: Comparing translational energy and scattering angle distribution from HBEAM experiment (top) with path integral based (RPMD) simulations using the HDNN-PES (bottom) for H-atom scattering from graphene. The incidence kinetic energy  $E_I$  and surface temperate  $T$  are given in gray boxes. The incidence as well as specular polar angle  $\theta_I$  is shown in red. Statistics and further analysis of trajectories are given in Tab. A.15.



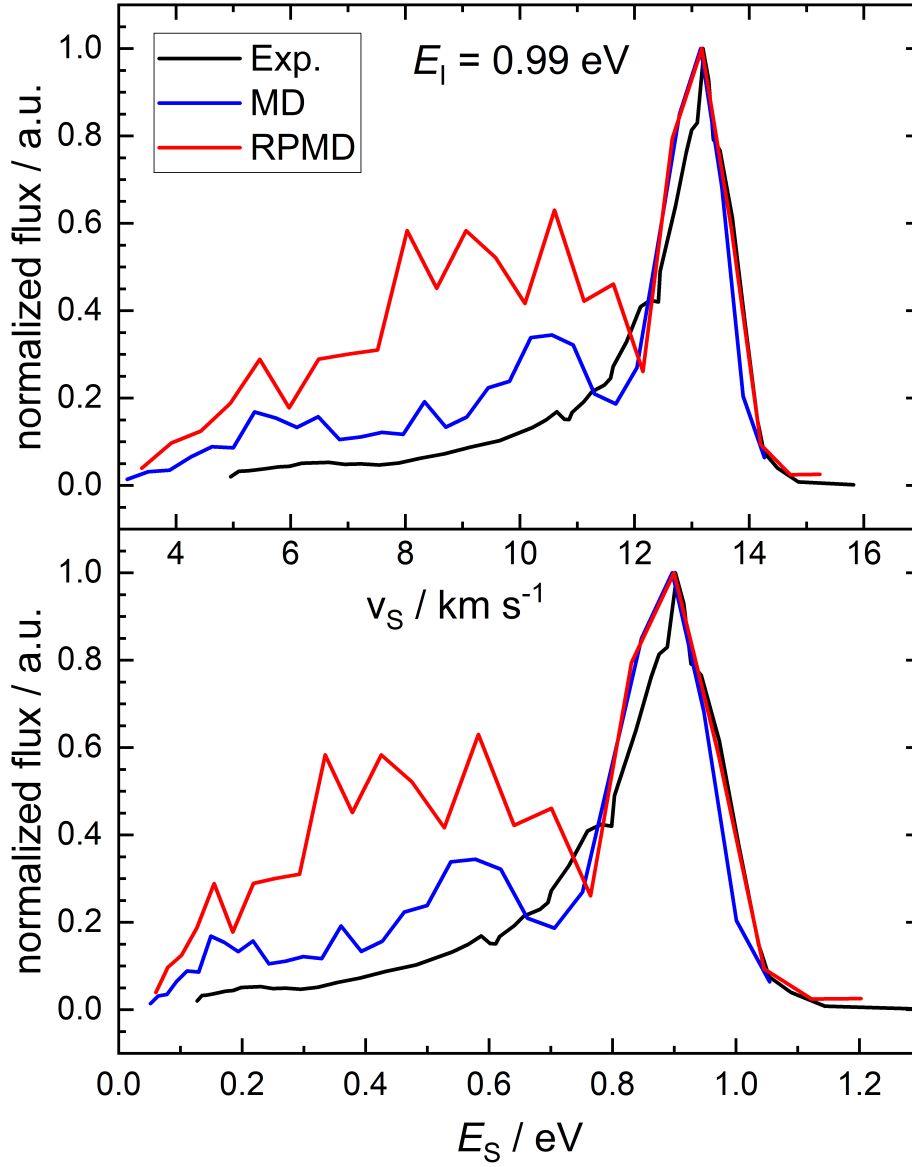


Figure 4.70: Comparing the flux of final velocities ( $v_S / \text{km s}^{-1}$ ) and energies ( $E_S / \text{eV}$ ) for H-atom scattering from graphene with  $E_I = 0.99 \text{ eV}$  from experiment to simulations, respectively. Classical simulations (MD) have been carried out and are compared to ring-polymer MD simulations (RPMD), which account for tunneling and zero point energy. Note, RPMD is not able to properly describe the fast channel (peak at high velocities/energies), which is discussed in 3.10. Normalization has been done to the maximum value for energies and velocities.

RPMD simulations only show a narrow energy loss range but have a much broader angular range. In contrast to that, in QMD simulations the range of the energy loss is very similar to the one found in experiment, but it is shifted to higher normalized scattering energies. For the angle distribution, we only see signal between  $\pm 15^\circ$  polar angle.

In RPMD, tunneling and zero point energy can be accounted for and the method was mainly developed for equilibrium conditions [155], although it was shown that the method can also be used for non-equilibrium conditions [158]. It is however still questionable, if and how good simulations can predict the energy loss and angle distribution in dynamics very far from equilibrium conditions. If the obtained results from RPMD are compared to the ones from MD as shown in Fig. 4.67 in the bottom panel, although the signal is elongated to higher as well as smaller normalized final scattered energies, there is not much of a difference, indicating only minor influence of nuclear quantum effects. This is in agreement with the comparison to the results with  $(\theta_I = 30.0^\circ)$  compared to RAT experiment as well as QMD simulations as shown in Fig. 4.68, where even the fully quantum mechanically treatment does not significantly improve the reproduction of experimentally found results. Previous reported results indicating that there are only small nuclear quantum effects agree with the shown results [28]. In contrast to these findings, recent QMD studies of H-atom scattering indicate the importance of quantum-coherence, which can be accounted for. In QMD simulations using MCTDH, only a reduced dimensionality of the graphene surface is described. Only 4 atoms are described quantum mechanically and are allowed to move, all other atoms are kept fixed at their equilibrium positions. The H-atom is launched as a wave package along the surface normal to a fully relaxed surface at  $T = 0$  K with  $E_I = 1.96$  eV and is propagated. After interaction of the wavefunction from the impinging atom with the surface, the wave package is split into a component, that is trapped on the surface and one that is dissipating from the surface. With this, it is possible to determine sticking coefficients. Compared to classical calculations, in RPMD astonishingly the sticking coefficient is even decreasing from 0.01 (MD) to 0.005 (RPMD) but not significantly. However, in QMD simulations, the sticking coefficient was estimated to be 0.06, which is reasonable compared to the sticking coefficients estimated depending on the normal energy of the impinging atom (Fig. 3 in [25]).

By comparing the final velocity and corresponding energy distribution from MD and RPMD simulations with the measured distributions, which is shown in Fig. 4.72, classical simulations seem to be far off the experiment. Here, there is no contribution from quasi-elastic scattering anymore, therefore the distributions from RPMD seems reasonable. Compared to classic simulations, it makes sense that scattered velocities as well as energies are closer to experiment, because due to NQEs, the barrier height is influenced. Although the distribution is still off of the experiment, the trend when accounting for NQEs is going to the right direction. But still, a comparison to results from QMD simulations would help to classify the results from RPMD.

To summarize the whole section, with the preliminary results and our knowledge so far, it seems that using RPMD to account for quantum effects indicates only minor influence from quantum effects, which seems to be independent from the incidence conditions. It is even questionable from the results shown, if RPMD is even a proper choice to account for NQEs at least in this system. But to give a profound answer, there are definitely more investigations needed to describe the system fully quantum mechanically. From the results so far, it seems very important to account for quantum effects to get better reproduced results, which can give valuable insights into the dynamics taking place on the surface for incidence angles close or along the surface normal.

At least we could figure out three nuclear quantum effects, that are under further investigation, which are all connected to quantum coherence not included in RPMD simulations. The wave like behavior of the atoms is considered in QMD simulations. Three different aspects are related to this behavior. In preliminary results, we see diffraction contributes to the signal of the slow

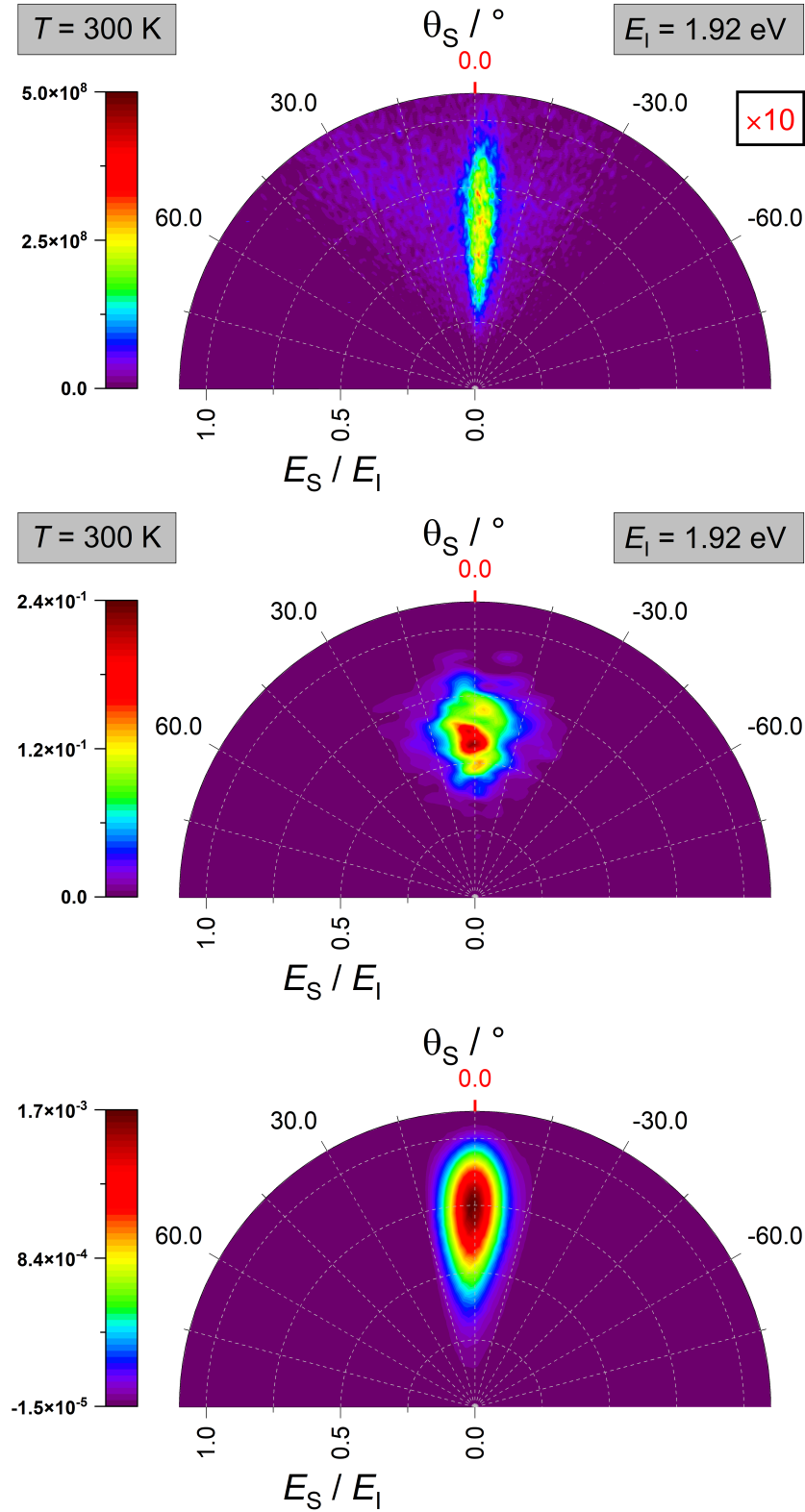


Figure 4.71: Comparing translational energy and scattering angle distribution from HBEAM experiment (top) with path integral based (RPMD) simulations using the HDNN-PES (middle) and QMD simulations (bottom) for H-atom scattering from graphene. The incidence kinetic energy  $E_I$  and surface temperature  $T$  are given in gray boxes. The incidence as well as specular polar angle  $\theta_I$  is shown in red. Statistics and further analysis of trajectories are given in Tab. A.15.

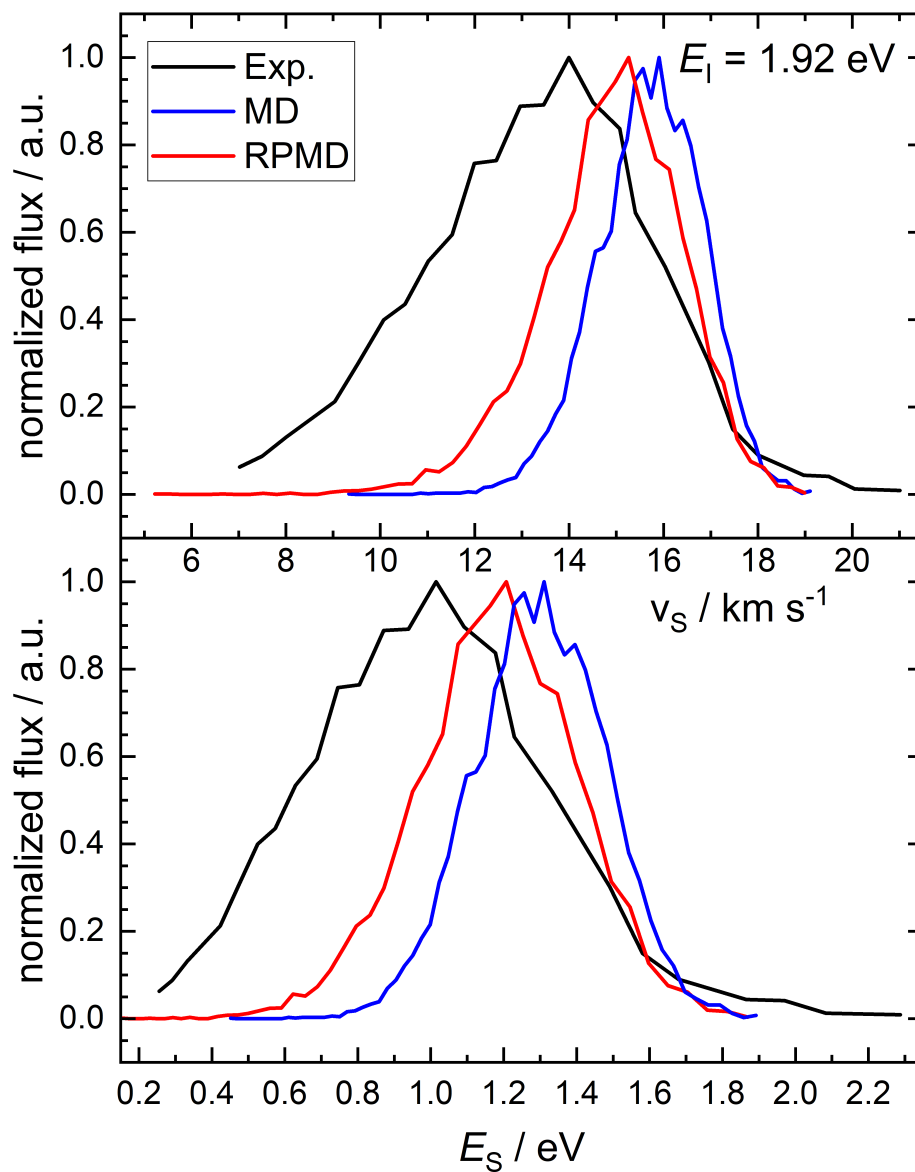


Figure 4.72: Comparing the flux of final velocities ( $v_S / \text{km s}^{-1}$ ) and energies ( $E_S / \text{eV}$ ) for H-atom scattering from graphene with  $E_I = 1.92 \text{ eV}$  from experiment to simulations, respectively. Classical simulations (MD) have been carried out and are compared to ring-polymer MD simulations (RPMD), which account for tunneling and zero point energy. Note, RPMD is not able to properly describe the fast channel (peak at high velocities/energies), which is discussed in 3.10. Normalization has been done to the maximum value for energies and velocities.

and the fast channel. Next, because the wavepackage of the projectile is propagated, there is an interference of the scattered wavefunction with the initial one. Related to that and because we have a distribution of the impinging atom, the fraction that will arrive later at the surface will see a changed surface because of previous interactions. What is still missing and will be analyzed in the future is the contribution of each of the mentioned effect and its magnitude to the flux and the ratio of the fast and slow channel.



---

## Conclusions and Outlook

During my PhD studies, I developed a high-dimensional neural network potential energy surface (HDNN-PES) to describe the interaction of H-atoms with a free-standing graphene surface. The description of the HDNN-PES providing the energies and forces is in the subroutines from the RuNNer program. They were integrated in our developed MDT2 program, which has been used to obtain results from MD simulations. However, the fitting of the HDNN-PES was done with the RuNNer program. The resulting potential reproduces a large set of electronic structure data on the PBE-D2 level of theory with excellent agreement. The configuration space of interest is well covered, i.e. the PES yields almost the same dynamics as AIMD trajectories for the same initial conditions. The RMSE of this PES is 0.6 meV / atom for the energies of the training and the test data set which makes this newly constructed potential much more accurate compared to the previously reported REBO-PES for the system [25]. Hence, this newly generated PES ensures more accurate molecular dynamics simulations. Note that due to the small density of states around the Fermi level, there are no indications why a non-adiabatic description should be used for H-atoms with a kinetic energy below 10 eV scattering from graphene. Hence, simulations in an electronically adiabatic scheme is sufficient.

One example for the increased accuracy over its predecessor, the REBO PES in Ref. [25], the neural network potential comprises a physisorption well. This has drastic consequences on the underlying scattering dynamics. The intensity of the two scattering channels is in much better agreement with intensity seen in the experiment than the signal obtained from simulations performed on the REBO-PES. Moreover, no adjustment of the incidence polar angle was required as it was done before [25]. However, the underlying picture of the two different scattering channels remain the same. The fast channel represents quasi-elastic scattering, where the impinging atom loses only a minor fraction of its initial kinetic energy. These scattering events corresponds to projectiles traversing the physisorption well which are unable to cross the barrier to chemisorption. By comparing the results using a simple binary collision model, the location of the maximum intensity of the peak in the fast channel can be reasonably well estimated. With the aid of this model, we can rationalize that the peak maximum corresponds to ballistic scattering above a C–C bond. This is confirmed by visualization of individual scattering trajectories, see Fig. 4.15. The slow channel results from trajectories which traverse the barrier of a transient C–H bond formation resulting in higher energy losses.

The agreement between the simulations and the experiment decrease with decreasing incidence

polar angle,  $\theta_i$ . On the one hand, this disagreement can be explained with the fact that the HDNN-PES underestimates the barrier height of the C–H bond formation. Although a larger fraction of impinging H atoms manage to cross the barrier, the life time of the transient C–H bond is also drastically reduced, preventing an efficient energy transfer to the lattice. On the other hand, the absence of the metal substrate in my simulations might give rise to further disagreements with the experiment. Recently performed quantum dynamics simulations in the work group of Fabien Gatti [30] with the MCTDH approach [166] are in better agreement with complimentary experiments compared to classical MD simulations under the same conditions. This indicates that nuclear quantum effects are most pronounced at small incidence polar angles.

Recapitulatory, by using neural network functions to set up a PES and further increasing the performance of our MDT2 program, better statistics are now accessible in a reasonable timeframe. I could show that calculation of millions of trajectories on this PES reproduces experimental findings within good accuracy.

If one wishes to conduct research based on the work presented in this thesis, the following routes could be taken in order to do so. In my opinion, explicit treatment of the underlying substrate is the most promising approach one could take to improve the description of the H/graphene system in computer simulations. Since the interaction between graphene and Pt/Ir are reported to be weak [278–282, 311, 312], one could treat them with a simple Lennard-Jones potential. For nickel, however, it is strongly recommended to explicitly include the Ni slab into the generation of a new neural network potential. At the same time, a careful evaluation of the underlying shape of the simulation cell needs to be done as I found out during my PhD that the form of the simulation cell drastically effects the accuracy of the underlying DFT data, see Sec. 4.2. Furthermore, if one wishes to cover a configuration space at more extreme conditions, i.e. higher initial kinetic energies and surface temperatures, it is strongly recommended to include more reference data under those conditions. As a last suggestion, one could switch to an exchange-correlation functional which yields a more accurate barrier for the C–H bond formation when carrying out DFT calculations. Fitting those reference data anew, is certainly going to increase the quality of the subsequently performed MD simulations.






---

# Appendix

## A.1 High-dimensional neural network potential energy surface

### A.1.1 Symmetry Functions for the H on Graphene System

Table A.1: Parameters for the atom-centered symmetry functions of radial type for H- and C-atoms. The unit Bohr is given as  $a_0$ . Equations for the types used can be found in Sec. 2.3.4 in Eq. 2.27.

Number	$\eta(a_0^{-2})$	$R_{\text{shift}}(a_0)$	$r_{\text{cut}}(a_0)$
Radial			
1	0.000	0.0	12.0
2	0.005	0.0	12.0
3	0.013	0.0	12.0
4	0.027	0.0	12.0
5	0.060	0.0	12.0
6	0.156	0.0	12.0

Table A.2: Parameters for the atom-centered symmetry functions for H- and C-atoms. Equations for the types used can be found in Sec. 2.3.4 in Eq. 2.28.

Number	$\eta(a_0^{-2})$	$\lambda$	$\zeta$	$r_{\text{cut}}(a_0)$
Angular				
7	0.000	1	1	12.0
8	0.000	1	2	12.0
9	0.000	1	4	12.0
10	0.000	1	16	12.0
11	0.000	-1	1	12.0
12	0.000	-1	2	12.0
13	0.000	-1	4	12.0
14	0.000	-1	16	12.0
15	0.013	1	1	12.0
16	0.013	1	2	12.0
17	0.013	1	4	12.0
18	0.013	1	16	12.0
19	0.013	-1	1	12.0
20	0.013	-1	2	12.0
21	0.013	-1	4	12.0
22	0.013	-1	16	12.0
15	0.156	1	1	12.0
16	0.156	1	2	12.0
17	0.156	1	4	12.0
18	0.156	1	16	12.0
19	0.156	-1	1	12.0
20	0.156	-1	2	12.0
21	0.156	-1	4	12.0
22	0.156	-1	16	12.0

### A.1.2 Architecture

Table A.3: Different architectures of obtained NNPs and their respective root mean square errors (RMSE) for energies  $E$  and forces  $F$  from the training and test set, respectively. In bold, the architecture of choice as used in simulations performed in this work is given.

Architecture	Training Set RMSE		Test Set RMSE	
	$E$ (meV atom $^{-1}$ )	$F$ (meV Å $^{-1}$ )	$E$ (meV atom $^{-1}$ )	$F$ (meV Å $^{-1}$ )
<b>15-15</b>	0.6	91	0.6	89
20-20	0.5	89	0.6	86

### A.1.3 Dispersion plots

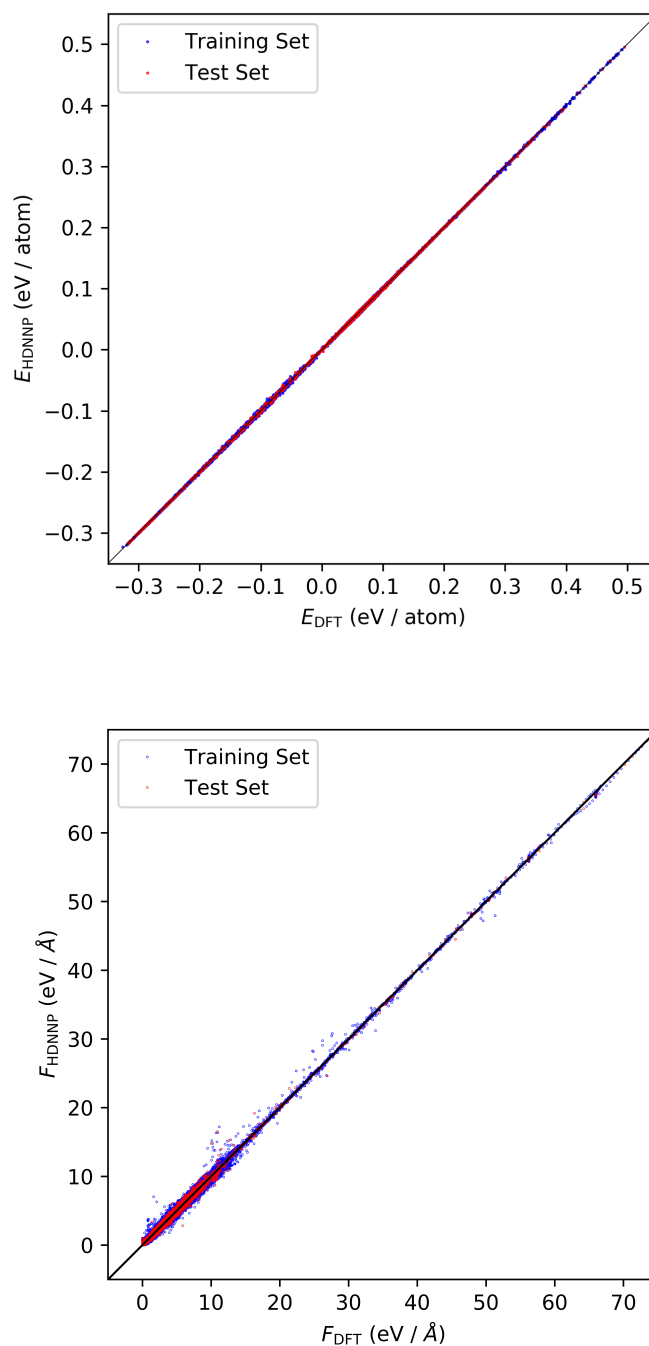


Figure A.1: Correlation of energies (top) and forces (bottom) from the training and test data used to fit a 15-15 NNP. Reproduced from Ref. [204] with permission from the Royal Society of Chemistry.

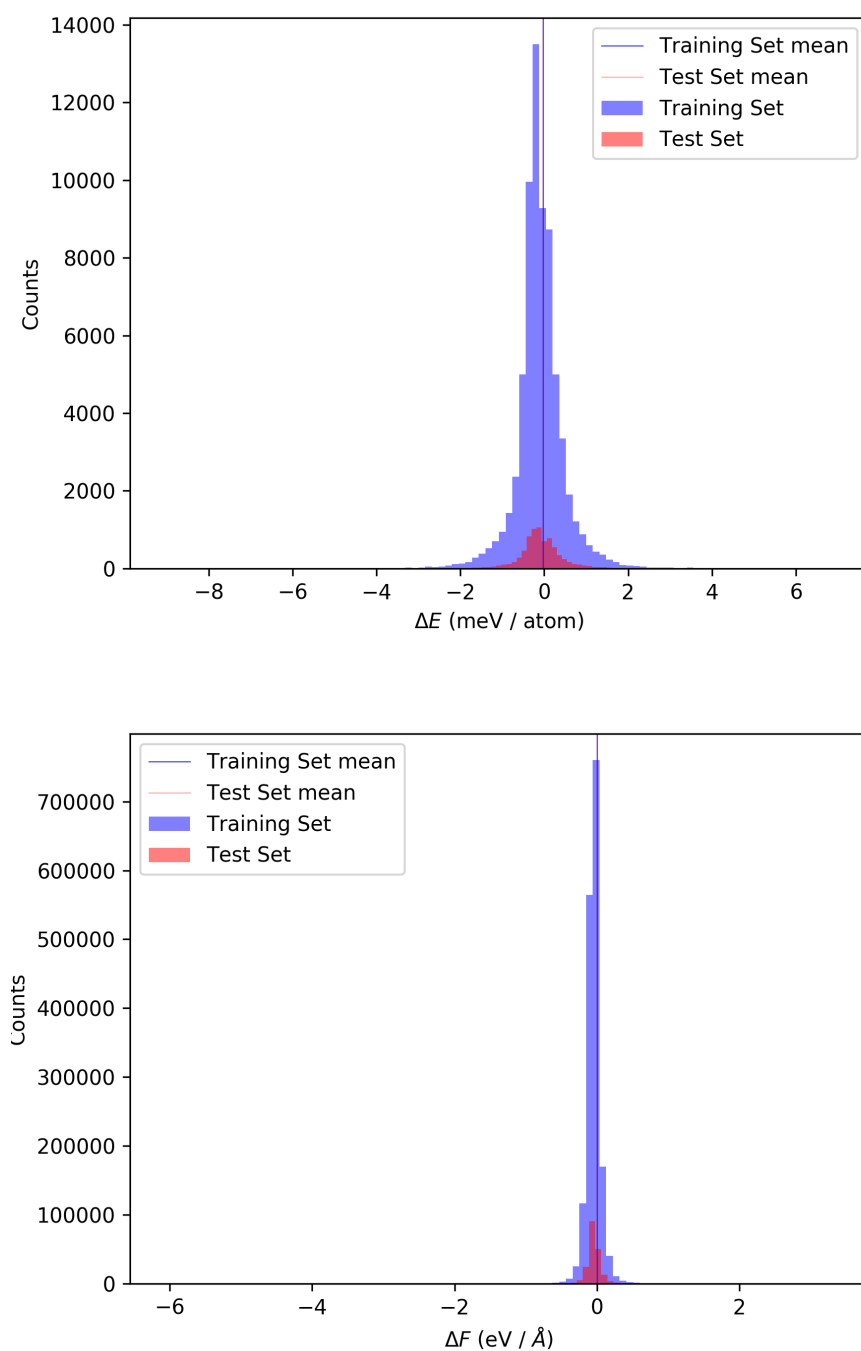


Figure A.2: Histogram of energies (top) and forces (bottom) from the training and test data used to fit a 15-15 NNP. Reproduced from Ref. [204] with permission from the Royal Society of Chemistry.

## A.2 Input files

```

SYSTEM      = H on Graphene # comment line

ISTART      = 0              # restart

ICHARGE     = 2              # initial charge from atomic charge densities
NPAR        = 1              # number of bands treated parallel

PREC        = Normal        # precision of calculations
ENMAX       = 400            # energy cutoff of planewaves in eV
ALGO        = Very Fast     # Diagonalization in scf step

NELM        = 300            # maximum number of scf steps

EDIFF       = 1.0E-05        # threshold for energy in eV
EDIFFG      = -1.0E-03       # break condition for the ionic relaxation loop

NELMIN      = 4              # minimum number of scf steps
ISYM        = 0              # symmetry

ISPIN       = 2              # set spin polarized calculations

MAGMOM      = 1*1 24*0      # set magnetic moment for all atoms

LWAVE       = .FALSE.        # don't write WAVECAR
LCHARG      = .FALSE.        # don't write CHGCAR

AMIX        = 0.3            # specifies the linear mixing parameter
BMIX        = 0.00001        # cutoff wave vector for Kerker mixing scheme
AMIX_MAG    = 0.3            # mixing parameter for magnetization density
BMIX_MAG    = 0.00001        # cutoff wave vector for Kerker mixing scheme
MAXMIX      = 20             # maximum number steps in Broyden mixer

LREAL       = .FALSE.        # projection in reciprocal space
ISMEAR      = -5             # tetrahedron method with bloechl correction
SIGMA       = 0.2            # smearing parameter

GGA         = PE             # PBE functional

LVDW        = .TRUE.         # turn dispersion correction on
IVDW        = 11             # Grimme D2 dispersion correction

```

Listing A.1: Example INCAR input file for VASP.

```

K-Points
  0                ! 0 -> determine number of k points automatically
Gammacentered     ! generate a Gamma centered mesh
  8  8  1          ! subdivisions along the reciprocal lattice vectors
  0  0  0          ! optional shift of the mesh (s_1, s_2, s_3)

```

Listing A.2: Example KPOINTS file for VASP.

```

# relaxed graphene at 0K with H on top of second C-atom
1.0
      8.550000      0.000000      0.000000
      0.000000      7.400000      0.000000
      0.000000      0.000000     13.000000
H C
1 24
Cartesian
      1.424599      0.000000      6.000000
      0.712300      1.233739      0.000000
      1.424599      0.000000      0.000000
      2.849199      0.000000      0.000000
      3.561498      1.233739      0.000000
      4.986098      1.233739      0.000000
      5.698397      0.000000      0.000000
      7.122997      0.000000      0.000000
      7.835296      1.233739      0.000000
      0.712300      3.701218      0.000000
      1.424599      2.467479      0.000000
      2.849199      2.467479      0.000000
      3.561498      3.701218      0.000000
      4.986098      3.701218      0.000000
      5.698397      2.467479      0.000000
      7.122997      2.467479      0.000000
      7.835296      3.701218      0.000000
      0.712300      6.168697      0.000000
      1.424599      4.934958      0.000000
      2.849199      4.934958      0.000000
      3.561498      6.168697      0.000000
      4.986098      6.168697      0.000000
      5.698397      4.934958      0.000000
      7.122997      4.934958      0.000000
      7.835296      6.168697      0.000000

```

Listing A.3: Example POSCAR structure file for VASP.

```
# Physical model settings
#
xc                b3lyp
vdw_correction_hirshfeld
charge            0.
spin              collinear
relativistic      atomic_zora scalar
#
# SCF convergence settings
#
occupation_type   gaussian 0.4
mixer              pulay
  n_max_pulay      10
  charge_mix_param 0.4
  spin_mix_param   0.4
# ini_linear_mixing 10
# ini_linear_mix_param 0.05
  preconditioner kerker 1.5
  precondition_max_l 0
  preconditioner turnoff charge 1e-4
  preconditioner turnoff sum_ev 1e-1
sc_accuracy_rho    1E-5
sc_accuracy_eev    1E-4
sc_accuracy_etot   1E-5
sc_iter_limit      1000
#
# For periodic boundary conditions
#
k_grid 6 6 1
```

Listing A.4: Example main input file control.in for FHI-aims.

```

# relaxed graphene at 0K with H over 6-membered C-ring
lattice_vector      8.547596      0.000000      0.000000
lattice_vector      0.000000      7.402435      0.000000
lattice_vector      0.000000      0.000000     13.005471
atom      2.136900      0.000000      0.800000  H
      initial_moment 1
atom      0.712300      1.233739      0.000000  C
atom      1.424599      0.000000      0.000000  C
atom      2.849199      0.000000      0.000000  C
atom      3.561498      1.233739      0.000000  C
atom      4.986098      1.233739      0.000000  C
atom      5.698397      0.000000      0.000000  C
atom      7.122997      0.000000      0.000000  C
atom      7.835296      1.233739      0.000000  C
atom      0.712300      3.701218      0.000000  C
atom      1.424599      2.467479      0.000000  C
atom      2.849199      2.467479      0.000000  C
atom      3.561498      3.701218      0.000000  C
atom      4.986098      3.701218      0.000000  C
atom      5.698397      2.467479      0.000000  C
atom      7.122997      2.467479      0.000000  C
atom      7.835296      3.701218      0.000000  C
atom      0.712300      6.168697      0.000000  C
atom      1.424599      4.934958      0.000000  C
atom      2.849199      4.934958      0.000000  C
atom      3.561498      6.168697      0.000000  C
atom      4.986098      6.168697      0.000000  C
atom      5.698397      4.934958      0.000000  C
atom      7.122997      4.934958      0.000000  C
atom      7.835296      6.168697      0.000000  C

```

Listing A.5: Example structure file geometry.in for FHI-aims. First, the simulation cell parameters are given followed by the coordinates of all atoms. Note, the spin for the H-atom was set to 1.



```

### #####
### This is the input file for RuNNer
### #####
### General remarks:
### - commands can be switched off by using the # character
### - the input file can be structured by blank and comment lines
### - the order of the keywords is arbitrary
### - if keywords are missing, default values will be used and
###   written to runner.out
### - if mandatory keywords or keyword options are missing, RuNNer
###   will stop with an error message

### #####
### general keywords
### #####

nn_type_short 1
runner_mode 1/2/3
parallel_mode 1
number_of_elements 2
elements H C
random_seed 73
random_number_type 5
energy_threshold 0.00
bond_threshold 0.1d0

### #####
### NN structure of the short-range NN
### #####

use_short_nn
global_hidden_layers_short 2
global_nodes_short 15 15
global_activation_short t t 1

### #####
### symmetry function generation ( mode 1):
### #####

test_fraction 0.10000

### #####
### symmetry function definitions (all modes):
### #####

symfunction_short C 2 C 0.000000 0.000000 12.000000
symfunction_short C 2 H 0.000000 0.000000 12.000000
symfunction_short H 2 C 0.000000 0.000000 12.000000

symfunction_short C 2 C 0.005000 0.000000 12.000000
symfunction_short C 2 H 0.005000 0.000000 12.000000
symfunction_short H 2 C 0.005000 0.000000 12.000000

symfunction_short C 2 C 0.013000 0.000000 12.000000
symfunction_short C 2 H 0.013000 0.000000 12.000000
symfunction_short H 2 C 0.013000 0.000000 12.000000

```

symfunction_short	C	2	C	0.027000	0.000000	12.000000	
symfunction_short	C	2	H	0.027000	0.000000	12.000000	
symfunction_short	H	2	C	0.027000	0.000000	12.000000	
symfunction_short	C	2	C	0.060000	0.000000	12.000000	
symfunction_short	C	2	H	0.060000	0.000000	12.000000	
symfunction_short	H	2	C	0.060000	0.000000	12.000000	
symfunction_short	C	2	C	0.156000	0.000000	12.000000	
symfunction_short	C	2	H	0.156000	0.000000	12.000000	
symfunction_short	H	2	C	0.156000	0.000000	12.000000	
symfunction_short	C	3	C	C 0.0000	1.0	1.0	12.00000
symfunction_short	C	3	C	H 0.0000	1.0	1.0	12.00000
symfunction_short	H	3	C	C 0.0000	1.0	1.0	12.00000
symfunction_short	C	3	C	C 0.0000	1.0	2.0	12.00000
symfunction_short	C	3	C	H 0.0000	1.0	2.0	12.00000
symfunction_short	H	3	C	C 0.0000	1.0	2.0	12.00000
symfunction_short	C	3	C	C 0.0000	1.0	4.0	12.00000
symfunction_short	C	3	C	H 0.0000	1.0	4.0	12.00000
symfunction_short	H	3	C	C 0.0000	1.0	4.0	12.00000
symfunction_short	C	3	C	C 0.0000	1.0	16.0	12.00000
symfunction_short	C	3	C	H 0.0000	1.0	16.0	12.00000
symfunction_short	H	3	C	C 0.0000	1.0	16.0	12.00000
symfunction_short	C	3	C	C 0.0000	-1.0	1.0	12.00000
symfunction_short	C	3	C	H 0.0000	-1.0	1.0	12.00000
symfunction_short	H	3	C	C 0.0000	-1.0	1.0	12.00000
symfunction_short	C	3	C	C 0.0000	-1.0	2.0	12.00000
symfunction_short	C	3	C	H 0.0000	-1.0	2.0	12.00000
symfunction_short	H	3	C	C 0.0000	-1.0	2.0	12.00000
symfunction_short	C	3	C	C 0.0000	-1.0	4.0	12.00000
symfunction_short	C	3	C	H 0.0000	-1.0	4.0	12.00000
symfunction_short	H	3	C	C 0.0000	-1.0	4.0	12.00000
symfunction_short	C	3	C	C 0.0000	-1.0	16.0	12.00000
symfunction_short	C	3	C	H 0.0000	-1.0	16.0	12.00000
symfunction_short	H	3	C	C 0.0000	-1.0	16.0	12.00000
symfunction_short	C	3	C	C 0.0130	1.0	1.0	12.00000
symfunction_short	C	3	C	H 0.0130	1.0	1.0	12.00000
symfunction_short	H	3	C	C 0.0130	1.0	1.0	12.00000
symfunction_short	C	3	C	C 0.0130	1.0	2.0	12.00000
symfunction_short	C	3	C	H 0.0130	1.0	2.0	12.00000
symfunction_short	H	3	C	C 0.0130	1.0	2.0	12.00000
symfunction_short	C	3	C	C 0.0130	1.0	4.0	12.00000
symfunction_short	C	3	C	H 0.0130	1.0	4.0	12.00000
symfunction_short	H	3	C	C 0.0130	1.0	4.0	12.00000

```

symfunction_short C 3 C C 0.0130 1.0 16.0 12.00000
symfunction_short C 3 C H 0.0130 1.0 16.0 12.00000
symfunction_short H 3 C C 0.0130 1.0 16.0 12.00000

symfunction_short C 3 C C 0.0130 -1.0 1.0 12.00000
symfunction_short C 3 C H 0.0130 -1.0 1.0 12.00000
symfunction_short H 3 C C 0.0130 -1.0 1.0 12.00000

symfunction_short C 3 C C 0.0130 -1.0 2.0 12.00000
symfunction_short C 3 C H 0.0130 -1.0 2.0 12.00000
symfunction_short H 3 C C 0.0130 -1.0 2.0 12.00000

symfunction_short C 3 C C 0.0130 -1.0 4.0 12.00000
symfunction_short C 3 C H 0.0130 -1.0 4.0 12.00000
symfunction_short H 3 C C 0.0130 -1.0 4.0 12.00000

symfunction_short C 3 C C 0.0130 -1.0 16.0 12.00000
symfunction_short C 3 C H 0.0130 -1.0 16.0 12.00000
symfunction_short H 3 C C 0.0130 -1.0 16.0 12.00000

symfunction_short C 3 C C 0.1560 1.0 1.0 12.00000
symfunction_short C 3 C H 0.1560 1.0 1.0 12.00000
symfunction_short H 3 C C 0.1560 1.0 1.0 12.00000

symfunction_short C 3 C C 0.1560 1.0 2.0 12.00000
symfunction_short C 3 C H 0.1560 1.0 2.0 12.00000
symfunction_short H 3 C C 0.1560 1.0 2.0 12.00000

symfunction_short C 3 C C 0.1560 1.0 4.0 12.00000
symfunction_short C 3 C H 0.1560 1.0 4.0 12.00000
symfunction_short H 3 C C 0.1560 1.0 4.0 12.00000

symfunction_short C 3 C C 0.1560 1.0 16.0 12.00000
symfunction_short C 3 C H 0.1560 1.0 16.0 12.00000
symfunction_short H 3 C C 0.1560 1.0 16.0 12.00000

symfunction_short C 3 C C 0.1560 -1.0 1.0 12.00000
symfunction_short C 3 C H 0.1560 -1.0 1.0 12.00000
symfunction_short H 3 C C 0.1560 -1.0 1.0 12.00000

symfunction_short C 3 C C 0.1560 -1.0 2.0 12.00000
symfunction_short C 3 C H 0.1560 -1.0 2.0 12.00000
symfunction_short H 3 C C 0.1560 -1.0 2.0 12.00000

symfunction_short C 3 C C 0.1560 -1.0 4.0 12.00000
symfunction_short C 3 C H 0.1560 -1.0 4.0 12.00000
symfunction_short H 3 C C 0.1560 -1.0 4.0 12.00000

symfunction_short C 3 C C 0.1560 -1.0 16.0 12.00000
symfunction_short C 3 C H 0.1560 -1.0 16.0 12.00000
symfunction_short H 3 C C 0.1560 -1.0 16.0 12.00000

### #####
### fitting: general inputs for short range AND electrostatic part:
### #####

```

```

epochs 100
points_in_memory 2000/25
mix_all_points
scale_symmetry_functions
fitting_unit eV
precondition_weights

### #####
### fitting options (mode 2): short range part only:
### #####

optmode_short_energy 1
optmode_short_force 1
short_energy_error_threshold 0.8000001
short_force_error_threshold 1.2000001
kalman_lambda_short 0.98000
kalman_nue_short 0.99870
short_energy_group 1
short_energy_fraction 1.000
short_force_group 10
short_force_fraction 0.01
use_short_forces
weights_min -1.0
weights_max 1.0
scale_min_short_atomic 0.0
scale_max_short_atomic 1.0

### #####
### output options for mode 2 (fitting):
### #####

write_weights_epoch 1

### #####
### output options for mode 3 (prediction):
### #####

check_forces
calculate_forces
md_mode
use_sf_groups

```

Listing A.6: Example RuNNer input settings file for a  $N_{\text{SF}}\text{-}15\text{-}15\text{-}1$  architecture NNP, with the SF listed in Tab. A.1 and A.2

```

begin
comment "relaxed graphene at 0K with H on top of second C-atom"
lattice 16.15262187 0.00000000 0.00000000
lattice 0.00000000 13.98858136 0.00000000
lattice 0.00000000 0.00000000 24.57678978
atom 2.742641825 0.143053893 6.000000000 H
0.00000000 0.00000000 -0.000000059 0.000000083 0.00013580
atom 1.342003065 2.413572723 0.000000000 C
0.00000000 0.00000000 -0.01576994 -0.01170684 -0.01351035
atom 2.742641825 0.143053893 0.000000000 C
0.00000000 0.00000000 -0.01005626 -0.04784520 0.02023112
atom 5.407758489 0.024793517 0.000000000 C

```

```

0.00000000 0.00000000 0.00753657 0.01706645 -0.00175550
atom 6.729284889 2.368828740 0.000000000 C
0.00000000 0.00000000 0.01094741 -0.02414458 -0.00681824
atom 9.399528337 2.393681900 0.000000000 C
0.00000000 0.00000000 0.01478585 -0.00280140 -0.01399463
atom 10.768049184 0.078535434 0.000000000 C
0.00000000 0.00000000 0.00404893 0.00178749 0.02004419
atom 13.485239713 0.102186967 0.000000000 C
0.00000000 0.00000000 -0.01598963 -0.01463105 0.00933127
atom 14.743689659 2.406134550 0.000000000 C
0.00000000 0.00000000 0.03043936 0.03649592 -0.00182637
atom 1.366032313 7.049398560 0.000000000 C
0.00000000 0.00000000 -0.00371805 -0.01485643 -0.00517079
atom 2.726074297 4.661470682 0.000000000 C
0.00000000 0.00000000 -0.01502752 0.03311723 0.00544167
atom 5.402157682 4.619052225 0.000000000 C
0.00000000 0.00000000 -0.00426129 0.04146242 0.00693232
atom 6.725670091 7.000495993 0.000000000 C
0.00000000 0.00000000 0.01955971 0.00793593 0.00620088
atom 9.482208823 7.108635932 0.000000000 C
0.00000000 0.00000000 -0.04019872 -0.01981995 -0.00822553
atom 10.739778104 4.731747273 0.000000000 C
0.00000000 0.00000000 0.01413677 0.01463207 -0.00536835
atom 13.421804081 4.826745151 0.000000000 C
0.00000000 0.00000000 0.00523383 -0.04607931 0.00515985
atom 14.797158485 7.113098065 0.000000000 C
0.00000000 0.00000000 0.02317168 -0.01866777 0.00405337
atom 1.462074228 11.699425758 0.000000000 C
0.00000000 0.00000000 -0.03920031 0.03181440 -0.01009942
atom 2.709079898 9.346322235 0.000000000 C
0.00000000 0.00000000 0.01453799 0.00583226 0.00367083
atom 5.406283288 9.331358388 0.000000000 C
0.00000000 0.00000000 0.00729981 0.00766376 -0.00178251
atom 6.784663946 11.707084098 0.000000000 C
0.00000000 0.00000000 -0.02288436 -0.01696082 0.00358925
atom 9.446473376 11.723383208 0.000000000 C
0.00000000 0.00000000 0.00091191 0.01351946 -0.01020150
atom 10.785859060 9.431120963 0.000000000 C
0.00000000 0.00000000 0.01811652 -0.01363129 0.00301800
atom 13.507947574 9.394231488 0.000000000 C
0.00000000 0.00000000 -0.01232402 0.04227963 -0.00730378
atom 14.868847971 11.774572363 0.000000000 C
0.00000000 0.00000000 0.00870433 -0.02246319 -0.00175159
charge 0.00000000
energy -8.20899094
end

```

Listing A.7: Example RuNNer input.data structure file with a single structure. A structure is given between the begin and end keywords, comments can be included after the comment keyword, the lattice vectors are given explicitly starting with the lattice keyword. After the atom keyword, all information for a single atom is given. First, the Cartesian coordinates in  $x$ ,  $y$  and  $z$  followed by the element symbol, the atomic charge, the atomic energy and forces in  $x$ ,  $y$  and  $z$ , respectively.

```

run md

start 1
ntrajs 10000
nsteps 2000
step 0.1

!projectile 1 H 1.0 and
!projectile 1 H 1.0 pil
projectile 1 H 1.0 ver
!projectile 1 H 2.0 ver

!lattice 1 C 12.0 and
!lattice 1 C 12.0 pil
lattice 1 C 12.0 ver
!lattice 1 C 13.0 ver

!andersen_time 30
!pile_tau 200

Einc 1.92
polar 50
azimuth +13.5
!azimuth 0
!azimuth -13.5

pip r r 6.0
pul 6.1

Tsurf 300
Tproj 300

conf merge 'conf/proj/' 1 'conf/latt_300K/' 1000

pes 'pes/nene.pes'

rng_seed traj_id

output scatter 1

```

Listing A.8: Example MDT2 md\_tian.inp file

```

pes nene
H      C      proj      latt

pes nene
C      C      latt      latt

pes nene
H      H      proj      proj
inp_dir 'RuNNer_input/'
maxnum_extrapolation_warnings 100

```

Listing A.9: Example MDT2 md\_tian.inp file

### A.3 Random number generators

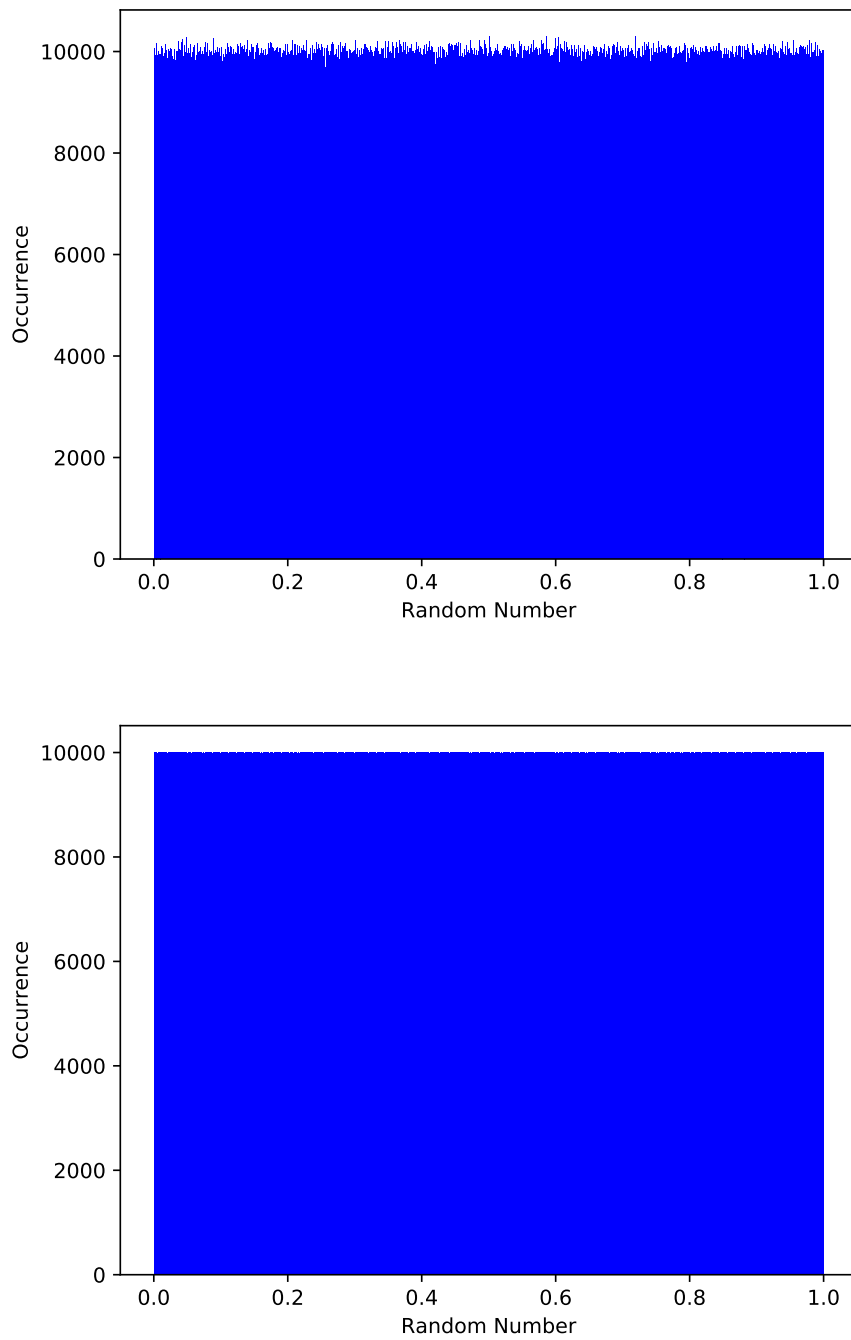


Figure A.3: Histogram with 1000 bins each showing the distribution of  $2.5 \cdot 10^6 \times 4$  random numbers. top: global option, bottom: traj\_id option of RNG. The second option offers a much better uniform distribution and is significantly faster in calculating random numbers.

## A.4 DFT data

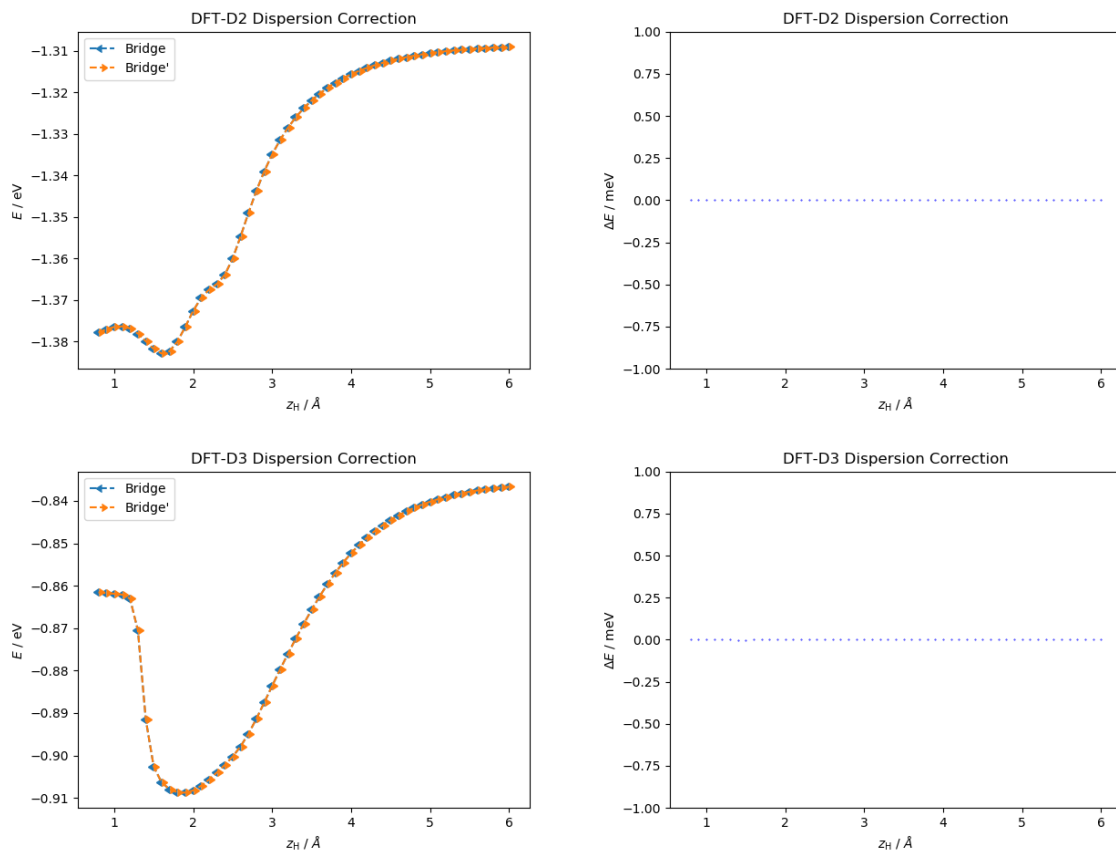


Figure A.4: Grimme-D2 and D3 dispersion correction energy depending on the z-coordinate of the H atom at two energetic different bridge positions. The energetic difference of the two different bridge sites is shown as well to support, that the two bridge sites have the same dispersion energy correction and the scheme does not have an influence to this circumstance.



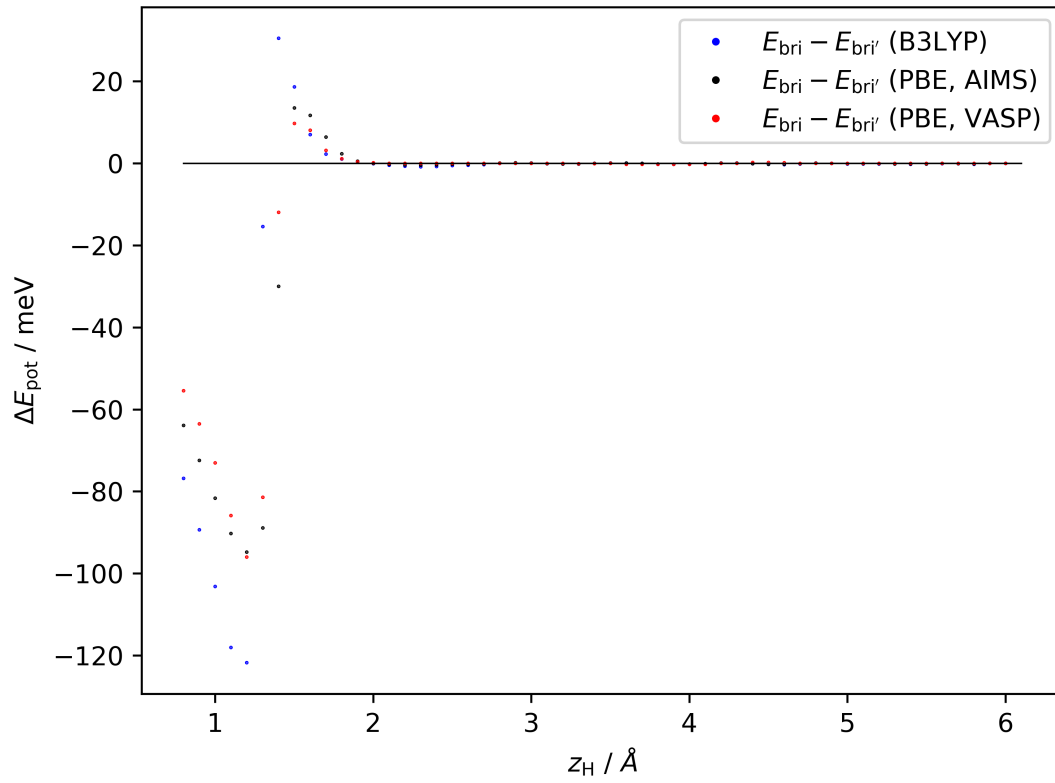


Figure A.5: Energetic difference of inequivalent bridge sites depending on different functionals without dispersion correction. Note that for the PBE results, two different electronic structure codes are used: FHI-aims next to VASP as used before. Independent of the functional and the electronic structure code, there is an energetic difference of seemingly equivalent bridge points.

Table A.4: H-atom put at lateral position of 1.2 Å for all three bridge points in the hexagonal, orthogonal and modified orthogonal unit cell. In the modified orthogonal cell, two H-atoms are put at two symmetrically equivalent bridge positions to account for the changed hydrogen coverage when changing the primitive cell type. The calculations have been carried out using VASP. The precision of the calculations is set to *accurate*. The Monkhorst-Pack scheme used to sample the surface Brillouin zone is given as  $\Gamma$ -centered  $k$ -point mesh (KPOINTS). The kinetic energy cutoff (ENCUT) is given in eV. The maximum energetic difference of three bridge points is given in meV.

primitive cell type	ENCUT / eV	KPOINTS / $x \times y \times z$	$\Delta E$ / meV
hexagonal	400	$32 \times 32 \times 1$	0.001
hexagonal	600	$8 \times 8 \times 1$	0.002
hexagonal	600	$10 \times 10 \times 1$	0.003
hexagonal	600	$16 \times 16 \times 1$	0.001
hexagonal	600	$32 \times 32 \times 1$	0.001
hexagonal	800	$32 \times 32 \times 1$	0.001
orthogonal	600	$8 \times 8 \times 1$	211
orthogonal	600	$16 \times 8 \times 1$	162
orthogonal	600	$8 \times 16 \times 1$	176
orthogonal	800	$20 \times 32 \times 1$	133
orthogonal	800	$32 \times 20 \times 1$	132
orthogonal	800	$32 \times 32 \times 1$	132
orthogonal	1000	$16 \times 8 \times 1$	132
orthogonal	1000	$40 \times 40 \times 1$	133
orthogonal (2 H)	400	$40 \times 40 \times 1$	0.09
orthogonal (2 H)	600	$40 \times 40 \times 1$	0.09
orthogonal (2 H)	800	$8 \times 8 \times 1$	7.90
orthogonal (2 H)	800	$16 \times 16 \times 1$	0.68
orthogonal (2 H)	800	$32 \times 32 \times 1$	0.07
orthogonal (2 H)	800	$40 \times 40 \times 1$	0.09
orthogonal (2 H)	1000	$40 \times 40 \times 1$	0.09

Table A.5: Showing the size of the system, the atoms it contains and the length of lattice vectors in  $x$ - and  $y$ -direction in Å. The difference of the interaction energies of two H-atoms put at the lateral position of 1.2 Å above the surface in symmetrically equivalent bridge points. The interaction energies are shown in Fig. 4.13.

slabsize	number of atoms	length of lattice vector / Å		$\Delta E_{\text{Interact}} / \text{meV}$
		$x$ -vector	$y$ -vector	
3×4	24	8.55	7.40	95
4×4	32	9.84	8.52	88
5×4	40	12.30	8.52	57
5×6	60	12.30	12.78	16
6×6	72	14.76	12.78	42
8×8	128	19.68	17.04	6
9×8	144	22.14	17.04	20
9×10	180	22.14	21.30	9
10×10	200	24.60	21.30	17

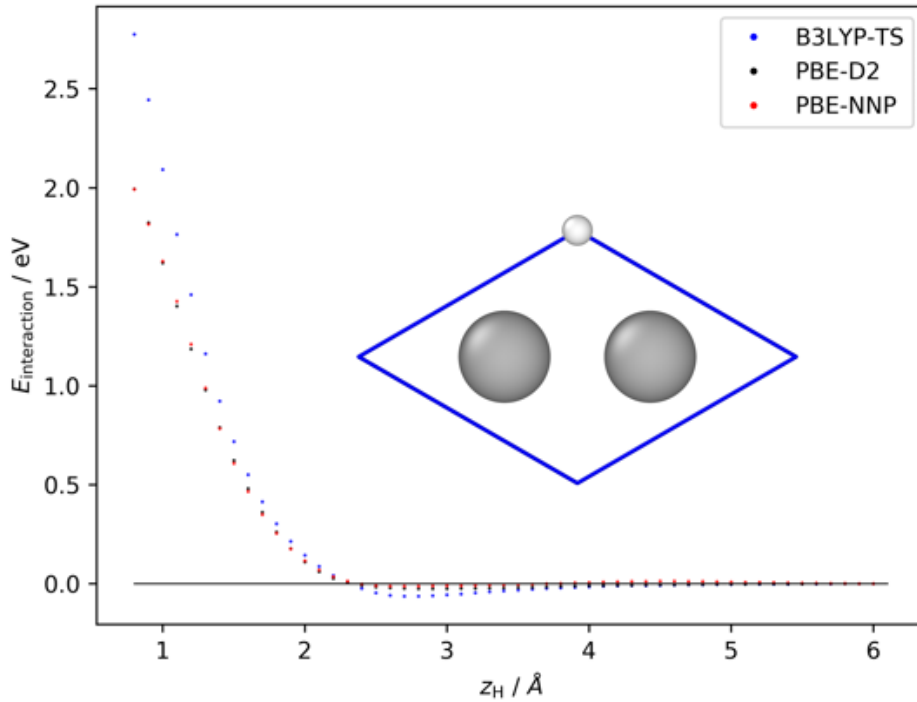


Figure A.6: Interaction energies for the H-atom approaching the graphene surface plane in mid position. The interaction energy given in eV is plotted against the lateral position  $z_H$  of the atom given in Å. Around  $z_H = 2.8$  Å, the physisorption well can be seen and around  $z_H = 2.0$  Å the repulsive wall is rising. This is due to Pauli-repulsion and explains, why the physisorption well is involved in fast channel. This scattering event can be therefore seen as quasi.elastic, because it is like scattering from a wall.

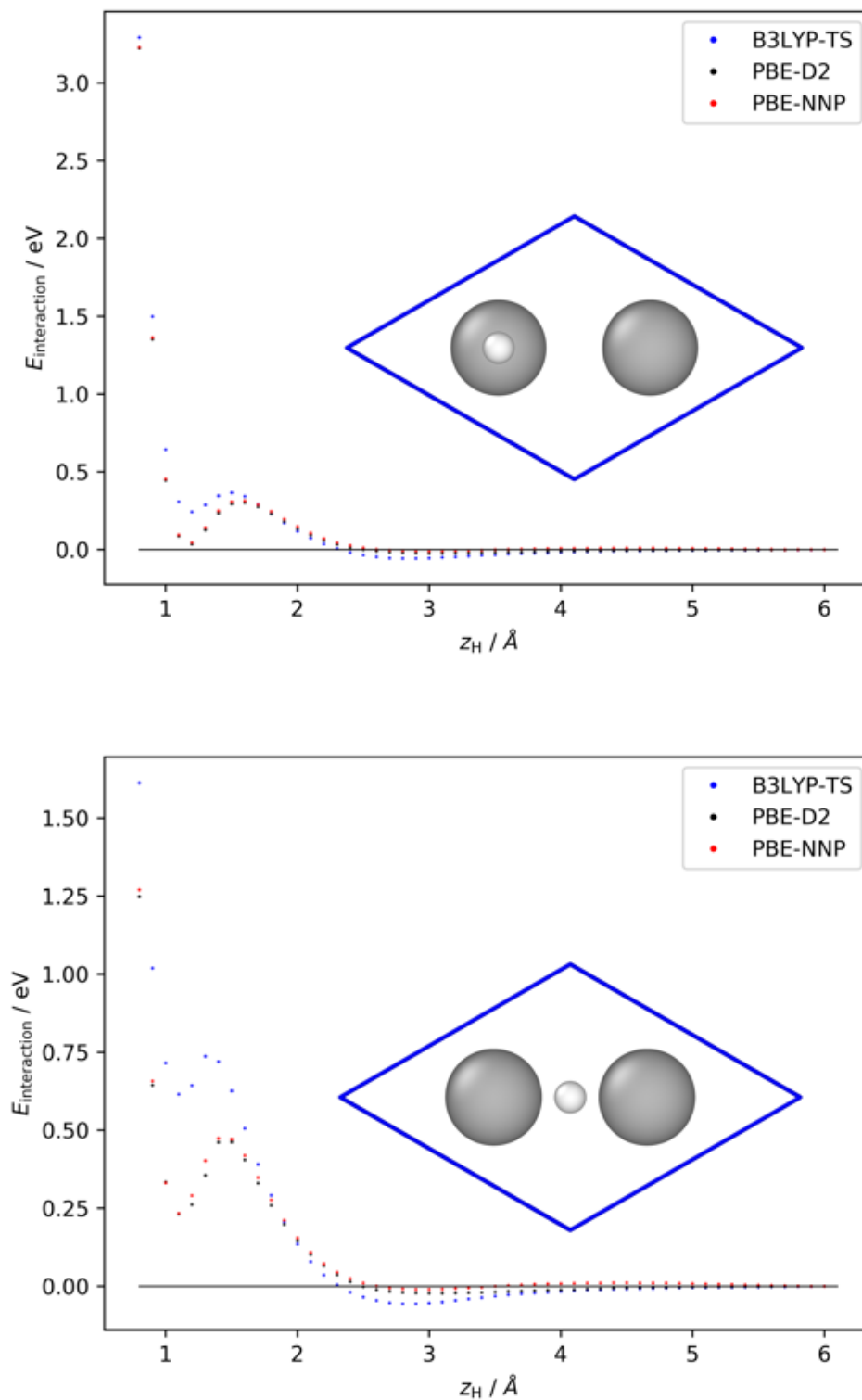


Figure A.7: Interaction energies for the H-atom approaching the graphene surface plane in top (top) and bri (bottom) position. The interaction energy given in eV is plotted against the lateral position  $z_{\text{H}}$  of the atom given in  $\text{\AA}$ . Around  $z_{\text{H}} \approx 2.8 \text{\AA}$ , the physisorption well can be seen and around  $z_{\text{H}} = 2.0 \text{\AA}$  the barrier to chemisorption is presented whereas at around  $1.1 \text{\AA}$  the chemisorption well can be seen, which corresponds to the equilibrium distance of a C–H bond. The trend with the wells follows the trend seen at mid position, but at bri, the well depth is doubled, which corresponds to two carbon atoms involved.

## A.5 Determining the timestep in molecular dynamics simulations

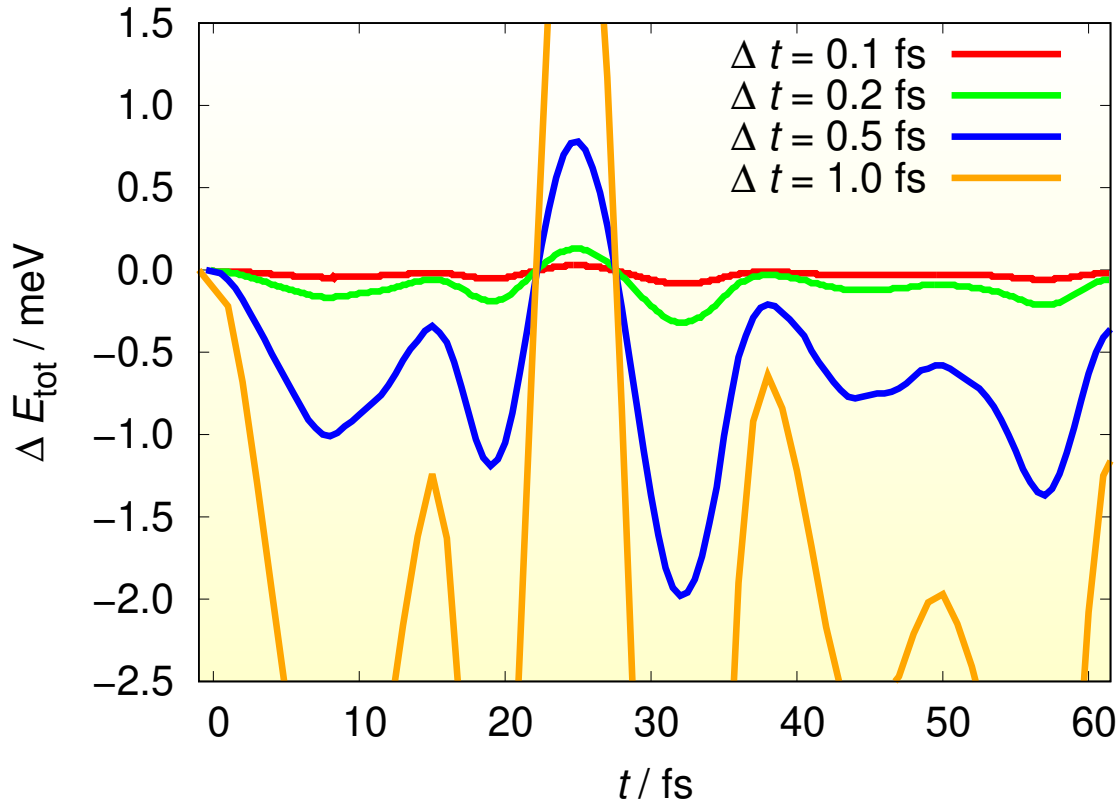


Figure A.8: Analysis of timestep given in fs to chose in the molecular dynamics simulations when simulating the scattering of an H-atom from a free-standing graphene sheet. The energetic difference is shown in the order of a few meV. The desired range of energy in the simulations is around 0.1 meV. It is fine that the energy will fluctuate a bit, because the scattering event is a fast process, where the energy is rapidly changing due to strong gas-surface interactions. When looking at the graphs, the scattering can be followed. First, the particle feels the physisorption well and is accelerated and finally hits the surface around 25 fs, which can be seen independent of the timestep. The projectile feels the repulsive wall, is scattered and traverse into the gas-phase again. In the red graph, this is barely seen and the energy is conserved. From the green curve one can see, that not a single, but at least two carbon atoms are involved in the scattering process. With an increasing timestep, the projectile comes very close to the surface atoms, feels a very high energetic barrier until emerging back into the gas-phase. From the orange graph we can see, that the energy is no longer preserved.

## A.6 Energy loss pathways example trajectories

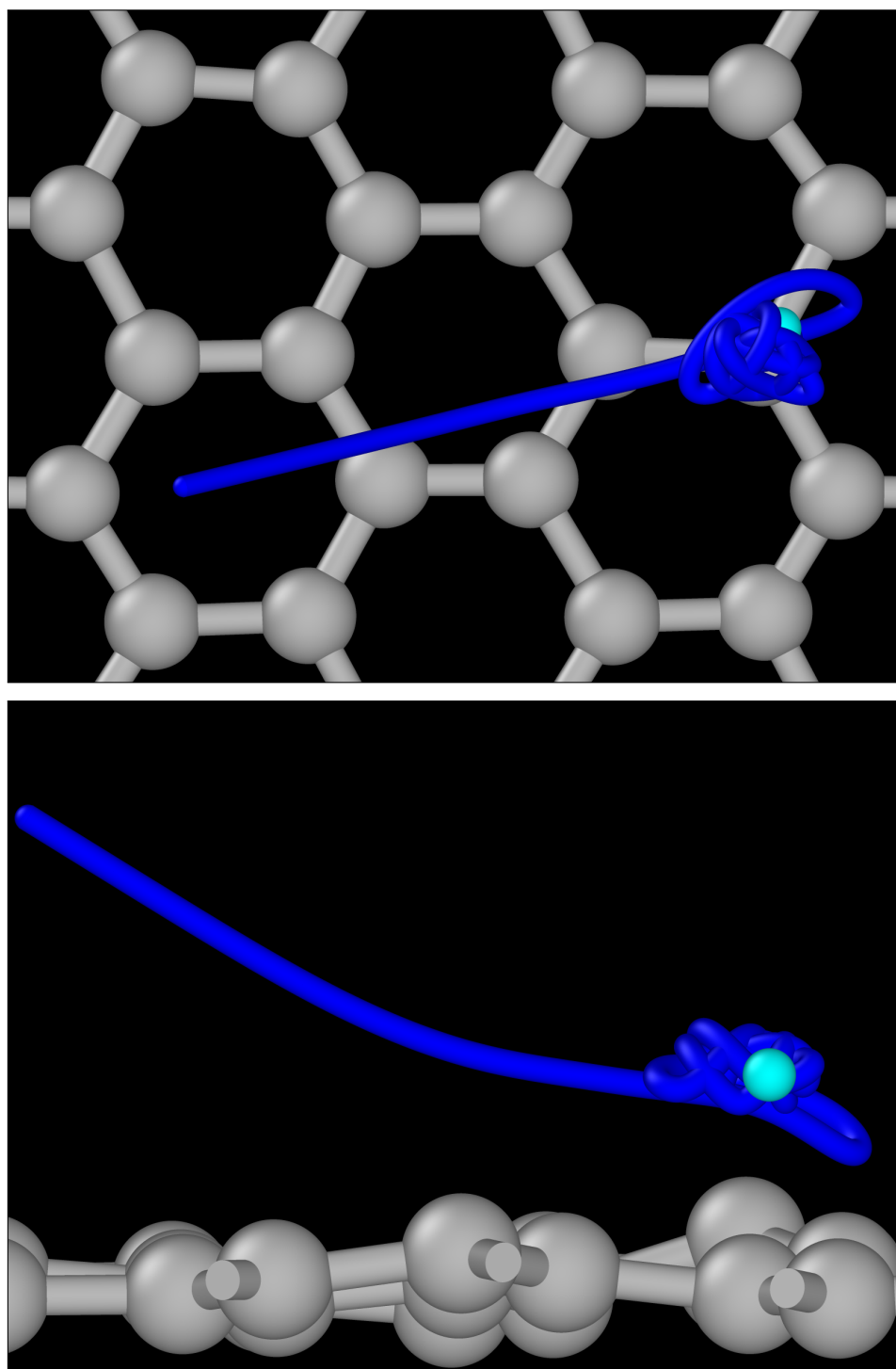


Figure A.9: Example trajectory showing the adsorption in a sort of "top view" and "side view". The trajectory of the H-atom is shown in dark-blue and the H-atoms final position is shown as a cyan colored sphere. The carbon atoms are shown as gray colored spheres.

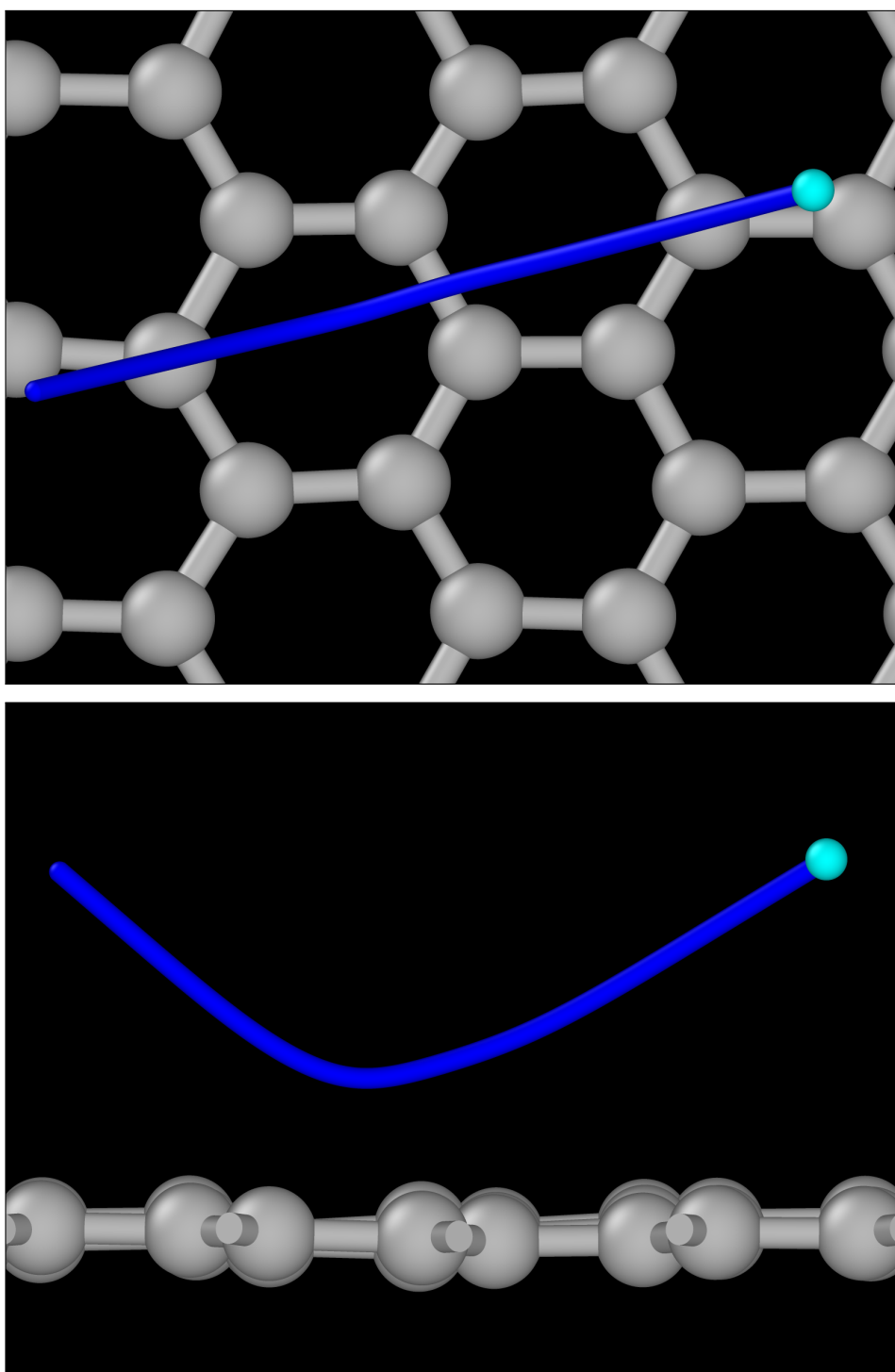


Figure A.10: Example trajectory showing the fast channel in a sort of "top view" and "side view". The trajectory of the H-atom is shown in dark-blue and the H-atoms final position is shown as a cyan colored sphere. The carbon atoms are shown as gray colored spheres.

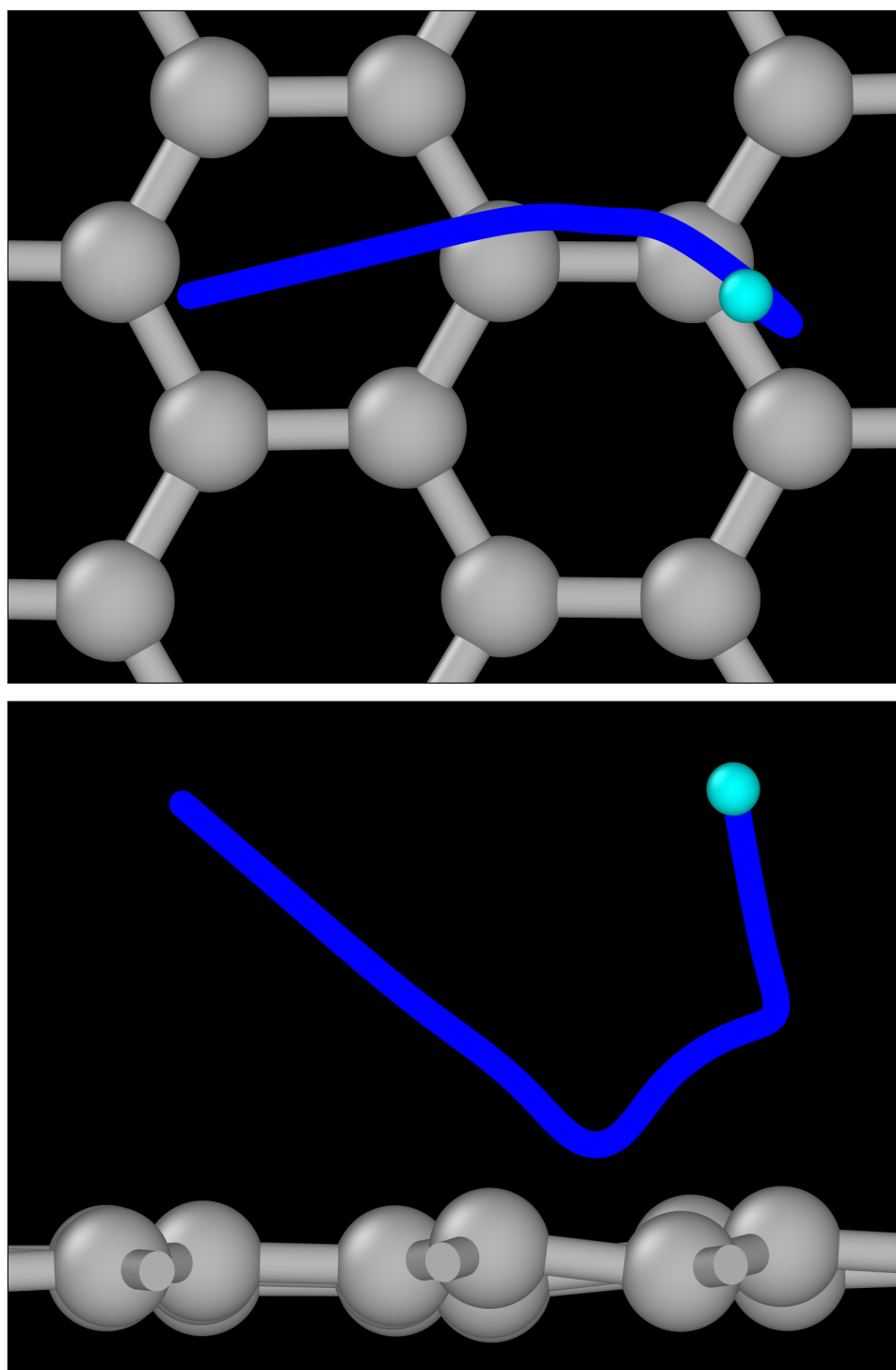


Figure A.11: Example trajectory showing the fast channel in a sort of "top view" and "side view". The trajectory of the H-atom is shown in dark-blue and the H-atoms final position is shown as a cyan colored sphere. The carbon atoms are shown as gray colored spheres.



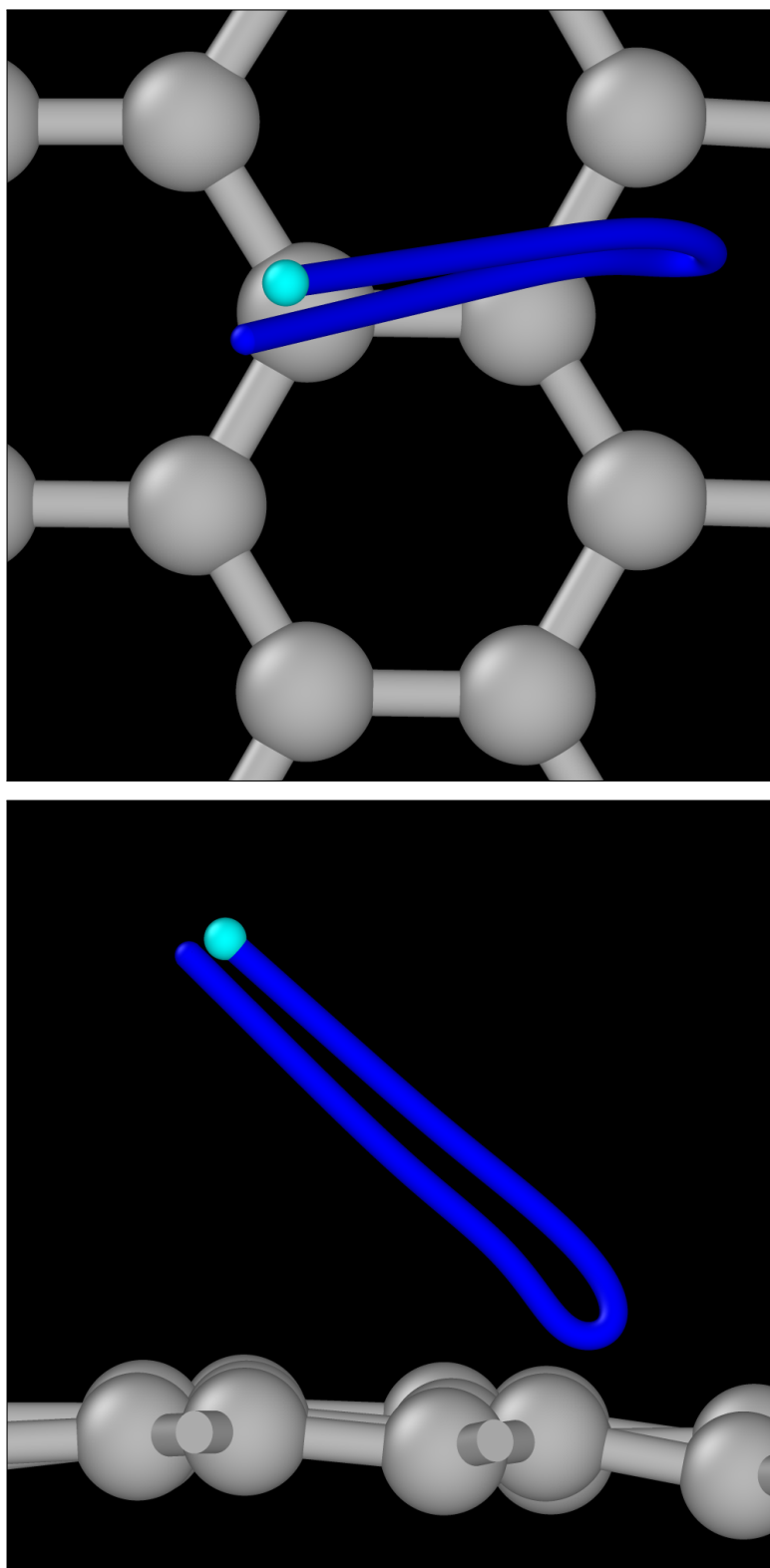


Figure A.12: Example trajectory backward scattering in a sort of "top view" and "side view". The trajectory of the H-atom is shown in dark-blue and the H-atoms final position is shown as a cyan colored sphere. The carbon atoms are shown as gray colored spheres.

## A.7 Scattering trajectories

Table A.6: Showing the total number of simulated trajectories  $N_{\text{total}}$ , scattered trajectories within detection limit compared to experimental setup  $N_{3^\circ}$ , the normal component of incidence energy  $E_N$  and sticking probability  $S_0$  for H- and D-atoms at incidence polar angle  $\theta_I$ . The results from experiment compared to HDNN-PES and REBO-EMFT PES are shown. The flux scaling factors are given to use the same color code when showing the translational energy and scattering angle distributions.

	$\theta_I$	$N_{\text{total}}$	$N_{3^\circ}$	$E_N$ / eV	$S_0$	Flux Scaling Factor
Experiment						
H	40.0	—	—	1.13	—	1.0
	50.0	—	—	0.79	—	14.0
	59.5	—	—	0.49	—	40.0
D	43.0	—	—	1.00	—	1.0
	51.0	—	—	0.74	—	7.0
	59.5	—	—	0.48	—	28.5
HDNN-PES						
H	40.0	1,000,000	40,298	1.13	0.21	1.0
	50.0	1,273,176	48,935	0.79	0.39	13.1
	59.5	1,000,000	169,074	0.49	0.22	40.8
D	43.0	899,964	21,613	1.00	0.52	1.0
	51.0	799,987	20,817	0.74	0.68	14.6
	59.5	919,984	136,104	0.48	0.39	69.1
REBO-EMFT PES						
H	40.0	100,000	5,941	1.13	0.53	1.0
	50.0	100,000	3,640	0.79	0.44	8.6
	60.0	100,000	48,722	0.48	0.05	69.3

Table A.7: Showing the incidence polar angle  $\theta_I$  of H- and D-atoms from RAT experiment. The incidence kinetic energy  $E_I$  and its normal component  $E_N$  as well as the flux scaling factors are given to use the same color code when showing the translational energy and scattering angle distributions.

	$\theta_I$	$E_I$ / eV	$E_N$ / eV	Flux Scaling Factor
H	26.0	1.92	1.55	1.74
	28.0	1.92	1.50	3.52
	30.0	1.92	1.44	4.38
	32.0	1.92	1.38	7.64
	34.0	1.92	1.32	9.91
	36.0	1.92	1.26	20.0
	38.0	1.92	1.19	49.25
	40.0	1.92	1.13	70.48
	42.0	1.92	1.06	96.86
	44.0	1.92	0.99	103.19
	46.0	1.92	0.93	152.28
	48.0	1.92	0.86	129.86
	50.0	1.92	0.79	96.84
	52.0	1.92	0.73	87.62
	54.0	1.92	0.66	103.28
	56.0	1.92	0.60	86.26
	57.5	1.92	0.55	79.42
	59.5	1.92	0.49	70.99
D	61.5	1.92	0.44	74.39
	43.0	1.87	1.00	2.96
	45.0	1.87	0.93	5.37
	47.0	1.87	0.87	7.75
	49.0	1.87	0.80	18.14
	51.0	1.87	0.74	30.2
	53.0	1.87	0.68	37.45
	55.0	1.87	0.61	45.61
	57.5	1.87	0.54	118.68
	59.5	1.87	0.48	143.06
	61.5	1.87	0.43	152.46

Table A.8: Showing the total number of simulated trajectories  $N_{\text{total}}$ , scattered trajectories within detection limit compared to experimental setup  $N_{3^\circ}$ , the normal component of incidence energy and sticking probability  $S_0$  for H- and D-atoms at incidence polar angle  $\theta_I$ . The number of trajectories within detection limit considering also backward-scattering  $N_{3^\circ, \text{all}}$  is given as well. The flux scaling factors are given to use the same color code when showing the translational energy and scattering angle distributions.

	$\theta_I$	$N_{\text{total}}$	$N_{3^\circ}$	$N_{3^\circ, \text{all}}$	$E_N$ / eV	$S_0$	Flux Scaling Factor
HDNN-PES							
H	10.0	200,000	18,674	22,776	1.86	0.01	1.00
	20.0	200,000	19,825	22,128	1.70	0.02	0.86
	30.0	200,000	15,261	16,843	1.44	0.04	0.53
	38.0	100,000	4,596	5,326	1.19	0.15	0.14
	40.0	1,000,000	40,298	48,429	1.13	0.21	0.96
	42.0	100,000	3,275	4,106	1.06	0.27	0.14
	44.0	100,000	3,323	4,274	0.99	0.33	0.11
	46.0	100,000	2,987	3,792	0.93	0.37	0.08
	48.0	100,000	3,211	3,969	0.86	0.39	0.13
	50.0	1,273,176	48,935	58,025	0.79	0.39	2.99
	54.0	100,000	6,148	6,667	0.66	0.36	0.74
	59.5	1,000,000	169,074	172,451	0.49	0.22	39.24
	70.0	200,000	135,603	135,840	0.22	0.00	72.18
	80.0	200,000	191,651	191,395	0.06	0.00	124.99
D	10.0	200,000	15,964	19,688	1.86	0.04	1.00
	20.0	200,000	16,368	18,771	1.70	0.06	0.76
	30.0	200,000	11,604	13,625	1.44	0.14	0.44
	43.0	899,964	21,613	32,075	1.03	0.52	0.45
	45.0	100,000	1,993	3,083	0.96	0.58	0.06
	47.0	100,000	1,944	2,987	0.89	0.64	0.10
	49.0	100,000	1,914	2,901	0.83	0.67	0.14
	51.0	799,987	20,817	2,609	0.76	0.68	2.16
	53.0	100,000	3,424	3,990	0.70	0.66	0.41
	55.0	100,000	5,389	5,806	0.63	0.61	0.80
	57.0	100,000	8,172	8,481	0.57	0.53	1.49
	59.5	919,984	136,104	138,629	0.49	0.39	31.41
	70.0	200,000	137,259	137,539	0.22	0.00	85.38
	80.0	200,000	193,787	194,018	0.06	0.00	135.71

Table A.9: Showing the surface temperature  $T$ , incidence polar angle  $\theta_I$ , incidence kinetic energy  $E_I$  as well as its normal component  $E_N$  for H-atom scattering in RAT experiment.

	$T / \text{K}$	$\theta_I$	$E_I / \text{eV}$	$E_N / \text{eV}$
H	300	46.0	1.92	0.79
	600	46.0	1.92	0.79

Table A.10: Showing the total number of simulated trajectories  $N_{\text{total}}$ , scattered trajectories within detection limit compared to experimental setup  $N_{3^\circ}$ , the normal component of incidence energy and sticking probability  $S_0$  for H- and D-atoms with incidence polar angle  $\theta_I = 50^\circ$  and surface temperature  $T$ . The number of trajectories within detection limit considering also backward-scattering  $N_{3^\circ, \text{all}}$  is given as well

	$T / \text{K}$	$N_{\text{total}}$	$N_{3^\circ}$	$N_{3^\circ, \text{all}}$	$E_N / \text{eV}$	$S_0$
H	77	999,999	45,205	52,144	0.79	0.41
	300	200,000	7,324	9,002	0.79	0.38
	600	198,201	6,249	7,961	0.79	0.34
D	77	1,000,000	27,173	36,464	0.77	0.70
	300	200,000	4,536	6,469	0.77	0.67
	600	195,245	3,947	5,584	0.77	0.62

Table A.11: Showing the incidence polar angle  $\theta_I$ , incidence kinetic energy  $E_I$  and its normal component  $E_N$  for H- and D-atoms from RAT experiment.

	$\theta_I$	$E_I / \text{eV}$	$E_N / \text{eV}$
H	46.5	0.99	0.41
	46.0	1.92	0.79
	46.0	2.18	0.90
	46.0	2.62	1.08
	46.0	3.31	1.37
D	47.5	0.94	0.39
	48.0	1.87	0.77
	49.1	3.25	1.34

Table A.12: Showing the total number of simulated trajectories  $N_{\text{total}}$ , scattered trajectories within detection limit compared to experimental setup  $N_{3^\circ}$ , the incidence kinetic energy  $E_I$ , its normal component  $E_N$  and sticking probability  $S_0$  for H- and D-atoms at given incidence polar angle  $\theta_I$ . The number of trajectories within detection limit considering also backward-scattering  $N_{3^\circ, \text{all}}$  is given as well.

	$\theta_I$	$E_I$ / eV	$N_{\text{total}}$	$N_{3^\circ}$	$N_{3^\circ, \text{all}}$	$E_N$ / eV	$S_0$
H	50.0	0.99	199,981	32,054	32,397	0.41	0.33
	50.0	1.92	1,273,176	48,935	58,025	0.79	0.39
	50.0	2.18	200,000	6,738	7,897	0.90	0.27
	50.0	2.62	200,000	8,982	9,422	1.08	0.11
	50.0	3.31	200,000	16,269	16,357	1.37	0.01
D	47.5	0.94	199,958	22,927	23,305	0.39	0.49
	47.0	1.87	199,977	4,426	6,239	0.87	0.64
	49.1	3.25	199,985	11,552	11,728	1.34	0.12

Table A.13: Showing the total number of simulated trajectories  $N_{\text{total}}$ , the normal component of incidence energy  $E_N$  and sticking probability  $S_0$  for H- and D-atoms at incidence polar angle  $\theta_I$ .

	$\theta_I$	$N_{\text{total}}$	$E_N$ / eV	$S_0$
H	10.0	100,000	1.86	0.01
	20.0	100,000	1.70	0.01
	30.0	100,000	1.44	0.04
	40.0	100,000	1.13	0.19
	50.0	1,000,000	0.79	0.35
	60.0	100,000	0.48	0.20
D	10.0	100,000	1.86	0.03
	20.0	100,000	1.70	0.05
	30.0	100,000	1.44	0.12
	43.0	1,000,000	1.13	0.50
	51.0	100,000	0.79	0.66
	60.0	100,000	0.48	0.37

Table A.14: Showing the type of simulations performed, total number of simulated trajectories  $N_{\text{total}}$ , scattered trajectories within detection limit compared to experimental setup  $N_{3^\circ}$ , the incidence kinetic energy  $E_I$ , its normal component  $E_N$  and sticking probability  $S_0$  for H-atoms at incidence polar angle  $\theta_I$  in RAT experiment.

	Method	$\theta_I$	$E_I$	$N_{\text{total}}$	$N_{3^\circ}$	$E_N$ / eV	$S_0$
H	Exp	30	1.92	–	–	1.44	–
	MD	30	1.92	200,000	15,261	1.44	0.04
	RPMD	30	1.92	100,000	4,078	1.44	0.01
	QMD	30	2.00	–	–	1.50	–

Table A.15: Showing the type of simulations performed, total number of simulated trajectories  $N_{\text{total}}$ , scattered trajectories within detection limit compared to experimental setup  $N_{\text{geom}}$ , the normal component of incidence energy  $E_N$  and sticking probability  $S_0$  for H- and D-atoms at incidence polar angle  $\theta_I$ . This table shows the result for the comparison to HBEAM experiment.

	Simulation	$\theta_I$	$N_{\text{total}}$	$N_{\text{geom}}$	$E_N = E_I$ / eV	$S_0$
H	MD	0.0	35,000	1,544	1.92	0.01
	RPMD	0.0	98,349	4,428	1.92	0.05
	QMD	0.0	–	–	1.92	0.06
	MD	0.0	40,000	1,553	1.50	0.04
	MD	0.0	70,000	1,177	0.99	0.53
	RPMD	0.0	46,467	575	0.99	0.60
	QMD	0.0	–	–	0.99	0.79
	MD	0.0	20,000	800	1.92	0.02
D	QMD	0.0	–	–	1.92	0.33
	MD	0.0	10,000	335	1.50	0.10
	MD	0.0	30,000	402	0.99	0.65
	MD	0.0	30,000	402	0.99	0.65

---

---

# Bibliography

- [1] R. Masel, *Principles of adsorption and reaction on solid surfaces* (Wiley-VCH, New-York, 1996).
- [2] H. Knözinger and K. Kochloefl, *Ullmann's Encyclopedia of Industrial Chemistry* (John Wiley & Sons, Ltd, 2003) [https://onlinelibrary.wiley.com/doi/pdf/10.1002/14356007.a05\\_313](https://onlinelibrary.wiley.com/doi/pdf/10.1002/14356007.a05_313) .
- [3] K. W. Kolasinski, *Surface Science: Foundations of Catalysis and Nanoscience* (John Wiley and Sons, Ltd, UK, 2012).
- [4] R. Brückner, *Reaktionsmechanismen*, 3rd ed. (Spektrum Akad. Verl., Berlin, 2009).
- [5] M. Appl, *Ullmann's Encyclopedia of Industrial Chemistry* (John Wiley & Sons, Ltd, 2006) [https://onlinelibrary.wiley.com/doi/pdf/10.1002/14356007.a02\\_143.pub2](https://onlinelibrary.wiley.com/doi/pdf/10.1002/14356007.a02_143.pub2) .
- [6] G. Ertl, "Elementary steps in heterogeneous catalysis," *Angewandte Chemie International Edition in English* **29**, 1219–1227 (1990), <https://onlinelibrary.wiley.com/doi/pdf/10.1002/anie.199012191> .
- [7] A. de Klerk, "Fischer–tropsch process," in *Kirk-Othmer Encyclopedia of Chemical Technology* (John Wiley & Sons, Ltd, 2013) pp. 1–20, <https://onlinelibrary.wiley.com/doi/pdf/10.1002/0471238961.fiscdekl.a01> .
- [8] B. C. Krüger, G. B. Park, S. Meyer, R. J. V. Wagner, A. M. Wodtke, and T. Schäfer, "Trapping-desorption and direct-scattering of formaldehyde at au(111)," *Phys. Chem. Chem. Phys.* **19**, 19896–19903 (2017).
- [9] C. T. Rettner, J. Kimman, and D. J. Auerbach, "Inelastic scattering of no from ag(111): Internal state, angle, and velocity resolved measurements," *The Journal of Chemical Physics* **94**, 734–750 (1991), <https://doi.org/10.1063/1.460342> .
- [10] K. Laidler, "Chemical kinetics, (harper and row, new york, 1987)." b) AA Frost, RG Pearson, *Kinetics and Mechanism*, second ed., Wiley, New York , 88 (1988).
- [11] J. R. Ross, "Chapter 7 - the kinetics and mechanisms of catalytic reactions," in *Contemporary Catalysis*, edited by J. R. Ross (Elsevier, Amsterdam, 2019) pp. 161–186.
- [12] M. Born and W. Heisenberg, "Zur Quantentheorie der Molekeln," *Ann. Phys.* **379**, 1—31 (1924).
- [13] M. Born and R. Oppenheimer, "Zur Quantentheorie der Molekeln," *Annalen der Physik* **389**, 457–484 (1927).
- [14] O. Bünermann, H. Jiang, Y. Dorenkamp, A. Kandratsenka, S. M. Janke, D. J. Auerbach, and A. M. Wodtke, "Electron-hole pair excitation determines the mechanism of hydrogen atom adsorption," *SCIENCE* **350**, 1346–1349 (2015).
- [15] S. M. Janke, D. J. Auerbach, A. M. Wodtke, and A. Kandratsenka, "An accurate full-dimensional potential energy surface for H-Au(111): Importance of nonadiabatic electronic excitation in energy transfer and adsorption," *JOURNAL OF CHEMICAL PHYSICS* **143**, 124708 (2015).
- [16] Y. Dorenkamp, C. Volkmann, V. Roddatis, S. Schneider, A. M. Wodtke, and O. Bünermann, "Inelastic h atom scattering from ultrathin aluminum oxide films grown by atomic



- layer deposition on pt(111),” The Journal of Physical Chemistry C **122**, 10096–10102 (2018), <https://doi.org/10.1021/acs.jpcc.8b02692> .
- [17] A. Kandratsenka, H. Jiang, Y. Dorenkamp, S. Janke, M. Kammler, A. Wodtke, and O. Bünermann, “Unified description of h-atom-induced chemicurrents and inelastic scattering,” Proceedings of the National Academy of Sciences **115**, 201710587 (2018).
- [18] N. Hertl, R. Martin-Barrios, O. Galparsoro, P. Larrégaray, D. J. Auerbach, D. Schwarzer, A. M. Wodtke, and A. Kandratsenka, “Random force in molecular dynamics with electronic friction,” The Journal of Physical Chemistry C **125**, 14468–14473 (2021).
- [19] N. Hertl, A. Kandratsenka, and A. M. Wodtke, “Effective medium theory for bcc metals: electronically non-adiabatic h atom scattering in full dimensions,” Phys. Chem. Chem. Phys. **24**, 8738–8748 (2022).
- [20] D. A. Siegel, C.-H. Park, C. Hwang, J. Deslippe, A. V. Fedorov, S. G. Louie, and A. Lanzara, “Many-body interactions in quasi-freestanding graphene,” Proceedings of the National Academy of Sciences **108**, 11365–11369 (2011), <https://www.pnas.org/doi/pdf/10.1073/pnas.1100242108> .
- [21] M. Gao, Y. Pan, C. Zhang, H. Hu, R. Yang, H. Lu, J. Cai, S. Du, F. Liu, and H.-J. Gao, “Tunable interfacial properties of epitaxial graphene on metal substrates,” Applied Physics Letters **96**, 053109 (2010), <https://doi.org/10.1063/1.3309671> .
- [22] Cushing, Gregory W. and Johánek, Viktor and Navin, Jason K. and Harrison, Ian, “Graphene Growth on Pt(111) by Ethylene Chemical Vapor Deposition at Surface Temperatures near 1000 K,” The Journal of Physical Chemistry C **119**, 4759–4768 (2015), <https://doi.org/10.1021/jp508177k> .
- [23] P. Sutter, J. T. Sadowski, and E. Sutter, “Graphene on pt(111): Growth and substrate interaction,” Phys. Rev. B **80**, 245411 (2009).
- [24] O. Bünermann, H. Jiang, Y. Dorenkamp, D. J. Auerbach, and A. M. Wodtke, “An ultrahigh vacuum apparatus for H atom scattering from surfaces,” Rev. Sci. Instr. **89**, 094101 (2018).
- [25] H. Jiang, M. Kammler, F. Ding, Y. Dorenkamp, F. R. Manby, A. M. Wodtke, T. F. Miller, A. Kandratsenka, and O. Bünermann, “Imaging covalent bond formation by h atom scattering from graphene,” Science **364**, 379–382 (2019), <https://www.science.org/doi/pdf/10.1126/science.aaw6378> .
- [26] L. Hornekaer, Z. Sljivancanin, W. Xu, R. Otero, E. Rauls, I. Stensgaard, E. Lægsgaard, B. Hammer, and F. Besenbacher, “Metastable structures and recombination pathways for atomic hydrogen on the graphite (0001) surface,” Physical review letters **96**, 156104 (2006).
- [27] M. Yang, A. Nurbawono, C. Zhang, R. Wu, Y. Feng, and Ariando, “Manipulating absorption and diffusion of h atom on graphene by mechanical strain,” AIP Advances **1**, 032109 (2011), <https://doi.org/10.1063/1.3622614> .
- [28] H. Jiang, X. Tao, M. Kammler, F. Ding, A. M. Wodtke, A. Kandratsenka, T. F. Miller, and O. Bünermann, “Small nuclear quantum effects in scattering of h and d from graphene,” The Journal of Physical Chemistry Letters **12**, 1991–1996 (2021), pMID: 33596383, <https://doi.org/10.1021/acs.jpcclett.0c02933> .
- [29] K. Golibrzuch, V. Walpole, A. Schönemann, and A. M. Wodtke, “Generation and Scattering of Nanosecond H-Atom Pulses from Single-Crystal Epitaxial Graphene,” Journal Article (2022), (in preparation).
- [30] F. Gatti and L. Shi, “private communications,” (2022).
- [31] D. J. Griffiths, *Introduction to Quantum Mechanics*, 2nd ed. (Pearson Prentice Hall, 2004).
- [32] P. Blöchl, “FSX Advanced Topics of Theoretical Physics I, Introduction to Solid State Theory,” <https://www2.pt.tu-clausthal.de/atp/downloads/scripts/sst1.pdf> (2021),

- accessed: 10.10.2021.
- [33] E. Schrödinger, “Quantisierung als Eigenwertproblem (1. Mitteilung),” *Ann. d. Physik* **79**, 361–376 (1926).
  - [34] M. Born and K. Huang, *Dynamical Theory of Crystal Lattices* (Oxford University Press, Oxford, 1954).
  - [35] W. Kutzelnigg, *Einführung in die Theoretische Chemie*, 1st ed. (WILEY-VCH Verlag GmbH, Weinheim, 2002).
  - [36] D. Marx and J. Hutter, *Ab Initio Molecular Dynamics: Basic Theory and Advanced Methods* (Cambridge University Press: Cambridge, 2009).
  - [37] W. Kutzelnigg, “The adiabatic approximation I. The physical background of the Born-Handy ansatz,” *Mol. Phys.* **90**, 909–916 (1997).
  - [38] P. Hohenberg and W. Kohn, “Inhomogeneous Electron Gas,” *Phys. Rev.* **136**, B864–B871 (1964).
  - [39] W. Kohn and L. J. Sham, “Self-Consistent Equations Including Exchange and Correlation Effects,” *Physical Review* **140**, 1133–1138 (1965).
  - [40] P. W. Atkins and R. S. Friedman, *Molecular Quantum Mechanics*, 5th ed. (Oxford University Press Inc., New York, 2011).
  - [41] F. Bloch, “Bemerkung zur Elektronentheorie des Ferromagnetismus und der elektrischen Leitfähigkeit,” *Z. Physik* **57**, 545–555 (1929).
  - [42] P. a. M. Dirac, “Note on Exchange Phenomena in the Thomas Atom,” *Mathematical Proceedings of the Cambridge Philosophical Society* **26**, 376–385 (1930).
  - [43] E. H. Lieb and S. Oxford, “Improved lower bound on the indirect coulomb energy,” *International Journal of Quantum Chemistry* **19**, 427–439 (1981), <https://onlinelibrary.wiley.com/doi/pdf/10.1002/qua.560190306>.
  - [44] J. C. Slater, “A Simplification of the Hartree-Fock Method,” *Phys. Rev.* **81**, 385–390 (1951).
  - [45] S.-k. Ma and K. A. Brueckner, “Correlation Energy of an Electron Gas with a Slowly Varying High Density,” *Phys. Rev.* **165**, 18–31 (1968).
  - [46] O. Gunnarsson and B. I. Lundqvist, “Exchange and correlation in atoms, molecules, and solids by the spin-density-functional formalism,” *Phys. Rev. B* **13**, 4274–4298 (1976).
  - [47] S. H. Vosko, L. Wilk, and M. Nusair, “Accurate spin-dependent electron liquid correlation energies for local spin density calculations: a critical analysis,” *Canadian Journal of Physics* **58**, 1200–1211 (1980).
  - [48] C. Lee, W. Yang, and R. G. Parr, “Development of the colle-salvetti correlation-energy formula into a functional of the electron density,” *Phys. Rev. B* **37**, 785–789 (1988).
  - [49] D. C. Langreth and J. P. Perdew, “Theory of nonuniform electronic systems. i. analysis of the gradient approximation and a generalization that works,” *Phys. Rev. B* **21**, 5469–5493 (1980).
  - [50] D. C. Langreth and M. J. Mehl, “Beyond the local-density approximation in calculations of ground-state electronic properties,” *Phys. Rev. B* **28**, 1809–1834 (1983).
  - [51] J. P. Perdew, K. Burke, and M. Ernzerhof, “Generalized gradient approximation made simple,” *Phys. Rev. Lett.* **77**, 3865–3868 (1996).
  - [52] S. K. Ghosh and R. G. Parr, “Phase-space approach to the exchange-energy functional of density-functional theory,” *Phys. Rev. A* **34**, 785–791 (1986).
  - [53] A. D. Becke and M. R. Roussel, “Exchange holes in inhomogeneous systems: A coordinate-space model,” *Phys. Rev. A* **39**, 3761–3767 (1989).
  - [54] J. Tao, J. P. Perdew, V. N. Staroverov, and G. E. Scuseria, “Climbing the density functional ladder: Nonempirical meta-generalized gradient approximation designed for molecules and solids,” *Phys. Rev. Lett.* **91**, 146401 (2003).
  - [55] C. J. Cramer, *Essentials of Computational Chemistry: Theories and Models*, 2nd ed.

- (John Wiley & Sons, 2004).
- [56] A. D. Becke, "Density-functional thermochemistry. iii. the role of exact exchange," *The Journal of Chemical Physics* **98**, 5648–5652 (1993), <https://doi.org/10.1063/1.464913>.
  - [57] P. J. Stephens, F. J. Devlin, C. F. Chabalowski, and M. J. Frisch, "Ab initio calculation of vibrational absorption and circular dichroism spectra using density functional force fields," *The Journal of Physical Chemistry* **98**, 11623—11627 (1994).
  - [58] D. R. Hartree, "The Wave Mechanics of an Atom with a Non-Coulomb Central Field. Part I. Theory and Methods," *Math. Proc. Camb. Phil. Soc.* **24**, 89—110 (1928).
  - [59] V. Fock, "Näherungsmethode zur Lösung des quantenmechanischen Mehrkörperproblems," *Z. Physik* **61**, 126–148 (1930).
  - [60] D. B. Cook, *Handbook of Computational Quantum Chemistry*, 1st ed. (Dover Publications Inc., Mineola, New York, 2005).
  - [61] J. C. Slater, "A generalized self-consistent field method," *Phys. Rev.* **91**, 528–530 (1953).
  - [62] F. Jensen, *Introduction to Computational Chemistry*, 2nd ed. (Wiley-VCH Verlag GmbH, Weinheim, 2007).
  - [63] A. D. Becke, "Density-functional exchange-energy approximation with correct asymptotic behavior," *Phys. Rev. A* **38**, 3098–3100 (1988).
  - [64] B. Miehlich, A. Savin, H. Stoll, and H. Preuss, "Results obtained with the correlation energy density functionals of becke and lee, yang and parr," *Chemical Physics Letters* **157**, 200–206 (1989).
  - [65] E. J. Meijer and M. Sprik, "A density-functional study of the intermolecular interactions of benzene," *The Journal of Chemical Physics* **105**, 8684–8689 (1996), <https://doi.org/10.1063/1.472649>.
  - [66] S. M. Cybulski and C. E. Severn, "Critical examination of the supermolecule density functional theory calculations of intermolecular interactions," *The Journal of Chemical Physics* **122**, 014117 (2005), <https://doi.org/10.1063/1.1829044>.
  - [67] S. Grimme, *J. Comp. Chem.* **27**, 1787–1799 (2006).
  - [68] S. Grimme, S. Ehrlich, and L. Goerigk, "Effect of the damping function in dispersion corrected density functional theory," *Journal of Computational Chemistry* **32**, 1456–1465 (2011), <https://onlinelibrary.wiley.com/doi/pdf/10.1002/jcc.21759>.
  - [69] S. Grimme, J. Antony, S. Ehrlich, and S. Krieg, *J. Chem. Phys.* **132**, 154104 (2010).
  - [70] A. Tkatchenko and M. Scheffler, *Phys. Rev. Lett.* **102**, 073005 (2009).
  - [71] T. M. Mitchell, *Machine Learning* (McGraw-Hill, 1997).
  - [72] E. Alpaydin, *Introduction to Machine Learning*, 3rd ed., Adaptive Computation and Machine Learning (MIT Press, Cambridge, MA, 2014).
  - [73] C. M. Bishop, *Pattern Recognition and Machine Learning* (Springer, 2006) pp. 1–3.
  - [74] D. Silver, J. Schrittwieser, K. Simonyan, I. Antonoglou, A. Huang, A. Guez, T. Hubert, L. Baker, M. Lai, A. Bolton, Y. Chen, T. Lillicrap, F. Hui, L. Sifre, G. van den Driessche, T. Graepel, and D. Hassabis, "Mastering the game of Go without human knowledge," *Nature* **550**, 354–359 (2017).
  - [75] W. Pronobis, A. Tkatchenko, and K.-R. Müller, "Many-Body Descriptors for Predicting Molecular Properties with Machine Learning: Analysis of Pairwise and Three-Body Interactions in Molecules," *J. Chem. Theory Comput.* **14**, 2991–3003 (2018).
  - [76] F. A. Faber, A. S. Christensen, B. Huang, and O. A. von Lilienfeld, "Alchemical and structural distribution based representation for universal quantum machine learning," *J. Chem. Phys.* **148**, 241717 (2018).
  - [77] C. Cortes and V. Vapnik, "Support-vector networks," *Mach. Learn* **20**, 273–297 (1995).
  - [78] A. P. Thompson, L. P. Swiler, C. R. Trott, S. M. Foiles, and G. J. Tucker, "Spectral neighbor analysis method for automated generation of quantum-accurate interatomic potentials," *Journal of Computational Physics* **285**, 316–330 (2015).

- [79] A. P. Bartók, M. C. Payne, R. Kondor, and G. Csányi, “Gaussian Approximation Potentials: The Accuracy of Quantum Mechanics, without the Electrons,” *Phys. Rev. Lett.* **104**, 136403 (2010).
- [80] W. S. McCulloch and W. Pitts, “A logical calculus of the ideas immanent in nervous activity,” *Bulletin of Mathematical Biophysics* **5**, 115–133 (1943).
- [81] K. Hornik, M. Stinchcombe, and H. White, “Universal approximation of an unknown mapping and its derivatives using multilayer feedforward networks,” *Neural Netw.* **3**, 551–560 (1990).
- [82] Y. Cho and L. K. Saul, “Large-Margin Classification in Infinite Neural Networks,” *Neural Computation* **22**, 2678–2697 (2010), [https://direct.mit.edu/neco/article-pdf/22/10/2678/838954/neco\\_a\\_00018.pdf](https://direct.mit.edu/neco/article-pdf/22/10/2678/838954/neco_a_00018.pdf).
- [83] J. Behler, “Perspective: Machine learning potentials for atomistic simulations,” *The Journal of Chemical Physics* **145**, 170901 (2016), <https://doi.org/10.1063/1.4966192>.
- [84] E. Kocer, T. W. Ko, and J. Behler, “Neural network potentials: A concise overview of methods,” *Annual Review of Physical Chemistry* **73**, 163–186 (2022), PMID: 34982580, <https://doi.org/10.1146/annurev-physchem-082720-034254>.
- [85] E. Benavides, W. Fuertes, S. Sanchez-Gordon, and M. Sanchez, *Classification of Phishing Attack Solutions by Employing Deep Learning Techniques: A Systematic Literature Review* (Springer Singapore, 2020) pp. 51–64.
- [86] P. M. Atkinson and A. R. L. Tatnall, “Introduction neural networks in remote sensing,” *International Journal of Remote Sensing* **18**, 699–709 (1997), <https://doi.org/10.1080/014311697218700>.
- [87] T. D. Sanger, “Optimal unsupervised learning in a single-layer linear feedforward neural network,” *Neural Networks* **2**, 459–473 (1989).
- [88] D. E. Rumelhart, G. E. Hinton, and R. J. Williams, *Learning Internal Representations by Error Propagation. In: Rumelhart, D.E., McClelland, J.L. and the PDP Research Group, Eds., Parallel Distributed Processing: Explorations in the Microstructure of Cognition, Vol. 1* (Foundations, MIT Press, Cambridge, MA, 1986) pp. 318–362.
- [89] D. E. Rumelhart, G. E. Hinton, and R. J. Williams, “Learning representations by back-propagating errors,” *Nature* **323**, 533–536 (1986).
- [90] F. Agostinelli, M. Hoffman, P. Sadowski, and P. Baldi, “Learning activation functions to improve deep neural networks,” (2015), arXiv:1412.6830 [cs.NE].
- [91] P. Ramachandran, B. Zoph, and Q. V. Le, “Searching for activation functions,” *CoRR abs/1710.05941* (2017), 1710.05941.
- [92] A. Plastino, A. S. Srinivasa Rao, and C. Rao, “Series page,” in *Information Geometry, Handbook of Statistics*, Vol. 45 (Elsevier, 2021) p. ii.
- [93] T. W. Ko, J. A. Finkler, S. Goedecker, and J. Behler, “General-Purpose Machine Learning Potentials Capturing Non-local Charge Transfer,” Submitted (2020).
- [94] P. J. Werbos, *Beyond Regression: New Tools for Prediction and Analysis in the Behavioral Sciences*, Ph.D. thesis, Harvard University (1975).
- [95] J. Behler and M. Parrinello, “Generalized Neural-Network Representation of High-Dimensional Potential-Energy Surfaces,” *Phys. Rev. Lett.* **98**, 146401 (2007).
- [96] J. Behler, “Representing potential energy surfaces by high-dimensional neural network potentials,” *J. Phys.: Condens. Matter* **26**, 183001 (2014).
- [97] J. Behler, “Constructing high-dimensional neural network potentials: A tutorial review,” *International Journal of Quantum Chemistry* **115**, 1032–1050 (2015).
- [98] J. Behler, “First Principles Neural Network Potentials for Reactive Simulations of Large Molecular and Condensed Systems,” *Angewandte Chemie International Edition* **56**, 12828–12840 (2017).
- [99] J. Behler, “Atom-centered symmetry functions for constructing high-dimensional

- neural network potentials,” The Journal of Chemical Physics **134**, 074106 (2011), <https://doi.org/10.1063/1.3553717> .
- [100] A. P. Bartók, R. Kondor, and G. Csányi, “On representing chemical environments,” Phys. Rev. B **87**, 184115 (2013).
- [101] S. Jindal, S. Chiriki, and S. S. Bulusu, “Spherical harmonics based descriptor for neural network potentials: Structure and dynamics of Au<sub>147</sub> nanocluster,” J. Chem. Phys. **146**, 204301 (2017).
- [102] A. P. Bartók, M. C. Payne, R. Kondor, and G. Csányi, “Gaussian approximation potentials: The accuracy of quantum mechanics, without the electrons,” Phys. Rev. Lett. **104**, 136403 (2010).
- [103] R. Kondor, “A novel set of rotationally and translationally invariant features for images based on the non-commutative bispectrum,” (2007), arXiv:cs/0701127 [cs.CV] .
- [104] B. Jiang and H. Guo, “Permutation invariant polynomial neural network approach to fitting potential energy surfaces,” J. Chem. Phys. **139**, 054112 (2013).
- [105] J. Behler, “Neural network potential-energy surfaces in chemistry: a tool for large-scale simulations,” Phys. Chem. Chem. Phys. **13**, 17930–17955 (2011).
- [106] J. Behler, “Constructing high-dimensional neural network potentials: A tutorial review,” International Journal of Quantum Chemistry **115**, 1032–1050 (2015), <https://onlinelibrary.wiley.com/doi/pdf/10.1002/qua.24890> .
- [107] M. Eckhoff and J. Behler, “High-dimensional neural network potentials for magnetic systems using spin-dependent atom-centered symmetry functions,” npj Computational Materials **7**, 170 (2021).
- [108] J. Behler, “Four generations of high-dimensional neural network potentials,” Chem. Rev. **121**, 10037—10072 (2021).
- [109] T. Ko, J. Finkler, S. Goedecker, and J. Behler, “A fourth-generation high-dimensional neural network potential with accurate electrostatics including non-local charge transfer,” Nat. Commun. **12**, 398 (2021).
- [110] A. Wald, *Statistical decision functions* (Wiley, 1950).
- [111] Cramér, H., *On the mathematical theory of risk* (Centraltryckeriet, 1930).
- [112] B. Klebanov, S. T. Rachev, and F. J. Fabozzi, *Robust and Non-Robust Models in Statistics* (New York: Nova Scientific Publishers, Inc., 2009).
- [113] T. B. Blank and S. D. Brown, “Adaptive, global, extended kalman filters for training feedforward neural networks,” J. Chemom. **8**, 391–407 (1994).
- [114] R. E. Kalman, “A New Approach to Linear Filtering and Prediction Problems,” J. Basic Eng **82**, 35–45 (1960).
- [115] R. L. Stratonovich, “Optimum nonlinear systems which bring about a separation of a signal with constant parameters from noise,” Radiofizika **2:6**, 892–901 (1959).
- [116] R. L. Stratonovich, “On the theory of optimal non-linear filtering of random functions,” Theory of Probability and Its Applications **4**, 223–225 (1959).
- [117] R. L. Stratonovich, “Application of the markov processes theory to optimal filtering,” Radio Engineering and Electronic Physics **5:11**, 1–19 (1960).
- [118] R. L. Stratonovich, “Conditional markov processes,” Theory of Probability and Its Applications **5**, 156–178 (1960).
- [119] O. A. Stepanov, “Kalman filtering: Past and present. An outlook from Russia. (On the occasion of the 80th birthday of Rudolf Emil Kalman),” Gyroscopy and Navigation **2**, 105 (2011).
- [120] S. J. Julier and J. K. Uhlmann, “Unscented filtering and nonlinear estimation,” Proceedings of the IEEE **3**, 401–422 (2004).
- [121] E. Courses and T. Surveys, *Sigma-Point Filters: An Overview with Applications to Integrated Navigation and Vision Assisted Control. Nonlinear Statistical Signal Processing*

- Workshop* (2006 IEEE, Berlin Heidelberg, 2006) p. 201–202.
- [122] N. Artrith and J. Behler, “High-dimensional neural network potentials for metal surfaces: A prototype study for copper,” *Phys. Rev. B* **85**, 045439 (2012).
  - [123] R. D. Ruth, “A canonical integration technique,” *IEEE Transactions on Nuclear Science* **30**, 2669–2671 (1983).
  - [124] M. Tao, “Explicit symplectic approximation of nonseparable hamiltonians: Algorithm and long time performance,” *Phys. Rev. E* **94**, 043303 (2016).
  - [125] H. Yoshida, “Construction of higher order symplectic integrators,” *Physics Letters A* **150**, 262–268 (1990).
  - [126] J. Candy and W. Rozmus, “A symplectic integration algorithm for separable hamiltonian functions,” *Journal of Computational Physics* **92**, 230–256 (1991).
  - [127] S. Blanes and P. Moan, “Practical symplectic partitioned runge–kutta and runge–kutta–nystrom methods,” *Journal of Computational and Applied Mathematics* **142**, 313–330 (2002).
  - [128] J. L. Lagrange, “*Mécanique analytique*. Vol. 1,” (1811).
  - [129] J. L. Lagrange, “*Mécanique analytique*. Vol. 2,” (1815).
  - [130] S. H. Schot, “Jerk: The time rate of change of acceleration,” *American Journal of Physics* **46**, 1090–1094 (1978).
  - [131] C. Runge, “Über die numerische Auflösung von Differentialgleichungen,” *Mathematische Annalen* **46**, 167–178 (1895).
  - [132] W. Kutta, “Beitrag zur näherungsweisen Integration totaler Differentialgleichungen,” *Zeit. Math. Phys.* **46**, 435–53 (1901).
  - [133] J. Stoer and R. Bulirsch, *Einfuehrung in die Numerische Mathematik II* (Springer, Berlin; Heidelberg, 1973).
  - [134] P. Schofield, “Computer simulation studies of the liquid state,” *Computer Physics Communications* **5**, 17–23 (1973).
  - [135] D. Beeman, “Some multistep methods for use in molecular dynamics calculations,” *Journal of Computational Physics* **20**, 130–139 (1976).
  - [136] M. Levitt, H. Meirovitch, and R. Huber, “Integrating the equations of motion,” *Journal of Molecular Biology* **168**, 617–620 (1983).
  - [137] E. Hairer, C. Lubich, and G. Wanner, “Geometric numerical integration illustrated by the Störmer–Verlet method,” *Acta Numerica* **12**, 399–450 (2003).
  - [138] R. A. Lippert, K. J. Bowers, R. O. Dror, M. P. Eastwood, B. A. Gregersen, J. L. Klepeis, I. Kolossvary, and D. E. Shaw, “A common, avoidable source of error in molecular dynamics integrators,” *The Journal of Chemical Physics* **126**, 046101 (2007), <https://doi.org/10.1063/1.2431176>.
  - [139] M. P. Allen and D. J. Tildesley, *Computer Simulation of Liquids* (Clarendon Press, USA, 1989).
  - [140] E. Forest and R. D. Ruth, “Fourth-order symplectic integration,” *Physica D: Nonlinear Phenomena* **43**, 105–117 (1990).
  - [141] I. Omelyan, I. Mryglod, and R. Folk, “Optimized forest–ruth- and suzuki-like algorithms for integration of motion in many-body systems,” *Computer Physics Communications* **146**, 188–202 (2002).
  - [142] R. D. Skeel, “Variable Step Size Destabilizes the Störmer/Leapfrog/Verlet Method,” *BIT Numerical Mathematics* **33**, 172–175 (1993).
  - [143] W. C. Swope, H. C. Andersen, P. H. Berens, and K. R. Wilson, “A computer simulation method for the calculation of equilibrium constants for the formation of physical clusters of molecules: Application to small water clusters,” *J. Chem. Phys.* **76**, 637 (1982).
  - [144] H. C. Andersen, “Molecular dynamics simulations at constant pressure and/or temperature,” *J. Chem. Phys.* **72**, 2384–2393 (1980).

- [145] W. G. Hoover, A. J. C. Ladd, and B. Moran, “High-Strain-Rate Plastic Flow Studied via Nonequilibrium Molecular Dynamics,” *Phys. Rev. Lett.* **48**, 1818–1820 (1982).
- [146] J. M. Haile and S. Gupta, “Extensions of the molecular dynamics simulation method. II. Isothermal systems,” *The Journal of Chemical Physics* **79**, 3067–3076 (1983), <https://doi.org/10.1063/1.446137> .
- [147] S. Nosé, “A unified formulation of the constant temperature molecular dynamics methods,” *J. Chem. Phys.* **81**, 511–519 (1984).
- [148] W. G. Hoover, “Canonical dynamics: Equilibrium phase-space distributions,” *Phys. Rev. A* **31**, 1695–1697 (1985).
- [149] D. M. Heyes, G. P. Morriss, and D. J. Evans, “Nonequilibrium molecular dynamics study of shear flow in soft disks,” *The Journal of Chemical Physics* **83**, 4760–4766 (1985), <https://doi.org/10.1063/1.449001> .
- [150] W. G. Hoover, “Canonical dynamics: Equilibrium phase-space distributions,” *Phys. Rev. A* **31**, 1695–1697 (1985).
- [151] D. Frenkel and B. Smit, *Understanding Molecular Simulation: From Algorithms to Applications*, 2nd ed., Computational Science Series, Vol. 1 (Academic Press, San Diego, 2002).
- [152] J. W. Gibbs, “Elementary Principles in Statistical Mechanics, Developed with especial Reference to the Rational Foundations of Thermodynamics,” *Bull. Amer. Math. Soc.* **12**, 194–210 (1906).
- [153] R. F. Fox, “A Review of: “Equilibrium and nonequilibrium statistical mechanics, By R. Balescu (John Wiley & Sons, New York, 1975)” and “Statistical Physics, by A. Isihara (Academic Press, New York, 1971)”,” *Transport Theory and Statistical Physics* **6**, 77–79 (1977), <https://doi.org/10.1080/00411457708247951> .
- [154] E. F. Caldin, “Tunneling in proton-transfer reactions in solution,” *Chemical Reviews* **69**, 135–156 (1969), <https://doi.org/10.1021/cr60257a006> .
- [155] S. Habershon, D. E. Manolopoulos, T. E. Markland, and T. F. Miller, “Ring-Polymer Molecular Dynamics: Quantum Effects in Chemical Dynamics from Classical Trajectories in an Extended Phase Space,” *Annual Review of Physical Chemistry* **64**, 387–413 (2013), PMID: 23298242, <https://doi.org/10.1146/annurev-physchem-040412-110122> .
- [156] I. Craig and D. Manolopoulos, “Quantum statistics and classical mechanics: Real time correlation functions from ring polymer molecular dynamics,” *JOURNAL OF CHEMICAL PHYSICS* **121**, 3368–3373 (2004).
- [157] A. Wipf, *Statistical approach to quantum field theory: an introduction*, 2nd ed. (Springer, Heidelberg, 2013).
- [158] R. Welsch, K. Song, Q. Shi, S. C. Althorpe, and T. F. Miller, “Non-equilibrium dynamics from rpmd and cmd,” *The Journal of Chemical Physics* **145**, 204118 (2016), <https://doi.org/10.1063/1.4967958> .
- [159] D. Chandler and P. G. Wolynes, “Exploiting the isomorphism between quantum theory and classical statistical mechanics of polyatomic fluids,” *The Journal of Chemical Physics* **74**, 4078–4095 (1981), <https://doi.org/10.1063/1.441588> .
- [160] R. Collepardo-Guevara, Y. V. Suleimanov, and D. E. Manolopoulos, “Bimolecular reaction rates from ring polymer molecular dynamics,” *The Journal of Chemical Physics* **130**, 174713 (2009), <https://doi.org/10.1063/1.3127145> .
- [161] Y. V. Suleimanov, R. Collepardo-Guevara, and D. E. Manolopoulos, “Bimolecular reaction rates from ring polymer molecular dynamics: Application to  $\text{H} + \text{CH}_4 \rightarrow \text{H}_2 + \text{CH}_3$ ,” *The Journal of Chemical Physics* **134**, 044131 (2011), <https://doi.org/10.1063/1.3533275> .
- [162] Y. V. Suleimanov, “Surface Diffusion of Hydrogen on Ni(100) from Ring Polymer Molecular Dynamics,” *The Journal of Physical Chemistry C* **116**, 11141–11153 (2012),

- <https://doi.org/10.1021/jp302453z> .
- [163] R. Pérez de Tudela, F. J. Aoiz, Y. V. Suleimanov, and D. E. Manolopoulos, “Chemical Reaction Rates from Ring Polymer Molecular Dynamics: Zero Point Energy Conservation in  $\text{Mu} + \text{H}_2 \rightarrow \text{MuH} + \text{H}$ ,” *The Journal of Physical Chemistry Letters* **3**, 493–497 (2012), pMID: 26286053, <https://doi.org/10.1021/jz201702q> .
  - [164] T. F. Miller and D. E. Manolopoulos, “Quantum diffusion in liquid para-hydrogen from ring-polymer molecular dynamics,” *The Journal of Chemical Physics* **122**, 184503 (2005), <https://doi.org/10.1063/1.1893956> .
  - [165] M. F. Herman, E. J. Bruskin, and B. J. Berne, “On path integral monte carlo simulations,” *The Journal of Chemical Physics* **76**, 5150–5155 (1982), <https://doi.org/10.1063/1.442815> .
  - [166] F. Gatti, B. Lasorne, H.-D. Meyer, and A. Nauts, *Applications of Quantum Dynamics in Chemistry* (Springer International Publishing AG, 2017).
  - [167] M. Ceriotti, M. Parrinello, T. E. Markland, and D. E. Manolopoulos, “Efficient stochastic thermostating of path integral molecular dynamics,” *Journal of Chemical Physics* **133** (2010), 10.1063/1.3489925.
  - [168] F. Briec, H. Dammak, and M. Hayoun, “Quantum thermal bath for path integral molecular dynamics simulation,” *Journal of chemical theory and computation* **12** (2016), 10.1021/acs.jctc.5b01146.
  - [169] G. Bussi and M. Parrinello, “Accurate sampling using Langevin dynamics,” *Physical review. E, Statistical, nonlinear, and soft matter physics* **75**, 056707 (2007).
  - [170] D. J. Auerbach, N. Hertl, S. M. Janke, M. Kammler, A. Kandratsenka, L. Lecroart, and S. Wille, “Molecular Dynamics Tian Xia 2 (MDT2): program for simulating the scattering of atoms and molecules from surfaces. Available at [https://github.com/akandra/md\\_tian2](https://github.com/akandra/md_tian2),” (2021).
  - [171] G. Kresse and J. Furthmüller, “Efficient iterative schemes for ab initio total-energy calculations using a plane-wave basis set,” *Phys. Rev. B* **54**, 11169–11186 (1996).
  - [172] G. Kresse, “Ab initio molecular dynamics for liquid metals,” *Journal of Non-Crystalline Solids* **192-193**, 222–229 (1995), *structure of Non-Crystalline Materials* 6.
  - [173] G. Kresse and J. Furthmüller, “Efficiency of ab-initio total energy calculations for metals and semiconductors using a plane-wave basis set,” *Computational Materials Science* **6**, 15–50 (1996).
  - [174] G. Kresse and D. Joubert, “From ultrasoft pseudopotentials to the projector augmented-wave method,” *Phys. Rev. B* **59**, 1758–1775 (1999).
  - [175] P. E. Blöchl, “Projector augmented-wave method,” *Phys. Rev. B* **50**, 17953–17979 (1994).
  - [176] P. E. Blöchl, O. Jepsen, and O. K. Andersen, “Improved tetrahedron method for brillouin-zone integrations,” *Phys. Rev. B* **49**, 16223–16233 (1994).
  - [177] H. J. Monkhorst and J. D. Pack, “Special points for brillouin-zone integrations,” *Phys. Rev. B* **13**, 5188–5192 (1976).
  - [178] V. Blum, R. Gehrke, F. Hanke, P. Havu, V. Havu, X. Ren, K. Reuter, and M. Scheffler, “Ab initio molecular simulations with numeric atom-centered orbitals,” *Comput. Phys. Commun.* **180**, 2175–2196 (2009).
  - [179] V. Havu, V. Blum, P. Havu, and M. Scheffler, “Efficient  $\mathcal{O}(n)$  integration for all-electron electronic structure calculation using numeric basis functions,” *Journal of Computational Physics* **228**, 8367–8379 (2009).
  - [180] X. Ren, P. Rinke, V. Blum, J. Wieferink, A. Tkatchenko, A. Sanfilippo, K. Reuter, and M. Scheffler, “Resolution-of-identity approach to hartree-fock, hybrid density functionals, RPA, MP2 and GW with numeric atom-centered orbital basis functions,” *New Journal of Physics* **14**, 053020 (2012).
  - [181] A. Marek, V. Blum, R. Johanni, V. Havu, B. Lang, T. Auckenthaler, A. Heinecke, H.-J.



- Bungartz, and H. Lederer, “The ELPA library: scalable parallel eigenvalue solutions for electronic structure theory and computational science,” *Journal of Physics: Condensed Matter* **26**, 213201 (2014).
- [182] S. V. Levchenko, X. Ren, J. Wieferink, R. Johanni, P. Rinke, V. Blum, and M. Scheffler, “Hybrid functionals for large periodic systems in an all-electron, numeric atom-centered basis framework,” *Computer Physics Communications* **192**, 60–69 (2015).
- [183] W. P. Huhn and V. Blum, “One-hundred-three compound band-structure benchmark of post-self-consistent spin-orbit coupling treatments in density functional theory,” *Phys. Rev. Materials* **1**, 033803 (2017).
- [184] “Fritz haber institute ab initio molecular simulations fhi-aims - a users’ guide,” (Fritz Haber Institut, 2020).
- [185] E. v. Lenthe, E. J. Baerends, and J. G. Snijders, “Relativistic regular two-component hamiltonians,” *The Journal of Chemical Physics* **99**, 4597–4610 (1993), <https://doi.org/10.1063/1.466059>.
- [186] E. van Lenthe, J. G. Snijders, and E. J. Baerends, “The zero-order regular approximation for relativistic effects: The effect of spin-orbit coupling in closed shell molecules,” *The Journal of Chemical Physics* **105**, 6505–6516 (1996), <https://doi.org/10.1063/1.472460>.
- [187] J. Behler, “RuNNer - a neural network code for high-dimensional potential-energy surfaces,” (Universität Göttingen, 2022), [www.uni-goettingen.de/de/560580.html](http://www.uni-goettingen.de/de/560580.html).
- [188] D. J. Auerbach, S. M. Janke, and A. Kandratsenka, “Molecular Dynamics Tian Xia (md\_tian): program for simulating the scattering of atoms and molecules from surfaces. Available at [https://github.com/akandra/md\\_tian](https://github.com/akandra/md_tian),” (2016).
- [189] K. W. Jacobsen, J. K. Norskov, and M. J. Puska, “Interatomic interactions in the effective-medium theory,” *Phys. Rev. B* **35**, 7423–7442 (1987).
- [190] K. Jacobsen, P. Stoltze, and J. Nørskov, “A semi-empirical effective medium theory for metals and alloys,” *Surface Science* **366**, 394–402 (1996).
- [191] S. M. Janke, *Theoretical Description of Hydrogen Atom Scattering off Noble Metals* (PhD thesis, Georg-August Universität Göttingen, 2016).
- [192] M. Kammler, *MD simulations of atomic hydrogen atom scattering from zero band-gap materials* (PhD thesis, Georg-August Universität Göttingen, 2019).
- [193] JGraph, “draw.io software version 15.5.2 - javascript diagramming and whiteboard application <https://www.diagrams.net/>,” Github Repository (<https://github.com/jgraph/drawio>) (2021).
- [194] E. Yoshikawa, *Taiko* (A. Knaus Verlag, München, 1993).
- [195] S. Tunbull, *Toyotomi Hideyoshi* (Oxford, 2010).
- [196] W. H. Samonides, *Patronizing Images: Kodai-in and Toyotomi Hideyoshi at Kodai-ji* (Japan Review, 1996).
- [197] J. Behler, “RuNNer online manual,” (2022).
- [198] A. Singraber, J. Behler, and C. Dellago, “Library-Based LAMMPS Implementation of High-Dimensional Neural Network Potentials,” *J. Chem. Theory Comput.* **15**, 1827–1840 (2019).
- [199] S. Plimpton, “Fast Parallel Algorithms for Short-Range Molecular Dynamics,” *Journal of Computational Physics* **117**, 1–19 (1995).
- [200] Y. Li and G. Wahnström, “Nonadiabatic effects in hydrogen diffusion in metals,” *Physical Review Lett* **68**, 3444–3447 (1992).
- [201] Y. Li and G. Wahnström, “Molecular-dynamics simulation of hydrogen diffusion in palladium,” *Physical Review B* **46**, 14528–14542 (1992).
- [202] J. Juaristi, M. Alducin, R. Díez Muiño, H. Busnengo, and S. A., “Role of electron-hole pair excitations in the dissociative adsorption of diatomic molecules on metal surfaces,” *Physical Review Letters* **100**, 116102 (2008).

- [203] A. Stukowski, “Visualization and analysis of atomistic simulation data with OVITO-the Open Visualization Tool,” *Modelling and Simulation in Materials Science and Engineering* **18**, 015012 (2010).
- [204] S. Wille, H. Jiang, O. Bünermann, A. M. Wodtke, J. Behler, and A. Kandratsenka, “An experimentally validated neural-network potential energy surface for h-atom on free-standing graphene in full dimensionality,” *Phys. Chem. Chem. Phys.* **22**, 26113–26120 (2020).
- [205] T. Gray and N. Mann, *The Elements – A Visual Exploration of Every Known Atom in the Universe* (Little Brown, 2001).
- [206] C. Lee, X. Wei, J. W. Kysar, and J. Hone, “Measurement of the elastic properties and intrinsic strength of monolayer graphene,” *Science* **321**, 385–388 (2008), <https://www.science.org/doi/pdf/10.1126/science.1157996> .
- [207] R. Saito, G. Dresselhaus, and M. S. Dresselhaus, *Physical Properties of Carbon Nanotubes* (PUBLISHED BY IMPERIAL COLLEGE PRESS AND DISTRIBUTED BY WORLD SCIENTIFIC PUBLISHING CO., 1998) <https://www.worldscientific.com/doi/pdf/10.1142/p080> .
- [208] B. Dunlap and J. Boettger, “Local-density-functional study of the fullerenes, graphene and graphite,” *JOURNAL OF PHYSICS B-ATOMIC MOLECULAR AND OPTICAL PHYSICS* **29**, 4907–4913 (1996).
- [209] W. Andreoni, *The Physics of Fullerene-Based and Fullerene-Related Materials* (Springer, Berlin, 2000).
- [210] P. R. Wallace, “The band theory of graphite,” *Phys. Rev.* **71**, 622–634 (1947).
- [211] J. W. McClure, “Diamagnetism of graphite,” *Phys. Rev.* **104**, 666–671 (1956).
- [212] J. Tersoff, “Empirical interatomic potential for carbon, with applications to amorphous carbon,” *Phys. Rev. Lett.* **61**, 2879–2882 (1988).
- [213] S. G. Srinivasan, A. C. T. van Duin, and P. Ganesh, “Development of a reaxff potential for carbon condensed phases and its application to the thermal fragmentation of a large fullerene,” *The Journal of Physical Chemistry A* **119**, 571–580 (2015), PMID: 25562718, <https://doi.org/10.1021/jp510274e> .
- [214] A. Singh, X. Chen, Y. Li, S. Koric, and E. Guleryuz, *AIAA Scitech 2020 Forum* (AIAA Scitech 2020 Forum, 2020) <https://arc.aiaa.org/doi/pdf/10.2514/6.2020-1861> .
- [215] Shaidu, Y., Küçükbenli, E., Lot, R. et al., “A systematic approach to generating accurate neural network potentials: the case of carbon.” *npj Comput Mater* **7**, 52 (2021).
- [216] P. Rowe, G. Csányi, D. Alfè, and A. Michaelides, “Development of a machine learning potential for graphene,” *Physical Review B* **97** (2018), 10.1103/physrevb.97.054303.
- [217] P. Rowe, V. L. Deringer, P. Gasparotto, G. Csányi, and A. Michaelides, “An accurate and transferable machine learning potential for carbon,” *The Journal of Chemical Physics* **153**, 034702 (2020), <https://doi.org/10.1063/5.0005084> .
- [218] M. Wen and E. B. Tadmor, “Hybrid neural network potential for multilayer graphene,” *Phys. Rev. B* **100**, 195419 (2019).
- [219] R. Z. Khaliullin, H. Eshet, T. D. Kühne, J. Behler, and M. Parrinello, “Graphite-diamond phase coexistence study employing a neural-network mapping of the ab initio potential energy surface,” *Phys. Rev. B* **81**, 100103 (2010).
- [220] R. Z. Khaliullin, H. Eshet, T. D. Kühne, J. Behler, and M. Parrinello, “Nucleation mechanism for the direct graphite-to-diamond phase transition,” *Nature Materials* **10**, 693–697 (2011).
- [221] V. L. Deringer and G. Csányi, “Machine learning based interatomic potential for amorphous carbon,” *Phys. Rev. B* **95**, 094203 (2017).
- [222] K. Novoselov, A. Geim, S. Morozov, D. Jiang, Y. Zhang, S. Dubonos, I. Grigorieva, and A. Firsov, “Electric field effect in atomically thin carbon films.” *Science* **306**, 666–669

- (2004).
- [223] N. Media, “Nobel prizes,” Report (2018).
- [224] A. D. Zdetsis and E. N. Economou, “A pedestrian approach to the aromaticity of graphene and nanographene: Significance of huckel’s  $(4n+2)\pi$  electron rule,” *The Journal of Physical Chemistry C* **119**, 16991–17003 (2015), <https://doi.org/10.1021/acs.jpcc.5b04311> .
- [225] P. J. F. Harris, “Transmission electron microscopy of carbon: A brief history,” *C* **4** (2018), 10.3390/c4010004.
- [226] A. H. Castro Neto, F. Guinea, N. M. R. Peres, K. S. Novoselov, and A. K. Geim, “The electronic properties of graphene,” *Rev. Mod. Phys.* **81**, 109–162 (2009).
- [227] K. Novoselov, A. Geim, and S. e. a. Morozov, “Two-dimensional gas of massless dirac fermions in graphene,” *Nature* **438**, 197–200 (2005).
- [228] M. Schmitz, T. Ouaj, Z. Winter, K. Rubi, K. Watanabe, T. Taniguchi, U. Zeitler, B. Beschoten, and C. Stampfer, “Fractional quantum hall effect in CVD-grown graphene,” *2D Materials* **7**, 041007 (2020).
- [229] X. Qian, J. Liu, L. Fu, and J. Li, “Quantum spin hall effect in two-dimensional transition metal dichalcogenides,” *Science* **346**, 1344–1347 (2014), <https://www.science.org/doi/pdf/10.1126/science.1256815> .
- [230] Y. Cao, V. Fatemi, and S. e. a. Fang, “Unconventional superconductivity in magic-angle graphene superlattices,” *Nature* **556**, 43//50 (2018).
- [231] H. M. Hill, “Twisted bilayer graphene enters a new phase,” *Physics Today* **73**, 18–20 (2020), <https://doi.org/10.1063/PT.3.4384> .
- [232] M. Oh, K. Nuckolls, D. Wong, and et al, “Evidence for unconventional superconductivity in twisted bilayer graphene,” *Nature* **600**, 240–245 (2021).
- [233] M. Craciun, S. Russo, and M. e. a. Yamamoto, “Trilayer graphene is a semimetal with a gate-tunable band overlap,” *Nature Nanotech* **4**, 383–388 (2009).
- [234] M. Christos, S. Sachdev, and M. S. Scheurer, “Correlated insulators, semimetals, and superconductivity in twisted trilayer graphene,” *Phys. Rev. X* **12**, 021018 (2022).
- [235] T. Paronyan, A. Thapa, and A. e. a. Sherehiy, “Incommensurate graphene foam as a high capacity lithium intercalation anode,” *Sci. Rep.* **7**, 39944 (2017).
- [236] F. Schütt, F. Rasch, N. Deka, A. Reimers, L. M. Saure, S. Kaps, J. Rank, J. Carstensen, Y. Kumar Mishra, D. Misseroni, A. Romani Vázquez, M. R. Lohe, A. Shaygan Nia, N. M. Pugno, X. Feng, and R. Adelung, “Electrically powered repeatable air explosions using microtubular graphene assemblies,” *Materials Today* **48**, 7–17 (2021).
- [237] J. S. Bunch, S. S. Verbridge, J. S. Alden, A. M. van der Zande, J. M. Parpia, H. G. Craighead, and P. L. McEuen, “Impermeable atomic membranes from graphene sheets,” *Nano Letters* **8**, 2458–2462 (2008), pMID: 18630972, <https://doi.org/10.1021/nl801457b> .
- [238] M. Lozada-Hidalgo, S. Zhang, and S. e. a. Hu, “Scalable and efficient separation of hydrogen isotopes using graphene-based electrochemical pumping,” *Nat Commun* **8**, 15215 (2017).
- [239] F. Rehman, F. Hussain, Z. Bhatti, M. Iqbal, F. Soomro, A. Ali, and K. Thebo, “Graphene-based composite membranes for isotope separation: Challenges and opportunities,” *Reviews in Inorganic Chemistry* (2021), 10.1515/revic-2021-0035.
- [240] P. Sun, Q. Yang, and W. e. a. Kuang, “Limits on gas impermeability of graphene,” *Nature* **5794**, 229–232 (2020).
- [241] G. Lu, K. Yu, Z. Wen, and J. Chen, “Semiconducting graphene: converting graphene from semimetal to semiconductor,” *Nanoscale* **5**, 1353–1368 (2013).
- [242] P. Avouris, Z. Chen, and V. Perebeinos, “Carbon-based electronics,” *Nature Nanotech* **2**, 605–615 (2007).
- [243] F. Bonaccorso, Z. Sun, and T. e. a. Hasan, “Graphene photonics and optoelectronics,” *Nature Photon* **4**, 611–622 (2010).

- [244] Y. Miura, H. Kasai, W. Diño, H. Nakanishi, and T. Sugimoto, “First principles studies for the dissociative adsorption of  $\text{H}_2$  on graphene,” *Journal of Applied Physics* **93**, 3395–3400 (2003), <https://doi.org/10.1063/1.1555701> .
- [245] A. Dillon, K. Jones, and T. e. a. Bekkedahl, “Storage of hydrogen in single-walled carbon nanotubes,” *Nature* **386**, 377–379 (1997).
- [246] R. Balog, B. Jørgensen, L. Nilsson, M. Andersen, E. Rienks, M. Bianchi, M. Fanetti, E. Laegsgaard, A. Baraldi, S. Lizzit, Z. Sljivancanin, F. Besenbacher, B. Hammer, T. G. Pedersen, P. Hofmann, and L. Hornekaer, “Bandgap opening in graphene induced by patterned hydrogen adsorption,” *Nature materials* **9**, 315–319 (2010).
- [247] J. O. Sofo, A. S. Chaudhari, and G. D. Barber, “Graphane: A two-dimensional hydrocarbon,” *Phys. Rev. B* **75**, 153401 (2007).
- [248] D. W. Boukhvalov and M. I. Katsnelson, “Chemical functionalization of graphene,” *Journal of Physics: Condensed Matter* **21**, 344205 (2009).
- [249] Z. Wang, P. Hu, and Q. Ge, “Gas surface interaction and surface reactions,” in *Springer Handbook of Surface Science*, edited by M. Rocca, T. S. Rahman, and L. Vattuone (Springer International Publishing, Cham, 2020) pp. 905–928.
- [250] Y. Ferro, F. Marinelli, and A. Allouche, “Density functional theory investigation of the diffusion and recombination of  $\text{H}$  on a graphite surface,” *Chemical Physics Letters* **368**, 609–615 (2003).
- [251] N. Rougeau, D. Teillet-Billy, and V. Sidis, “Double  $\text{H}$  atom adsorption on a cluster model of a graphite surface,” *Chemical Physics Letters* **431**, 135–138 (2006).
- [252] M. Bonfanti, B. Jackson, K. H. Hughes, I. Burghardt, and R. Martinazzo, “Quantum dynamics of hydrogen atoms on graphene. ii. sticking,” *The Journal of Chemical Physics* **143**, 124704 (2015), <https://doi.org/10.1063/1.4931117> .
- [253] Z. Sljivancanin, E. Rauls, L. Hornekaer, W. Xu, F. Besenbacher, and B. Hammer, “Extended atomic hydrogen dimer configurations on the graphite(0001) surface,” *The Journal of Chemical Physics* **131**, 084706 (2009), <https://doi.org/10.1063/1.3187941> .
- [254] S. Hu, M. Lozada-Hidalgo, and F. e. a. Wang, “Proton transport through one-atom-thick crystals,” *Nature* **516**, 227–230 (2014).
- [255] I. Poltavsky, L. Zheng, M. Mortazavi, and A. Tkatchenko, “Quantum tunneling of thermal protons through pristine graphene,” *The Journal of Chemical Physics* **148**, 204707 (2018), <https://doi.org/10.1063/1.5024317> .
- [256] L. Hornekaer, A. Baurichter, V. V. Petrunin, D. Field, and A. C. Luntz, “Importance of surface morphology in interstellar  $\text{H}_2$  formation,” *Science* **302**, 1943–1946 (2003), <https://www.science.org/doi/pdf/10.1126/science.1090820> .
- [257] D. Hollenbach and E. E. Salpeter, “Surface Recombination of Hydrogen Molecules,” *The Astrophysical Journal* **163**, 155 (1971).
- [258] V. Wakelam, E. Bron, S. Cazaux, F. Dulieu, C. Gry, P. Guillard, E. Habart, L. Hornekær, S. Morisset, G. Nyman, V. Pirronello, S. D. Price, V. Valdivia, G. Vidali, and N. Watanabe, “ $\text{H}_2$  formation on interstellar dust grains: The viewpoints of theory, experiments, models and observations,” *Molecular Astrophysics* **9**, 1–36 (2017).
- [259] O. Biham, I. Furman, V. Pirronello, and G. Vidali, “Master equation for hydrogen recombination on grain surfaces,” *The Astrophysical Journal* **553**, 595–603 (2001).
- [260] N. Katz, I. Furman, O. Biham, V. Pirronello, and G. Vidali, “Molecular hydrogen formation on astrophysically relevant surfaces,” *The Astrophysical Journal* **522**, 305–312 (1999).
- [261] J. Petucci, C. LeBlond, M. Karimi, and G. Vidali, “Diffusion, adsorption, and desorption of molecular hydrogen on graphene and in graphite,” *The Journal of Chemical Physics* **139**, 044706 (2013), <https://doi.org/10.1063/1.4813919> .
- [262] V. Pirronello, C. Liu, J. E. Roser, and G. Vidali, “Measurements of molecular hydrogen

- formation on carbonaceous grains,” *Astronomy and Astrophysics* **344**, 681–686 (1999).
- [263] G. Vidali, J. Roser, G. Manicó, V. Pirronello, H. B. Perets, and O. Biham, “Formation of molecular hydrogen on analogues of interstellar dust grains: experiments and modelling,” *Journal of Physics: Conference Series* **6**, 36–58 (2005).
- [264] Schlappbach, L. and Züttel, A., “Hydrogen-storage materials for mobile applications,” *Nature* **414**, 353–358 (2001).
- [265] V. Tozzini and V. Pellegrini, “Prospects for hydrogen storage in graphene,” *Phys. Chem. Chem. Phys.* **15**, 80–89 (2013).
- [266] R. Nagar, B. P. Vinayan, S. S. Samantaray, and S. Ramaprabhu, “Recent advances in hydrogen storage using catalytically and chemically modified graphene nanocomposites,” *J. Mater. Chem. A* **5**, 22897–22912 (2017).
- [267] J. Abe, A. Popoola, E. Ajenifuja, and O. Popoola, “Hydrogen energy, economy and storage: Review and recommendation,” *International Journal of Hydrogen Energy* **44**, 15072–15086 (2019).
- [268] V. Meregalli and M. Parrinello, “Review of theoretical calculations of hydrogen storage in carbon-based materials,” *Appl. Phys. A* **72**, 143–146 (2001).
- [269] S. Zhou, G. Gweon, and A. e. a. Fedorov, “Substrate-induced bandgap opening in epitaxial graphene,” *Nat. Mater.* **6**, 770–775 (2007).
- [270] D. Haberer, D. V. Vyalikh, S. Taioli, B. Dora, M. Farjam, J. Fink, D. Marchenko, T. Pichler, K. Ziegler, S. Simonucci, M. S. Dresselhaus, M. Knupfer, B. Büchner, and A. Grüneis, “Tunable band gap in hydrogenated quasi-free-standing graphene,” *Nano Letters* **10**, 3360–3366 (2010), pMID: 20695447, <https://doi.org/10.1021/nl101066m>.
- [271] D. Haberer, L. Petaccia, Y. Wang, H. Quian, M. Farjam, S. Jafari, H. Sachdev, A. Federov, D. Usachov, D. Vyalikh, X. Liu, O. Vilkov, V. Adamchuk, S. Irle, M. Knupfer, B. Büchner, and A. Grüneis, “Electronic properties of hydrogenated quasi-free-standing graphene,” *physica status solidi (b)* **248**, 2639–2643 (2011).
- [272] D. C. Elias, R. R. Nair, T. M. G. Mohiuddin, S. V. Morozov, P. Blake, M. P. Halsall, A. C. Ferrari, D. W. Boukhvalov, M. I. Katsnelson, A. K. Geim, and K. S. Novoselov, “Control of graphene’s properties by reversible hydrogenation: Evidence for graphane,” *Science* **323**, 610–613 (2009), <https://www.science.org/doi/pdf/10.1126/science.1167130>.
- [273] R. Grassi, T. Low, and M. Lundstrom, “Scaling of the energy gap in pattern-hydrogenated graphene,” *Nano Letters* **11**, 4574–4578 (2011), pMID: 21999430, <https://doi.org/10.1021/nl2017338>.
- [274] K. Tada, J. Haruyama, H. X. Yang, M. Chshiev, T. Matsui, and H. Fukuyama, “Graphene magnet realized by hydrogenated graphene nanopore arrays,” *Applied Physics Letters* **99**, 183111 (2011), <https://doi.org/10.1063/1.3653286>.
- [275] C. Lin, Y. Feng, Y. Xiao, M. Dürr, X. Huang, X. Xu, R. Zhao, E. Wang, X.-Z. Li, and Z. Hu, “Direct observation of ordered configurations of hydrogen adatoms on graphene,” *Nano Letters* **15**, 903–908 (2015), pMID: 25621539, <https://doi.org/10.1021/nl503635x>.
- [276] S. Naghdi, G. Sanchez-Arriaga, and K. Y. Rhee, “Tuning the work function of graphene toward application as anode and cathode,” *Journal of Alloys and Compounds* **805**, 1117–1134 (2019).
- [277] S. E. Huber, T. Hell, M. Probst, and A. Ostermann, “Numerical investigation of the elastic scattering of hydrogen (isotopes) and helium at graphite (0001) surfaces at beam energies of 1 to 4 eV using a split-step fourier method,” *Theor. Chem. Acc.* **132**, 1337 (2013).
- [278] T. Aizawa, R. Souda, S. Otani, Y. Ishizawa, and C. Oshima, “Bond softening in monolayer graphite formed on transition-metal carbide surfaces,” *Phys. Rev. B* **42**, 11469–11478 (1990).
- [279] T. A. et al., “Phonon-dispersion of monolayer graphite on pt(111) and nbc surfaces –

- bond softening and interface structures,” *Surface Science* **260**, 311 (1992).
- [280] A. A. Taleb and D. Farías, “Phonon dynamics of graphene on metals,” *Journal of Physics: Condensed Matter* **28**, 103005 (2016).
- [281] A. Politano, A. Marino, D. Campi, D. Farias, R. Miranda, and G. Chiarello, “Elastic properties of a macroscopic graphene sample from phonon dispersion measurements,” *Carbon* **50**, 4903–4910 (2012).
- [282] I. Hamada and M. Otani, “Comparative van der Waals density-functional study of graphene on metal surfaces,” *PHYSICAL REVIEW B* **82** (2010), 10.1103/PhysRevB.82.153412.
- [283] Inkscape Project, “Inkscape version 0.92.5,” (2004–2005), <https://inkscape.org>.
- [284] I. Popov, K. Bozhenko, and A. Boldyrev, “Is graphene aromatic?” *Nano Research* **5**, 117–123 (2012).
- [285] M. E. Fornace, J. Lee, K. Miyamoto, F. R. Manby, and T. F. Miller, “Embedded mean-field theory,” *Journal of Chemical Theory and Computation* **11**, 568–580 (2015), pMID: 26580914, <https://doi.org/10.1021/ct5011032>.
- [286] F. Ding, F. R. Manby, and T. F. Miller, “Embedded mean-field theory with block-orthogonalized partitioning,” *Journal of Chemical Theory and Computation* **13**, 1605–1615 (2017), pMID: 28245122, <https://doi.org/10.1021/acs.jctc.6b01065>.
- [287] F. Ding, T. Tsuchiya, F. R. Manby, and T. F. Miller, “Linear-response time-dependent embedded mean-field theory,” *Journal of Chemical Theory and Computation* **13**, 4216–4227 (2017), pMID: 28783359, <https://doi.org/10.1021/acs.jctc.7b00666>.
- [288] D. Brenner, O. Shenderova, J. Harrison, S. Stuart, B. Ni, and S. Sinnott, “A second-generation reactive empirical bond order (REBO) potential energy expression for hydrocarbons,” *JOURNAL OF PHYSICS-CONDENSED MATTER* **14**, 783–802 (2002).
- [289] D. W. Brenner, “Empirical potential for hydrocarbons for use in simulating the chemical vapor deposition of diamond films,” *Phys. Rev. B* **42**, 9458–9471 (1990).
- [290] D. W. Brenner, “Erratum: Empirical potential for hydrocarbons for use in simulating the chemical vapor deposition of diamond films,” *Phys. Rev. B* **46**, 1948–1948 (1992).
- [291] S. V. Dmitriev, J. A. Baimova, A. V. Savin, and Y. S. Kivshar, “Ultimate strength, ripples, sound velocities, and density of phonon states of strained graphene,” *Computational Materials Science* **53**, 194–203 (2012).
- [292] D. W. Brenner, “Empirical potential for hydrocarbons for use in simulating the chemical vapor deposition of diamond films,” *Phys. Rev. B* **42**, 9458–9471 (1990).
- [293] S. J. Stuart, A. B. Tutein, and J. A. Harrison, “A reactive potential for hydrocarbons with intermolecular interactions,” *The Journal of Chemical Physics* **112**, 6472–6486 (2000), <https://doi.org/10.1063/1.481208>.
- [294] K. Chenoweth, A. C. T. van Duin, and W. A. Goddard, “Reaxff reactive force field for molecular dynamics simulations of hydrocarbon oxidation,” *The Journal of Physical Chemistry A* **112**, 1040–1053 (2008), <https://doi.org/10.1021/jp709896w>.
- [295] J. Petucci, S. Semone, C. LeBlond, M. Karimi, and G. Vidali, “Formation of h<sub>2</sub> on graphene using eley-rideal and langmuir-hinshelwood processes,” *The Journal of Chemical Physics* **149**, 014702 (2018), <https://doi.org/10.1063/1.5026691>.
- [296] G. Van Rossum and F. L. Drake Jr, *Python tutorial* (Centrum voor Wiskunde en Informatica Amsterdam, The Netherlands, 1995).
- [297] G. Van Rossum and F. L. Drake, *Python 3 Reference Manual* (CreateSpace, Scotts Valley, CA, 2009).
- [298] M. Pilgrim and S. Willison, *Dive Into Python 3*, Vol. 2 (Springer, 2009).
- [299] J. D. Hunter, “Matplotlib A 2D Graphics Environment,” *Computing in Science Engineering* **9**, 90–95 (2007).
- [300] T. Williams, C. Kelley, and many others, “Gnuplot 5.2 patchlevel 8: an interactive

- plotting program,” <http://gnuplot.sourceforge.net/> (2019).
- [301] “Supporting information for doctoral thesis,” (2022), [https://github.com/SebastianWille/movies\\_thesis](https://github.com/SebastianWille/movies_thesis).
- [302] M. Bonfanti, R. Martinazzo, G. F. Tantardini, and A. Ponti, “Physisorption and Diffusion of Hydrogen Atoms on Graphite from Correlated Calculations on the H-Coronene Model System,” *The Journal of Physical Chemistry C* **111**, 5825–5829 (2007), <https://doi.org/10.1021/jp070616b>.
- [303] Y. Wang, H.-J. Qian, K. Morokuma, and S. Irle, “Coupled cluster and density functional theory calculations of atomic hydrogen chemisorption on pyrene and coronene as model systems for graphene hydrogenation,” *The Journal of Physical Chemistry A* **116**, 7154–7160 (2012), pMID: 22646976, <https://doi.org/10.1021/jp3023666>.
- [304] X. Sha, B. Jackson, D. Lemoine, and B. Lepetit, “Quantum studies of h atom trapping on a graphite surface,” *The Journal of Chemical Physics* **122**, 014709 (2005), <https://doi.org/10.1063/1.1827601>.
- [305] E. R. M. Davidson, J. Klimeš, D. Alfè, and A. Michaelides, “Cooperative interplay of van der waals forces and quantum nuclear effects on adsorption: H at graphene and at coronene,” *ACS Nano* **8**, 9905–9913 (2014), pMID: 25300825, <https://doi.org/10.1021/nn505578x>.
- [306] L. Hornekaer, “Stabilizing a c&#x2013;h bond on graphene with sound,” *Science* **364**, 331–332 (2019), <https://www.science.org/doi/pdf/10.1126/science.aax1980>.
- [307] X. Sha and B. Jackson, “First-principles study of the structural and energetic properties of h atoms on a graphite (0001) surface,” *Surface Science* **496**, 318–330 (2002).
- [308] T. Zecho, A. Güttler, X. Sha, B. Jackson, and J. Küppers, “Adsorption of hydrogen and deuterium atoms on the (0001) graphite surface,” *The Journal of Chemical Physics* **117**, 8486–8492 (2002), <https://doi.org/10.1063/1.1511729>.
- [309] OriginPro, Version 2022. OriginLab Corporation, Northampton, MA, USA.
- [310] H.-D. Meyer, G. A. Worth, M. H. Beck, A. Jäckle, U. Manthe, M. Ehara, A. Raab, M.-C. Heitz, S. Sukiasyan, C. Cattarius, S. Wefing, F. Gatti, M. Nest, F. Otto, M. R. Brill, O. Vendrell, M. Schröder, and D. Peláez, “The MCTDH Package, Version 8.5,” See <http://mctdh.uni-hd.de/> (2013).
- [311] N. Diaye, J. Coraux, T. N. Plasa, C. Busse, and T. Michely, “Structure of epitaxial graphene on ir(111),” *New Journal of Physics* **10**, 043033 (2008).
- [312] R. Brako, D. Šokčević, P. Lazić, and N. Atodiresei, “Graphene on the ir(111) surface: from van der waals to strong bonding,” *New Journal of Physics* **12**, 113016 (2010).